Structural Response to Vapour Cloud Explosions

Anqi Chen

Department of Civil and Environmental Engineering

Imperial College London

A thesis submitted for the degree of

Doctor of Philosophy

2014

Abstract

Over the last few decades, a number of major industrial blast accidents involving oil and gas installations occurred worldwide. These include the blast explosion that occurred in an industrial facility at Buncefield in the United Kingdom in 2005. Extensive damage occurred due to the blast, both to the industrial plant and surrounding buildings, as a consequence of much higher overpressures than would normally be expected from a vapour cloud explosion of this nature. In response to this event, a great deal of work was carried out on collecting and analysing available evidence from the incident in order to understand the explosion mechanism and estimate the overpressure levels within the gas cloud that formed. Subsequent investigations included the examination of steel switch boxes on the site located within the area covered by the vapour cloud. These boxes suffered varying degrees of damage and could therefore be used as overpressure indicators. A series of tests were commissioned after the event in order to compare the damage of the field boxes with detonation tests on similar boxes.

The thesis firstly reports on numerical studies carried out on assessing the damage to steel boxes subjected to both detonation and deflagration scenarios in order to aid the investigation of the explosion. Several modelling approaches are adopted in the numerical studies, including: Pure Lagrangian, Uncoupled Lagrangian-Eulerian and Coupled Lagrangian-Eulerian techniques. The numerical models are validated against data collected from gas detonation experiments on similar steel boxes. It is found that the coupled approach is able to predict the results accurately, although such an approach cannot be used in detailed parametric investigations due to its prohibitive computational demand. The pure Lagrangian approach is therefore used

instead, but the overpressure range in the parametric assessments is limited to 4 bar (side-on) as an adequate level of accuracy from this modelling technique cannot be ensured beyond this range. The results are summarised in the form of pressure-impulse diagrams, and typical residual shapes are selected with the aim of aiding forensic investigations of future explosion incidents.

The investigation is extended thereafter to the response of a steel-clad portal frame structures located outside the gas cloud and which suffered varying degrees of damage. A typical warehouse building is studied through a pure Lagrangian approach. A non-linear finite element model of a representative sub-structure of the warehouse wall is validated against a full scale test carried out at Imperial College London. A series of pressure-impulse diagrams of the sub-structure is then constructed based on the results of parametric non-linear dynamic assessments using the developed numerical model under various combinations of overpressures and impulses. A new failure criterion based on the total failure of the self-tapping screws is proposed in conjunction with pressure-impulse diagrams. This failure condition provides a more direct assessment of the damage to the side walls of the warehouse. The pressure-impulse diagrams can be used to assess the response of a typical warehouse structure to blast loading, and to provide some guidance on the safe siting in a hazardous environment around oil and storage sites. Simplified approaches based on single degree of freedom representations are also employed, and their results are compared with those from the detailed non-linear finite element models. The findings show that the simplified approaches offer a reasonably reliable and practical tool for predicting the response of the side rails. However, it is illustrated that such idealisations are not suited for assessing the ultimate response of cladding panels, as the side rail-cladding interactions cannot be captured by simplified approaches and necessitate the deployment of detailed numerical procedures.

Declaration of Originality

I hereby declare that this thesis and the work reported herein was composed by and originated entirely from me. Information derived from the published and unpublished work of others has been acknowledged in the text and references are given in the list of sources.

Copyright Declaration

The copyright of this thesis rests with the author and is made available under a Creative Commons Attribution Non-Commercial No Derivatives licence. Researchers are free to copy, distribute or transmit the thesis on the condition that they attribute it, that they do not use it for commercial purposes and that they do not alter, transform or build upon it. For any reuse or redistribution, researchers must make clear to others the licence terms of this work.

I would like to dedicate this thesis to my loving parents Jun and Zhengming, and my dear wife Lijia for their love and support.

Acknowledgements

I would like to express my deepest gratitude and appreciation to my supervisors Dr Luke Louca and Prof Ahmed Elghazouli for their continuous encouragement, involvement, fruitful advice and support throughout my research steps. I greatly appreciate they provided me with the opportunity of research and working with them in such an excellent environment at Civil Engineering Department of Imperial College London.

I would like to acknowledge the financial and mental support I received from my parents and my wife without them this work would have never been completed.

I would like to also acknowledge the technical support from Dr Graham Atkinson from Health and Safety Laboratory, Dr Bassam Burgan from Steel Construction Institute and Mr Bob Simpson from Health and Safety Executive.

Finally, the test data used to validate the model for the analysis of instrument boxes was generated in a Joint Industry Project entitled "Dispersion and Explosion Characteristics of Large Vapour Clouds". The project was managed by the Steel Construction Institute and sponsored by:

- BP Exploration Operating Company Limited
- Health and Safety Executive (UK)
- Petrleo Brasileiro S.A. Petrobras
- Shell Research Limited
- Statoil Petroelum AS

- Total Refining and Chemicals
- Le Ministre de Lcologie, du Dveloppement Durable, des Transports et du Logement (France)
- National Institute for Public Health and The Environment (Netherlands)

The author wishes to thank the sponsors for allowing this data to be used in the present research.

Contents

Contents vii

List of Figures xiii

Nomenclature xxix

1 Introduction 1

1.1 Background 1

1.2 Buncefield incident 3

1.3 Motivation and objectives 4

2 Literature review 8

2.1 Vapour cloud explosion 8

2.1.1 Explosion mechanisms 8

2.1.2 Methods for explosion analysis 11

2.2 Review of past incidents 15

2.2.1 Buncefield incident 15

2.2.2 Other major accidents 18

2.3 Blast wave and loading 19

2.3.1 Blast wave characteristics 20

2.3.1.1 Normal shock 20

2.3.1.2 Blast wave and scaling law 26

2.3.2 Dynamic blast loads 29

2.3.2.1 Front surface load 30

2.3.2.2 Rear surface load 32

2.3.2.3 Top and side surface loads 32
2.3.2.4 Loads on the frame 32
2.3.2.5 Non-ideal blast wave 35
2.4 Structural response 36
2.4.1 Analysis methods 36
2.4.1.1 Single degree of freedom method 36
2.4.1.2 Pressure - impulse diagram 43
2.4.1.3 Finite element method 45
2.4.2 Material properties at high strain rate 46
2.4.3 Modelling structural components 47
2.5 Design guidelines 52

3 Numerical tools **54**
3.1 Non-linear finite element method 54
3.2 Solution methods for non-linear FE problems 59
3.2.1 Newton - Raphson method 60
3.2.2 Arc length method 61
3.2.3 Explicit direct integration method 63
3.3 Eulerian analysis for blast wave 64
3.4 Approaches for study of blast responses 66
3.4.1 Lagrangian approach 68
3.4.2 Uncoupled Eulerian - Lagrangian approach 69
3.4.3 Coupled Eulerian - Lagrangian approach 69
3.5 Numerical model validations 69
3.5.1 One dimensional model 70
3.5.2 Blast wave propagation 72
3.5.3 Reflection of ideal blast wave 73
3.5.4 Square plate subjected to close HE explosion 76
3.6 Finite element analysis packages 82

4 Blast response of field objects **85**
4.1 Experimental observations 86
4.1.1 Steel switch boxes 87

4.1.1.1 Box150 . . . 87
4.1.1.2 Box200 . . . 88
4.1.2 TNT detonation tests . . . 89
4.1.3 Gas detonation tests . . . 91
4.2 Numerical methodology . . . 98
4.2.1 Numerical model of boxes . . . 98
4.2.1.1 Model of Box150 . . . 98
4.2.1.2 Model of Box200 . . . 101
4.2.2 Lagrangian analysis . . . 101
4.2.2.1 Consideration of internal pressure . . . 105
4.2.3 Uncoupled Eulerian - Lagrangian analysis . . . 106
4.2.4 Coupled Eulerian - Lagrangian analysis . . . 110
4.2.5 Comparison of computational demands . . . 111
4.3 Comparative assessment . . . 112
4.3.1 Comparison of numerical results . . . 112
4.3.1.1 Blast wave and dynamic loading . . . 113
4.3.1.2 Box response to gas detonations . . . 119
4.3.2 Model selection for parametric studies . . . 126
4.4 Parametric study and discussion . . . 135
4.4.1 Reflection of deflagration blast waves . . . 135
4.4.2 Pressure - Impulse diagram and residual shapes . . . 138
4.4.3 Comparison with recovered boxes . . . 145
4.5 Conclusion . . . 149

5 Modelling of warehouse structures 150
5.1 Damages to Buncefield warehouses . . . 150
5.2 Typical portal frame configuration . . . 153
5.3 Description of warehouse components . . . 154
5.3.1 Portal frames . . . 154
5.3.2 Gable wall frames . . . 155
5.3.3 Roof bracing . . . 155
5.3.4 Side wall bracing . . . 156
5.3.5 Eaves beam . . . 157

5.3.6 Purlin and side rail . . . 157
5.3.7 Cladding . . . 158
5.3.8 Self-tapping screw fasteners . . . 158
5.3.9 M12 Bolt-Cleat connections . . . 159
5.4 Material properties . . . 160
5.4.1 Strength increase factor (SIF) . . . 160
5.4.2 Dynamic increase factor (DIF) . . . 161
5.5 Numerical models of warehouse . . . 162
5.5.1 Double span full model . . . 162
5.5.2 Single span full model . . . 164
5.5.3 Sub-assemblage model . . . 164
5.5.4 Component model . . . 164
5.5.5 Comparison of displacement histories . . . 165
5.6 Validation of sub-assemblage model . . . 166
5.6.1 Tests on cladding-side rail assemblage . . . 166
5.6.2 Numerical simulations . . . 169
5.7 Refined sub-assemblage model . . . 173
5.7.1 Fastener model and validation . . . 174
5.7.2 Coupled response of fasteners . . . 179
5.7.3 M12 Bolt-Cleat Connection model . . . 183
5.8 Complete warehouse sub-assemblage model . . . 187

6 Response of warehouse structures 190
6.1 Response measurement and damage levels . . . 190
6.2 Modal analysis and loading scenarios . . . 194
6.3 Side rail deflection . . . 196
6.4 Cladding and fasteners . . . 198
6.5 Side rail axial response and connection behaviour . . . 212
6.6 Combined response . . . 213
6.7 Pressure - impulse diagrams . . . 217
6.7.1 Side rail transverse displacement . . . 218
6.7.2 Side rail axial displacement . . . 219
6.7.3 Percentage of total connector failure . . . 219

6.7.4 Iso-curves for TNT explosive charges 221
6.7.5 Combined pressure - impulse diagrams 222
6.8 Strain rate hardening of fasteners 224
6.8.1 Estimation of local strain rate hardening 224
6.8.2 Influence of strengthened fasteners 231

7 Simplified approaches and design considerations 236
7.1 Single degree of freedom approach 236
7.1.1 Wall cladding 237
7.1.2 Side rail 238
7.1.3 Component interaction 241
7.1.4 Response of simplified model of side rail 242
7.1.5 Response of simplified model of cladding 245
7.1.6 Pressure - impulse diagrams of simplified models 248
7.2 Assessment of blast overpressures 249
7.2.1 Blast wave simulation on rigid warehouse 249
7.2.2 Discussion of blast loading results 254
7.3 Design considerations for steel-clad industrial buildings 263
7.3.1 Pressure - impulse diagrams 263
7.3.2 Example of application of P-I diagrams 264
7.3.3 SDOF and FE models 267
7.3.4 Side-rail connections 268
7.3.5 Cladding connections (fasteners) 268
7.3.6 Other considerations 269

8 Conclusions and further work 270
8.1 Blast response of field objects 270
8.2 Blast responses of warehouse structures 271
8.3 Assessment of blast loading 273
8.4 Recommendations for further work 274

Appendix A: Results of assessment of blast overpressure 276

Appendix B: Loading scenarios for parametric study of sub-assemblage model **284**

References **286**

List of Figures

1.1 The fire during Buncefield incident (SCI, 2009) 4
1.2 Damages due to explosion (SCI, 2009) 5

2.1 Blast waves 10
2.2 Blast waves parameters in TNO multi-energy method (Berg, 1985) 13
2.3 Buncefield site with location of buildings (Atkinson, 2011) 16
2.4 Buncefield Explosion Damages (SCI, 2009) 17
2.5 Stationary normal shock in a moving stream 20
2.6 Explosive shock front moving in still air 22
2.7 Normal reflected shock on a rigid surface 24
2.8 Reflected pressure coefficients vs. angle of incidence (β) (USDOD, 2008) 25
2.9 Shape of blast waves 27
2.10 Passage of a blast wave over a rigid object 29
2.11 Blast curves (Kinney and Graham, 1985) 30
2.12 Blast load-time history on front surface (Kinney and Graham, 1985) 31
2.13 Blast load-time history other surface (Kinney and Graham, 1985) 33
2.14 Blast load-time history on frame (Kinney and Graham, 1985) . . 34
2.15 Typical equivalent single-degree-of-freedom system 36
2.16 Resistance curve R(δ) for a typical SDOF system 39
2.17 Response for all regimes 42
2.18 Pressure - impulse diagrams 44
2.19 Pressure - impulse diagrams comparison 45
2.20 Material response at high strain rate (USDOD, 2008) 46
2.21 Strain rate hardening models 48

3.1 Newton Raphson Method 61
3.2 Modified Riks method 62
3.3 Lagrangian v.s. Eulerian deformation 64
3.4 Eulerian time incrementation (Spinelli and Vitali, 2009) 65
3.5 One dimensional Eulerian model 70
3.6 Mesh study of 1D Eulerian model 71
3.7 Comparison for shock strength decay 72
3.8 Normal reflection in Eulerian model $p_{in} = 34.5kPa$ 74
3.9 Oblique reflection ($p_{in} = 34.5kPa$) 75
3.10 Comparison for shock strength decay (USDOD, 2008) 76
3.11 Boyd's experiment configuration (Boyd, 2000) 77
3.12 Numerical model in AUTODYN 78
3.13 Comparison of responses and the modified model 80

4.1 Damaged steel switch box in the vapour cloud (SCI, 2009) 86
4.2 Photos of steel switch boxes 87
4.3 Box150 (300×300×150mm) 88
4.4 Box200 (300×300×200mm) 89
4.5 Configuration of TNT detonation test (SCI, 2009) 90
4.6 Residual deformations of "Box150" exposed to TNT detonation, incident overpressure from left to right: 100kPa, 200kPa, 480kPa and 750kPa (SCI, 2009) 90
4.7 Simplifield layout of gas detonation test 92
4.8 Configuration of box support (Courtesy of Steel Construction Institute) 92
4.9 Test in progress (Allason, 2013) 93
4.10 Pressure - time histories recorded by transducers 94
4.11 Before and after photographs of Box200-1,3,5 and 7 (Allason, 2013) 96
4.12 Digital scan of boxes 97
4.13 Deformation measurement of scanned box 97
4.14 Box150 numerical model details 99
4.15 Box150 model boundary conditions with mesh 100
4.16 Box numerical mode mesh study 100

4.17 Box200 numerical model with mesh 102
4.18 Box faces subjected to reflected and side-on pressure loading in pure Lagrangian approach 103
4.19 Load application in Lagrangian analysis (Box200-7, Transducer B11) 103
4.20 Modelling of internal pressure 105
4.21 Calibration of blast wave in Eulerian model 107
4.22 3D Eulerian model 108
4.23 A quarter of 3D Eulerian model for UEL analysis Step 1 109
4.24 Overpressure loading curves for UEL analysis 110
4.25 CEL numerical model 111
4.26 Numerical blast wave and loading results for Box200-1 (Transducer B16) 113
4.27 Numerical blast wave and loading results for Box200-3 (Transducer B9) 114
4.28 Numerical blast wave and loading results for Box200-5 (Transducer B10) 115
4.29 Numerical blast wave and loading results for Box200-7 (Transducer B11) 116
4.30 Displacement - time histories of box front face centre 119
4.31 Comparison of residual shapes of Box200-1 123
4.32 Comparison of residual shapes of Box200-3 124
4.33 Comparison of residual shapes of Box200-5 125
4.34 Comparison of residual shapes of Box200-7 126
4.35 Numerical results of overpressures for TNT explosions 128
4.36 Numerical results of displacements for boxes in TNT explosions . 129
4.37 Numerical displacements error compared with CEL model 132
4.38 Numerical residual shapes for Box150 in TNT explosions. Peak side-on pressure: 1 bar, 2 bar and 3 bar 133
4.39 Numerical residual shapes for Box150 in TNT explosions. Peak side-on pressure: 4 bar, 4.8 bar and 7.5 bar 134
4.40 Numerical Eulerian model for reflection of deflagration 136
4.41 Reflection coefficient for deflagration(non-ideal blast wave) 137
4.42 Overpressure dynamic loadings for parametric study 138

4.43 Pressure - Impulse diagrams for Box150 (back support) 143
4.44 Pressure - Impulse diagrams for Box150 (bottom support) 144
4.45 Numerical residual shapes of Box150 (back support) 146
4.46 Numerical residual shapes of Box150 (bottom support) 147
4.47 Comparison of numerical residual shapes to damaged boxes from Buncefield (SCI, 2009) 148

5.1 Damage to Warehouse 1 (Atkinson, 2011) 151
5.2 Damage to Warehouse 2 (Atkinson, 2011) 152
5.3 Typical warehouse configuration (Burgan and Moutaftsis, 2011) . 153
5.4 Portal frame layout (Burgan and Moutaftsis, 2011) 155
5.5 Gable wall frames (Burgan and Moutaftsis, 2011) 155
5.6 Roof plan (Burgan and Moutaftsis, 2011) 156
5.7 Side wall frames (Burgan and Moutaftsis, 2011) 156
5.8 Cross-sectional details of eaves beam, purlin and side rail [units:mm] (Hadley, 2004) 157
5.9 Built-up cladding details (Burgan and Moutaftsis, 2011) 158
5.10 Self-tapping screw (CA, 2008) 159
5.11 M12 Bolt-Cleat connection (Hadley, 2004) 159
5.12 Numerical modelling levels 163
5.13 Comparison of displacement histories of side wall models 165
5.14 Full scale test configuration of cladding-side rail assembly (Elghazouli et al., 2014) 167
5.15 Profile of cladding TR35/207 (thickness=1 mm) [unit:mm] 167
5.16 Material models for cladding and side rail 168
5.17 Numerical model used for validation 169
5.18 Mesh of test assembly numerical model 170
5.19 Comparison of numerical results and experimental measurements 171
5.20 Deformed shapes of test assembly (Riks method) 172
5.21 Comparison of pressure - central displacement responses 173
5.22 Details of sub-assembly model representing the side wall of warehouse 174
5.23 Self-tapping screw connector model 175

5.24 Lap joint pulling test using static test components (validation of detailed fastener model) 177
5.25 Shear response estimation of the fastener for connector model . . 178
5.26 Definition of the connector shear response for fasteners 182
5.27 Finite element model of M12 Bolt-Cleat connection 184
5.28 Response estimation of M12 Bolt - Cleat connection 185
5.29 Connector model for M12 Bolt-cleat connection 186
5.30 Sub-assemblage model of the wall structure in the warehouse building 187

6.1 Details of sub-assemblage model 191
6.2 Structural component mid-span deflection and end rotation 192
6.3 Sub-assemblage mode shapes 194
6.4 Loading scenarios: combinations of overpressure and impulse . . . 195
6.5 Displacement history at the mid-span of the central side rail with loading profiles 197
6.6 Deformed shapes of the sub-assemblage 198
6.7 Response of central fastener of the sub-assemblage model in Case 98 199
6.8 Response of central cladding of the sub-assemblage in Case 98 . . 201
6.9 Relative displacement at the middle of the cladding with failure of the corresponding fastener 202
6.10 Response of central fastener of the sub-assemblage model in Case 157 203
6.11 Response of central cladding of the sub-assemblage in Case 157 . 205
6.12 Response of side fastener of the sub-assemblage model in Case 75 206
6.13 Response of side cladding of the sub-assemblage in Case 75 207
6.14 Comparison of failure behaviour of central and side cladding with fasteners for the sub-assemblage model in Case 98 209
6.15 Cases with identical failure behaviour of cladding and fasteners at centre and side 210
6.16 Response of middle fastener of the sub-assemblage model in Case 98 211
6.17 Numerical response of the M12 bolt-cleat connection 212
6.18 Axial and transverse displacement time history of side rail 214
6.19 Side rail transverse response with failure of fasteners 216

6.20 Percentage of total fastener failure with side rail displacement . . 217
6.21 Pressure - impulse diagrams: maximum side rail displacement . . 218
6.22 Pressure - impulse diagram: maximum axial displacement 219
6.23 Pressure - impulse diagram 220
6.24 Iso-curves for TNT explosive charges 221
6.25 Combined pressure - impulse diagrams 222
6.26 Strain rate effect on dynamic increase factor 224
6.27 Estimation of strain rate in the screw connection 225
6.28 Stress, strain and strain rate time histories in the sampling shell element 226
6.29 Simplified model to estimate the strain rate in a screw connection 227
6.30 Applied 0.2 mm displacement over total time step of 0.01 second . 228
6.31 Strain rate analysis around the hole 229
6.32 Relationship between nominal and concetrated strain rates 230
6.33 Connector response with and without the estimated strain rate effect 230
6.34 Comparison of response of side rail with and without rate stiffened fasteners 232
6.35 Effect of the rate stiffened fastener on the pressure - impulse diagrams of the side rail maximum displacement 233
6.36 Effect of the rate stiffened fastener on the percentage failure of fasteners 233
6.37 Influence of the rate effect on the pressure - impulse diagram of maximum percentage of fastener failure (50% failure) 234

7.1 Cladding panel and side rail simplified SDOF model 237
7.2 Resistance curve of SDOF model for cladding panel 239
7.3 Resistance curve of SDOF model for side rail 241
7.4 Response of simplified model of side rail 243
7.5 Comparison of pressure - impulse diagrams (maximum dynamic displacement) 244
7.6 Responses of simplified model of cladding 246
7.7 Combined pressure - impulse diagram using the simplified approach 248

7.8 Numerical modelling of blast wave (semi-spherical 7500kg TNT charge and 324m stand-off) and the rigid warehouse structure . . 251
7.9 Coupled model of blast wave with rigid warehouse 252
7.10 Location of numerical pressure gauges 252
7.11 Pre-cut holes on the blastward wall of the rigid warehouse model . 253
7.12 30% venting area with different shapes of holes 254
7.13 Simulation of blast loading on rigid warehouse model 255
7.14 Overpressure loading results for Case 4 (30% venting area) 256
7.15 Internal pressurisation due to venting area on front wall 257
7.16 Overpressure loadings at the back wall 259
7.17 Overpressure loadings of side wall 260
7.18 Effect of venting area shapes on internal pressurisation 262
7.19 Application of pressure - impulse diagram 265

1 Overpressure loadings on rigid warehouse (Case 1) 276
2 Overpressure loadings on rigid warehouse (Case 2) 277
3 Overpressure loadings on rigid warehouse (Case 3) 277
4 Overpressure loadings on rigid warehouse (Case 4) 278
5 Overpressure loadings on rigid warehouse (Case 5) 278
6 Overpressure loadings on rigid warehouse (Case 6) 279
7 Overpressure loadings of back wall (Case 1 & 2) 279
8 Overpressure loadings of back wall (Case 3 & 4) 280
9 Overpressure loadings of back wall (Case 5 & 6) 280
10 Overpressure loadings of side wall (Case 1 & 2) 280
11 Overpressure loadings of side wall (Case 3 & 4) 281
12 Overpressure loadings of side wall (Case 5 & 6) 281
13 Overpressure loadings of front roof (Case 1 & 2) 281
14 Overpressure loadings of front roof (Case 3 & 4) 282
15 Overpressure loadings of front roof (Case 5 & 6) 282
16 Overpressure loadings of back roof (Case 1 & 2) 282
17 Overpressure loadings of back roof (Case 3 & 4) 283
18 Overpressure loadings of back roof (Case 5 & 6) 283

19 Combination of overpressures and impulses with corresponding case number and positive duration 285

Nomenclature

Roman Symbols

$[B]$ Strain matrix

$[c]$ Constitutive matrix

$[D]$ Assembled nodal displacement matrix

$[D_e]$ Global nodal displacement matrix

$[d_e]$ Local nodal displacement matrix

$[F]$ Assembled consistent nodal force vector

$[f_b]$ Body force vector

$[F_e]$ Global consistent nodal force vector

$[f_e]$ Local consistent nodal force vector

$[f_s]$ Surface force vector

$[I]$ Internal forces of the flexible body

$[K]$ Assembled stiffness matrix

$[K_e]$ Global stiffness matrix

$[k_e]$ Local stiffness matrix

$[M]$ Assembled mass matrix

$[T]$ Transformation matrix

$[U]$ Displacement matrix

$\bar{u}^{pl}$ ABAQUS connector equivalent plastic relative motion

ΔP_s Blast strength number (1-10)

ΔP_s Maximum overpressure

Δt Step time increment

$\Delta \overline{P}_s$ Dimensionless maximum overpressure

$\dot{u}^{pl}$ ABAQUS collection of plastic relative motion rate

$\overline{R}$ Energy scaled distance

$\bar{t}_+$ Dimensionless positive duration

A Cross sectional area

a, b TNO multi-energy correlation constants

a_0 Local speed of sound

a_x Local sound of speed (atmosphere)

C Strain rate hardening parameter for Johnson-Cook model

c_0 Atmospheric speed of sound

C_d Dilatation wave speed

C_d Discharge coefficient

c_p Specific heat at constant pressure

D Average obstacle size

D Diameter of the self-tapping screw shaft

D, p Strain rate hardening parameter for Cowper-Symonds model

E Combustible energy of vapour cloud

E Detonation energy per initial volume

E Young's modulus

F Axial pre-tension

F Distributed load

F Opening percentage

f ABAQUS collection of active connector forces

F^0 ABAQUS connector equivalent yield force

F_e Equivalent force of SDOF system

f_e TNT efficiency factor

F_N ABAQUS connector equivalent tensile (normal) force

F_S ABAQUS connector equivalent shear force

f_u Material ultimate stress

f_x, f_y, f_z ABAQUS connector force

f_y Material yield stress

f_{du} Material dynamic ultimate stress

f_{dy} Material dynamic yield stress

$g(t)$ Time function of the applied distributed load

H_{TNT} Explosive heat of TNT

H_{vapour} Combustion heat of the fuel in vapour cloud

I Specific impulse

K Stiffness of SDOF model

K Torque coefficient

k Specific heat ratio (1.4 for ideal gas)

k Stiffness

K, r ABAQUS connector defining parameter

K_e Equivalent stiffness of SDOF system

K_{LM} Load-mass factor

k_{TM} Strain energy

L Characteristic length of the target

L Lagrange

L Length of a simply supported beam

L_e Characteristic element length

L_f Flame path

m Mass

M_e Equivalent mass of SDOF system

M_e Global mass matrix

m_e Equivalent TNT mass

m_e Local mass matrix

M_p Ultimate plastic moment

M_x Upstream flow Mach number

m_x, m_y, m_z ABAQUS connector moment

M_y Downstream flow Mach number

m_{vapour} Total mass of the vapour cloud

N Admissible functions

n n^{th} incremental step

P ABAQUS connector potential

P Total applied load P=FL

p Blast wave overpressure

$p(x,t)$ Applied distributed load

P_0 Atmospheric pressure

P_a Atmospheric pressure

p_A Atmospheric pressure

p_i Incident overpressure

p_o Peak overpressure value

P_r Reflected pressure

p_r Reflected overpressure

P_x Upstream flow pressure

P_y Downstream flow pressure

P_{atm} Atmospheric pressure

$P_{incident}$ Incident overpressure

P_{stag} Stagnation pressure

p_{stag} Stagnation overpressure

$P_{transmission}$ Transmitted overpressure through perforated barriers

Q_i Generalised force

q_i Admissible functions

R Ideal gas constant

R Stand-off distance

r Distance to target

R_0 Charge radius

r_c Radius of high explosive charge

R_m Maximum plastic load of SDOF resistance curve

R_N ABAQUS connector equivalent tensile (normal) capacity

R_S ABAQUS connector equivalent shear capacity

S Characteristic width of the reflected surface

S_c TNO multi-energy correlation scale factor

S_l Laminar burning velocity

s_x Upstream flow entropy

s_y Downstream flow entropy

T Kinetic energy

T Natural period

T Tension membrane force

T Tightening torque

t Time

t_+ Positive duration

t_a Shock front arrival time

t_d Shock wave positive duration

T_H Temperature dependency parameter for Johnson-Cook material model

T_n Natural period of structure

t_r Deflagration finite rise time

T_x Upstream flow temperature

T_y Downstream flow temperature

T_{atm} Atmospheric temperature

u_p Blast wave particle velocity

u_x Upstream flow velocity (shock front velocity)

u_x, u_y, u_z ABAQUS connector displacement

u_y Downstream flow velocity

ur_x, ur_y, ur_z ABAQUS connector rotation

V Plastic dissipation energy

V Relative volume or the expansion of the explosive product

V Strain energy

W High explosive charge weight

W Work done by external forces

$w(x,t)$ Response solution of a simply supported beam

Z Scaled distance

$\bar{u}_{DI}^{pl}$ ABAQUS connector damage initiation displacement

$\bar{u}_{f}^{pl}$ ABAQUS connector shear failure displacement

$e^p{}_{eff}$ Effective plastic strain

f_z^{fail} ABAQUS connector tensile failure force

Greek Symbols

$[\epsilon]$ Strain matrix

$[\sigma]$ Stress matrix

α Blast wave form parameter

β Shock wave incident angle

δ Delta operator

$\delta(t)$ Generalised time response of a supported beam

δ_e Transverse displacement of beam at yieldings

δ_m Maximum transverse displacement of beam

δ_y Yielding displacement

δ_{TM} Strain energy

ϵ The base of natural logarithm

ϵ_p Plastic strain

ϵ_y Material yield strain

Λ_n Pressure reflected ratio

μ Ductility ratio

ω Undamped natural circular frequency

Φ ABAQUS connector yield function

$\phi(x)$ Assumed mode shape function

π Potential energy

Ψ_m ABAQUS connector mode-mix ratio

ρ Density

ρ_x Density of the upstream flow

ρ_y Density of the downstream flow

ρ_{atm} Atmospheric density

σ_p Plastic stress

σ_y Material yield stress

Θ Temperature

θ Support rotation of beam

Θ^z Absolute zero

$\dot{\epsilon}$ Strain rate

$\dot{\epsilon}^P_{eff}$ Effective plastic strain rate

$\dot{\epsilon}_0$ Reference strain rate

Acronyms

CEL Coupled Eulerian - Lagrangian

DIF Dynamic increase factor

$NLFEM$ Non-linear finite element model

$SDOF$ Single degree of freedom

UEL Uncoupled Eulerian - Lagrangian

VBR Volume blockage ratio

VCE Vapour cloud explosion

Chapter 1

Introduction

The 2005 Buncefield event was unexpectedly destructive for a vapour cloud explosion. It showed huge cost associated with blast damages to commercial and residential buildings surrounding a major explosion incident. The main characteristic of the Buncefield explosion was that its intensity and the severity of damage caused to structures/buildings had not been anticipated by any major hazardous design practice. The work presented in this thesis focuses on assessing structural damage of vapour cloud explosions and aiming to provide insight into the structure and objects response to blast loadings.

1.1 Background

An explosion is a sudden release of substantial energy, which transfers to its surrounding in the form of a rapidly moving rise in pressure called a blast wave. There are three categories of explosion: physical, nuclear and chemical (Smith and Hetherington, 1994). The most common physical explosion can be found for example in a failure of a vessel of compressed gas or other pressurized devices. The violent expansion of the compressed gas is the source of the released energy. The Nuclear explosion is much more destructive than the other two. The energy in a nuclear explosion comes from the formation of different atomic nuclei by redistribution of the neutrons and proton within the reacting nuclei.

Chemical explosions are exothermic reactions. The surrounding temperature

is raised by the heat from oxidation of the fuel element contained within the explosive compound. Then the volume of the gases becomes much larger than the compound, generating a high pressure and subsequent blast wave. The energy released arises from the formation of new molecular bonds in the products of the reaction. Explosives that fall into this category are such as Trinitrotoluene (TNT, high explosive), gunpowder (low explosive) and even the wheat flour dust in a grain elevator. This explosion is known as a detonative process.

There is a special case of chemical explosion called vapour cloud explosion (VCE) that involves a fuel (e.g. propane or butane) mixed with the atmosphere, and usually this occurs in an offshore platform or industrial/chemical plant. If the mixture is ignited, the flame velocity would be fast enough to generate a blast wave. Although the overpressure in the blast wave might not be as high as in other explosions, it can be strong enough to damage or even destroy nearby structures. In a vapour cloud explosion, deflagration is the result that the flame front travels slower than the speed of sound and if it moves faster than the speed of sound, we would expect a detonation to occur (deflagration transition to detonation). It is more destructive as it generates stronger blast waves than deflagration.

The blast wave (high overpressure) from an uncontrolled explosion can be destructive and even lethal. To prevent its damage to buildings, there is a need to understand the characteristics of explosions, blast waves and subsequently the response of building structures. Empirical charts/tools are widely adopted for analysis of characteristics of an explosion. The blast wave parameters can be readily determined by using charts or empirical equations based on scaled explosive charge weight and stand-off distance. Empirical methods are available for both high explosive and vapour cloud explosions. With the development of scientific computers, a more complex method known as Computational Fluid Dynamics (CFD) is now widely available. It is capable of producing results with better accuracy but involves greater cost of computational resource and operator manpower.

Several methods are available for analysis of dynamic structural response. Biggs' Single Degree of Freedom (SDOF) model has been extensively used to investigate the response of structural component to dynamic loadings. Results can be presented in a graphical, analytical or numerical forms. This method is

based on a representation of the actual component configurations by an equivalent spring-mass system which has only one degree of freedom (Biggs, 1964). An improved SDOF model is presented in the Technical Note 7 (SCI, 2002) which overcomes some difficulties in Biggs' model and includes complex supporting conditions. By using energy methods to generate equilibrium equations, the mode approximation method has been extended by Schleyer (Schleyer and Hsu, 2000) and Langdon (Langdon and Schleyer, 2006b) and to incorporate full elastic response and include variable support constraints. This method divides the dynamic response of a component into different stages/modes and obtain results by solving a Multi-Degree of Freedom system.

Finite element methods are also widely used to analyse the dynamic response of structures. Commercial codes such as **?**, ANSYS and LS-DYNA are commonly used in research and industries. Borvik (Borvik et al., 2009) used LS-DYNA to investigate whether a pure Lagrangian model can be used to determine the structural response in a specified blast problem or a more complicated fully coupled Eulerian - Lagrangian model should be adopted. By using non-linear finite element package Louca (Louca et al., 1996) studied the response of a typical blast wall and a stiffened panel subject to hydrocarbon explosion. Langdon (Langdon and Schleyer, 2006c) used **?** to predict the response time histories and permanent deformations of a stainless steel blast wall and connection systems.

1.2 Buncefield incident

Over the last few decades, there have been a number of major industrial accidents involving oil and gas installations worldwide. These include the Buncefield event in the UK in December 2005. The incident was a vapour cloud explosion which occurred at the Buncefield Oil Storage Depot, Hemel Hempstead, Hertfordshire.

Fortunately there were no casualties but 43 people were injured. The explosion and subsequent fire caused extensive damage to the plant and surrounding buildings, both commercial and residential properties. An aerial view of the site during the fire is shown in Figure 1.1. The economic impact of the incident broadly adds up to £1 billion.

The subsequent investigation by the Buncefield Major Incident Investigation



Figure 1.1: The fire during Buncefield incident (SCI, 2009)

Board (BMIIB) identified that the explosion was a consequence of oil spilling from an over filled storage tank (tank 912) on the site. Both detonation and deflagration explosion mechanisms were assessed for their consistency with the observed explosion characteristics. Neither of the two mechanisms can explain the evidence conclusively. Work undertaken in the joint industry project (BMIIB, 2007) has concluded that an early deflagration followed by transition to detonation at congested area would be the most likely scenario.

1.3 Motivation and objectives

The work undertaken in the joint industry project (BMIIB, 2007) represented a major advance in the understanding of the Buncefield explosion. The work has also identified a number of areas that require further research. The work, although defined within the frame of Buncefield, will lead to a greater understanding of large vapour cloud explosions and associated structural response. Therefore, a further research project has been initiated by the recommendation from the BMIIB. As part of the research work, interests of the present study are

mainly lying in the structural response of various field objects and the steel portal warehouse building.

The objective of the project is to study damage produced to buildings from low-lying vapour cloud explosion which occurred in the previous accidents. Data in the public domain on the damage observed will be used to investigate the characteristics of the pressure time histories required to produce the damage processes observed. Much effort will be placed in studying the impact of selected pressure loads on representative building structures through detailed non-linear finite element analysis. Analytical methods will be used in simple structures where applicable. The anticipated outcome of this work would be to propose guidance for the assessment of loading and the evaluation of structural response.



(a) Damaged Drum (b) Damaged Box (c) Damaged Warehouse

Figure 1.2: Damages due to explosion (SCI, 2009)

For the purpose of assessing the overpressure history across the incident site, evidence relating to overpressure is important as part of the forensic studies. Within the body of the vapour cloud, there were very few large objects such as buildings. Buildings which suffered structural damage in the vicinity of the site were located towards the edge or outside of the gas cloud. However, it was found that there were many small objects such as steel drums and switch boxes distributed across the site and nearby areas. These field objects could be used as overpressure indicators, as their permanent deformation can provide an indication of the possible overpressure at their locations after the passage of blast waves. Typical damage of drums and boxes are shown in Figure 1.2a and 1.2b.

During the explosion, both steel frame and masonry buildings were damaged to different levels. Large steel portal frame warehouse type structures were affected at a quite long distance. Among the damaged structures, steel frame cladding warehouses are of the most interests. A damaged warehouse is shown in Figure 1.2c. The high surface area and light-weight construction make the pressure applied by wind a key structural design aspect. The common design wind pressure of a steel cladding warehouse is lower than it is of a typical brick building, and almost all of the surface structural steel and cladding is potentially at risk (rather than just windows/doors). Therefore it is relatively more vulnerable to accidental overpressure and the level of damage to a warehouse maybe be particularly extensive and time consuming to repair, leading to longer periods of business disruption.

Given the above considerations, field objects such as steel switch boxes were chosen to perform a forensic study. While the steel frame cladding warehouse is the subject of the analysis of structural response to vapour cloud explosions. The main objectives of this project are:

- to model steel switch boxes subject to various blast loading
- to examine the blast response of steel boxes in the form of pressure-impulse diagrams and permanently deformed shapes
- to provide information for forensic studies to investigate the current and future explosions
- to model light weight steel portal frame warehouse structures under different blast loadings
- to generate pressure-impulse diagrams of steel frame cladding warehouses
- to provide design implications for steel portal frame warehouses

In the following chapters, a literature review covering the recent research work on study and investigation of blast explosion and structural response is presented, following by a introduction of the numerical tools that adopted in the current research project. Forensic works carried out on the field objects which can be

used to help the investigation are presented. A detailed finite element analysis on the response of light weight steel clad warehouse structure is presented and the results are discussed. Some design implication and improvements to the structures are included at the end of this thesis.

Chapter 2

Literature review

This chapter presents an overview of different types of explosions and their characteristics. The Buncefield and other previous major incidents are reviewed and their main characteristics are noted. Blast wave, the associated dynamic loading and various tools for structural dynamic analysis are presented. A review of previous work on studies of responses to blast loading is also included and discussed.

2.1 Vapour cloud explosion

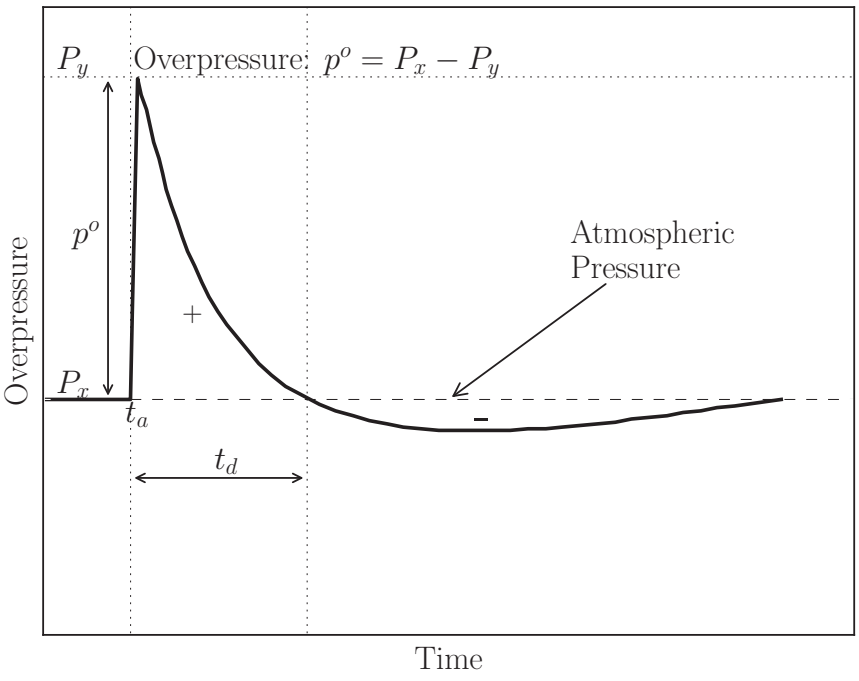
2.1.1 Explosion mechanisms

A cloud of combustible material (e.g. propane, butane and pentane etc.) in either confined or unconfined atmosphere can explode under certain conditions. Conditions leading to an unconfined vapour cloud explosion are first, a quick release of a large quantity of fuel which forms a vapour cloud. Secondly the cloud is ignited by a spark or flame. There are two mechanisms that a vapour cloud could explode: deflagration and detonation. If the ignition occurs immediately after the release of the combustible material before it mixes with the surrounding air, the explosion is very likely to be a deflagration. When ignition of the combustible cloud occurs after its formation so that the air has became well mixed with the combustible vapour, and if the air-fuel mixture is just within the flammability range, a detonation is most likely to occur.

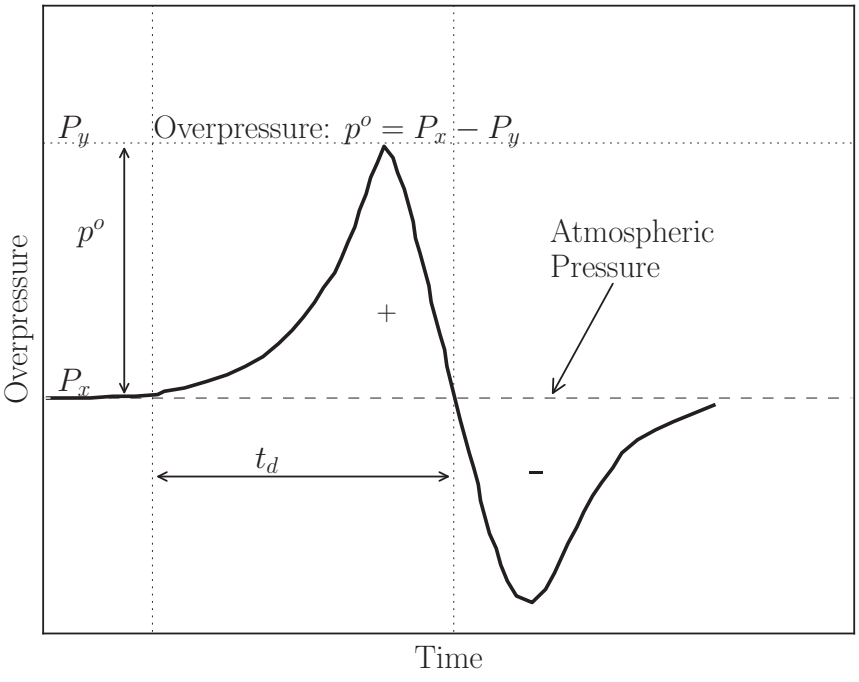
A vapour cloud explosion involving deflagration is certainly less destructive than detonation. The overpressure is generated by the flame front travelling at high speeds but under the local speed of sound. The mixture ahead is ignited by heat radiation from the flame front. The flame generates pressure because of the inertia of the unreacted mixture in front of the flame, similar to a object travelling at high speed through the air generates a pressure wave in front of it. It is well understood that deflagration of a vapour cloud in a confined or congested area (such as a section fully packed with pipe works) can generate damaging pressures due to acceleration of flame front. In some cases, the turbulence induced by the congested obstacles will promote the reaction rate, producing successively higher flame speeds and increasing overpressures. Thus it can eventually lead to deflagration - detonation transition (DDT). It is important to note that the high speed of flame is dependent on the congested obstacles, once the flame travels from a confined area to an open area it rapidly decelerates. Hence the overpressures decreases as the blast wave propagates away from the congested region.

As compared to deflagration, the detonation front has an initial sudden rise in pressure, which then decays. This abrupt rise of overpressure is known as shock front and the whole pressure wave as a shock wave. The shock front compresses the air-fuel mixture in the front and raises the temperature. In detonation the temperature rise can ignite the fresh mixture ahead as it exceeds the auto-ignition temperature of the mixture. The magnitude of the shock front is maintained by the energy released from the combustion process in detonation. The process is self-sustainable so it is not dependent on any congestion or obstacles.

The pressure - time history of a typical blast wave from detonation as recorded some distance away from the explosion centre is shown in Figure 2.1a. At an arrival time t_a after initiation of the explosion, the pressure at the remote location suddenly increased to a peak value. The overpressure then immediately starts to decay to atmospheric pressure over a period known as the duration of the positive phase t_d. Due to the inertia of the air in the wave, a negative pressure phase will occur after passage of the overpressure blast wave. The peak value of the negative phase is much lower but the duration is much longer than the positive phase. Generally three independent parameters are used to define a detonation blast wave: the peak overpressure p^o, the positive phase duration t_d



(a) Detonation



(b) Deflagration

Figure 2.1: Blast waves

and the specific impulse which is the area under the positive phase $I = \frac{1}{2}p^o t_d$. The specific impulse is defined as the blast wave impulse per unit area.

In the case of deflagration the volume of the air-combustible mixture is generally high and the energy release is relatively low. This occurs because the reaction rate in the deflagration is low compared with detonation. The flame propagation is also slow so the pressure effects are small. When turbulence is generated, the combustion speed increases and the pressure wave tends to pick up in magnitude and become similar to a detonation. The profile of a blast wave from vapour cloud deflagration is more likely an "N" curve, as shown in 2.1b. The leading wave is not a shock front, but a gradually increasing compression wave. Similarly, peak overpressure p^o, positive duration t_d and specific impulse I are still used to define the pressure profile. Moreover, the negative phase has a maximum of the same order of the magnitude as that in the peak positive phase. The duration of the negative phase is also of the same length as the positive phase.

2.1.2 Methods for explosion analysis

Predicting the blast damages to a piece of equipment and structure requires firstly to calculate the time history of the blast wave produced in air. Nowadays. computational advancement allow researchers to use sophisticated CFD tools to examine the vapour cloud explosion and the blast wave characteristics. FLACSv9 and AutoReaGas are two CFD-based codes, developed by Century Dynamics and Gexcon. Such codes usually comprise two solvers: a "Gas explosion" solver (Navier-Stokes) and a "Blast" solver (Euler). The gas explosion solver is used for analysis of the explosion process, including flame propagation, turbulence and the effects of obstacles/congestions in the flow field. The blast solver is responsible for accurate, efficient modelling of the shock phenomena and blast wave propagations. The above two codes are not readily available at Imperial College. However, recent updates of **?** offered the Eulerian capabilities, which enables us to model the blast wave without the explosion process. Modelling the blast wave is useful in terms of wave propagation and most importantly the interaction with the objects/structures. The Eulerian solver of ANSYS (AUTODYN) has also been used in this project.

In order to define a blast wave, in the absence of simulation of the vapour cloud explosion process, there are two methods available: the TNT-equivalency method and the TNO multi-energy method.

TNT-equivalency method

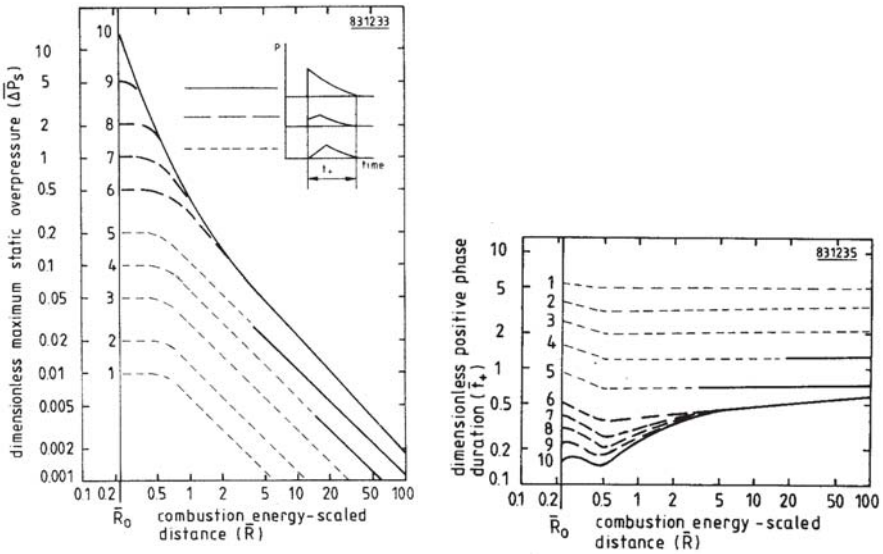
One way to predicting the blast wave from a vapour cloud explosion is to estimate the mass of high explosive TNT that would produce the comparable blast damage and similar blast wave time history. This is known as the TNT equivalency method. Due to its simplicity and acceptable accuracy for most of the vapour cloud explosions, it is still widely used today. However the method should produce a reasonable prediction of the blast wave in the far-field, where the blast wave from a vapour cloud explosion is transforming into an ideal blast wave (detonation type). In the near - field the predicted blast wave can be significantly different from an actual vapour cloud blast wave (Pritchard, 1989).

To estimate the equivalent TNT mass m_e from the energy of the vapour release, a factor called TNT efficiency f_e is used. It is the ratio, defined by the total explosive heat of the equivalent TNT to the total combustion heat released from the vapour cloud.

$$f_e = \frac{H_{TNT} m_e}{H_{vapour} m_{vapour}} \% \tag{2.1}$$

In Equation 2.1, H_{TNT} is the explosive heat of TNT, m_e is the equivalent mass of TNT, H_{vapour} is the combustion heat of the fuel in the vapour cloud and m_{vapour} is the total mass of the vapour cloud. It was suggested by Pritchard (Pritchard, 1989) that to estimate an explosive involving vapour cloud, the value between 1% and 10% is usually used for TNT efficiency f_e. The highest value for deflagration is 10%, beyond this value it is representative for a detonation. The major uncertainty of this method comes from value used for TNT efficiency. Once it is determined, the equivalent mass of TNT m_e can be readily obtained and the blast wave parameters at any distance from the explosion centre can be found by lots published charts/tables or equations by Kinney and Graham (1985).

TNO multi-energy method



(a) TNO overpressure chart (b) TNO duration chart

Figure 2.2: Blast waves parameters in TNO multi-energy method (Berg, 1985)

A more sophisticated approach was proposed by Berg (Berg, 1985). It is able to predict the vapour cloud explosion blast wave with more realistic shape and parameters.

This multi-energy method is based on the observation that the explosive strength of vapour cloud primarily comes from the obstructed or partially confined parts of the cloud. The blast from a vapour cloud is predicted by an idealised explosion of which blast parameters are available in the form of charts shown in Figure 2.2. Equations used to define the parameters in Figure 2.2 are presented as follows (Berg, 1985):

$$\Delta\overline{P}_s = \frac{\Delta P_s}{P_0} \tag{2.2a}$$

$$\bar{t}_+ = \frac{t_+ c_0}{(E/P_0)^{(1/3)}} \tag{2.2b}$$

$$\overline{R} = \frac{R}{(E/P_0)^{(1/3)}} \tag{2.2c}$$

$$P_0 = atmospheric\ pressure$$

$$c_0 = atmospheric\ soundspeed$$

$$E = amount\ of\ combustion\ energy$$

$$R = stand-off\ distance$$

where $\Delta\overline{P}_s$ is the dimensionless maximum overpressure, $\bar{t}_+$ is the dimensionless positive duration and $\overline{R}$ is the energy scaled distance to the explosion centre.

It is assumed that the strong blast only comes from the part of cloud that is subjected to high degree of confinement and the rest of the cloud will just burn out without making any significant contribution to the blast strength. Therefore the blast from the confined and unconfined area covered by vapour cloud can be modelled separately, using a high strength value for the partially confined area and low strength for the unconfined area, and combine to produce the overall results. Since the flame velocity in the unconfined part is relatively slow, and it is very unlikely that two source of strong blasts would be initiated at the same time, blasts generated from different part of the cloud could be somehow treated independently (Pritchard, 1989).

The method assumes a semi-spherical vapour cloud with stoichiometric fuel - air mixture and it has two characteristic parameters: the vapour cloud charge energy E and the strength ΔP_s. The charge energy E should be taken to be equal to the total combustible heat of the fuel participating in the explosion and the charge strength should be assumed to be maximum (Mercx et al., 2000). In Figure 2.2, number 1 indicates a blast with insignificant effect and 10 for a gas detonation. The shape will be changed according to the strength level as depicted in Figure 2.2a. The major uncertainty comes from the estimation of charge strength ΔP_s, between 1 and 10. The estimation could be made based

on the observed damage or experience. For an more sophisticated and accurate approach, the correlation with experiments to quantify the charge strength can be done according to the procedures laid out by Mercx (Mercx et al., 2000). The correlation equation is:

$$\Delta P_s = a\left[\frac{VBR \cdot L_f}{D}\right]^b {S_l}^{2.7} {S_c}^{0.7} \tag{2.3}$$

In equation 2.3, VBR is the volume blockage ratio, which is the portion of the volume occupied by the obstacles within the cloud. L_f is the flame path, which is the longest distance from the point of ignition to an outer edge of the obstacle. D is the average obstacle size (m). S_l is the laminar burning velocity (m/s). S_c is a scale factor and a, b are correlation fitting constants. Equation 2.3 takes into account of the effects from three influence factors: the boundary conditions, the mixture reactivity and the explosion scale. Once the charge strength is determined, the selection of curves can be completed. The overpressure and positive duration can be readily extracted from Figure 2.2 as a function of energy scaled distance $\overline{R}$.

2.2 Review of past incidents

2.2.1 Buncefield incident

On the morning of Sunday 11th December 2005, a vapour cloud explosion occurred at the Buncefield Oil Storage Depot, Hemel Hempstead, Hertfordshire, UK. The investigation immediately carried out by the Buncefield Major Incident Investigation Board (BMIIB) identified that the explosion was a consequence of the overflow of 250,000 litres of petrol from the storage tank 912 in the depot. The cloud was approximately circular with a radius of 200 metres before the explosion occurred, with average height of 2 metres (SCI, 2009).

The blast caused tremendous damage to the near and far field buildings. Due to lack of any significant congestion in the site, the severity of the explosion had not been anticipated in any major hazard assessment of the oil and gas storage site before. The red line in Figure 2.3 represents the approximate boundary of

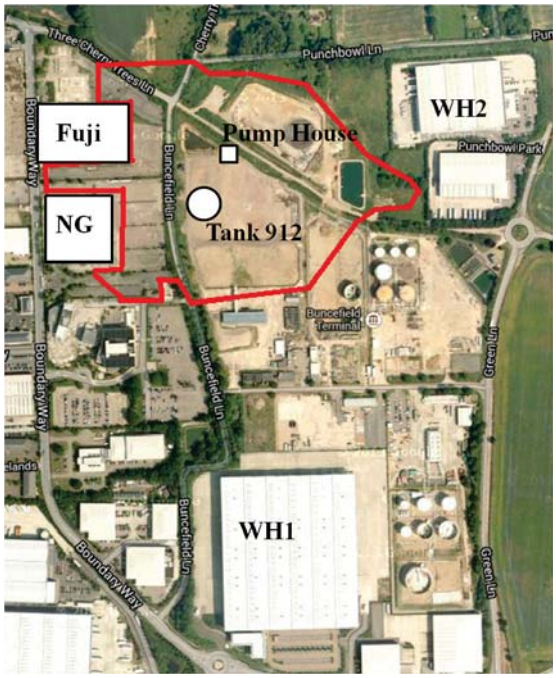


Figure 2.3: Buncefield site with location of buildings (Atkinson, 2011)

the vapour cloud immediately before explosion. The ignition point was found to be the pump house.

Damage during the explosion is vast and involved lots of different objects. Towards the edge of the vapour cloud, there are North Gate (NG) and Fuji buildings which suffered severe damage, as shown in Figure 2.4a and 2.4b. In the medium-far field a large warehouse structure (WH1) was located at the south of the site, its damage is shown in Figure 2.4c after the claddings were removed. Within the cloud, there are few buildings but lots of steel boxes (Figure 2.4d) and drums were found scattered all over the site. The storage tanks (Figure 2.4e) were almost destroyed completely. Damage to the instruments within the cloud suggested the overpressure was in excess of 2 bar. The overpressure rapidly decreased outside of the cloud. This can be seen in Figure 2.4f, in which the car furthest from the camera (i.e. nearest to the cloud) were clearly exposed to the blast wave and crushed completely. However the car furthest from the cloud only suffered slight damage at the rear.

During the investigation, both deflagration and detonation were compared



(a) Northgate Building



(b) Fuji Building



(d) Steel Box



(c) Warehouse - 1



(e) Drum and Tanks



(f) A line of cars

Figure 2.4: Buncefield Explosion Damages (SCI, 2009)

with the observed damages but neither is able to explain the explosion conclusively. It was concluded in the joint industry project (SCI, 2009) and by Johnson (Johnson, 2010) that due to the lack of congested pipe works within the vapour cloud (which is a prerequisite for a strong vapour cloud explosion), the explosion initially started as deflagration at the pump house. And when the flame approached to the trees and undergrowths along the lanes around the site, the combustion flame accelerated due to the turbulence generated by the wooden branches, then developed in to detonation. At least part of the cloud has been detonated afterwards.

Compared with the past major incidents, the 2005 Buncefield explosion offered lots of evidence and damage for forensic studies and investigations. The investigation work presented a great advancement in understanding vapour cloud explosions. It also identified some areas worthy of fundamental researches.

2.2.2 Other major accidents

Buncefield is not the first vapour cloud explosion that occurred in the oil and gas industries. A few previous incidents involving vapour cloud and gas explosions are summarised below:

- Flixborough, UK, 1974 (Sadee et al., 1977), in which the failure of a section of 700 mm diameter temporary pipe released approximately 100 tonnes of cyclohexane. The explosion caused significant damage to the building structures on site. The overpressure at the edge of the cloud was approximately 1 bar declining with distance as would be expected from a TNT charge detonation. Within the cloud the pressure was estimated to be as high as 10 bar.

- Port Hudson, Missouri, US, 1970 (Burgess and Zabetakis, 1973), in which the pipeline failure released approximately 120,000 litres of propane. The character and distribution of damage strongly resembled that at Buncefield (SCI, 2009). Damages to buildings within the cloud are significant and suggesting overpressure of at least 1 bar over the area covered by the cloud.

- Ufa, Ural Mountains, Russia, 1989 (Makhviladze and Yakush, 2002), in which the failure of a pipeline of 700 mm diameter released a total 2000-10,000 tonnes of liquefied petroleum gas (LPG). Trains were damaged as if they were clamped in a vice. Trees felled over a large area suggesting the overpressure exceeded 1 bar.

- Naples, 1985 (Maremonti et al., 1999), in which approximately 700 tonnes petrol escaped from an over-filled tank, and a subsequent vapour cloud explosion occurred. Maximum pressure was indicated by the damaged objects to be 0.48 bar. Windows were broken to a range of 1 km.

- Saint Herblain, France, 1991 (Lechaudel and Mouilleau, 1995), in which a hydrocarbon explosion occurred in a tank farm as a consequence of petrol leakage. Explosion caused severe damages to the buildings in the surrounding area and also to the tanks on site. Overpressure indicators were analysed and the maximum pressure of 0.25 bar was estimated.

- Texas City, Texas, U.S, 2005 (BP, 2005), in which a total of 28,700 litres hydrocarbons C5-C7 released into atmosphere and mixed with air. The damage was focused in congested areas of the site where there was enhancement of turbulence promoting the combustion rate. The overpressure was estimated to be over 1 bar within the congested area.

2.3 Blast wave and loading

Detonation and deflagration of a vapour cloud generate very different forms of blast waves as shown in Figure 2.1a and 2.1b. The shape of the blast wave from a deflagration will approach to detonation at the medium to far-field distance. The blast wave from a detonation led by a shock front (with instantaneous rise of pressure) is usually referred to as an ideal blast wave. Its parameters can be defined by the TNT-equivalent method (with stand-off distance and charge weight).

2.3.1 Blast wave characteristics

A detonation blast wave is usually referred to as an ideal blast wave or shock wave. It is led by a shock front when travelling through the air and compresses the fuel mixture or air in the front. The properties of the medium before and after the shock front can be related by the Rankine-Hugoniot relations. The shock wave characteristics can be defined by TNT explosion and scaling laws based on the charge weight and stand-off distance.

2.3.1.1 Normal shock

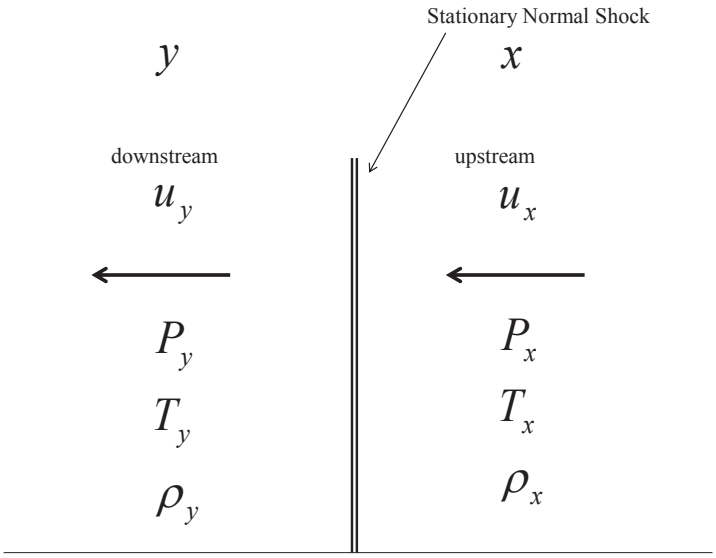


Figure 2.5: Stationary normal shock in a moving stream

The shock front of a blast wave is the determining factor in its characteristics. The normal shock has extremely thin thickness and it increases the pressure P, temperature T and density ρ of the flow passing through instantly. As a result the flow is decelerated rapidly across it. It is convenient to use the shock front itself as the reference datum to study its behaviours as shown in Figure 2.5.

The Rankine - Hugoniot relationships

In a moving stream, flow temperature, density, pressure and velocity are required to describe the flow completely. Four equations 2.4a to 2.4d can be used to define above properties. The direction of the flow can be considered by Equation 2.4e (White, 2003).

$$mass\ conservation:\ \rho_x u_x = \rho_y u_y \tag{2.4a}$$

$$linear\ momentum:\ P_x - P_y = \rho_y {u_y}^2 - \rho_x {u_x}^2 \tag{2.4b}$$

$$energy:\ c_p T_x + \frac{1}{2}{u_x}^2 = c_p T_y + \frac{1}{2}{u_y}^2 \tag{2.4c}$$

$$perfect\ gas:\ \frac{P_x}{\rho_x T_x} = \frac{P_y}{\rho_y T_y} \tag{2.4d}$$

$$entropy\ consideration:\ \frac{s_y - s_x}{R} = \frac{k}{k-1} ln\frac{T_y}{T_x} - ln\frac{P_y}{P_x} \tag{2.4e}$$

$$Mach\ number:\ M_x = \frac{u_x}{\sqrt{kRT_x}}\ \&\ M_y = \frac{u_y}{\sqrt{kRT_y}} \tag{2.4f}$$

In Equation 2.4, x and y are subscripts for denoting up and downstream (or before and after shock front respectively). ρ is the density of the flow. P is pressure and T is temperature of the flow stream. c_p is the specific heat at constant pressure and k is the ratio of specific hear constants. s is the entropy in the flow stream and R is the universal gas constant. M is the Mach number of the flow stream.

Assuming the properties of flow in the upstream (x) are known and the flow system is adiabatic, Rankine-Hugoniot relationships can be derived from Equation 2.4 to relate the properties on both sides of the normal shock, thus the flow conditions after the shock front can be determined. The entropy consideration Equation 2.4e implies that the pressure in the downstream must be higher than the upstream ($P_y/P_x > 1$), otherwise the change of entropy across the normal shock will be negative and this violates the second law of thermodynamics. And as a result the Mach number before the normal shock (in the upstream) must be supersonic ($M_x > 1$) and the flow after the shock is subsonic ($M_y < 1$) (White, 2003).

$$\frac{P_y}{P_x} = \frac{2k{M_x}^2 - (k-1)}{k+1} = \frac{7{M_x}^2 - 1}{6} \tag{2.5}$$

$$\frac{T_y}{T_x} = \frac{[2+(k-1){M_x}^2][2k{M_x}^2 - (k-1)]}{(k+1)^2{M_x}^3} = \frac{(5+{M_x}^2)(7{M_x}^2-1)}{36{M_x}^2} \tag{2.6}$$

$$\frac{u_y}{u_x} = \frac{2+(k-1){M_x}^2}{(k+1){M_x}^2} = \frac{1+5/{M_x}^2}{6} \tag{2.7}$$

Relationships giving the properties changes across the normal shock can be derived from the above equations (Kinney and Graham, 1985). Equations 2.5, 2.6 and 2.7 define the ratios of pressure, temperature and flow velocity between the up- and down-streams in terms of independent variable Mach number in the upstream (M_x).

Explosive shock

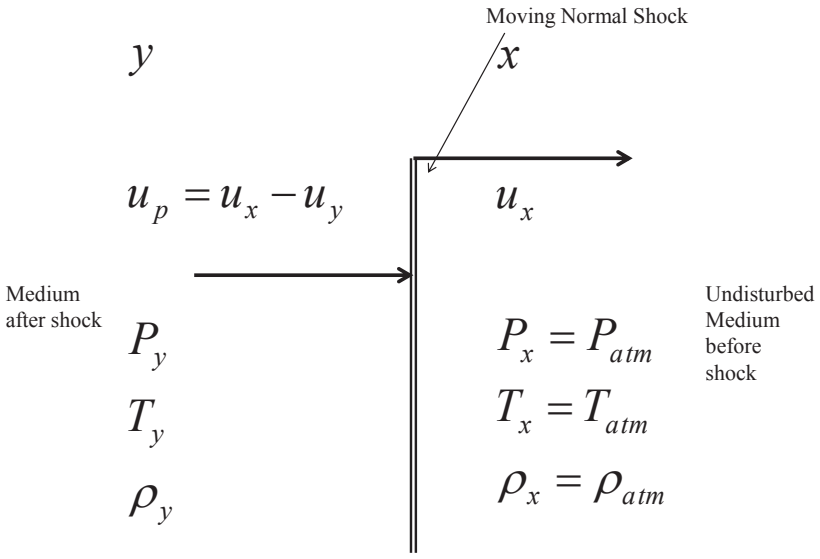


Figure 2.6: Explosive shock front moving in still air

The analysis of the stationary normal shock also applies to a moving shock

front generated in an explosion if we reverse the situation in which now the shock front is moving through the still air at velocity u_x and the undisturbed medium ahead of the moving shock is at atmospheric condition. The downstream flow then appears to follow the shock front at a lower speed u_p which is known as the particle velocity. This defines the blast wind after passage of the shock wave (Kinney and Graham, 1985).

$$p = P_y - P_x = \frac{2k({M_x}^2 - 1)}{k+1}P_x = \frac{7({M_x}^2 - 1)}{6}P_x \tag{2.8}$$

The peak overpressure p in the explosive shock is the difference of the pressures across the shock front as shown in Equation 2.8. It can also be presented in terms Mach number M_x and pressure P_x in the upstream.

$$u_p = u_y - u_x \tag{2.9a}$$

$$\frac{u_p}{a_x} = \frac{2({M_x}^2 - 1)}{(k+1)M_x} = \frac{5({M_x}^2 - 1)}{6{M_x}^2} \tag{2.9b}$$

$$\left(\frac{u_p}{a_x}\right)^2 = \frac{(2/k)(P_y/P_x - 1)^2}{(k+1)(P_y/P_x) + (k+1)} = \frac{25(P_y/P_x - 1)^2}{42(P_y/P_x) + 7} \tag{2.9c}$$

Particle velocity (u_p) in the blast wave is the difference between the flow velocities across the shock front as depicted in Equation 2.9a (Kinney and Graham, 1985). u_p/a_x , the ratio of the particle velocity (u_p) to the local speed of sound (a_x) in the upstream (in the medium before shock wave) can be presented either in terms of upstream Mach number M_x or ratio of absolute pressures P_y/P_x, as shown in Equations 2.9b and 2.9c.

$$P_{stag} = P_y\left[1 + \frac{(k-1)(u_p/a_x)^2}{2(T_y/T_x)}\right]^{k/(k-1)} = P_y\left[1 + \frac{(u_p/a_x)^2}{5(T_y/T_x)}\right]^{3.5} \tag{2.10a}$$

$$p_{stag} = P_{stag} - P_x \tag{2.10b}$$

Stagnation pressure (P_{stag}) is used in a flow to measure the sum of free stream dynamic and static pressures. In a explosive shock it applies to the blast wind

following the shock front, and defined by Equation 2.10a (Kinney and Graham, 1985). The stagnation overpressure (p_{stag}) which is the stagnation pressure minus initial pressure is defined in 2.10b.

Reflected shock

When blast waves encounter a rigid surface of a object they will reflect from it and, dependent on the size of the surface , diffract around it. The simplest case is that the blast wave impinges on an infinitely large rigid surface at zero angle of incidence β as shown in Figure 2.7.

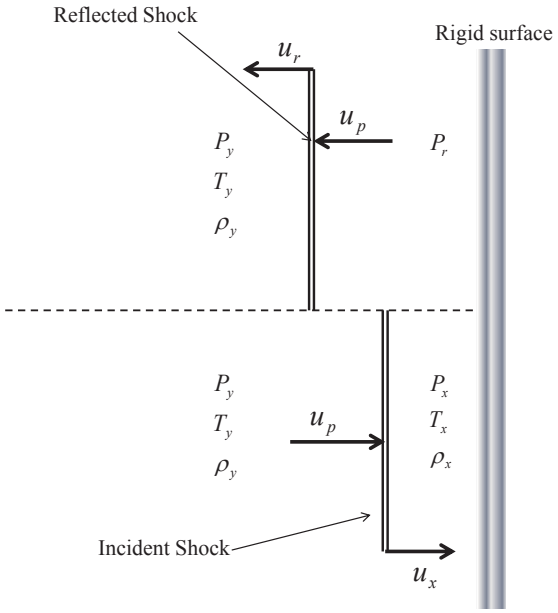


Figure 2.7: Normal reflected shock on a rigid surface

In a normal reflection, the reflected pressure (P_r) can be defined in terms of the pressures across the incident shock front P_y and P_x, as shown in Equation 2.11.

$$\frac{P_r}{P_x} = \frac{(P_r/P_x)[(3k-1)(P_y/P_x)-(k-1)]}{(k-1)(P_y/P_x)+(k+1)} = \frac{P_y(8P_y - P_x)}{P_x(P_y + 6P_x)} \tag{2.11}$$

The magnitude of a reflection shock can be also expressed in terms of reflection coefficient Λ and for a normal reflection Λ_n, as defined in Equation 2.12.

$$\Lambda_n = \frac{p_r}{p} = \frac{P_r - P_x}{P_y - P_x} = \frac{(3k-1)(P_y/P_x) + (k+1)}{(k-1)(P_y/P_x) + (k+1)} = \frac{8P_y + 6P_x}{P_y + 6P_x} \tag{2.12}$$

where p_r is the reflected overpressure. Equation 2.12 for the normal reflection coefficient allows two limiting values to be determined. For a very weak shock wave in which $P_y \approx P_x$, the coefficient Λ_n is approaching to 2. While for a strong shock in which $P_y \gg P_x$, the coefficient approaches to 8. Thus the theoretical limits for Λ_n can be found to be between 2 and 8. However, because of gas dissociation effect at very close range (Smith and Hetherington, 1994), reflection coefficients higher than 8 can be observed in actual blast. It can also be seen in Figure 2.8 that for a very high incident overpressure the reflection coefficient can be well above 8. The derivation of the expressions shown above can be found in more details in "Explosive shocks in air" (Kinney and Graham, 1985) and it is assumed that the specific heat ratio $k = 1.4$ for air (ideal gas).

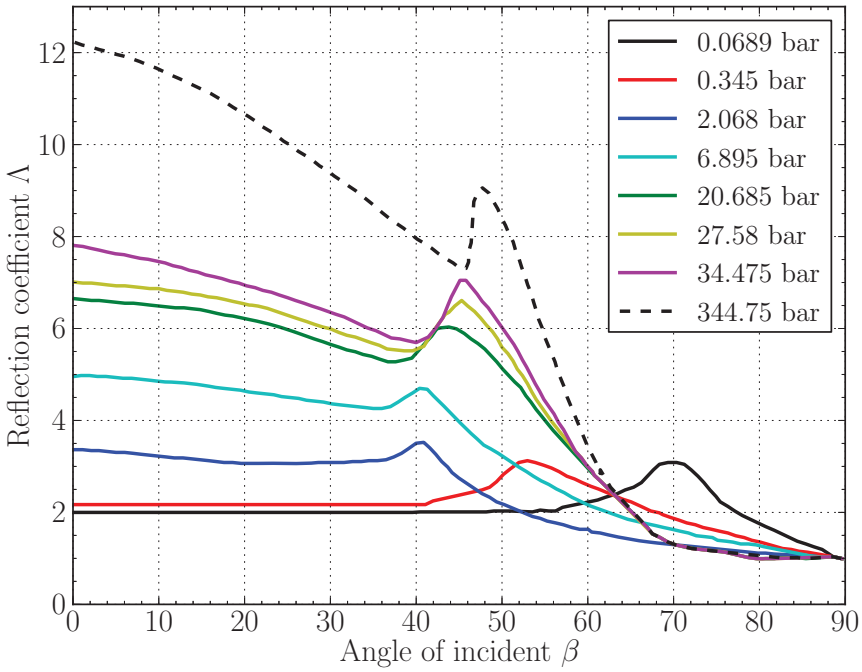


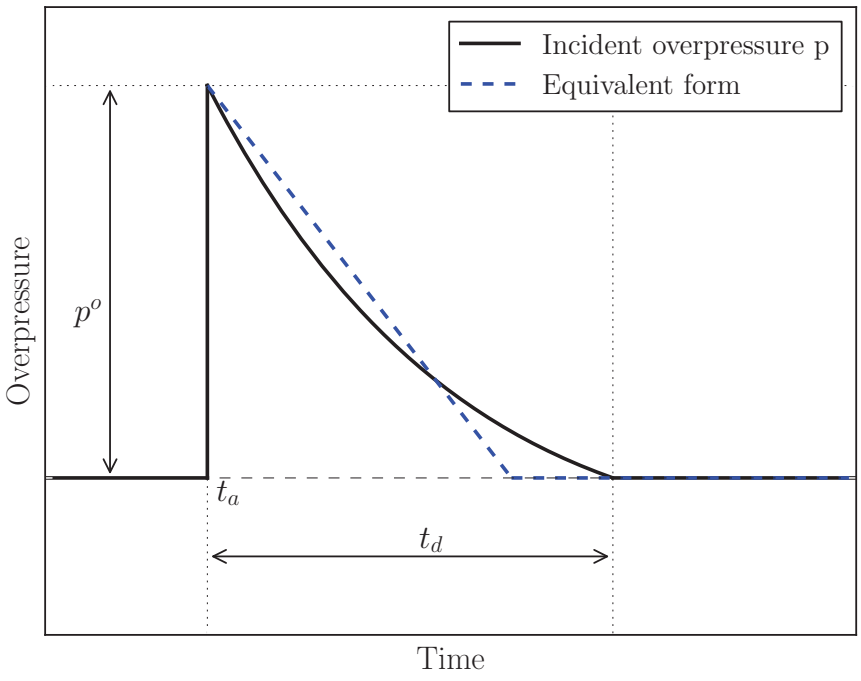
Figure 2.8: Reflected pressure coefficients vs. angle of incidence (β) (USDOD, 2008)

Equations 2.11 and 2.12 are only applicable when the blast wave impinges perpendicularly to the surface, which is a normal reflection. The angle of incident is zero ($\beta = 0^o$) and the magnitude of reflection is maximum. When the reflecting surface is parallel to the direction of the blast wave ($\beta = 90^o$) the surface will experience the minimum reflected pressure which is actually the incident pressure. The magnitude of the reflection depends on both the incident peak pressure and the angle of incidence. Typical reflection factors are depicted in Figure 2.8 (FEMA).

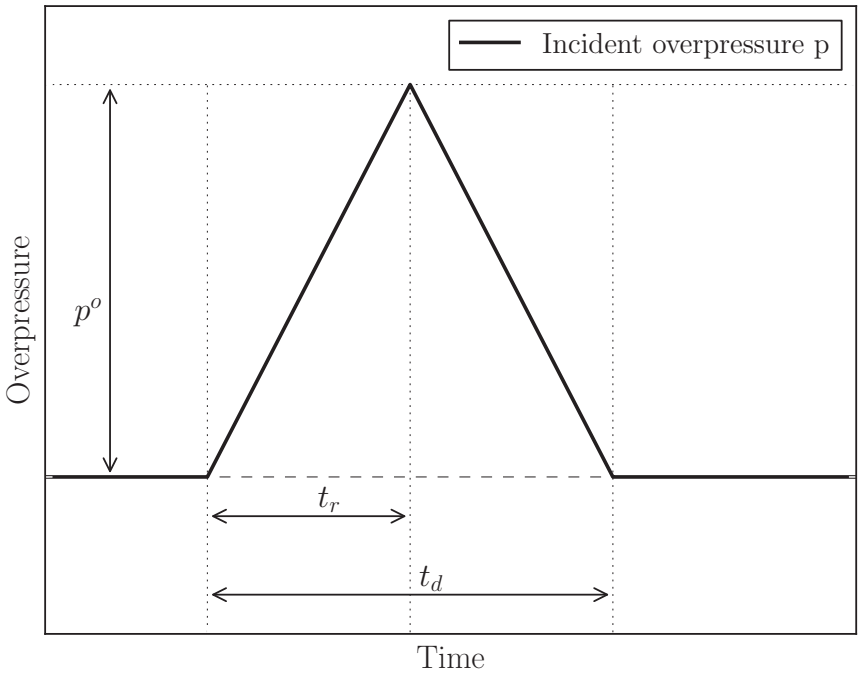
2.3.1.2 Blast wave and scaling law

A blast wave is generated when the surrounding medium (mostly air) is forcibly pushed outwards by the high temperature and pressure gases in the vapour cloud explosion. A detonation blast wave with the profile shown in Figure 2.9a is identical to a high explosive explosion thus it can be analysed by the TNT-equivalency method. The shape of the deflagration blast wave from a VCE is shown in Figure 2.9b. In the far field the deflagration shape will gradually approach to a detonation when the wave propagates away from the centre. This is because the high pressure portion of the deflagration wave is travelling at a higher local speed of sound than the other parts of the blast wave with lower pressures, hence the peak part will gradually catch up the leading compressive position and eventually form a detonation blast wave. The peak overpressure of a blast wave will reduce over the distance and its duration will be elongated due to the different velocities throughout the blast wave.

A detonation blast wave is also known as an ideal blast wave. Its characteristics are well understood and can be predicted based on the TNT-equivalency method and the scaled distance Z defined in Equation 2.14. As mentioned before, four parameters are used to define an ideal blast wave: peak overpressure p^o, arrival time t_a, positive phase duration t_d and the specific impulse I. The blast wave is leading by a normal shock front with peak overpressure p^o, and the exponential decay of the overpressure can be described by Equation 2.13, finally it will drop to zero at the end of the duration t_d. α is the shape factor which determines the rate of the exponential decay, usually $\alpha = 1$. For simplicity an



(a) Detonation



(b) Deflagration

Figure 2.9: Shape of blast waves

alternative (equivalent) form can be taken in which the decay is assumed to be linear and the impulse is preserved to be the same to the exponential form.

$$p = p^o \left(1 - \frac{t}{t_d}\right) \epsilon^{-\alpha t/t_d} \tag{2.13}$$

In the above equation, t is time and ϵ is the base of natural logarithm. α is used to define the form of the shape of the blast wave. Many methods have been used to obtain the characteristics of blast waves from explosions. It has been found that using network equations can relate the important parameters of an ideal blast wave to the scaled distance Z. In Equation 2.14, R is the stand-off distance to the centre of the explosion and W the weight of equivalent TNT charge to replace the vapour cloud in a detonation event. Equations 2.15 and 2.17 depict the relation between overpressure/positive duration and scaled distance. The arrival time of the blast wave then can be evaluated from the velocity of the shock front as shown in Equation 2.16.

$$Z = \frac{R}{W^{\frac{1}{3}}} \tag{2.14}$$

$$\frac{p^o}{P_a} = \frac{808\left[1 + \left(\frac{Z}{4.5}\right)^2\right]}{\sqrt{1 + \left(\frac{Z}{0.048}\right)^2}\sqrt{1 + \left(\frac{Z}{0.32}\right)^2}\sqrt{1 + \left(\frac{Z}{1.35}\right)^2}} \tag{2.15}$$

$$t_a = \frac{1}{a_x} \int_{r_c}^{r} \left[\frac{1}{1 + \frac{6p^o}{7P_a}}\right] dr \tag{2.16}$$

$$\frac{t_d}{W^{1/3}} = \frac{980\left[1 + \left(\frac{Z}{0.54}\right)^1 0\right]}{\sqrt{1 + \left(\frac{Z}{0.02}\right)^2}\sqrt{1 + \left(\frac{Z}{0.74}\right)^2}\sqrt{1 + \left(\frac{Z}{6.9}\right)^2}} \tag{2.17}$$

In the above equations, P_a is the atmospheric pressure. r_c is the radius of the high explosive charge and r is the distance from the charge to the target. Scaling of the ideal blast wave parameters are extensively used in practice. The scaling law states that two explosions can be expected to produce identical blast wave at distances which are proportional to the cube root of the respective energy release (Kinney and Graham, 1985). The source of the energy release is usually a high

explosive e.g. TNT. The shape of the two charges in the two explosions are expected to be similar as well. For high explosive the energy release is proportional to the charge weight as defined in Equation 2.14. Equations 2.14 and 2.15 imply that, for example, to produce the same level of overpressure at twice a distance requires eight times the weight of the explosive charge. Equation 2.17 states that the eight times weight of charge will produce a duration which is eight times longer.

On the other hand, deflagration blast wave does not have such scaling laws and the parameters can not be simply defined based on scaled parameters. Nonetheless, the TNO multi-energy method is widely used for prediction of a deflagration explosion and parameters such as overpressure p^o, positive duration t_d and finite rise time (duration of the compressive wave) t_r can be used to completely define a deflagration blast wave. In this project these wave parameters are directly specified within a range of overpressure and impulses since the detailed prediction of deflagration is outside of the scope of the present work.

2.3.2 Dynamic blast loads

The blast wave generated in an explosion imposes dynamic loads on the object in its travelling path. The load is characterised by a rapid rise in magnitude when the blast wave impinges on the target surfaces then decreases as the blast wave subsides. A simplified representation of a blast wave (shock front shown) passing over a rigid target is shown in Figure 2.10. The peak pressure experienced by the front face of the target is the reflected overpressure p_r and the other surfaces would experience a overpressure slightly lower than the side-on overpressure $p = P_y - P_x$.

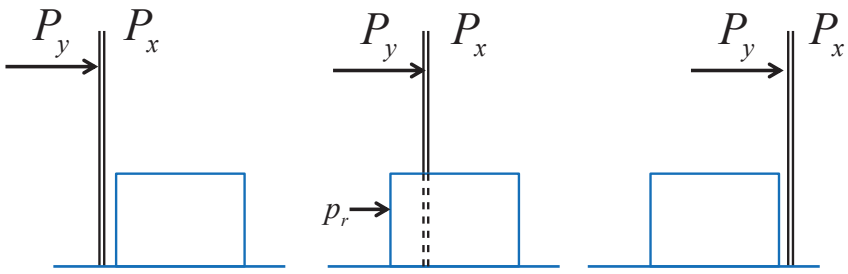


Figure 2.10: Passage of a blast wave over a rigid object

The ideal dynamic pressure loads experienced by the surfaces of a target are shown in Figure 2.11. The reflected pressure load is produced by the shock front impinging on the surface perpendicular to the blast wave (normal reflection). The stagnation pressure is caused by the movement of the particles behind the shock front, which are brought to halt by the surfaces. Side-on pressure is also known as the incident pressure and finally the drag pressure is the load exerted by the blast wind. The difference (stagnation - drag) is the load experienced at the rear surface of the body. Using the blast curves the actual dynamic loadings on the different faces of the target can be estimated in the following sections.

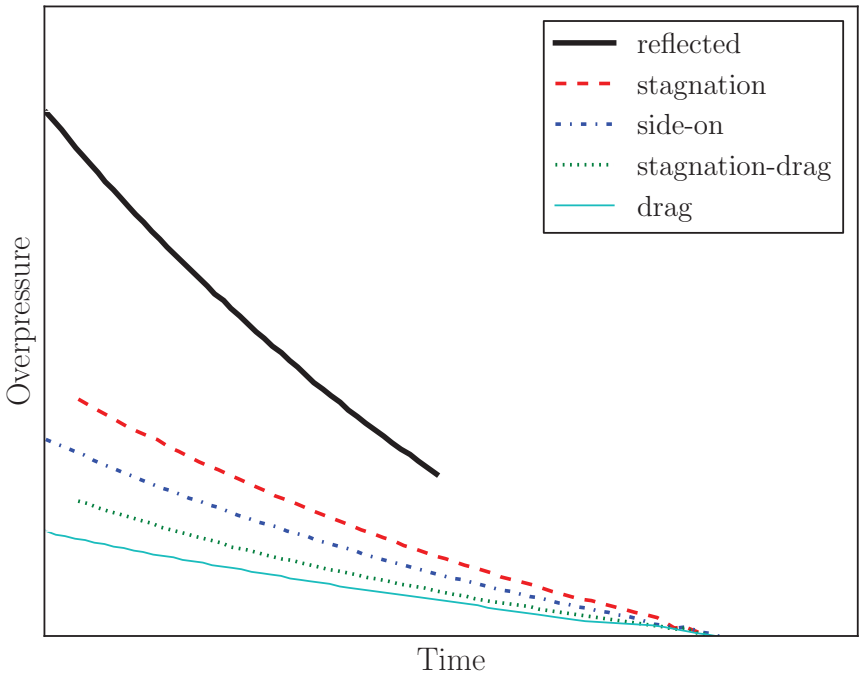


Figure 2.11: Blast curves (Kinney and Graham, 1985)

2.3.2.1 Front surface load

When the blast wave strikes the front surface, it will immediately experience a peak reflected pressure p_r which follows the reflected curve in Figure 2.11. The reflected pressure is significantly greater than the surrounding pressure. A rarefaction wave then forms over the front surface of the object and progresses

inwards from the edge, travelling at the speed of sound in the reflected medium. With the decaying of the reflected pressure the velocity of the rarefaction wave will reduce and an arbitrary small panel on the front surface will be subjected to the reflected pressure until at time d/U_x when the arrival of the rarefaction wave brings the relief effect so the pressure level drops significantly to stagnation overpressure, where d is the shortest distance of the small panel to the edge of the front face. Therefore an average sense is needed to take into account the progress of the rarefaction wave over the whole front surface, where the earliest panel to see the pressure relief is at the edge while in the centre the panels will experience the reflected pressure the longest. To generalise the effects, as shown in Figure 2.12, the overpressure will start with p_r at zero time and reduce to stagnation pressure at time $3S/u_x$, where S is the half width or height of the front surface, whichever is smaller. And after this time the overpressure will follow the stagnation pressure curve and reduces to ambient. In Figure 2.12, p_i is the incident pressure.

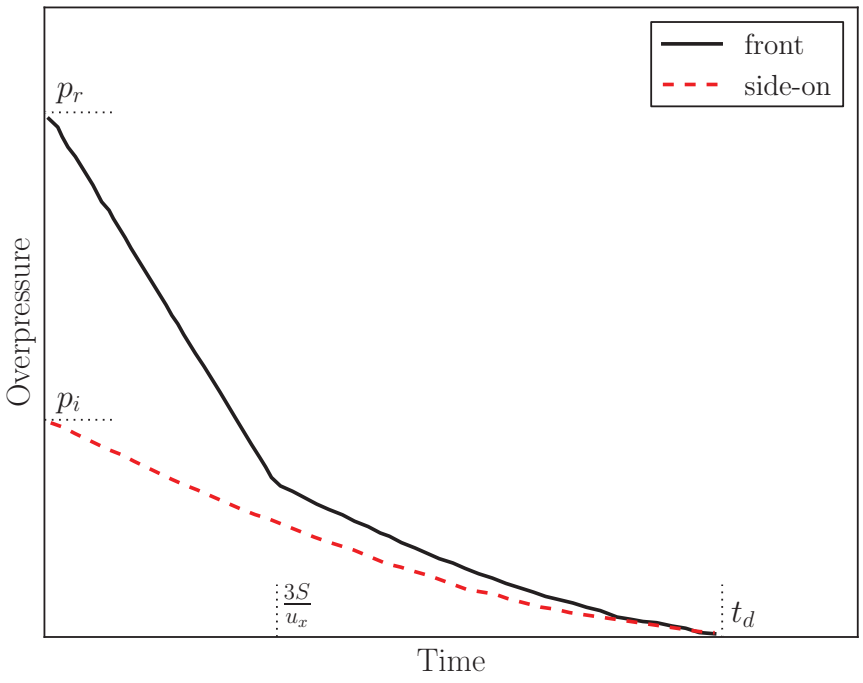


Figure 2.12: Blast load-time history on front surface (Kinney and Graham, 1985)

2.3.2.2 Rear surface load

The rear surface will not experience any load until the blast wave travels through the length of the target L at time L/u_x, as shown in Figure 2.13a. After this time the pressure loading will start to build up and reach the instantaneous value, which is the different between the stagnation and the drag pressure. The compression wave will take a finite time to travel from the edge to the centre hence different locations on the rear face will feel the pressure at different times with different magnitudes. The entire load on the rear face is an average of the loads on each location. Therefore, the average starts to rise at time L/u_x and reaches the peak value $p_{stag} - p_{drag}$ after a finite rise time of $3S/u_s$. Then the loadings vanishes along the stagnation-drag curve to zero at time $t_d + L/u_x$. It is important to note that the actual pressure loadings on the rear surface will be offset by a time L/u_x and the peak value is lower than the side-on peak overpressure.

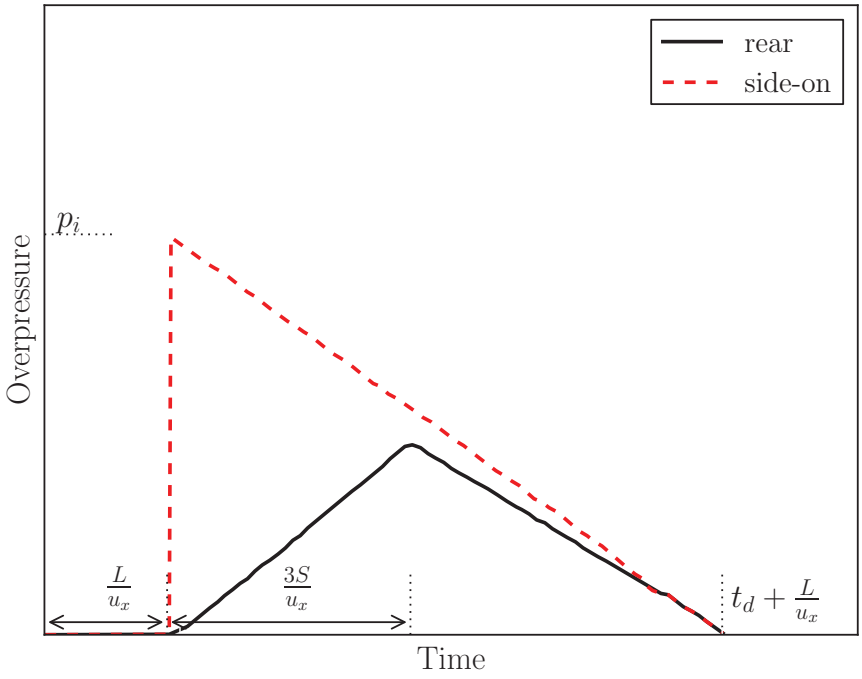
2.3.2.3 Top and side surface loads

Top and side faces are parallel to the direction of the blast wave, ideally they will be subjected to the side-on (incident or free-field) over pressure.

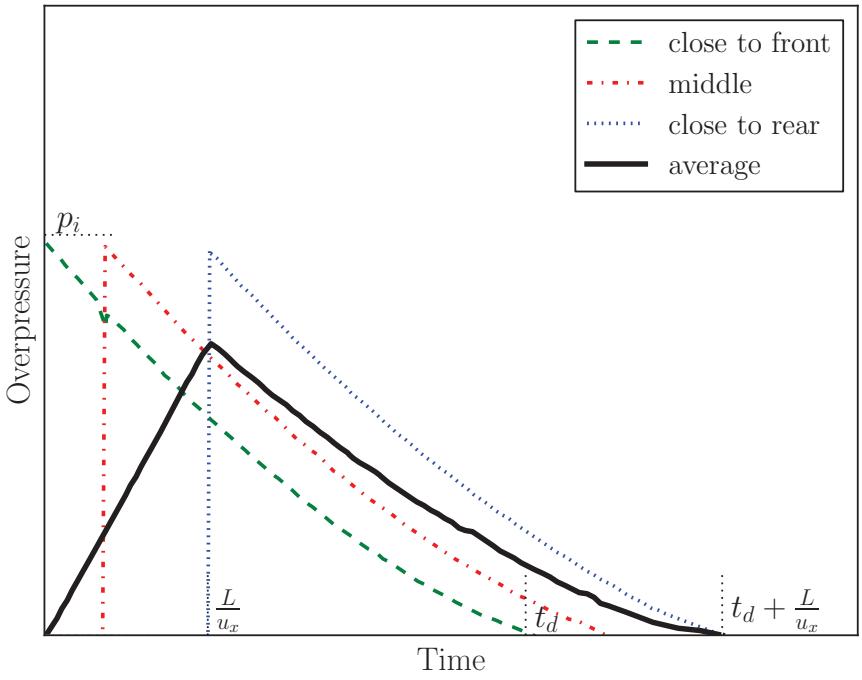
However, the edges between the front face and the top/side face will induce diffraction in the flow field and this diffracted wave will slightly reduce the peak overpressure. Similarly, an arbitrary panel at the front will experience the loadings earlier than panels located towards the back, as depicted in Figure 2.13b. The average will starts at time zero when the blast wave strikes on the front face and then gradually increase to a peak which is slightly lower than the peak side-on value at time L/u_x. It then decays to atmosphere pressure at time $t_d + L/u_x$. The time L/u_x and the rise of the loading are used to determine the load on the whole surface in an average manner.

2.3.2.4 Loads on the frame

Blast loadings on the surfaces of a structure will be transferred to its frames and eventually to the ground. Once the frame fails then the whole structure is severely damaged regardless of the condition of the claddings. The net lateral load on the frame of a structure can be calculated by the difference between the total loads

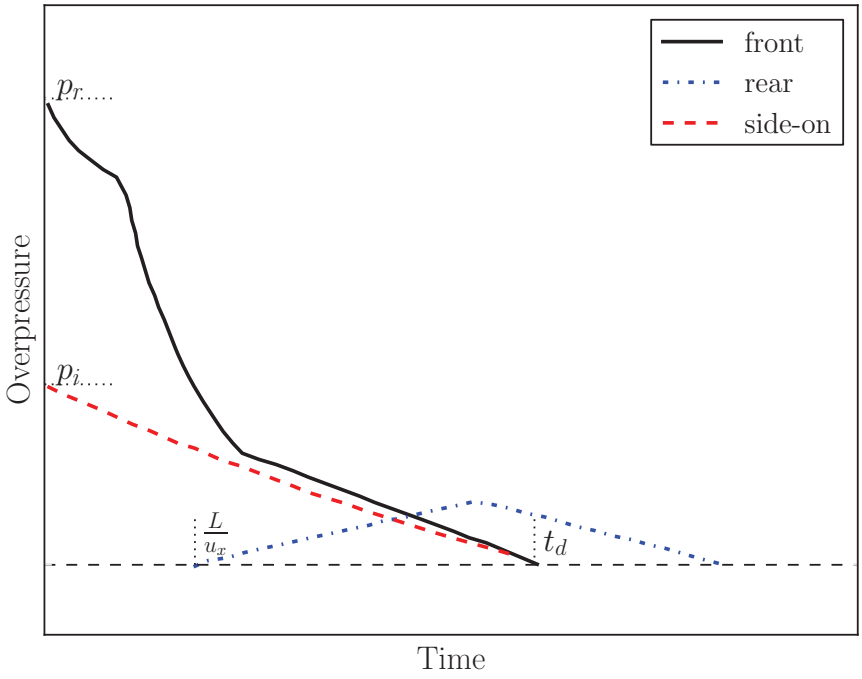


(a) Rear surface

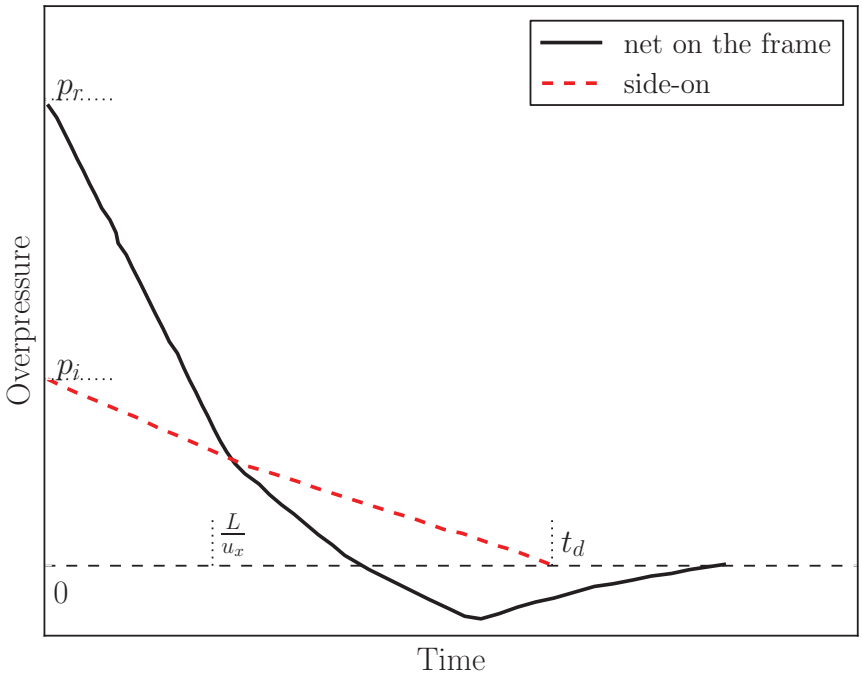


(b) Top/side surface

Figure 2.13: Blast load-time history other surface (Kinney and Graham, 1985)



(a) Frame



(b) Net on frame

Figure 2.14: Blast load-time history on frame (Kinney and Graham, 1985)

on the front and rear surfaces. This can be readily established as shown in Figure 2.14. Figure 2.14a superimposes the blast loadings on the front and rear faces. Figure 2.14b shows the net sidewise load on the frame by subtracting the rear load from the front. It can be noted that there is a negative load acting on the frame in the opposite direction. The negative phase is caused by the offset of the rear face load and occurs when the load on the front face decreases to a value lower than the rear surface load.

2.3.2.5 Non-ideal blast wave

The deflagration blast wave is also known as a non-ideal blast wave. Structural loads resulting from the non-ideal blast wave can not be readily determined by simple methods shown above. The non-ideal blast wave has a compressive wave in the front rather than a normal shock. This means that the Rankine-Hugoniot relationships are not applicable, thus the reflection curves are not applicable either. Due to the fact that the rise of the overpressure takes a finite amount of time, when the blast wave impinges on the surface, the reflected pressure can start to relieve even before the peak is reached. This finite rise time allows a flow around the target to be established. The loadings of a structure thus becomes strongly dependent on the dimension of the target and as well as the blast wave parameters.

The rate of energy release in the deflagration is slow so it could take up to several hundreds of milliseconds to reach the peak overpressure. The relief waves and flow due to rarefaction can be established even over relatively large buildings in such a long time period. If the deflagration blast wave takes 100 ms to reach the peak, for a building with dimension of 10 meters the rarefaction wave will travel across the surface in about 30 ms at ambient speed of sound. The relief from structure loads occurs on the same time scale as the loadings. Therefore the blast loads are more closely dependent on the parameters of the incident blast wave. It has been noted that the loadings, caused the compressive wave in a non-ideal blast wave, does not have a significant enhancements as normally expected from a ideal blast shock wave at the same level of peak overpressure (Needham, 2010).

2.4 Structural response

The response of a structure to blast load is governed by its energy absorption capacity and dynamic characteristics. Owning to the ductile properties, structural components made of reinforced concrete or steel can absorb a lot of strain energy, however components made of brittle materials such as glass, timber or cast iron will fail suddenly with minimum deformation. In many cases, it is important to understand how the structure will respond to a blast wave from an explosion. These include design of a blast resistant structure or blast damage assessment of a building in a high risk environment. They are also useful for conducting forensic studies on already damaged structures.

2.4.1 Analysis methods

2.4.1.1 Single degree of freedom method

Biggs' single degree of freedom model (Biggs, 1964) is probably the most widely used simplified method to determine the blast response of structures. By using transformation factors, structural components or systems can be transformed into an equivalent system consists of one discrete mass and one spring representing the resistance of the component, as shown in Figure 2.15. In many cases a

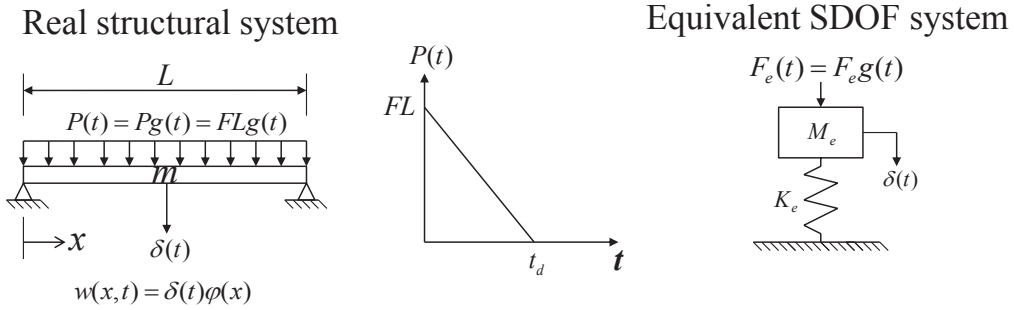


Figure 2.15: Typical equivalent single-degree-of-freedom system

structural component can be idealised into a SDOF equivalent system based on assumptions about the behaviour of the structure. For example, the resistance

function is based on static solutions. Moreover, the deformation shape of the component must be assumed in order to calculate the transformation factors.

The motion of a simply supported beam (with mass $m = \rho AL$) as shown in Figure 2.15 can be described by one single variable $\delta(t)$, which is also the motion of the equivalent SDOF system. $P = FL$ is the total load applied on the beam, where F is the distributed load and L is the length of the beam. $\phi(x)$ is the assumed shape of the deformed beam under the prescribed load. For the equivalent SDOF system, F_e, M_e and K_e are the equivalent force, mass and stiffness of the simplified model. The shape of the deformed beam can be chosen as the fundamental mode or the static deflection shape. For elastic response the deformation of the whole beam can be described using the static shape and in the plastic range the deformed shape is assumed to be a mechanism with a plastic hinge in the middle, as depicted in Equation 2.18.

$$w(x,t) = \delta(t) \cdot \phi(x) \tag{2.18a}$$

$$elastic: \ \phi(x) = \frac{16}{5L^4}(x^4 - 2Lx^3 + L^3x) \tag{2.18b}$$

$$plastic: \ \phi(x) = \begin{cases} \frac{2x}{L} & 0 \leq x \leq \frac{L}{2} \\ 2(1 - \frac{x}{L}) & \frac{L}{2} \leq x \leq L \end{cases} \tag{2.18c}$$

The energy terms and generalised forces for the beam in elastic and plastic range are calculated respectively as:

$$elastic- \ \ Strain\ energy\ (V) = \frac{1}{2}EI\int_0^L (w''(x,t))^2 dx \tag{2.19a}$$

$$Kinetic\ energy.\ (T) = \frac{1}{2}\int_0^L \rho A(\dot{w})^2 dx \tag{2.19b}$$

$$Generalised\ Force\ (Q_i) = \int_0^L p(x,t)\phi(x)dx \tag{2.19c}$$

$$plastic- \ \ Energy\ of\ dissipation\ (V) = \int_0^\theta M_p d\theta \tag{2.19d}$$

In the above equation, M_p is the plastic moment of the beam and θ is the rotation of the support end. In the plastic range, only the formulation of the strain energy is changed due to the existence of the plastic hinge in the mechanism. Kinetic energy and generalised force are the same as elastic response.

$$\frac{d}{dt}\left(\frac{\partial T}{\partial \dot{q}_i}\right) - \frac{\partial T}{\partial q_i} + \frac{\partial V}{\partial q_i} = Q_i \tag{2.20}$$

Applying Lagrangian equation (Equation 2.20) to the energy and force terms and the equation of motion of the equivalent system for both elastic and plastic can be obtained as follows, where q_i is admissible functions.

$$elastic- \ \ (0.78)m\ddot{\delta}(t) + k\delta(t) = P(t) \tag{2.21a}$$

$$plastic- \ \ (0.66)m\ddot{\delta}(t) + \frac{8M_p}{L} = P(t) \tag{2.21b}$$

The coefficient 0.78 and 0.66 are known as the "Mass-Load factor (K_{LM})" and they are used to modify the mass of the actual system (m) then the equation of motion of the simple equivalent SDOF model can adopt the actual stiffness (k) and the applied load $P(t)$.

The second terms on the left of Equation 2.21 can be replaced by a resistance

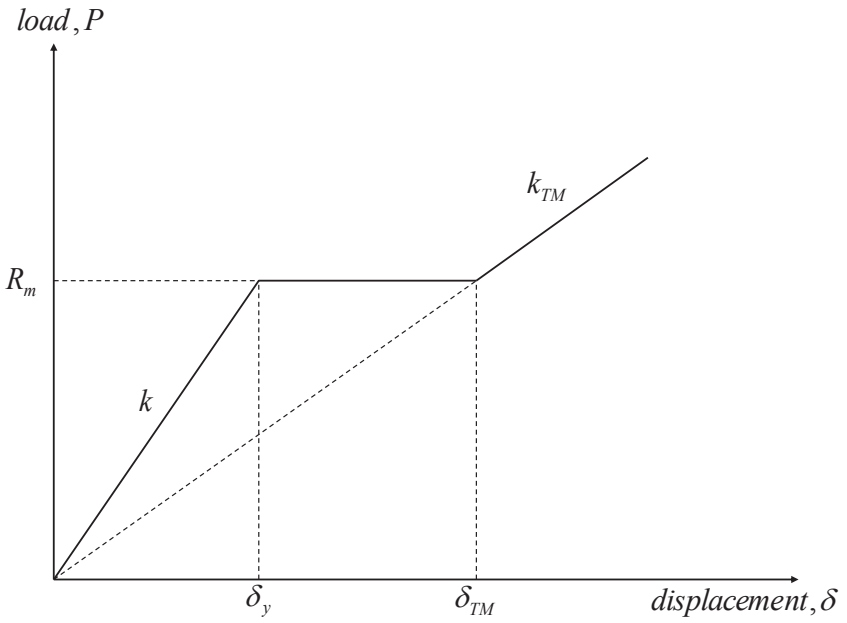


Figure 2.16: Resistance curve R(δ) for a typical SDOF system

function $R(\delta)$. In the elastic range $R(\delta)$ has the value of $k\delta(t)$, which is the flexural stiffness of the simply support beam and in the plastic range it becomes the maximum plastic load $R_m = \frac{8M_p}{L}$. The resistance function based on the deflection $\delta(t)$ is shown in Figure 2.16. In which δ_y is the displacement at yielding and δTM is the displacement at which the tensile membrane force dominates the response. k_{TM} is the stiffness of due to the tensile membrane force. Therefore the equation of motion for a equivalent SDOF system can be finally written as:

$$K_{LM} m\ddot{\delta}(t) + R(\delta) = P(t) \tag{2.22}$$

The simple support conditions shown in Figure 2.15 will introduce tension membrane forces due to the catenary action at large deflection. This is true for most components which always have a certain degree of axial constraints in the structure. Resistance function can be defined to include this effect when the deflection $\delta(t)$ reaches δ_{TM}, the start position of tension membrane stage. By using the assumed deflection shape and the equation of the length of an arc, the relation between the axial tension T in the beam and the maximum deflection at

the middle point $\delta(t)$ can be derived as:

$$\delta_{TM} = \delta_y + \sqrt{\frac{4TL^2}{\pi^2 EA}} \tag{2.23}$$

Above equation implies that it is assumed to be no axial tension in the beam until reaching the yielding displacement δ_y, and the catenary stage will start only when the axial tension reaches the value of T. EA is the axial rigidity of the beam. The membrane tension T is usually taken as the minimum of the plastic capacity of the beam section or the support. Membrane tension in the beam between δ_y and δ_{TM} is assumed to be small and the support is assumed to have limited flexibility to allow moderate axial displacement. When the catenary stage starts, taking equilibrium between the applied uniform load P(t) and the membrane tension T yields Equation 2.24, which provides the formula to evaluate the stiffness of the catenary stage and shows the relation between the applied load F and the maximum deflection δ of the beam in terms of the membrane tension T.

$$F = \frac{8T}{L^2}\delta, \; where \; K_{TM} = \frac{8T}{L^2} \tag{2.24}$$

The formulations presented above are for a simply supported beam with axial restraints. Without axial constraints the catenary stage can be simply ignored and the resistance function becomes a bi-linear elastic - perfect plastic curve. Formulations and Load-Mass factors of beams and plates with other support conditions were derived by Biggs (Biggs, 1964). SBEDS (USACE, 2008a), a spreadsheet software for single degree of freedom system published by US. Army Corps of Engineers, presents the formulations of the membrane stiffness shown in this section and this software was used in the current work to compare with the advanced finite element method. The original approach for evaluation of the transformation factors proposed by Biggs (Biggs, 1964) directly calculate the transformation factors by equating the energies and work done by the external forces between the actual and equivalent systems. His approach is nlengthy but shows more explicitly how the system is transformed.

The equation of motion (Equation 2.22) needs to be solved to determine the maximum dynamic response or the permanent deformation. A closed-form solu-

tion can be obtained for simple dynamic loading functions. However, in many cases the loading function will not have an analytical form, therefore the equation must be solved by time - stepping numerical integration methods (Craig, 1981). It has been shown that the Mass - Load factor K_{LM} has different value for elastic and plastic responses. The transformation factor and resistance are then chosen to match the type of behaviour expected. If little yielding is expected, the values for elastic response are used. Values for plastic behaviour can be used if severe plasticity is expected. Average values can be used if moderate plasticity is expected.

A simple analysis can reveal some insight into the response of a system to the dynamic load. If the load function is a simple triangle shown in Figure 2.15, then the equation of motion can be written as:

$$M_e\ddot{\delta}(t) + R(\delta) = P\left(1 - \frac{t}{t_d}\right) \tag{2.25}$$

For the initial conditions of no displacement and no velocity at time $t = 0$, the transient dynamic solution is (in which ω is the undamped natural circular frequency):

$$\frac{\delta(t)}{P/k} = (1 - \cos\omega t) + \frac{1}{t_d}\left(\frac{\sin\omega t}{\omega} - t\right) \tag{2.26}$$

Maximum deflection $\delta_{max} = \delta(t_m)$ is always of the most interests, it can be evaluated by differentiating Equation 2.26 and set to equal to zero:

$$0 = (\omega t_d) \cdot \sin(\omega t_m) + \cos(\omega t_m) - 1 \tag{2.27}$$

It can be deduced that there is a relation between (ωt_d) and (ωt_m) which can be written as $\omega t_m = f(\omega t_d)$, where $\omega = \sqrt{k/m}$, the natural circular frequency of the equivalent SDOF system. In the view of this relationship, we can deduced from Equation 2.26 that $\delta_{max}/(F/k)$ at $t = t_m$ (the time at which maximum dynamic deflection occurs) is a function of the ratio of load duration to the system's natural period T:

$$\frac{\delta_{max}}{F/k} = \phi(\omega t_d) = \phi'(\frac{t_d}{T}) \tag{2.28}$$

in which F/k is the static deflection and $T = 2\pi/\omega$.

The trail and error solution of the Equation 2.28 is shown as the solid line in Figure 2.17. It can be noted that the solution curve can be approximated by two straight lines. For very small value of ωt_d or t_d/T, the impulsive asymptote is a accurate approximations to the general solution. While for very large value of ωt_d or t_d/T, the quasi-static asymptote approximates the solution very well.

The asymptotes can be obtained by energy balance equations. For Quasi-static asymptote, the strain energy is equated with the work done by external force, i.e. $(1/2)k\delta_{max}^2 = P \cdot \delta_{max}$. It can be re-written as $\frac{\delta_{max}}{P/k} = 2.0$ which defines the asymptote. In the Quasi-static region, wherein the natural period of the structure is small compared with the duration of the load, the maximum dynamic deflection is twice the static deformation. The deformation depends only on the stiffness k and the applied peak load P. The load duration t_d and the structure mass m has little effect on the response in this regime. The dynamic load factor of 2 in many engineering problems comes from the response of structure to loads in the quasi-static regime.

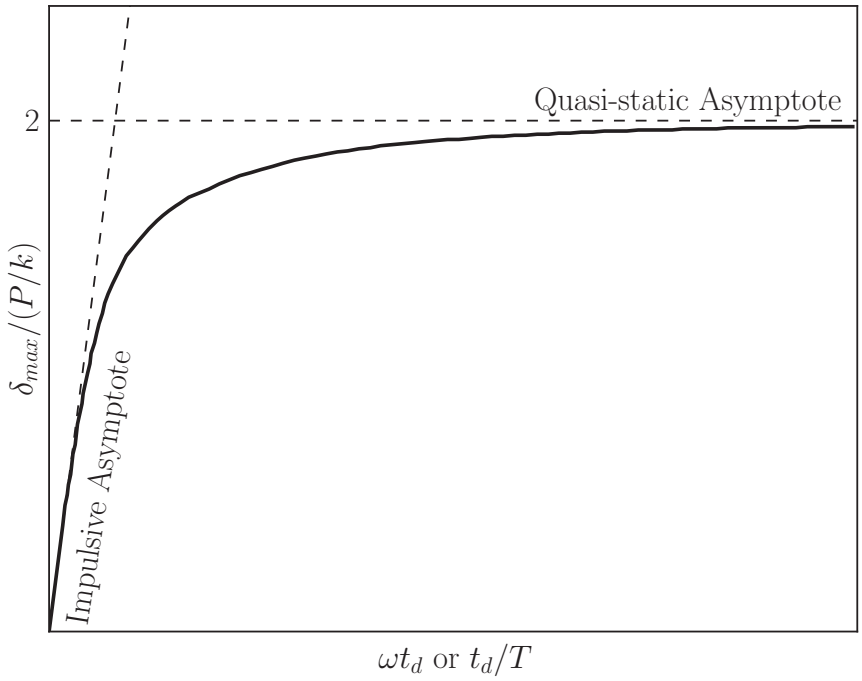


Figure 2.17: Response for all regimes

In the domain where the value of ωt_d or t_d/T is very small, the deformation is directly proportional to the impulse of the load, $I = \frac{1}{2}P \cdot t_d$. This region is therefore called the Impulsive region. The impulsive asymptote can be obtained by equating the kinetic energy, which imparted to the structure by the dynamic load, to the strain energy, i.e. $\frac{I^2}{2m} = (1/2)k\delta_{max}^2$. An expression can be derived as $\frac{\sqrt{km}\delta_{max}}{I} = 1.0$ and subsequently $\frac{\delta_{max}}{P/k} = \omega t_d$. This expression indicates that in the impulsive regime the ordinate is equal to the abscissa. Here both the duration of the load and the mass of the structure are important for the dynamic response. The response will strongly depend on the impulse of the dynamic loading.

A third region exists between the impulsive and quasi-static regimes. The regime is usually called the "dynamic region" because the response is more complex and depends on the whole history of the dynamic loading. No approximation is available for responses in this region. Here the deflection depends on both pressure and impulse as well as the stiffness and inertia of the structure. In general, the responses can be categorised into three realms in Figure 2.17 as shown below:

$$Impulsive: \ \frac{t_d}{T} \leq 0.1 \tag{2.29a}$$

$$Dynamic: \ 0.1 \leq \frac{t_d}{T} \leq 10 \tag{2.29b}$$

$$Quasi-static: \ 10 \leq \frac{t_d}{T} \tag{2.29c}$$

2.4.1.2 Pressure - impulse diagram

Pressure - impulse (P - I) diagram, shown in Figure 2.18, is an alternative representation of the response curve in Figure 2.17. It contains the same information. The difference is that the response curve focuses on the deformation as a function of the scaled time (i.e. the time ratio of the system to the load duration), while the P - I diagram emphasizes the damage level (or deformation level)as a function of combination of applied pressure and impulse (Baker et al., 1983).

The response regimes are still visible in the P - I diagram, the vertical asymptote denotes the impulsive region and the horizontal line is the quasi-static asymptote. In between lies the dynamic response regime. When some value of x_{max} is defined which denote the threshold of damage in a certain structure (speci-

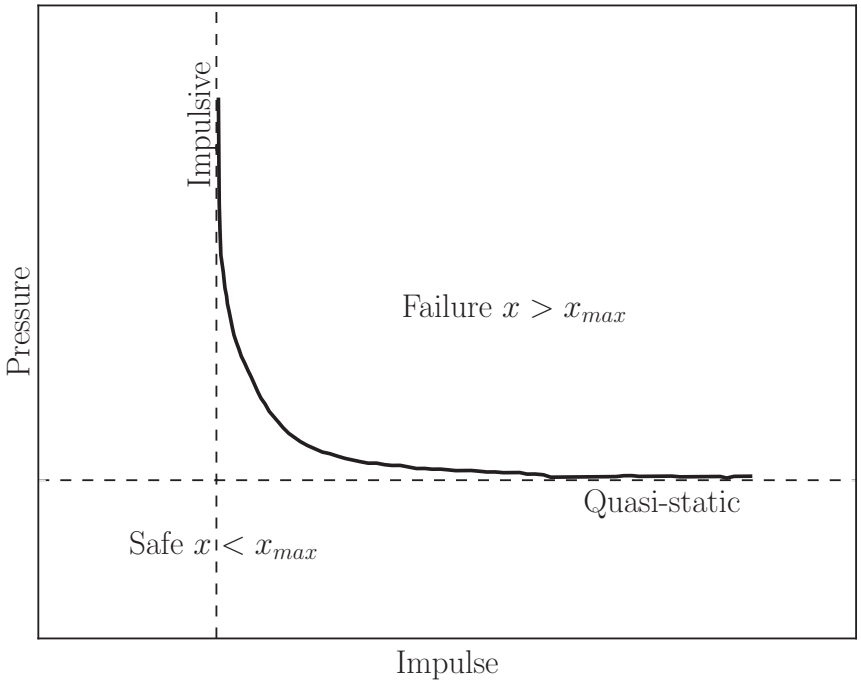


Figure 2.18: Pressure - impulse diagrams

fied stiffness k and mass m), the solid hyperbola shaped curve in Figure 2.18 is known as the iso-damage curve. It defines the combinations of pressure and impulse which produces this level of deformation (or damage). If it is the failure curve, then any combination of pressure and impulse to the upper right of the curve will result in failure in the structure, on the other hand combinations at the lower and left of the curve will cause no failure.

Iso-damage curve shown in Figure 2.18 is for an ideal detonation blast wave. The P - I diagram of the non-ideal deflagration blast wave with finite rise time has a few different characteristic to detonation. Figure 2.19 superimposes the P - I diagrams from detonation and deflagration. In the impulsive regime, there is no difference between the two curves because the shape of the load is not important in the impulsive region. There is a region shaded by green color that the response from a deflagration is more severe than detonation. This is due to the resonance between the loading rate (of deflagration) and the frequency of the structure. Finally towards to the quasi-static regime, the deflagration yields less damage than the detonation, which can be explained by that with a longer

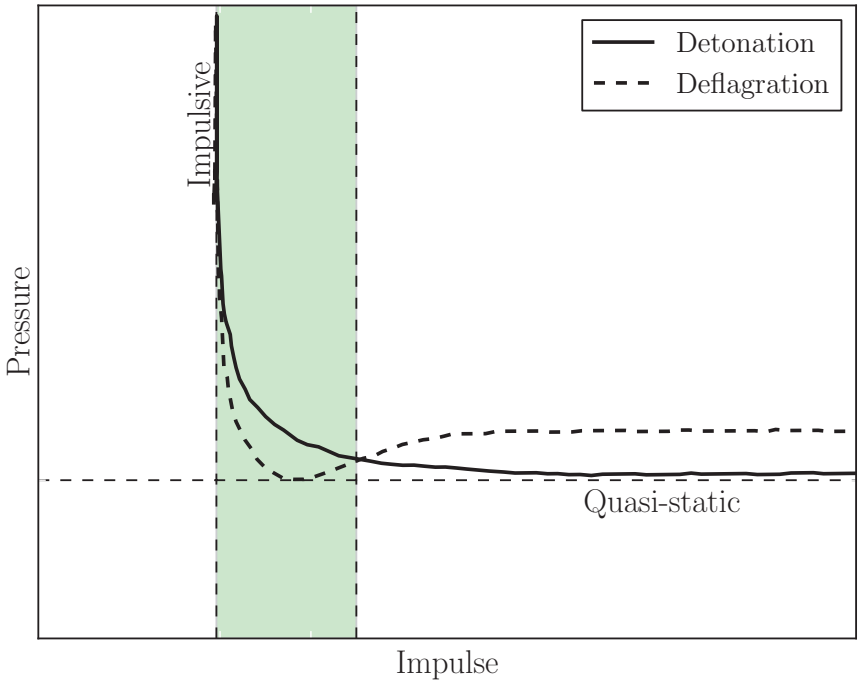


Figure 2.19: Pressure - impulse diagrams comparison

duration the deflagration blast wave becomes more similar to a static load, and less dynamic effect in the response of the structure. While the dynamic load factor of detonation approaches to 2 in the quasi-static cases the deflagration is approaching 1, i.e. equivalent to a static load.

2.4.1.3 Finite element method

Finite element modelling is widely used in dynamic/transient problems in research and industry. It has advantages in being able to representing complex structural geometry and boundary conditions, and components of different material. While the simplified SDOF method treats the components individually, the finite element method can include all components of essential interests and model them as an assembly so that the interactions between components can be well captured.Many commercial finite element packages are available and extensively used, for example: **?**, ANSYS and LS-DYNA. As the main analysis tool for the present project, a more formal introduction of finite element method is presented

in the following section.

2.4.2 Material properties at high strain rate

The mechanical properties of structural steel can be affected by high rates of straining under extreme loading as shown in Figure 2.20. The effects of high strain rates can be summarised as below:

- The elastic modulus will not be affected by strain rate.
- The yield stress will be increased to a higher value.
- The ultimate stress will be increased as well but the percentage of increase is less than that of the yield stress.
- The elongation at rupture is slightly reduced at high strain rate.

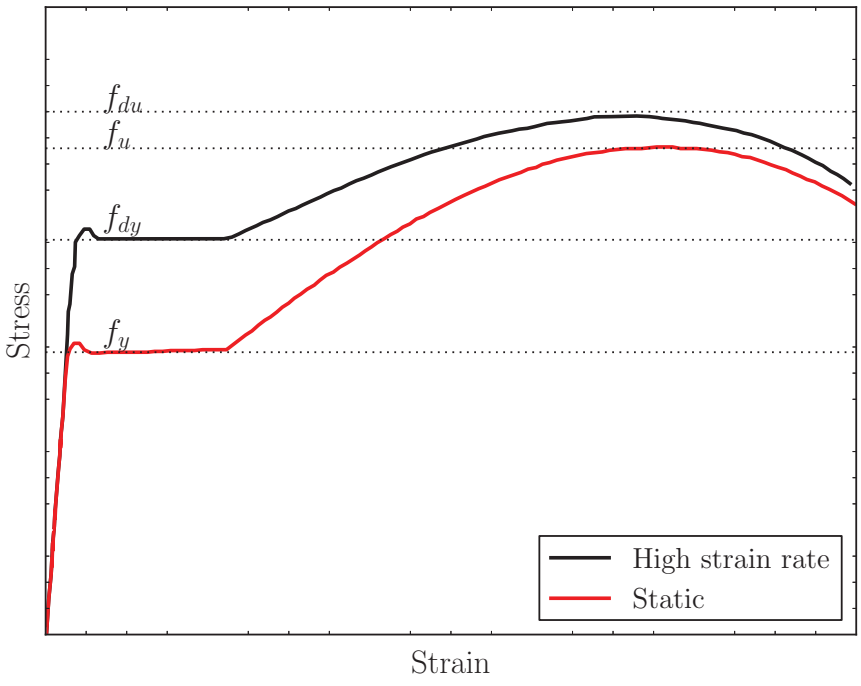


Figure 2.20: Material response at high strain rate (USDOD, 2008)

In Figure 2.20, f_y and f_u are the material yield and ultimate stresses at very low strain rate while f_dy and f_du are the dynamic yield and ultimate stresses

at high strain rate. It should be noted that material strain rate sensitivity is a material effect and is independent of the structural geometry. A dynamic increase factor (DIF) is usually used to incorporate the increase of strength of the material at high strain rate. The increase depends primarily on the strain rate and the material properties. Johnson - Cook (Johnson and Cook, 1983) and Cowper - Symonds (Cowper and Symonds, 1957) are two commonly used models to estimate the dynamic increase factor. The dynamic increase factor proposed by Johnson - Cook model is:

$$DIF = 1 + C \ln \left(\frac{\dot{\epsilon}^P_{eff}}{\dot{\epsilon}_0} \right) \tag{2.30}$$

where C is the parameter to be determined based on test data. $\dot{\epsilon}_0$ is the reference strain rate and $\dot{\epsilon}^P_{eff}$ is the effective plastic strain rate. Similarly, Cowper - Symonds model defines the dynamic increase factor as:

$$DIF = 1 + \left(\frac{\dot{\epsilon}^P_{eff}}{D} \right)^p \tag{2.31}$$

where p and D are parameters to be determined based on the test data. As an example, for steel S275 the strain rate models can be presented graphically in Figure 2.21 (Schwer (2007)).

Both models are widely used to capture the strain rate effect of materials. Schwer (2007) in his work showed that the Cowper-Symonds model was fitted better with the experimental data than Johnson-Cook model mainly due to its exponential nature. As it can be seen in Figure 2.21, in the low to moderate strain rate range the Johnson-Cook model over-predicts the enhancement effect as much as 10%. While in the high strain rate range it significantly under-predicts the hardening effect compared to Cowper-Symonds model.

2.4.3 Modelling structural components

Single-Degree-of-Freedom Blast Effects Design Spreadsheets (SBEDS) (USDOD, 2008) were developed by BakerRisk for the U.S. Army Corps of Engineers as a tool to be used by structural design engineers to assess the performance of a building

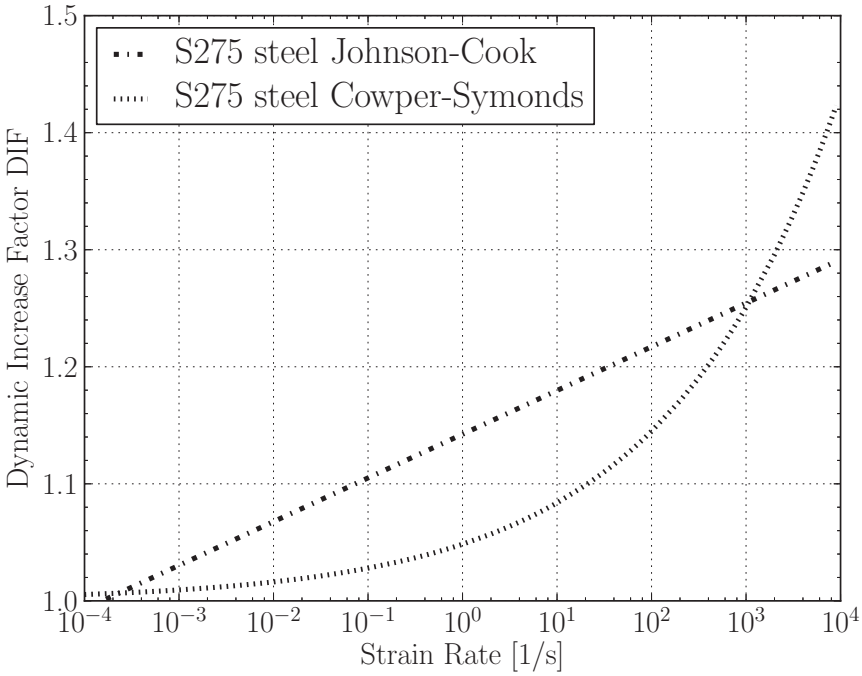


Figure 2.21: Strain rate hardening models

structure under blast dynamic loadings. SBEDS is based on the original Biggs' single-degree-of freedom model with some extension to include tension membrane and compression membrane effects. It has the capability to analyse a wide range of components such as single or double span steel members, masonry, wood and pre-stressed concrete components. It evaluates the model parameters based on the geometry and material data of a component and uses time-stepping numerical integration methods to solve the equation of motion. Steel Construction Institute has carried out a work on screening the vulnerability to blast loadings of a steel structure for Health and Safety Executive using this SBEDS (Burgan and Moutaftsis, 2009).

Izzuddin (Izzuddin, 2005) and the Technical Note 7 of FABIG (SCI, 2002), which was prepared by Izzuddin for SCI, presented an improved SDOF model. The original Biggs' model does not consider the catenary action and the supports are simple. Izzuddin and TN7 included the effects of support stiffness and moment capacities at the supports. His work incorporated the catenary action in a similar manner as SBEDS. However his resistance curve is slightly different to SBEDS

due to the order of formation of plastic hinges at the centre and supports of the beam. There are additional elastic-plastic stages before the plastic bending stage and one transient catenary stage that introduces a non-linear relationship between the applied load and deflection before the final catenary stage starts.

Langdon has (Langdon and Schleyer, 2006a),(Langdon and Schleyer, 2006b), (Langdon and Schleyer, 2006c) studied the response of various blast walls to dynamic overpressure loading. The experimental works investigated a small scale blast wall with connections subject to pulse pressure loading to determine the failure modes and revealed the importance of contribution of the support connection to blast resistance. The stiffness and capacities of the end connections are also determined in the experiments, which provided data for the subsequent analytical work. Mode approximation techniques have been used in the analytical analysis of the blast wall. The model represents a typical single trough of the corrugated steel wall and incorporates the stiffness and capacities of the end connections. Instead of deriving a resistance curve, the mode approximation method breaks the response into three stages: elastic, elastic-plastic and plastic. Each stage is approximated by two or three assumed mode shapes in order to represent the possible combination of response modes. Equation of motion for each stage is formulated based on energies and the Lagrange equation.

Leach (P.Leach, 1993) has extended Biggs' method to corrugated cladding panels with different boundary conditions and has provided design charts for the elasto-plastic response of panels subjected to blast loadings. Louca (Louca et al., 1996) used a non-linear finite element analysis package to study the response of a blast wall subject to hydrocarbon explosions. The work showed boundary restraints have significant influence on both the torsional response of the stiffeners and the overall deformation of the panel. He also reported that, for a SDOF model of the blast wall, the static resistance curve provided by Biggs' table cannot produce comparable results, however the results can be much improved by using a non-linear FE analysis to establish the static resistance curves. The SDOF model in Technical Note 5 (SCI, 1999a) issued by the Fire and Blast Information Group (FABIG) and Steel Construction Institute (SCI) is widely used for design of profiled panels. Louca (Louca et al., 2004) reviewed the adequacy of this design guide by using non-linear finite element analysis. Liang (Liang and Louca,

2007) derived new transformation factors for corrugated panels and the Biggs' method has been extended to profiled panels with end plates. Fallah (Fallah and L.A.Louca, 2007) formulated and sovled the SDOF model with elastic-plastic-hardening and softening properties. Pressure - impulse diagrams are constructed based on the improved SDOF models.

Plates are one of the basic elements of structures. The steel switch boxes recovered from the Buncefield site are essentially made up of several thin plates, although the boundary conditions would be significantly different to the studies in literatures. Plate subject to uniform blast loading can be analysed by using Biggs' method as a two-way spanning member. Studies of plastic responses of rectangular and circular plates are presented by Jones (Jones, 1997). Langdon (Langdon and Schleyer, 1999) and Schleyer (Schleyer et al., 1999) studied the response of metal plates subject to static and dynamic pressure loading through a series of experiments in newly designed pressure test chamber. The pressure profiles produced in the pressure chamber were of deflagration. Jacinto (Jacinto et al., 2001) has carried out detonation tests on unstiffened metal plates and compared the non-linear dynamic finite element model with the experimental results. In his numerical studies, the applied external loading is obtained as the difference between the pressure traces recorded at the front and back of the thin plate. This way of applying pressure loading significantly improved the accuracy of the numerical model compared with only applying the pressure loading as recorded at the front. Another method of applying external loading which proved to be adequate for thin plates is using the blast load predicted by empirical tools and introducing a cut-off time at which the pressure loading is suddenly reduced to zero before it naturally subsides. Either method is designed to capture the phenomena that when the pressure wave travels to the back of the plate it will exert a counter force to the pressure loading at the front.

The advancement in numerical simulations allows engineers and researchers to model the blast wave in Eulerian finite elements and even consider the interaction of blast wave and structures in the coupled numerical model. Borvik (Borvik et al., 2009) studied the response of a ISO container to a planar blast wave by using LS-DYNA. In their work the numerical results were compared with tests and the numerical model was validated. The work consists of different

approaches to examine the blast problem. The container was analysed in pure Lagrangian models (subjected to CONWEP load, CONWEP is a collection of conventional weapons effects calculations from the equations and curves of TM 5-855-1 (USDOA, 1986)) and coupled models which take into account the fluid-structure interaction. It was found that it is difficult to only base the design on a structural model alone since the fully coupled model could yield better results. Zarkrisson (Zarkrisson et al., 2011) performed numerical simulations of air blast loading in the near-field acting on deformable steel plates. The work was carried out in LS-DYNA and results were compared with experiments. The objective was to investigate the accuracy of simulating the blast load using an Eulerian domain. The results showed that blast loading from simplified empirical data (CONWEP load) assuming spherical or semi-spherical charges significantly under-estimated the deformation of the steel plates while the Eulerian approach only under-predicted the measured plate deformation with $9.4 - 11\%$.

Luccioni (Luccioni et al., 2006), Rememnikov (Rememnikov) and Fairlie (Fairlie, 1997) studied the pressure and impulse produced by hydrocodes AUTODYN in ANSYS. Numerical results are compared with those obtained with analytical expressions for different scaled distances (i.e. Equations 2.14 - 2.17). Practical analyse were carried out in a urban congested environment and results obtained for different locations are compared. Good agreements were observed between numerical results and small scale experiments.

ABAQUS/Explicit has been widely used for dynamic problems in industry and academia for many years. The recent addition of Eulerian and therefore the Coupled Eulerian - Lagrangian (CEL) capability significantly enhanced its application in blast engineering applications. The blast wave can be modelled in the Eulerian domain and coupled with Lagrangian parts (structures) if necessary. Carlucci (Carlucci et al., 2010) carried out a class of problems using ABAQUS Eulerian model and compared the numerical results with experiments. The validation work includes Dynamic tensile extrusion of copper, explosive loading validation (using JWL Equation of state) and compressible inviscid flow (validation using a shock tube). Generally the numerical results are compared favourably with test and theoretical data. It provided necessary confidence of using the new Eulerian tool in ABAQUS. Further validation work on ABAQUS Eulerian

capacity was carried out by Mougeotte (Mougeotte et al., 2010). The work was especially focused on using Eulerian and CEL methods to conducting blast loading analysis. It also showcased a number of techniques to simulate the blast wave in ABAQUS. Blast wave propagation, reflection and interaction with solid structures are studied in the work and the results are reasonably accurate which showed the new capacity can be used as a valuable tool for blast loading analysis.

2.5 Design guidelines

Many guidelines and codes have been published for design of structure to resist accidental blast loading. Most of the codes are based on Biggs' single degree of freedom model and covering both determination of blast loading and structural response. A few commonly used design guidelines are introduced in this section.

- Structure to resist the effects of accident explosions UFC 3-340-02 ((US-DOD, 2008))

  UFC 3-340-02 is the most widely used publication in both military and civilian organisations for design of structures to prevent blast damage to structure or personnel from accidental explosions. It establishes design procedures and construction techniques whereby propagation of explosion or destructive detonation can be mitigated. It includes information on blast, shock loading prediction, principles of dynamic analysis and reinforced concrete/steel design for blast.

- FEMA 426 Reference manual to mitigate potential terrorist attacks against buildings (FEMA)

  FEMA 426 is prepared for reducing physical damage to structure and non-structural components of buildings. It is applicable for commercial office, retail commercial facilities and light industrial and manufacturing buildings. Not only has it covered information on explosion blast and building design for such events, but also site/layout design, assets evaluation and risk/threat assessment.

- SCI FABIG Technical Note 5 (SCI, 2002), 7 (SCI, 1999a) and 10 (SCI, 1999b)

  Technical Note 5 offers guidance on the design of stainless steel blast walls made from corrugated sheeting, material behaviour, response to blast loading and design for bending including the effect of plasticity. Particular attention has been placed on simple trapezoidal corrugation with or without stiffeners. This note is based on the European design standard for structural stainless steel, Eurocode 3: Part 1.4. Technical Note 7 is prepared for improved Biggs' SDOF model, by incorporating the effects of support stiffness, moment capacities at the supports and also catenary action in beam components. Technical Note 10 improves the advanced SDOF model in TN 7 by in including the material rate sensitivity.

Chapter 3

Numerical tools

The current research work emphasises mainly on using non-linear finite element analysis to study the impact of selected pressure loads on representative buildings structures and also to carry out advanced numerical simulation to provide information on incident forensic studies. Finite element package **?** is the main numerical tool used in this project. ANSYS (AUTODYN) has been used for a few problems as well. In this chapter, the numerical tools used in the current work are introduced and some general validation of numerical models are presented.

3.1 Non-linear finite element method

Finite element method (FEM) as its name suggests involves the discretisation of the continuum (or domain) of interests as the core step in the process. There are two typical ways of using FEM: numerical approximation to mathematical problems and model based simulation of physical systems. When FEM is used to solve mathematical models, often ordinary or partial differential equations (ODEs and PDEs), the discretisation step involves generating a discrete finite element model from a variational or weak form of the mathematical model. It is a procedure for obtaining the numerical approximations to the solution of initial and boundary value problems posed over a domain Ω. This domain is replaced by a group of sub-domains called finite elements Ψ. In general both the solution and geometry of the domain Ω are approximated by that of Ψ.

Simulation of the response of physical systems to loading is another widely used application of FEM. In the process, the physical system is idealised and discretised to produce a discrete model. The solutions are approximations to the response and behaviour of the physical systems. Sometimes the discrete model has a counterpart in continuum fields which can be well defined by an ideal mathematical model, for example, a cantilever has both a discrete model and a mathematical model. However, it is difficult or even impossible to have both discrete and mathematical models for some complex engineering systems, such as a steel switch box or the light weight steel clad walls. Components in the clad walls like corrugated panels or side rails may have mathematical models when they are studied alone. As an assembly, it is extremely difficult to obtain a mathematical model for the whole system.

Two types of error exist in the FEM simulation of physical systems. One is known as solution error, which occurs when solving the equations of the pertaining discrete model. The other is simulation error. It arises during the validation process which tries to compare the discrete solution against physical observation. Simulation error combines modelling and solution errors. Since that due to the latter is typically unimportant, the simulation error can be identified as the modelling error. And it should always be minimized in any work or study so that the discrete model can better represent the physics.

FEM in simulation of physical system has two major stages: Discretisation and assembly & solution.

$$\delta \int_{t_1}^{t_2} L dt = 0 \; where \; L = T - \Pi + W \tag{3.1a}$$

$$Kinetic\ Energy\ T = \frac{1}{2} \int_V \rho [\dot{U}]^T [\dot{U}] dV \tag{3.1b}$$

$$Strain\ Energy\ \Pi = \frac{1}{2} \int_V [\epsilon]^T [\sigma] dV = \frac{1}{2} \int_V [\epsilon]^T [c] [\epsilon] dV \tag{3.1c}$$

$$Work\ done\ by\ external\ forces\ W = \int_V [U]^T [f_b] dV + \int_{S_f} [U]^T [f_s] dV \tag{3.1d}$$

In the above equation, δ is the delta operator presenting the variation of the

following term L, which is know as the Lagrange. ρ is density and $[U]$ is admissible functions. $[\sigma]$ and $[\epsilon]$ are stress and strain matrix and $[c]$ is the constitutive matrix comprises of elastic modulus. $[f_b]$ and $[f_s]$ are body and surface force vectors respectively. The discretisation stage involves breakdown of the system into a finite number of small elements (a choice of bar, beam, shell and solid elements) and then formulating the stiffness of the single general element. Element formulation can be done by mechanical of material or variational approach. For latter, the process uses Hamilton's principle and the energies of the element, as shown in Equation 3.1 (Cook et al., 2002), in which the element displacement matrix $[U]$ is obtained by using admissible functions $[N]$ interpolating between the nodal displacement matrix $[d_e]$, i.e. $[U] = [N][d_e]$. Subsequently the strain can be obtained as $[\epsilon] = [L][U] = [L][N][d_e] = [B][d_e]$ where $[L]$ is the differential operator and $[B]$ is strain matrix. The potential energy then can be expanded as follows.

$$\begin{aligned}\Pi = \frac{1}{2}\int_{V_e}[\epsilon]^T[c][\epsilon]dV &= \frac{1}{2}\int_{V_e}[d_e]^T[B]^T[c][B][d_e]dV \\ &= \frac{1}{2}[d_e]^T\left(\int_{V_e}[B]^T[c][B]dV\right)[d_e] \\ &= \frac{1}{2}[d_e]^T[k][d_e] \; where \; [k] = \int_{V_e}[B]^T[c][B]dV\end{aligned} \tag{3.2}$$

Similarly, kinetic energy and work done by external forces can be expanded as following, in which $[m_e]$ is the mass matrix.

$$\begin{aligned}T = \frac{1}{2}\int_{V_e}\rho[\dot{U}]^T[\dot{U}]dV &= \frac{1}{2}\int_{V_e}\rho[\dot{d}_e]^T N^T N\dot{d}_e dV \\ &= \frac{1}{2}[\dot{d}_e]^T\left(\int_{V_e}\rho N^T N dV\right)\dot{d}_e \\ &= \frac{1}{2}[\dot{d}_e]^T[m_e][\dot{d}_e] \; where \; [m_e] = \int_{V_e}\rho N^T N dV\end{aligned} \tag{3.3}$$

$$
\begin{aligned}
W &= \int_{V_e} [d_e]^T [N]^T [f_b] dV + \int_{S_e} [d_e]^T [N]^T [f_s] dV \\
&= [d_e]^T \left(\int_{V_e} [N]^T [f_b] dV \right) + [d_e]^T \left(\int_{S_e} [N]^T [f_s] dV \right) \\
&= [d_e]^T [F_b] + [d_e]^T [F_s] = [d_e]^T [f_e]
\end{aligned} \tag{3.4}
$$

In the above equation 3.4, the consistent nodal force vectors are defined as:

$$[f_e] = [F_b] + [F_s] \tag{3.5a}$$

$$[F_b] = \int_{V_e} [N]^T [f_b] dV \tag{3.5b}$$

$$[F_s] = \int_{V_e} [N]^T [f_s] dV \tag{3.5c}$$

Inserting the energy expressions into the Hamilton's equation (Equation 3.1) yields:

$$\delta \int_{t_1}^{t_2} \left(\frac{1}{2} [\dot{d}_e]^T [m_e] [\dot{d}_e] - \frac{1}{2} [d_e]^T [k_e] [d_e] + [d_e]^T [f_e] \right) dt = 0 \tag{3.6}$$

Taking first variation of each term in the bracket and integrate the time derivative term (relating to mass) by parts gives,

$$\int_{t_1}^{t_2} \delta [d_e]^T \left(-[m_e] [\ddot{d}_e] - [k_e] [d_e] + [f_e] \right) dt = 0 \tag{3.7}$$

$\delta[d_e]$ is the first variation of nodal displacement $[d_e]$ and is defined as $\delta[d_e] = [\tilde{d}_e] - [d_e]$. The delta operator represents a small arbitrary change in the nodal displacement matrix $[d_e]$. $[\tilde{d}_e]$ is the varied path and $[d_e]$ is the extremising path which renders the Lagrangian L minimum between time t_1 and t_2. Since $\delta[d_e]$ is arbitrary the terms in the bracket in Equation 3.7 must equal to zero and this yields the local elemental governing equation for the element in question, in which

$[k_e]$ is the local stiffness matrix.

$$[m_e][\ddot{d}_e] + [k_e][d_e] = [f_e] \tag{3.8}$$

The finite element equation in the local coordinates can be transferred into global coordinates as shown below with the help of a transformation matrix [T]:

$$\begin{aligned} &[M_e][\ddot{D}_e] + [K_e][D_e] = [F_e] \\ &where \\ &[K_e] = [T]^T[k_e][T],\ [M_e] = [T]^T[m_e][T],\ [F_e] = [T]^T[f_e][T], \end{aligned} \tag{3.9}$$

In the above equations, $[M_e]$,$[D_e]$,$[K_e]$ and $[F_e]$ are mass, displacement, stiffness and force matrix for one element in global coordinates. $[T]$ is the transformation matrix. Now the discretisation stage is completed and next step is to assemble all the elements into a master governing equation representing the entire system and finally the discrete solution can be obtain by solving the master equations accordingly. Equation 3.10 shows the complete general finite element equations for static and dynamic problems, in which $[M]$,$[D]$,$[K]$ and $[F]$ are assembled mass, displacement, stiffness and force matrix in global coordinates.

$$dynamic\ -\ [M][\ddot{D}] + [K][D] = [F] \tag{3.10a}$$

$$static\ -\ [K][D] = [F] \tag{3.10b}$$

Non-linear behaviours in the engineering problems arise from a wide variety of phenomena. Each source of the non-linearity is perhaps difficult to formulate and they might interact with each other as well. Linear models might be sufficient for some applications but unfortunately substantial departure from linearity is common. There are four common sources of non-linear behaviours in engineering problems: material, geometric, force and displacement boundary conditions.

Material behaviour depends on the current deformation state and possibly the past history of the deformation. The structure might undergo non-linear elasticity, plasticity, viscoelasticity, creep or inelastic rate effects. In blast engineering, the plasticity and strain rate effects are the most important properties. Large

strain and deformation are also common in blast engineering problems. Geometric non-linearity should be considered for slender structures and tensile structures which have strong axial constraints.

Boundary conditions impose non-linearity as well. The applied force can depend on the deformation, for example, the pressure loads of fluids, this includes hydrostatic loads on the submerged structures and more importantly the hydrodynamic loads caused by wind and blast waves. Similarly, displacement boundary conditions can depend on the deformation of the structure. The most important application is the contact problem, in which no-penetration conditions are enforced on deformable bodies while the extent of the contact area is unknown.

3.2 Solution methods for non-linear FE problems

Engineering problems maybe classified according to whether the inertial effects should be taken into account or not. In static problems the inertia forces are ignored so Equation 3.10b can be solved to obtain the discrete displacement solution if the system is linear, the load of duration of the static problems are usually very long so the dynamic effect is negligible. In dynamic problems, the durations of load are shorter or comparable to the fundamental period of the system and the intertia forces of the system cannot be ignored, as discussed earlier. Equation 3.10a should be used for such problems.

There is a type of problems classified as quasi-static, in which the real time scale might not be considered and the dynamic effect is small in such a way the kinetic energy is less than 5% of the strain energy in the system for the most of the time during the analysis. The advantages of this approach are that static problems can be solved by Equation 3.10a if the load is applied over a comparably long period to minimise the kinetic energy. The problems then can be solved explicitly to overcome convergence difficulties. On the contrary, problems such as metal forming (a dynamic process) sometimes can be solved as static problem (i.e. quasi-static) provided by that ignoring the inertial force will not severely affect the solution. The static analysis will be more efficient than a dynamic one

over a long period.

Finite element equations for static and dynamics problems can be re-written in a more general form,

$$dynamic \; - \; [M][\ddot{D}] + [I] = [F] \tag{3.11a}$$

$$static \; - \; [I] = [F] \tag{3.11b}$$

where $[I]$ is the internal forces of the flexible body and $[I] = [K][D]$ for a linear system, the stiffness $[K]$ does not change. In a non-linear model the stiffness $[K]$ could be dependent on the displacement $[D]$ then an iterative process is needed for the solution. The internal force I can be obtained through internal stresses $I = \int_V [B]^T[\sigma]dV$.

3.2.1 Newton - Raphson method

One of the most widely used methods for non-linear static or quasi-static problems is the Newton - Raphson method, as depicted in Figure 3.1. At the start of the solution tangential stiffness K_{T0} is formed at displacement $d = 0$. By applying the step load ΔP_1 an intermediate displacement d_A is obtained and the corresponding internal force is calculated from the internal stresses as I_A. If residual force $Re_A = P_1 - I_A$ is smaller than some convergence criteria then the point a is the converged solution, otherwise further iteration is needed from point a. By using a newly formed tangential stiffness K_{Ta} and the residual force Re_A a new intermediate displacement $d_B = d_A + \delta_A$ can be obtained at point b, where $\delta_A = Re_A/K_{Ta}$. The residual Re_B will be checked and if no convergence is found forwarding to next point c with Re_B and K_{Tb}. At every iteration point the force residual will be checked until it is lower than the required criteria, then at point 1 a new converged point is said to be found. Thus an other incremental step load can be applied which will start a new iterative stage and forward the solution along the response path.

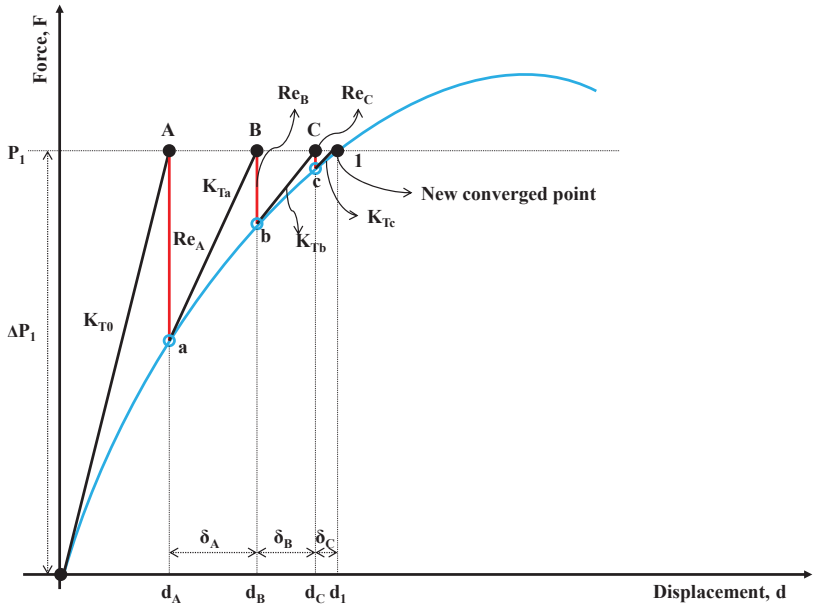


Figure 3.1: Newton Raphson Method

3.2.2 Arc length method

The Newton - Raphson method converges fairly quickly for most of the problems involving non-linearity. However it suffers when the response path reaches the limiting point (the ultimate load point) where the tangential stiffness approaches to zero. In computation, the Newton - Raphson method will give a very large incremental displacement δ as the limiting point is approached, and even negative δ as soon as the limiting point is past. This process has significant difficulties to find the converged points close to the actual response curve.

Snap-through or snap-back buckling problems have the unstable characteristics that the response path will descend with a negative tangential stiffness once past some ultimate point. The Newton - Raphson method usually fails before the limiting point when the tangential stiffness is zero. A method which often succeeds in this type of analysis is called the arc length method. ABAQUS uses a modified Riks method (Riks, 1979), an improvement of the arc length method shown in Figure 3.2, to tackle unstable problems.

In this method, the iterative change is made orthogonal to the predicted

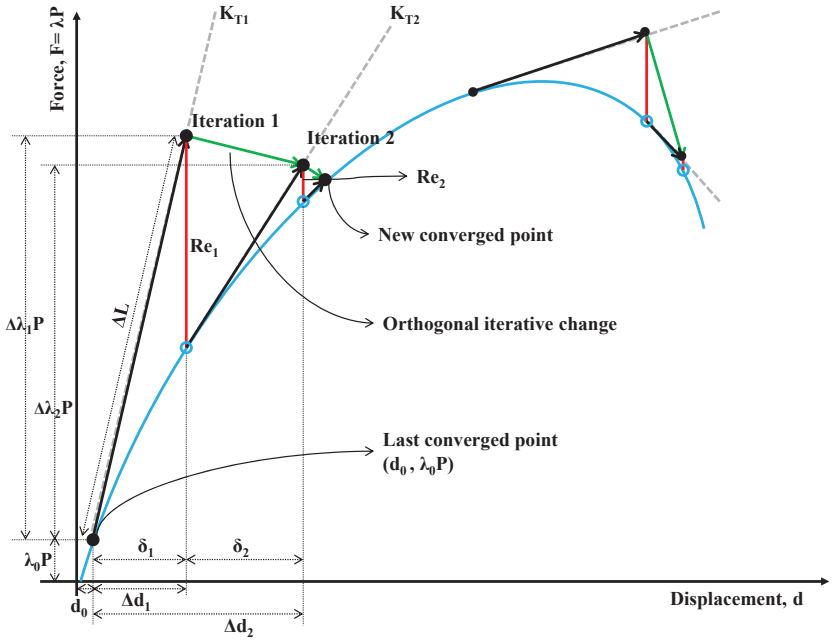


Figure 3.2: Modified Riks method

solution $(\Delta\lambda_p P, \Delta d_p)$. Both the load and the displacement form part of the solutions. Tangential stiffness K_{T1} at the last converged point $(d_0, \lambda_0 P)$ can be obtained. The incremental parameter $\Delta\lambda$ can be determined by prescribing an arc length ΔL along the direction of the tangential stiffness K_{T1}. Subsequently the force $F = \Delta\lambda_1 P$ and displacement Δd_1 at iteration point 1 are obtained. Similarly, balance of the forces must be checked at point 1 and if residual Re_1 is greater than an acceptable criteria, a further iteration is required. A new tangential stiffness K_{T2} can be formed at the predicted displacement $d_0 + \Delta d_1$. The iterative change will be made orthogonal to K_{T1} from the iteration point 1 to 2 intersecting the line of K_{T2}. Again the force balance is checked at point 2 and further orthogonal iteration is needed if the residual Re_2 is still too large. Eventually the process will find a new converged point close to or on the response path. The advantage of the modified Riks method is that the tangential stiffness is used as a direction rather than directly calculating the incremental displacement, so it is still possible to find a converged solution near or past the limiting point, as briefly depicted in Figure 3.2.

3.2.3 Explicit direct integration method

For dynamic problems the Equation 3.11a can be solved with direct integration techniques, where the response is evaluated at instances separated by time increment Δt. At time $n \times \Delta t$, the equation of motion that needs to be solved is:

$$[M][\ddot{D}]_n + [I]_n = [F]_n \tag{3.12}$$

where $[I]_n = [K][D]_n$ for linear systems. The explicit method is one of direct integration methods. Comparing with the implicit process it is best for transient problems, especially for study of structures under blast and impact loadings. At time step n with increment of Δt velocity and acceleration can be approximated by central difference equations:

$$[\dot{D}]_n = \frac{1}{2\Delta t}([D]_{n+1} - [D]_{n-1}) \tag{3.13a}$$

$$[\ddot{D}]_n = \frac{1}{\Delta t^2}([D]_{n+1} - 2[D]_n + [D]_{n-1}) \tag{3.13b}$$

Substitution of Equation 3.13 into 3.12 yields:

$$\frac{[M]}{\Delta t^2}[D]_{n+1} = [F]_n - [I]_n + \frac{2}{\Delta t^2}[M][D]_n - \frac{1}{\Delta t^2}[M][D]_{n-1} \tag{3.14}$$

All terms on the right hand side of the above equation are known. $[F]_n$ is the applied external force at n^{th} step, $[I]_n$ can be calculated from the internal stresses and $[D]_n$ and $[D]_{n-1}$ are obtained in the previous steps. Therefore the displacement at n+1 time step $[D]_{n+1}$ can be calculated and the velocity and acceleration at current n step can be obtained. In such a way, the solution can forward to $n+1$ step with increment Δt. For solution to be stable the time increment Δt is limited by the highest frequency of the discrete system which is $\Delta t \leq \frac{2}{\omega_{max}}$. In ABAQUS the implementation is that $\Delta t = min(\frac{L_e}{C_d})$, where L_e is the characteristic element length and C_d is the dilatation wave speed. Care must be taken in the mesh of the models. Unexpected small and irregular elements should be avoided, as they could limit the incremental time to an extremely small value hence increase the computational demands. Non-linearity is handled easily with the explicit method. Calculation is the same as in Equation 3.14 except that

$[I]_n$ is calculated from the internal stress at each time step in the elastic-plastic elements.

3.3 Eulerian analysis for blast wave

In most of the cases, the finite element method in structural mechanics uses Lagrangian formulations. In the traditional Lagrangian formulation the node is fixed with the material, and elements deform as the material deforms. Lagrangian finite elements are always 100% filled by a single material, so the material boundary coincides with the element boundary. Lagrangian formulations are best for small to moderate deformations. s For large deformation, the Eulerian formu-

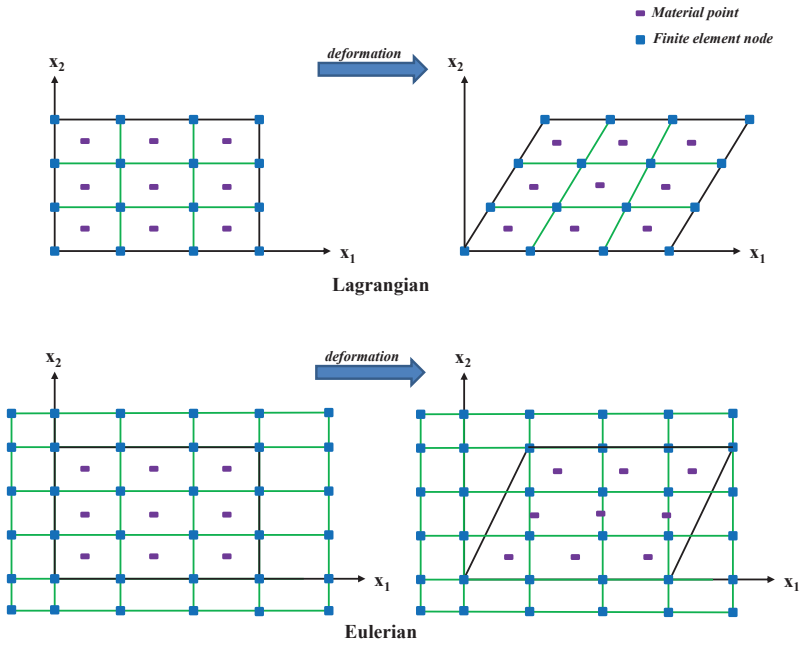


Figure 3.3: Lagrangian v.s. Eulerian deformation

lation is more appropriate, especially for fluid flow problems. In the Eulerian analysis, the nodes are fixed in space and the material flows through elements that do not deform. The Eulerian element might not be 100% filled with a single material, it can be filled with multiple material at any percentages, even completely void. Therefore the Eulerian material boundary will not coincide with

the element boundary in such problems and needs to be computed at each time step. The material can move out of the mesh grid and be lost from the analysis. A brief comparison between Lagrangian and Eulerian deformation is shown in Figure 3.3.

In the Lagrangian description, properties of the material body can be expressed as $p = p(\bar{X}, t)$, where particle $\bar{X}$ is defined in Lagrangian coordinates. The attention is focused on what is happening to the individual particle during the motion. In the Eulerian description, a property is expressed as $p = p(\bar{X}, t) = p[\phi^{-1}(\bar{\chi}, t), t] = p^*(\bar{\chi}, t)$, where $\bar{\chi}$, the spatial location, is defined in the Eulerian coordinates. $\bar{\phi}$ is the mapping function between Lagrangian and Eulerian coordinates, so that $\bar{\chi} = \phi(\bar{X}, t)$ and $\bar{X} = \phi^{-1}(\bar{\chi}, t)$. The emphasis now is placed on the events taking place at the position in space. Numerically, the fluid region of interests is divided into finite elements representing small increments in the direction of flow motion. The conservation equations for mass, momentum and energy with an equation of state are solved on this grid of zones by the explicit direct integration method.

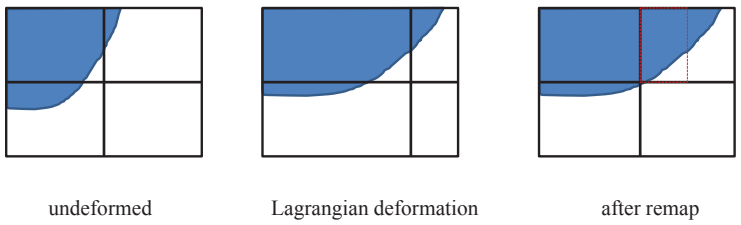


Figure 3.4: Eulerian time incrementation (Spinelli and Vitali, 2009)

The Eulerian incrementation has two steps: a traditional Lagrangian phase followed by an Eulerian transport phase. This is also known as Lagrange-plus-remap (**?**). As depicted in Figure 3.4, during the Lagrangian phase of the time increment, nodes are assumed to be temporarily fixed with the material so the elements deform with the material flow. During the subsequent Eulerian phase the time step is suspended, elements with significant deformation are re-meshed back to the original configuration, and the corresponding material flow between neighbouring elements is determined.

The shock front of a blast wave is extremely thin, hence it is often approximated as a discontinuous change in flow properties. A representative thickness of a shock plane with $M_x = 2$ is given in "Explosive shocks in air" (Kinney and Graham, 1985) to be about 0.00025 mm. This is much thinner than a typical finite element length used in a numerical model for practical use. Special treatment is used in programs to solve the discontinuity and still keep conservation laws, e.g. the Rankine-Hugoniot relations for shock waves. In order to model the shock numerically, an artificial viscosity is used (O.C.Zienkiewicz and Taylor, 2000) to damp out the shock front over several elements.

The fluid medium used in the blast analysis is usually air. The ideal gas equation of state for air can be defined as:

$$p + p_A = \rho R(\Theta - \Theta^z) \tag{3.15}$$

where p_A is the atmospheric pressure, R is the gas constant, ρ is the density of the air, Θ is the atmospheric temperature and Θ^z is the absolute zero on the temperature scale being used. The ABAQUS Eulerian capability used in this research project only involves the blast wave propagation though air. In the next sub-section, the AUTODYN is used to validate the coupled Lagrangian-Eulerian method and this Eulerian model consist of air and high explosive, which can be defined by the Jones-Wilkins-Lee (JWL) equation of state as follow:

$$p = A\left(1 - \frac{\omega}{R_1 V}e^{-R_1 V}\right) + B\left(1 - \frac{\omega}{R_2 V}e^{-R_2 V}\right) + \frac{\omega E}{V} \tag{3.16}$$

where A, B, R_1, R_2 and ω are empirically derived constants which are different for each explosive. V is the relative volume or the expansion of the explosive product, and E is the detonation energy per initial unit volume (ANSYS). The values of the parameters for air and high explosive (Pentolite) are shown in Table 3.1.

3.4 Approaches for study of blast responses

Most of the blast problems can be divided into four stages (Borvik et al., 2009).

Table 3.1: Definition of Eulerian materials

Material	Type	Property	Value	Unit
Air	Density	Mass density	1.2258	kg/m^3
	EOS	Specific gas constant	287	J/kgK
		Ambient pressure	101.325	kPa
	Specific heat	Specific heat	717.54	kJ/kg
	Viscosity	Dynamic viscosity	1×10^{-5}	$kg/(m \cdot s)$
	Initial state	Ambient temperature	288.15	Kelvin
		Ambient pressure	101.325	kPa
Pentolite	Density	Mass density	1.63	kg/m^3
	JWL EOS	Detonation speed	7360	m/s
		A	531.77	GPa
		B	8.933	GPa
		ω	0.33	-
		R_1	4.6	-
		R_2	1.05	-
	Initial state	Specific energy	8	kJ/cm^3
		Ambient pressure	101.325	kPa

- Stage I: the explosion stage where the explosives explode generating high temperature and pressure gases that propagate violently through the surrounding medium (usually air).
- Stage II: the propagation phase where high intensity blast waves generated by the expanding gases propagate through the medium at a distance, from the explosion centre to the target.
- Stage III: the interaction phase between the blast wave and the target structures where the blast loading is applied on the surfaces.
- Stage IV: the response of structures to the dynamic loading imposed by the incoming blast waves.

The four stages can be separated to simplify the problem but a strong coupling exists between each phase and they are all of the same importance to completely describe the structural response to blast loading problems. Stage I is out of the scope of this research study. The primary aim of the present work is not studying the explosion mechanism of explosives but the subsequent events. The main

focus will be placed on Stage IV the response of various objects to blast dynamic loadings, with attention to the blast - structure interaction and the propagation of blast waves. Throughout the current study the blast waves are defined either by scaled distance with charge side or directly specifying the wave parameters (i.e. incident peak overpressure and positive duration).

Separating the four stages can significantly simplify the blast problems. Three numerical modelling approaches can be developed with different levels of complexity.

3.4.1 Lagrangian approach

In this approach, a pure Lagrangian formulation is used to describe the deformation of the structures. The blast load is approximated as an idealised pressure - time curve directly applied on the relevant surface of the structures. During the simulation the pressure loading is always normal to the surface subjected to the load, independent of the structural deformation. If the deformation is small and the geometry is regular, this approach may give reasonable results. Only stage IV is considered in this approach. Stages I - III are replaced by empirical or analytical tools of predicting the blast wave.

The blast load can be defined directly with the incident peak overpressure and the positive duration, with either linear or exponential form. Then following the procedures presented in Section 2.3.2 the dynamic blast loads on the surfaces of a structure with simple geometry can be determined. This is referred as analytical blast load in the following sections.

CONWEP, a collection of conventional weapons effects calculations from the equations and curves of TM 5-855-1 manual (USDOA, 1986), is incorporated into the current release of **?**. This module provides another way to apply the detonation blast load. By specifying the weight and stand-off distance of the TNT high explosive charge, the dynamic pressure loads are automatically applied on the relevant surfaces of the target according to the incident angle. This is referred yo as CONWEP load (CONWEP) in the following sections.

3.4.2 Uncoupled Eulerian - Lagrangian approach

The second approach consists of two steps: (i) Eulerian simulation to determine the pressure loads and (ii) the Lagrangian modelling to analyse the structural response. In the first step the structure is often treated as a rigid body so the pressure loads on the surfaces can be determined and recorded without considering deformation. Then the pre-determined surface pressure - time curves can be applied directly on the relevant surfaces of the structures in the second step. The method will give reliable results if the iteration between the blast and structure is small, i.e. moderate structural deformation should be expected. The advantage of this uncoupled method is that it is considerably less computationally demanding than a fully coupled simulation.

This approach involves stage II - IV of a blast problem in a decoupled manner. In step one the Eulerian simulation considers the propagation of the blast wave and its interaction with a rigid structure (stage II and III). The second step is equivalent to stage IV in which the response of the structure is determined.

3.4.3 Coupled Eulerian - Lagrangian approach

The Eulerian algorithm can be coupled with the Lagrangian formulation to have a full coupling between the blast wave and deformation of structure. Stages I-IV or II-IV are coupled together and the interaction between the blast wave and the structure can be well described for even large deformations, at the cost of greater computational demands.

The general explicit contact definition of **?** implements the contact between Eulerian and Lagrangian parts automatically. In AUTODYN (ANSYS) there is a specific Eulerian - Lagrangian contact definition used to impose the coupling effect.

3.5 Numerical model validations

The finite element method and various simulation approaches were discussed in the above sections. In order to build confidence of using numerical models in the present study, it is necessary to validate the numerical models at the most general

level, particularly for the new Eulerian capacity. Validations of more specific numerical models are presented within the following relevant sections. Among the following validation works, pure Eulerian simulations were carried out in **?** and the coupled analysis (CEL) was implemented in AUTODYN (ANSYS).

3.5.1 One dimensional model

A one dimensional model consisting of a string of brick Eulerian elements is shown in Figure 3.5. This 1D model is used to generate a simple blast wave with a sharp discontinuity in the pressure with exponential decay. The material condition of the air was defined to be at ambient condition at sea level. The ideal gas equation of state is used and the parameters can be found in Table 3.1. Zero displacement boundary conditions are applied on the side of the model to restrict flow normal to the walls but allow tangential flow. The blast wave was implemented using a velocity boundary condition with an amplitude curve whose peak value is equivalent to the initial particle velocity of the blast wave, i.e. Equation 2.9. This can create a pressure pulse of the correct magnitude and duration with exponential decay.

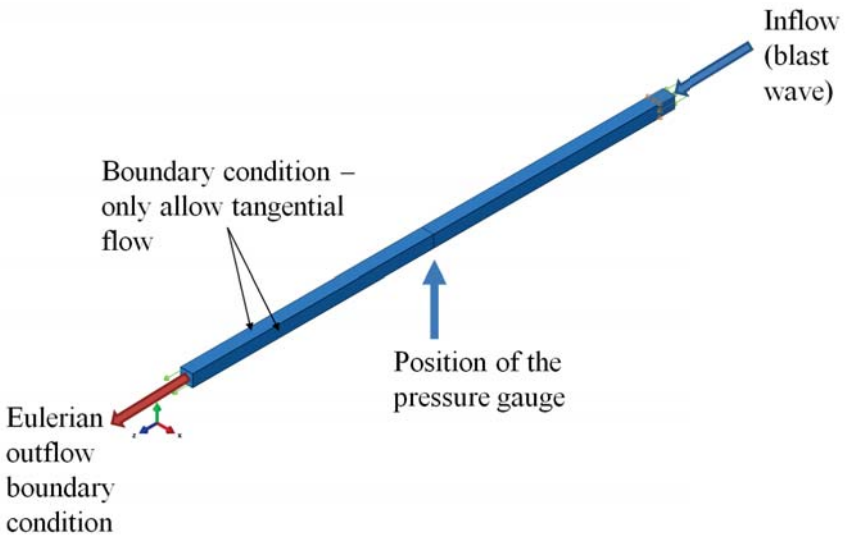


Figure 3.5: One dimensional Eulerian model

A mesh refinement study was carried out with the 1D model. The physical dis-

continuity of the shock front is difficult to model in the discrete elements. A very fine mesh is required to properly capture the instantaneous rise in overpressure. If the size of elements are too large, the peak of the overpressure will be rounded down and the rise time will be elongated. Figure 3.6 shows the results of the mesh refinement study. It is evident that large elements (size of 50mm) do not handle the shape discontinuity as well as the smaller elements. An Eulerian element with size of 10mm would suffice for the purpose. Very small elements throughout a large domain of Eulerian type is infeasible for many practical problems as the computational limits might be exceeded with a large number of elements. In practice a non-uniform mesh is often used for the Eulerian domain discretisation to minimise the computational demand, where very fine elements are only used in the area of interests and other areas are meshed with coarse elements. Figure

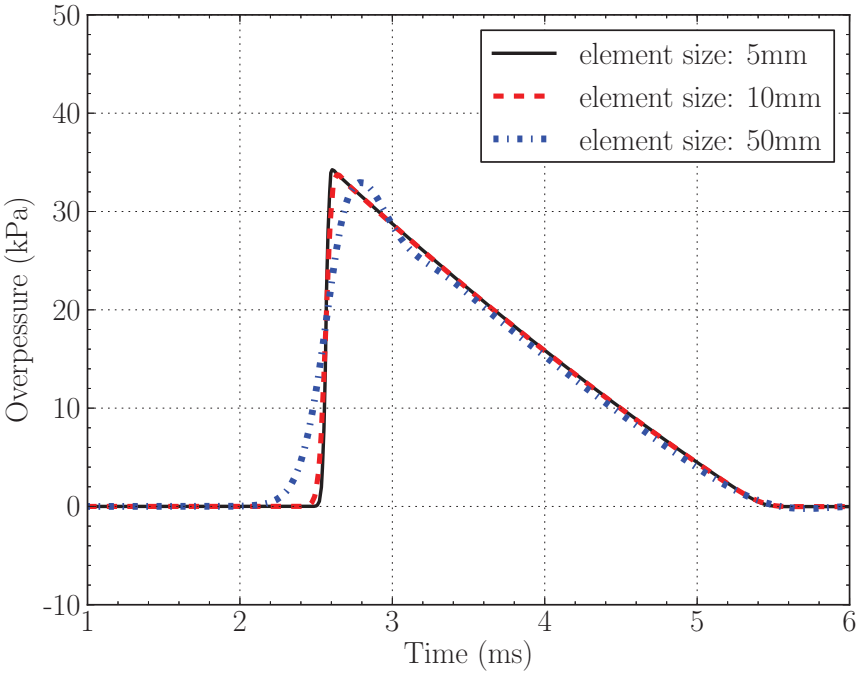


Figure 3.6: Mesh study of 1D Eulerian model

3.6 shows a blast wave with peak overpressure of $34.5kPa$ with corresponding initial particle velocity predicted to be $72.33m/s$. The error is only 0.7% when compared with the theoretical value of $72.84m/s$ determined by Equation 2.9c.

3.5.2 Blast wave propagation

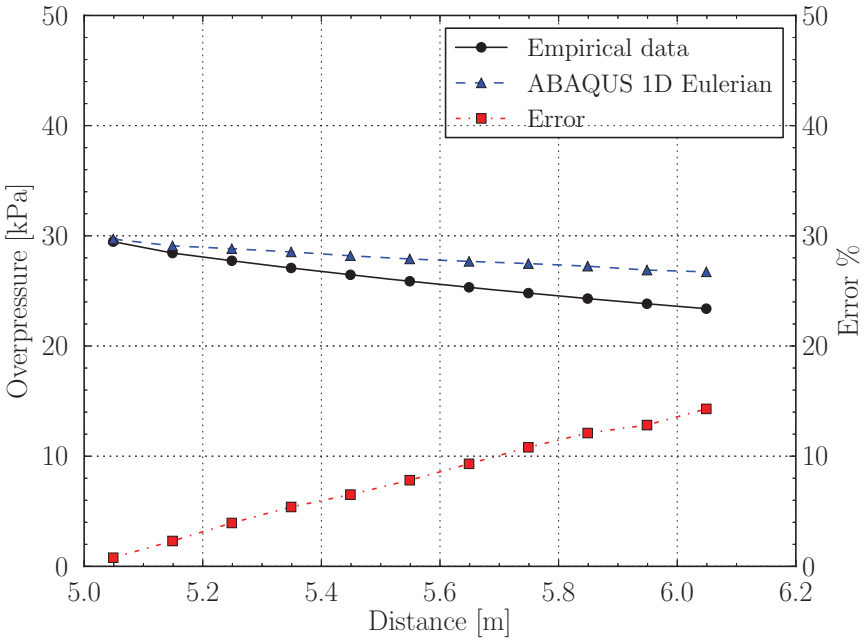


Figure 3.7: Comparison for shock strength decay

In this section, the decay of the strength of an arbitrary blast wave in a 1D Eulerian model is assessed. A long 1D Eulerian model was used with 11 pressure sampling points recording the decay of the peak overpressure along the path of the blast wave. Results are compared with the analytical data (equivalent to Equation 2.15). There are a few reasons that these two curves show increasing discrepancy along the propagation path. Given the same initial conditions, the strength of blast wave in the numerical model decays slower than the empirical data because there are some loss paths not taken into account. The Eulerian capacity of ABAQUS implements a simplified Navier - Stokes equation in which the air flow is assumed to be inviscid and compressible. Energy dissipation due to turbulence and viscous effects are not captured. In addition, empirical data are based on high explosives which produce spherically expanding blast waves. In the numerical model the shock wave is assumed to be planar for simplicity and it is also assumed that the blast wave from a gas explosion might not be spherical. Therefore expansion of the flow in the Eulerian model might not be the same as

Table 3.2: Reflection factor Λ comparison

	$\beta = 0^o$			$\beta = 45^o$	
	Empirical	1D	3D	Emprical	3D
p_{in} (kPa)	34.5	≈34.5	≈34.5	34.5	≈34.5
p_r (kPa)	78.6	78.16	73.39	82.11	81.9
Λ	2.28	2.27	2.13	2.38	2.37
error (%)	N/A	0.44	6.6	N/A	0.42

in reality. These may account for the differences between the two curves.

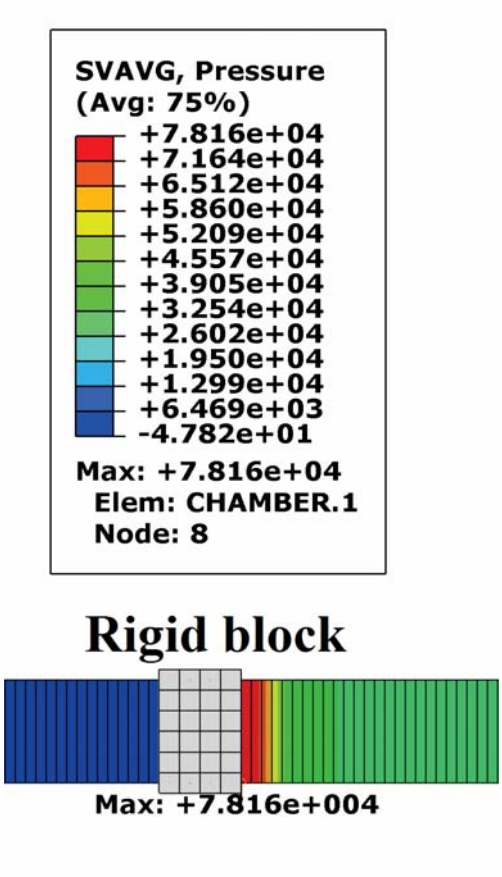
3.5.3 Reflection of ideal blast wave

Simulations presented above reasonably established that a transient blast (pressure) wave can be created accurately with the Eulerian capacity in ABAQUS. Now it is appropriate to examine the reflection of a blast wave on a Lagrangian part within the Eulerian domain using the coupled Eulerian - Lagrangian technique.

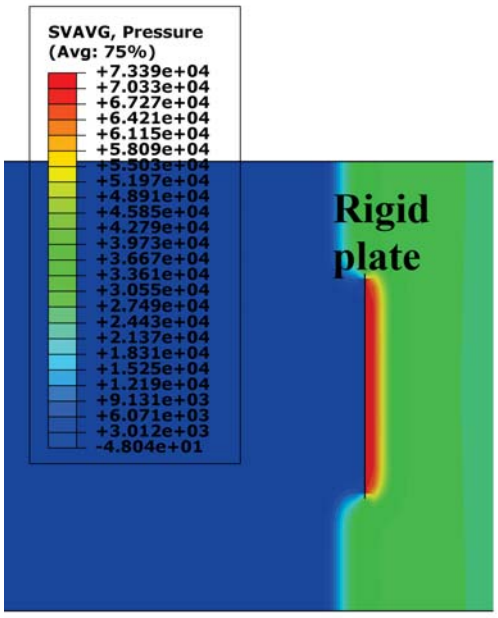
The incident blast wave with magnitude of $34.5kPa$ in Figure 3.6 was reproduced again in a 1D Eulerian part coupled with a Lagrangian brick acting as a rigid reflection surface. This represents a normal reflection with incident angle $\beta = 0^o$. As shown in Figure 3.8a the numerical reflected pressure is predicted to be $78.16kPa$ and the error is only 0.44% comparing with the theoretical value calculated by Equation 2.11. A similar model in 3D predicted the normal reflected peak overpressure to be $73.39kPa$ with 6.6% error compared with the theoretical value, shown in Figure 3.8b.

Oblique reflection has also been assessed against a rigid shell plate located in the three dimensional Eulerian part inclining 45^o to the direction of the blast wave, i.e $\beta = 45^o$. The oblique reflection peak overpressure can be seen in Figure 3.9 to be $81.9kPa$, this gives a error of 0.42% comparing with the empirical data. An overall comparison of reflection coefficient Λ between numerical and empirical values for normal ($\beta = 0^o$) and oblique ($\beta = 45^o$) reflection is presented in Figure 3.10 and Table 3.2 as well.

Numerical results presented above were obtained from Eulerian and coupled Eulerian - Lagrangian (CEL) capabilities of **?**. The work examined propagation



(a) 1D ($p_r = 78.16kPa$)



(b) 3D ($p_r = 73.39kPa$)

Figure 3.8: Normal reflection in Eulerian model $p_{in} = 34.5kPa$

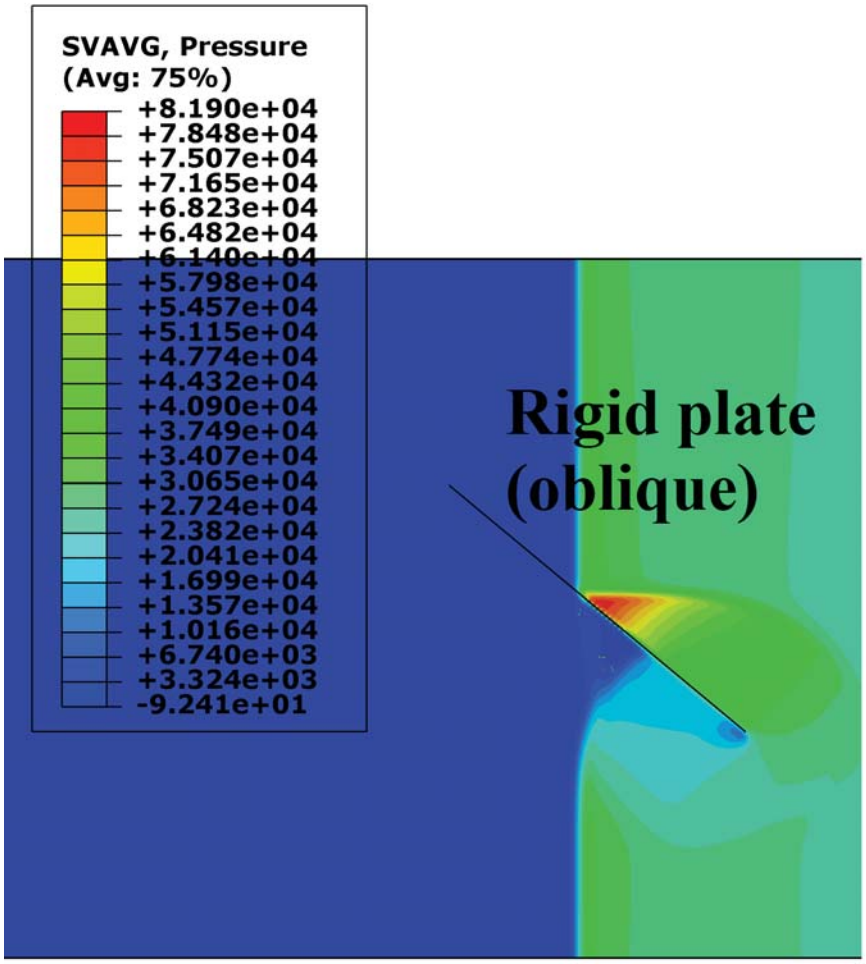


Figure 3.9: Oblique reflection ($p_{in} = 34.5kPa$)

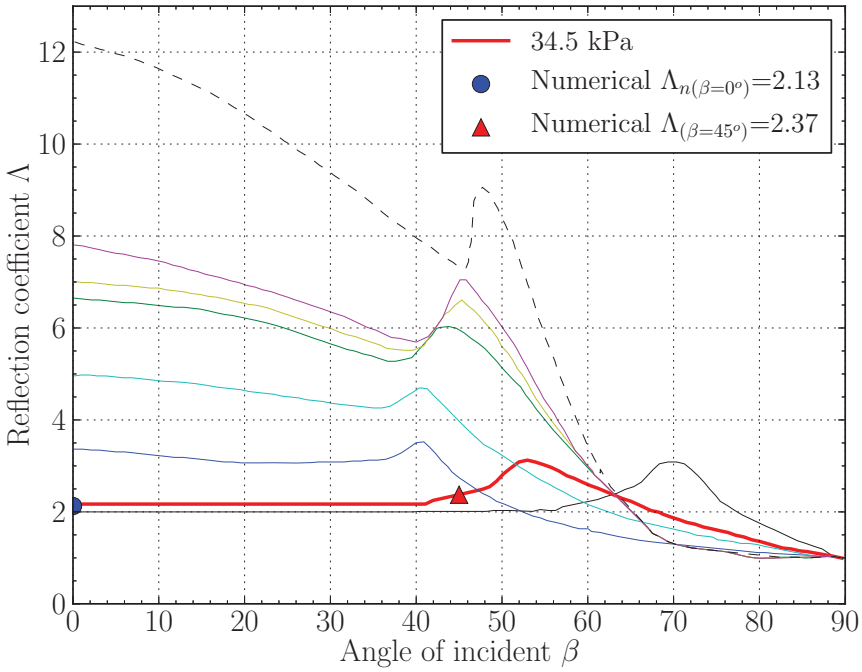


Figure 3.10: Comparison for shock strength decay (USDOD, 2008)

of a blast wave and the shock wave reflection on a rigid surface. Good correlations were found between the numerical and empirical/theoretical results.

3.5.4 Square plate subjected to close HE explosion

This section presents the validation work using a coupled Eulerian - Lagrangian (CEL) technique for general purpose. The numerical model of a square steel plate subjected to close range high explosive loading was created in AUTODYN (ANSYS) and analysed by coupled and uncoupled techniques.

Boyd (Boyd, 2000) conducted a series of experiments on the square steel plates subjected to explosive blast loading. A mild steel plate ($1200 \times 1200 \times 5mm$) clamped around its perimeter to a frame was subjected to a spherical high explosive as shown in Figure 3.11. The effective area free to move is about $1000 \times 1000mm$ under the close range explosion. The frame was placed on four pendine blocks and a $0.25kg$ Pentolite was detonated centrally above the plate. The test consists of several trials intended to measure the displacement and acceleration of

the plate by varying the stand-off distance of the Pentolite charge to 250, 400 and 500 mm. The test results from 250 mm stand-off stances were used for validation and comparison. The focus was on the central dynamic displacement of the plate under blast loading.

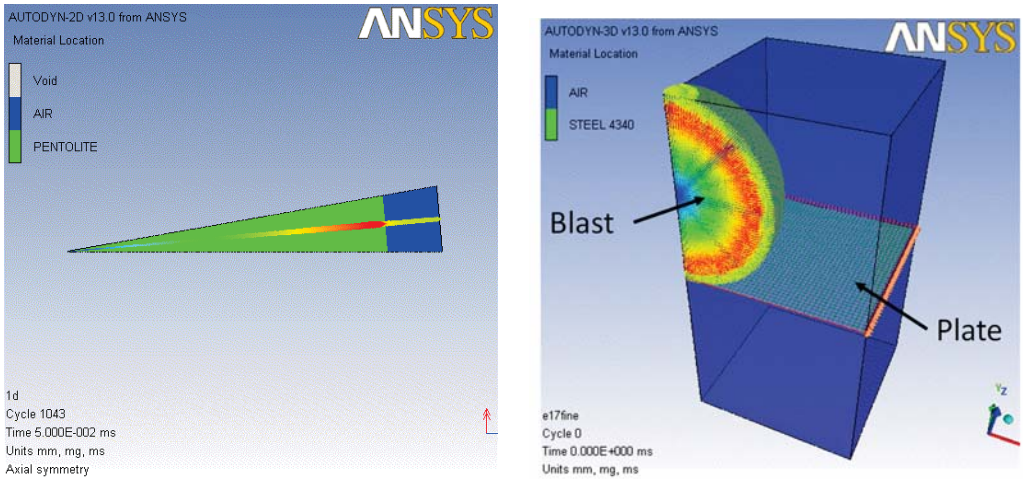


Figure 3.11: Boyd's experiment configuration (Boyd, 2000)

A quarter of the plate was re-created by the numerical shell model taking advantages of symmetry with thickness of 5 mm. AUTODYN is able to model the high explosive charge by using the JWL-equation of state within the Eulerian domain together with air. The parameters used to define Pentolite are listed in Table 3.1. Boyd in his work proposed the material properties for the mild steel plate: Density $\rho = 7850kg/m^3$, Poisson's ratio $v = 0.3$, Tangent modulus $E_T = 470MPa$, Yield stress $\sigma_y = 270MPa$ and Young's modulus $E = 203GPa$. In the present numerical model the Johnson - Cook material model shown below is used:

$$\sigma_y = \left[A + B(e^p_{eff})^N\right] \left[1 + Cln\frac{\dot{\epsilon}}{\dot{\epsilon}_0}\right] \left[1 - (T_H)^m\right] \tag{3.17}$$

In the above model, $e^p{}_{eff}$ is the effective plastic strain. A,B and N are strain hardening parameters to be determined based on test data. The Johnson - Cook parameters of the mild steel used in Boyd's test are not available, in order to better represent the mechanical behaviour a very similar material Steel 1006 was used but modifying the yield stress to $270MPa$. Therefore the parameters are defined as: $A = 270MPa$, $B = 275MPa$, $N = 0.36$, $C = 0.22$ and $m = 0.0$. The last parameter $m = 0.0$ implies that the temperature dependent properties will not be taken into account.



(a) 1D explosion remap (b) 3D $\frac{1}{4}$ coupled flexible plate model

Figure 3.12: Numerical model in AUTODYN

- Coupled Eulerian - Lagrangian approach (CEL)

The numerical model was developed in two steps. In the first step the explosive was detonated in a 1D model and the developed blast wave was subsequently remapped into a 3D model in the second step. In the latter the air was modelled using Eulerian elements in which the shock wave from the first step propagated and impinged on the target plate to deform. The interaction between the Eulerian and the Lagrangian (shell plate) part was taken into account.

The charge and the subsequent explosion were both spherical so a 1D wedge model was used to represent the charge and the surrounding air in the first step. The length of the wedge represents the stand-off distance from the centre of the charge to the plate. The ignition started at the centre and as the explosive expands the blast wave travels towards the end. The 1D simulation was terminated when the shock wave almost reached the far end as shown in Figure 3.12a and then the developed pressure wave was remapped into a 3D quarter Eulerian domain coupled with the flexible Lagrangian shell plate as depicted in 3.12b. After the remapping is completed in the second step, the response analysis was then accomplished by running the 3D coupled model.

- Uncoupled Eulerian - Lagrangian approach (UEL)

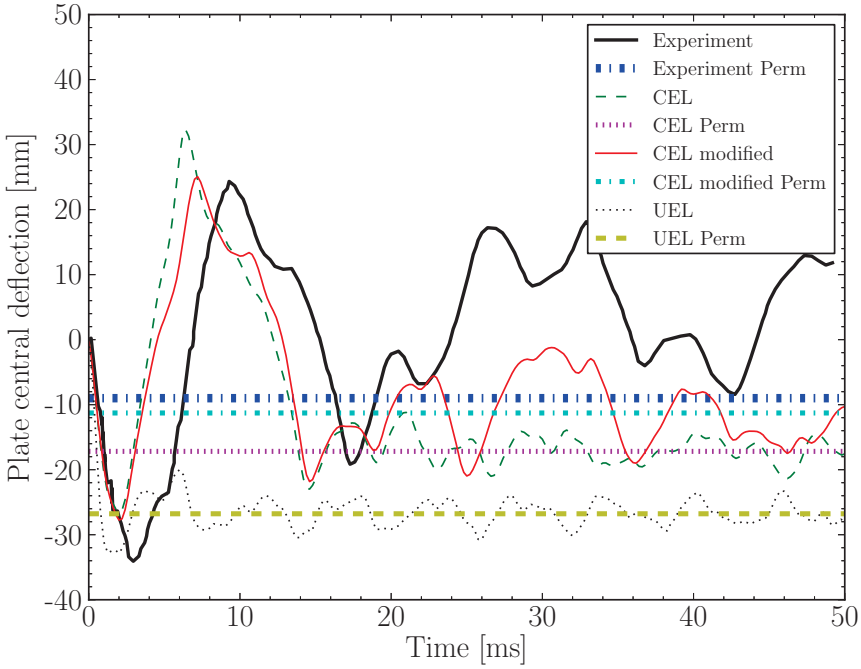
This approach involves one more stage than the coupled method with one major modification to the second step. The first step was the same, running the 1D wedge model up to the point that the blast wave reaches the plate. In the second step, the developed pressure wave was then remapped into a similar Eulerian domain without the plate but the height was reduced and an extra boundary condition was imposed on the bottom face to representing a rigid plate. Twenty-five pressure gauges (a 5×5 matrix) were placed in equal distance on the bottom surface to record the pressure loading on the "rigid plate". Two more gauges were placed near the "plate" centre. In the third step, the recorded pressure - time curves were directly applied on the segments of the surface of the flexible Lagrangian shell plate model. The structural analysis was then completed by running the pure Lagrangian plate model.

Although the uncoupled approach involves one more step the overall saving of analysis time is substantial. 1D simulation took about 3 minutes for either approach. The second step using the coupled technique took 2 hours to complete the numerical simulation (non-uniform optimum mesh). In comparison, the second step using the uncoupled technique only took 5 minutes and the subsequent pure Lagrangian analysis of plate takes another 5 minutes. Including the model set-up to complete an uncoupled analysis requires approximately 20 minutes, which is about 6 times less than the coupled approach.

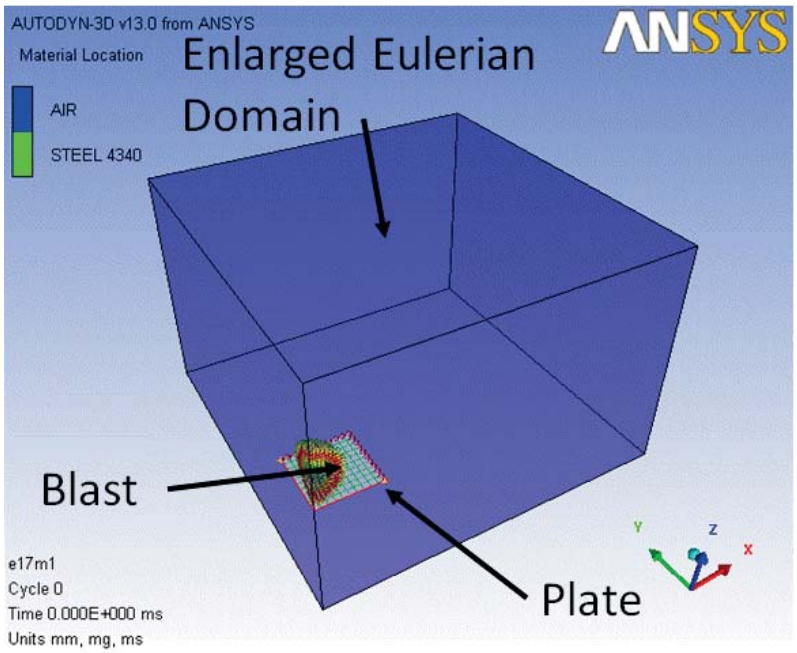
- Numerical responses discussion

Among the several tests carried out by Boyd, trial e17 with stand-off distance of 250 mm was used to compare with the numerical models. Generally both coupled and uncoupled techniques give comparable results as shown in Table 3.3. In terms of maximum dynamic deflection (δ_{max}), the numerical models produced underestimated results with -3.61% and -21.89% error for UEL and CEL technique, respectively. On the contrary, permanent deformations are overestimated by 197.5% and 90.88% for UEL and CEL respectively.

It seems that the permanent deformations predicted by numerical model are not in as good agreement as the maximum dynamic deformation to the experimental results. The UEL technique produced better correlation to maximum



(a) Displacement - time histories



(b) Modified Eulerian domain

Figure 3.13: Comparison of responses and the modified model

Table 3.3: Comparison of max. and permanent deflection (Trial e17)

	Test	UEL (error)	CEL (error)	CEL mod (error)
δ_{max} (mm)	-34.07	-32.84(-3.61%)	-26.61(-21.89%)	-27.74(-18.58%)
δ_{perm} (mm)	-9	-26.78(197.5%)	-17.18(90.88%)	-11.27(25.22%)

dynamic deformation but worse prediction for the permanent deformation. Deflection - time histories from numerical results are compared with experimental measurements in Figure 3.13a for trial e17. It can be noticed from this figure that the UEL technique is not able to capture the rebound response of the plate despite that it gives the better prediction for maximum dynamic deformation. For the time responses, the CEL technique is able to capture the rebound but only the first one then the vibration amplitudes are limited in a small range around its permanent position. Jacinto (Jacinto et al., 2001) in their work on plates subject to blast loading stated that:"The obtained results improved significantly when the used load was considered as the temporal superposition of the pressure over the anterior and posterior faces of plates." This indicated that the pressure history behind the plate is also important for the response and should not be easily neglected.

The original CEL model shown in Figure 3.12b had a drawback that the size of the Eulerian domain is limited to the plate width, therefore no pressure wave was able to travel to the back of plate from the edge. This might affect the subsequent response of the plate after the peak deformation. The Eulerian domain was then modified as shown in Figure 3.13b so that its dimension is much larger than the plate. In such a way the pressure waves were allowed to travel beneath the plate. This situation is similar to the actual test where there are large gaps between the supporting Pendine blocks through which the pressure waves can travel to the back of the plate. The modified CEL model produced significantly improved results particularly for the permanent deformation. As listed in Table 3.3, from original CEL to modified model, the error for maximum deformation was reduced from -21.89% to -18.58% and permanent deformation is reduced substantially from 90.88% to 25.22%. The response time histories from modified model are also shown in Figure 3.13a.

There were many factors that may have affected the results. The experiment

might have some unexpected errors such as the position of the plate and movement of the clamping frame. In addition, the simulation assumed that the plate is fully clamped around its edges, which might not be the case in the test. Slip may hence occurs during the explosion at the perimeter. Thus can have a large impact on the central deflection of the panel. Despite all the unidentifiable errors, this simple validation work showed the importance of proper consideration of the coupling between the blast wave and the movement of the target to the accuracy of the numerical model.

3.6 Finite element analysis packages

Two FE packages have been used in the present work: AUTODYN/ANSYS and ABAQUS. As demonstrated in the previous sections, both packages have explicit solvers and Eulerian capabilities to undertake high-speed blast and impact problems, either in a coupled or in an uncoupled manner. In this sub-section, brief comments on lessons learnt from the experience of using these two packages are provided.

For the validation work of Boyd's experiment (Boyd, 2000), only results from AUTODYN/ANSYS were presented due to the nature of the problem. AUTODYN provides a special approach (re-mapping) to simulate the close range high explosive detonation. This approach makes AUTODYN very efficient for modelling the actual explosion of the charge and the subsequent response of the target. ABAQUS recently incorporated a new Eulerian capability (starting from Version 6.9) which enables the simulation of this problem but without the re-mapping technique. ABAQUS has only been used in the UEL analysis (the Lagrangian step) for the validation work, since the Eulerian capability was not available when the validation work of Boyd's test has being undertaken.

Although it was shown that the UEL approach did not compare as well as the CEL approach with the experimental results, UEL simulation of ABAQUS produced very similar structural response of the plate to UEL results of AUTODYN/ANSYS. In addition, in collaboration with the Steel Construction Institute, both AUTODYN/ANSYS and ABAQUS were used to analyse a simple portal frame structure as well side rail and cladding components. The results between

the two numerical packages were also very similar. The new Eulerian capability of ABAQUS provides an alternative approach for the simulation of blast problems. In the previous and following sections, it is shown that the Eulerian explicit solver of ABAQUS can simulate blast waves and their interactions with adequate accuracy. During the course of the project, AUTODYN/ANSYS has also been used to reproduce the blast effects from equivalent TNT charges for the Buncefield investigation. The results compared reasonably well with empirical data.

The Eulerian capability of ABAQUS has been extensively used in this project for forensic studies. Although it does not offer the re-mapping technique, it has a customisable Eulerian inflow boundary condition within the unified CAE environment as well as more sophisticated meshing tools. The customisable Eulerian inflow module can be used to produce a variety of incident blast waves, either detonation or deflagration. The meshing tools of ABAQUS provide a comparatively high quality mesh of the Eulerian model hence increase the computational efficiency. In AUTODYN/ANSYS, a subroutine must be used in order to produce a customisable blast wave at the inflow boundary condition. The subroutine has to be written in C or FORTRAN which entails extra compilation cost and programming time. Partitioning is not available for the Eulerian model in AUTODYN/ANSYS, and the meshing capabilities of the domain are very limited - often resulting in an excessive number of unnecessary elements.

ABAQUS provides a unified CAE environment in which the Lagrangian (structural) and Eulerian (air/water) parts are created and assembled within one model. All the pre- and post-processing work can therefore be accomplished within one package. AUTODYN is one of the integrated modules within ANSYS, although it can be used as a stand-alone package. AUTODYN itself does not provide detailed CAD tools for the creation of complex Lagrangian and Eulerian parts. Accordingly, most of the pre-processing work has to be carried out in a dedicate modelling module in the ANSYS/WORKBENCH, and then the parts have to be transferred into AUTODYN for analysis. Subsequently, the results need to be transferred into another module for post-processing. Moreover, ABAQUS uses Python as a scripting interface, and the scripting is integrated with every function within the package. Scripting in ABAQUS is therefore extremely powerful in the pre- and post- processing phases of the numerical analysis. Creating, or

repeatedly modifying, the model and carrying out extensive parametric studies are hence relatively straightforward and efficient. While scripting in ANSYS is possible in the WORKBENCH environment and for creating models, it is not available for AUTODYN. As a result, the efficiency and practicality of the scripting procedures for AUTODYN/ANSYS are not as effective as in ABAQUS.

Advancements in computational facilities now enable the deployment of parallel processing techniques for extensive numerical analysis. Both packages are able to take advantage of multi-core processor or multi-processor technologies. In AUTODYN/ANSYS, the models have to be decomposed into specified domains corresponding to the number of available processors before submitting the job for analysis. In ABAQUS, the models are decomposed automatically after submission of the job for analysis according to the number of available processors, which does not require any direct user intervention. AUTODYN has been widely used in industry and academia and long before the introduction of the Eulerian capability in ABAQUS. The former has an extensive library of readily available material models, including not only metal materials such as steel, aluminium and copper but also fluids such as air and water. In contrast, for ABAQUS, the user has to input the necessary material parameters.

Based on the experience of using AUTODYN/ANSYS and ABAQUS, both packages can produce reasonably accurate results for Lagrangian (structural dynamics) and Eulerian (Blast wave) simulations. Due to the unified CAE environment, ABAQUS has comparatively better usability than AUTODYN/ANSYS, and also relatively more efficient scripting and parallel processing capabilities. This makes the former more effective in the numerical simulation of blast problems, particularly for extensive parametric studies (such as those involving detailed pressure-impulse diagrams). The new Eulerian capability in ABAQUS has only been introduced in recent years and is in the early stages in terms of validation. Nevertheless, the accuracy and usability demonstrated over the course of this research project suggest that it offers a powerful alternative to the currently available AUTODYN/ANSYS procedures.

Chapter 4

Blast response of field objects

In the previous chapters, an overview and motivation of the research study has been presented. The numerical tools were introduced and the validation work were carried out to provide confidence in the following numerical studies. In this chapter, focus is placed on a specific type of target to show how advanced finite element methods can be used in forensic studies to aid both the explosion incident investigation and future design.

For the purpose of assessing the pressure history across the Buncefield site, evidence relating to overpressure is important as part of the forensic studies. Within the body of the Buncefield vapour cloud, there were very few large objects such as buildings. Building structures that suffered damages in the vicinity of the site are located towards the edge or outside of the vapour cloud. However, it was found that there were many small objects such as steel switch boxes distributed across the site and nearby areas, as shown in Figure 4.1. These field objects have been used as overpressure indicators, as the residual deformation of these objects can provide an indication of possible overpressure at their location after the passage of the blast waves. Preliminary investigation carried out at the Health and Safety Laboratory (SCI, 2009) indicated that the overpressure required to cause the damage to switch boxes observed at Buncefield exceeds 200 kPa. This data was however limited to shock waves with relatively short duration (i.e. detonation blast waves). One of the objectives of the work presented here is therefore to overcome such limitations by using numerical tools and carry out analyses covering both detonation and deflagration scenarios within a range of

overpressures and impulses, in order to examine more realistically the possible blast characteristics experienced at Buncefield. The numerical results can be used in the investigation of future explosion incidents as well.



(a) Damaged box A (b) Damaged box B (c) Damaged box C

Figure 4.1: Damaged steel switch box in the vapour cloud (SCI, 2009)

In this chapter, test data from external experiments are used to validate the numerical models and several modelling approaches are adopted and compared to find an optimum model for parametric studies. Pressure - impulse diagrams covering both detonation and deflagration blast loadings are constructed with a range of overpressures and impulses. Reflections of non-ideal blast waves are studied quantitatively, and some assumptions in the parametric study are made based on the findings. The work attempts to compare the numerical results with the actual damaged boxes qualitatively and discuss the possible applications of the results for forensic studies.

4.1 Experimental observations

During the Buncefield major incident investigation, a high explosive (TNT) detonation test of steel switch boxes was commissioned by the investigation board. The TNT tests were carried out by BP and limited data were available in the Buncefield report (SCI, 2009). Information regarding the charge size, shape and stand-off distance were given as well. In addition, a more recent series of gas

detonation tests (Allason, 2013) were completed under management of the Steel Construction Institute, in which the blast and damage data of steel boxes were abundant and comprehensive. The actual tests were carried out by GL Noble Denton and results were presented by Allason (2013). Available data from both detonation tests were used in this research project and presented in this section.

4.1.1 Steel switch boxes

Steel switch boxes used in the two detonation tests were very similar in dimensions and properties. They were both made of mild steel and their dimensions were 300×300×150 mm and 300×300×200 mm respectively. Photos of the two boxes are shown in Figure 4.2 and their details are presented in the following sections.



(a) TNT test 300×300×150mm (SCI, 2009)

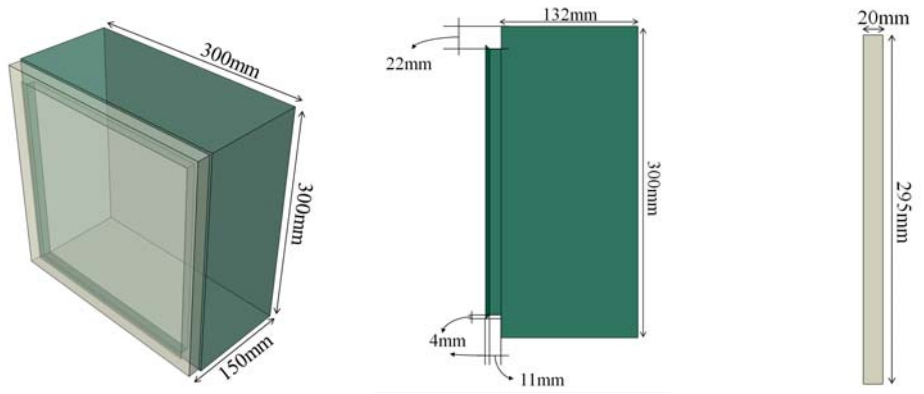
(b) Gas test 300×300×200mm (Allason, 2013)

Figure 4.2: Photos of steel switch boxes

4.1.1.1 Box150

A steel switch box of dimension 300×300×150mm was used in the TNT explosion test. The box has a depth of 150 mm measuring from the front face to the back panel. In order to distinguish between the two boxes, the depth is used as a

reference therefore this box will be referred as "Box150" from now on. Dimensions of the assembly, enclosure and door are shown in Figure 4.3. Width and height of the door are 295 mm, which is slightly smaller than the enclosure. The thickness of the door and enclosure are approximately 1.15 and 1.35 mm, respectively. The



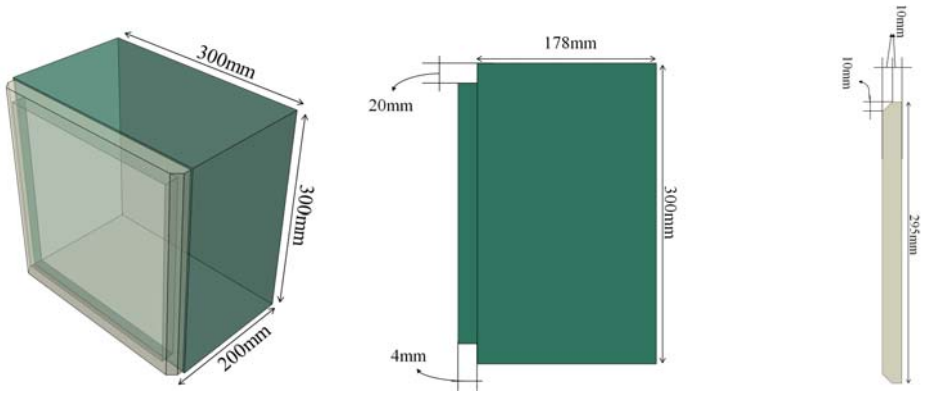
(a) assembly (b) enclosure (c) door

Figure 4.3: Box150 (300×300×150mm)

material is mild steel and it has been determined in a series of tensile coupon tests that a yield stress of 300 MPa with minimum strain hardening is representative for the material of box.

4.1.1.2 Box200

In the gas cloud detonation test, a number of boxes with dimension 300× 300×200 mm were exposed to the blast wave at different distances from the cloud. Similarly, this type of boxes will be referred as "Box200" in the rest of the chapter. The dimension of the enclosure is 300 mm and 295 mm for the door. Dimensions of the box and feature details are shown in Figure 4.4. The wall thickness is 1.25 mm and identical for both door and enclosure throughout. Eight mechanical tensile coupon tests have been carried out to determine the material properties of this box. The average values for yield and ultimate stress were 279 MPa and 297 MPa respectively. The material has only moderate strain hardening.



(a) assembly (b) enclosure (c) door

Figure 4.4: Box200 (300×300×200mm)

4.1.2 TNT detonation tests

A number of switch boxes of the type Box150 were exposed to blast overpressures from TNT explosion in a series of tests (SCI, 2009). TNT explosive produces ideal blast waves which is typical from detonation events, therefore the results of these tests can be used in the investigation to provide indications of the magnitude of overpressure needed to cause the deformation observed in Buncefield. Four explosion tests have been carried out, the TNT charge used in each test are listed in Table 4.1 along with the stand-off distances. Detailed overpressure profiles were not available but peak free-field overpressures at the location of the boxes in all four tests have been measured during the explosion. The characteristics of the blast wave from TNT explosion can be well defined by empirical tool. As shown in Table 4.1, the blast parameters predicted by the CONWEP compare well with the test measurements.

The typical arrangement of switch boxes in the TNT test is shown in Figure 4.5. It can be seen that one box had the front face (door) facing the charge while the other one had its side wall facing the charge. In the current study only the boxes that had their front face facing the charge were investigated. Peak side-on (free-field) overpressures in the four tests ranged from 100 to 750 kPa, as shown in Table 4.1. Reflected overpressures approximately ranged from 274 kPa to 4 MPa as can be readily calculated by Equation 2.11 and the durations ranged from 7 to 12 ms according to the semi-empirical tool CONWEP.



Figure 4.5: Configuration of TNT detonation test (SCI, 2009)



Figure 4.6: Residual deformations of "Box150" exposed to TNT detonation, incident overpressure from left to right: 100kPa, 200kPa, 480kPa and 750kPa (SCI, 2009)

The characteristics of the damage was dominated by crushing of the front face (door), as shown in Figure 4.6, while the other sides suffered from moderate to minor damages. It can be noted that for some boxes, the back face was pushed outward rather than crushed inwards. This was due to the effect of adiabatic compression. The deformation of the front face caused an increase in internal pressure which deformed the back face outward (SCI, 2009). The four boxes showed increasing levels of damages subject to different levels of side-on overpressures. No significant damage occurred until peak side-on overpressure exceeded 480 kPa (reflected peak overpressure of 2 MPa). As shown in the figure, no damage can be readily observed on the box subjected to 100 kPa side-on overpressure but the damage is clearly visible at 200 kPa. Although detailed experimental data were not available for the TNT detonation test, information of the TNT explosives and the photos of the damaged boxes are still extremely useful for the analysis of the overpressure indicators.

Table 4.1: Available data of box TNT test

			CONWEP (ABAQUS)		Test
Box ID	W_{TNT}(kg)	Stand-off(m)	Peak p_{in}(kPa)	t_d(ms)	Peak p_{in}(kPa)
Box150-1	130	13.5	103.78	12.48	100
Box150-2	262	13	197.74	12	200
Box150-3	90	6.5	475.46	7.68	470
Box150-4	97.2	5.0	754.47	8.28	800

4.1.3 Gas detonation tests

Many objects were exposed to the blast waves in the gas detonation test, including boxes, drums, cars and containers as illustrated by the test report (Allason, 2013). Responses of the steel boxes were studied in the current work. A simplified layout of the gas detonation test is presented in Figure 4.7. As shown in the map, the size of the propane - air mixture is 30×10×2m which was ignited 2m from the end. Four boxes of type "Box200" were placed outside the gas cloud at distances of 4, 6, 10.7, and 15 m away from the cloud edge, respectively. All four boxes had their front face (door) facing the explosion. Transducers were placed at the

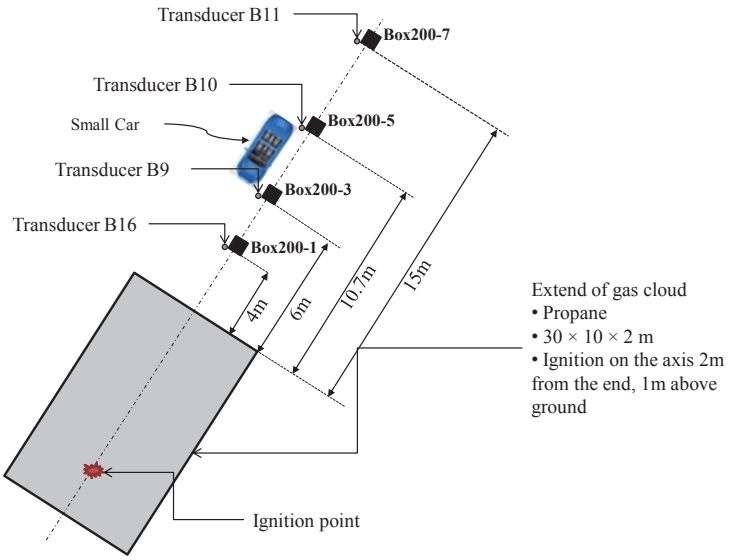


Figure 4.7: Simplifield layout of gas detonation test

location of each box to measure the free-field (side-on) overpressure that was experienced at the specific distance from the cloud.

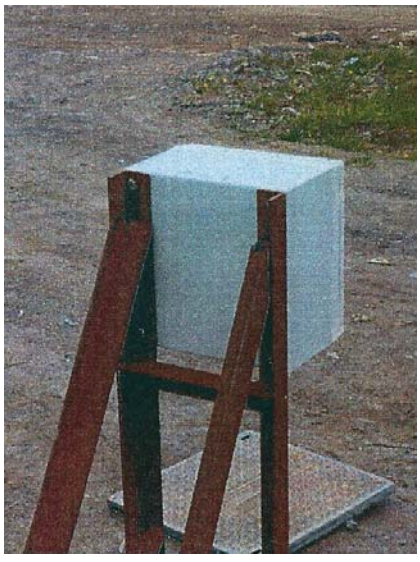


Figure 4.8: Configuration of box support (Courtesy of Steel Construction Institute)

The boxes were supported by strong steel frames bolted to concrete ground, and sand bags were placed onto the stand of support frames to prevent them tilting backwards under force transferred from the box. Figure 4.8 shows the fixing of the box to the support frame, as it can be seen that the box was constrained vertically along the two edges of the back panel. The support condition was identical to the TNT test presented above. A snap shot of the gas detonation in progress is shown in Figure 4.9. The Container and the car at far distance from the gas cloud are still visible while most of the boxes and drums were engulfed by the explosion.



Figure 4.9: Test in progress (Allason, 2013)

Pressure - time histories recorded by four transducers placed at the location of the four boxes are presented in Figure 4.10. The peak side-on values are 822.4kPa, 342.8kPa, 206.7kPa and 73.7kPa measured at distances of 4m, 6m, 10,7m and 15m, respectively. The decreasing of peak overpressure is expected with the increase of the distance to the explosion. The characteristic of the pressure temporal profiles recorded were of ideal blast wave type which was expected as the vapour cloud explosion was detonation. The blast waves reached to peak instantly in all four cases but the decaying of the waves were not all ideal. For

example the pressure - time curve of transducer B10 in Figure 4.10 did not show a exponential decay. The pressure dropped below ambient immediately after the peak and then increased gradually to a second peak with lower magnitude within a finite time. This might due to the turbulent flow caused by the complex envi-

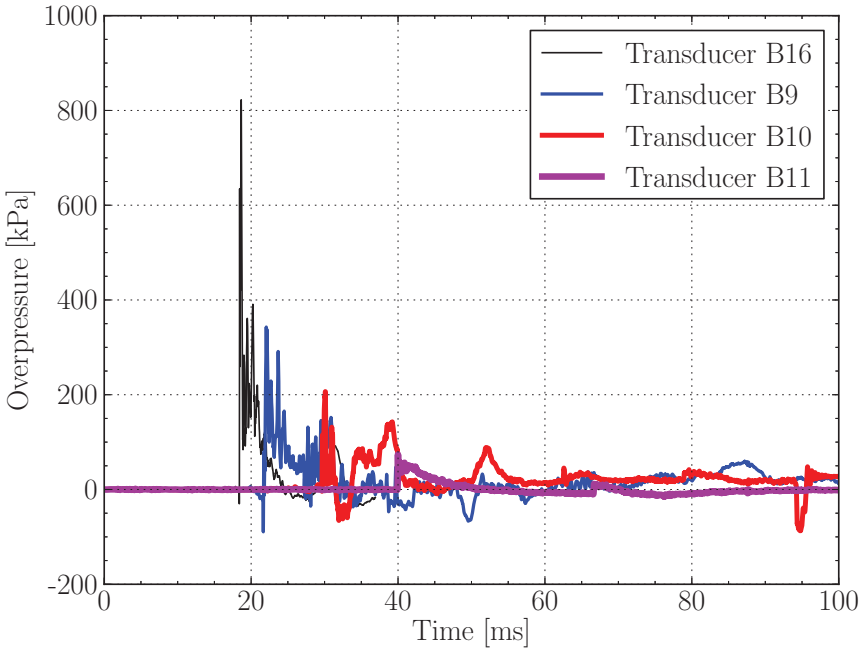


Figure 4.10: Pressure - time histories recorded by transducers

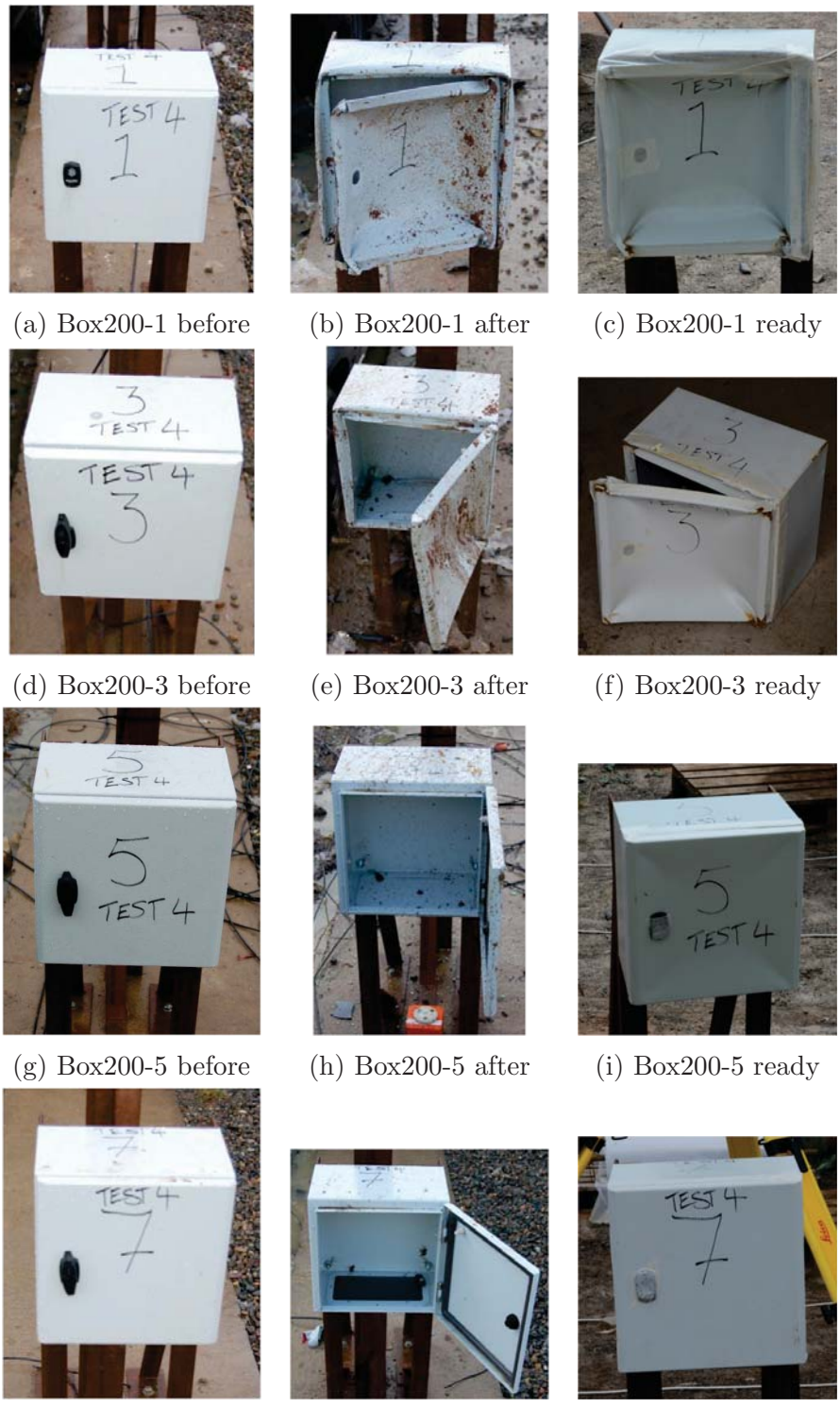
ronment around the boxes. As indicated earlier, many objects were exposed to blast wave in the same test including a car which was placed next to transducer B9 and B10. Transducer B9 was located at the front of the car, while the latter was at the rear. The turbulence or reflection generated by the blast wave when passing through the car would very likely to affect the pressure waves recorded by the transducers, particularly for B10. This can be examined in detail by looking at all four pressure curves shown in Figure 4.10. It can been see that there is no substantial distortions to the pressure profile of transducer B16 and B11, which were some distances away from the car. Transducer B9 placed near the front of the car registered a slightly distorted pressure profile which had a lower second peak. The pressure profile of transducer B10 was clearly significantly affected by the presence of the car. It is also worthy to note that the pressure waves did not

completely reduce to ambient and the time history scattered dramatically. These inaccuracies are attributed to the high sensitivity of the transducers. They might malfunction after the passage of blast waves with high peak overpressures.

Photos of the four boxes before and after they were exposed to blast waves in the gas detonation test are presented in Figure 4.11. Similar to the boxes exposed to pressure waves from TNT explosions, the damages of boxes from the gas cloud detonation were dominated by crushing of the front face as well. This can be expected since both explosions generated same types of blast waves. Box200-1 suffered the most severe damage at its front face (the door) when subjected to a peak side-on overpressure of 822.4 kPa and the damage is decreasing with decreased peak overpressures. No damage can be found observed at the front face of Box200-7 which was subjected to a peak side-on overpressure of 73.7 kPa.

After the gas explosion test, the damaged boxes were collected and scanned in a laser machine. The damaged boxes prepared for scanning are shown in Figure 4.11 as well. Scan photos of the residual shape of each box are shown in Figure 4.12. The digital files containing information of the residual shape of the boxes were used to study the response of the boxes to blast waves.

The residual deformation of the boxes have been measured in CAD software SolidWorks. Figure 4.13 shows the measurement of the deformation at the centre of the front face of the box (door). The measurement was taken from the middle of the right edge of the front face to the centre. The original position of the centre of the front face is unclear in the digital file. Due to the dominating damage at the front face, permanent deformations at the centre of the front face were used in the quantitative analysis of the response of the boxes. Permanent deformation at the centre of the front face of each box measured from the digital files are listed in Table 4.2, together with the experimental side-on peak overpressure at the location of each box.



(a) Box200-1 before (b) Box200-1 after (c) Box200-1 ready

(d) Box200-3 before (e) Box200-3 after (f) Box200-3 ready

(g) Box200-5 before (h) Box200-5 after (i) Box200-5 ready

(j) Box200-7 before (k) Box200-7 after (l) Box200-7 ready

Figure 4.11: Before and after photographs of Box200-1,3,5 and 7 (Allason, 2013)



(a) box200-1 (b) box200-3 (c) box200-5 (d) box200-7

Figure 4.12: Digital scan of boxes

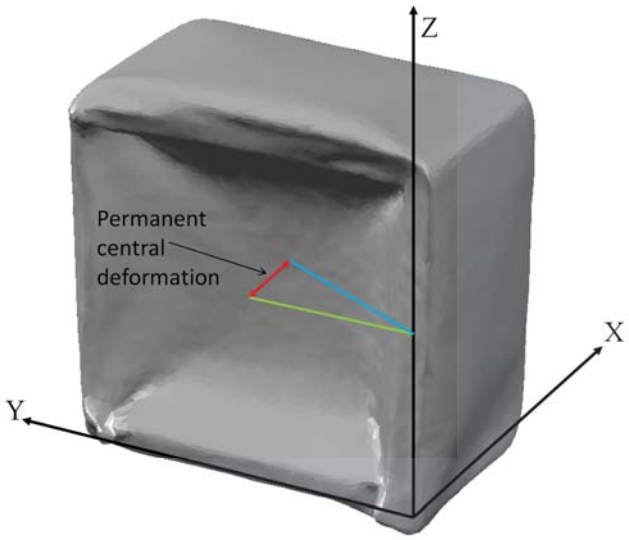


Figure 4.13: Deformation measurement of scanned box

Table 4.2: Brief information of box gas detonation test

Box ID	Transducer	Peak $p_{side-on}$ (kPa)	$\delta_{perm@door\ centre}$ (mm)
Box200-1	B16	822.4	50.82
Box200-3	B9	342.8	32.63
Box200-5	B10	206.7	9.19
Box200-7	B11	73.7	1.55

4.2 Numerical methodology

One of the objectives of the current study is using numerical models of a steel box to examine the response of boxes to blast loading. This section presents the details of the **?** numerical model and various analysis approaches adopted in the studies.

4.2.1 Numerical model of boxes

4.2.1.1 Model of Box150

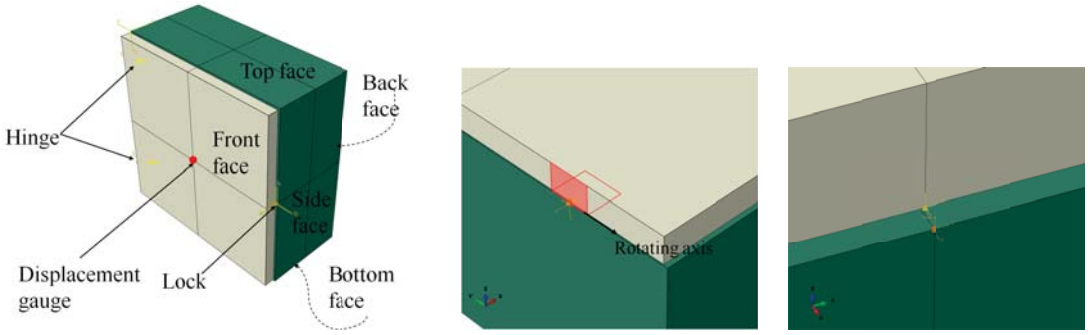
Material of Box150 is carbon steel and the Johnson-Cook plasticity and strain-rate model (Equation 3.17) was used. The parameters for the material are listed in Table 4.3, in which $m = 0$ since the material thermal dependencies are neglected here.

Table 4.3: Johnson-Cook parameters for material of Box150

A	300 MPa
B	200 MPa
N	0.228
C	0.01622
$\dot{\epsilon_0}$	0.000154

Details of the numerical model of Box150 are shown in Figure 4.14. Each face was assigned with a name to avoid confusion in the future when referring to them. In the common design of steel switch boxes, the door and the enclosure are joined with two hinges at one side of the box and the lock was located at the other side. Thus, two connectors were used to represent the axially rotating behaviour of the hinges. As shown in Figure 4.14b, the two segments (shaded area in red) of the door and the enclosure are rigidly tied to two reference points which were in turn joined by a hinge connector. These connectors only allow axial rotation about the longitudinal axis of the hinge. It was difficult to model the failure of the plastic lock that holds the door in position, both the capacity and failure mode are unclear and impractical to examine in detail within the scope of the current study. For simplicity, a rigid weld connector was used to join two single

nodes on the door and enclosure respectively, as shown in Figure 4.14c. The rigid connector would not fail and the door will always be kept in the closed position when the box is exposed to blast loading. Although it has been observed that the lock failed in all gas detonation tests, such simplification would not affect the results significantly and made the displacement - time history measurement easier to be interpreted. Otherwise if the lock was allowed to fail then the door would open and the displacement of the centre of the door will be affected by the rigid rotation of the door.

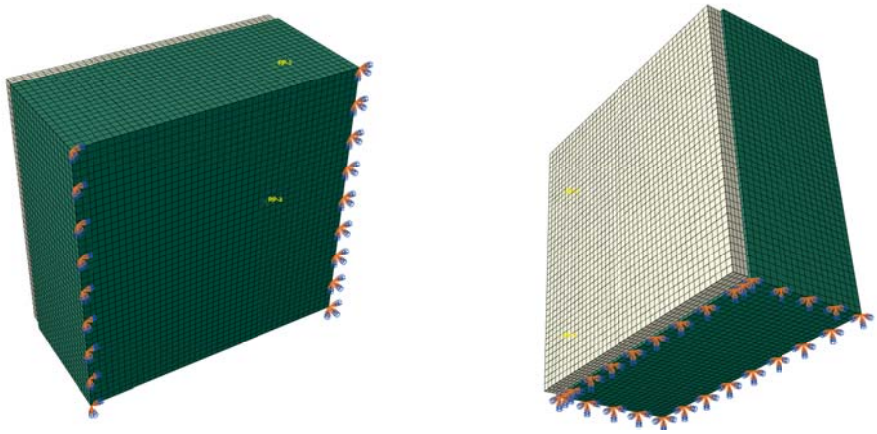


(a) model details (b) Hinge model (c) Lock model

Figure 4.14: Box150 numerical model details

Two types of boundary conditions were applied to the box model. Figure 4.15a approximately represents the support conditions of the boxes used in both tests. As it can be seen in Figures 4.5 and 4.8 that the boxes were fixed to the support frame on the back face along the two vertical edges. Figure 4.1 shows the actual boxes found at Buncefield. The support conditions for box B and C were not very clear due to the large deformation of the frames. It can be seen that box A was not supported at the back but instead at the bottom. Although exact support conditions were not known it would suffice to replicate the support condition by fully fixing the perimeters of the bottom face as depicted in Figure 4.15b.

ABAQUS shell element S4R was used to mesh the box models. A mesh convergence study was carried out by applying an arbitrary dynamic pressure load to the surfaces of the numerical model. As shown in Figure 4.16, the differences in maximum dynamic and permanent displacement are reducing as the total num-



(a) Box150 support on back face (b) Box150 support on bottom face

Figure 4.15: Box150 model boundary conditions with mesh

ber of elements is increasing. When the total number of elements exceeds 8601 there was no significant improvement to the predicted values, therefore the corresponding element size of 7 mm was used for the majority of the box model, while finer elements were used for features with relatively small dimensions. Figure 4.15 shows the mesh quality of Box150.

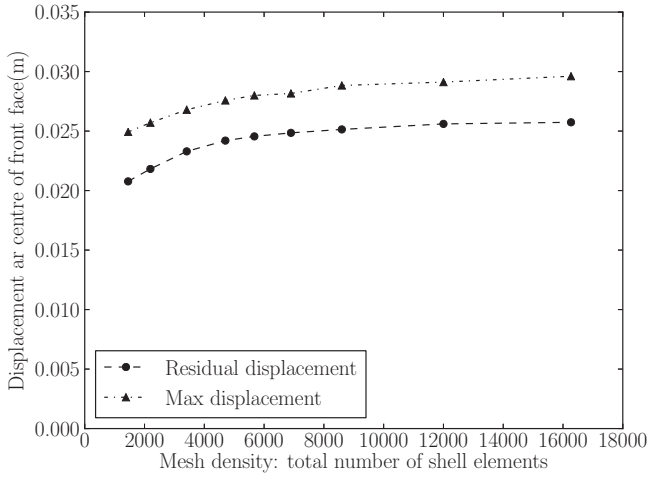


Figure 4.16: Box numerical mode mesh study

4.2.1.2 Model of Box200

Based on the results from the tensile tests for the material of Box200, a piece-wise plasticity with isotropic strain hardening model was used to represent the material behaviour of Box200. The Johnson - Cook strain rate hardening model is also used, i.e. he middle term of Equation 3.17. Parameters used in the material model are shown in the table below. Rate dependent data were not available from tensile tests. The strain rate hardening parameters of S275 steel were adopted, which has similar properties to the material of the boxes used in the current study.

Table 4.4: Piece-wise plasticity for material of Box200

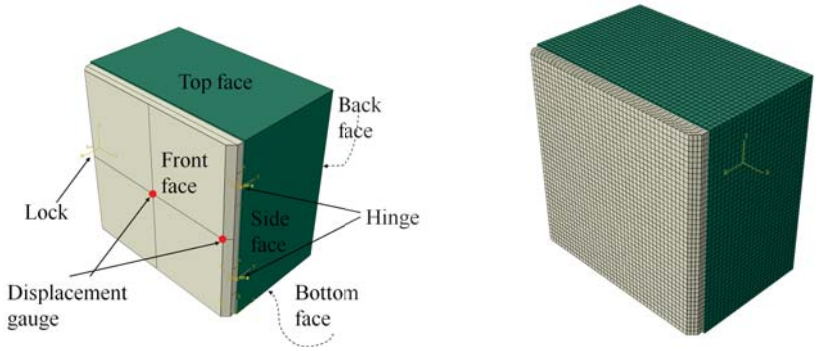
σ_y	ϵ_y
276 MPa	0.0
297 MPa	0.367
297 MPa	0.5
C	0.01622
$\dot{\epsilon_0}$	0.000154

The configurations of the two boxes are very similar, the door and enclosure of Box200 were joined by two hinges as well. A plastic lock was used to keep the door closed. The differences were the hinges of Box200 are slightly larger and located at the opposite side of Box150, as shown in Figure 4.17a. The hinge and lock were modelled in the same way as in Box150. Box200 was also meshed by 7 mm S4R shell elements as well, and with finer element at small features. The mesh quality of Box200 is shown in Figure 4.17b.

4.2.2 Lagrangian analysis

Deformation of the shell structural elements are described by Lagrangian formulations. The Lagrangian analysis model involves only numerical shell elements (S4R) and the dynamic loads are implemented by applying pressure loading directly on the segments of the surfaces of the structures. The finite element models are shown in Figures 4.15 and 4.17.

Dynamic pressure loading from the blast waves was applied directly on the

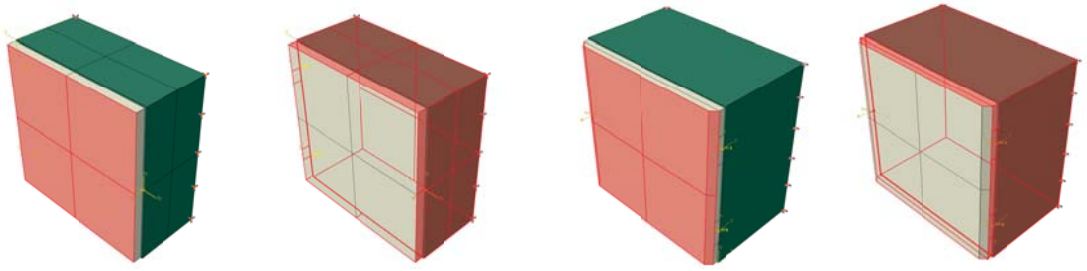


(a) model details (b) model mesh

Figure 4.17: Box200 numerical model with mesh

exterior faces: front, side/top/bottom and back. In the two experiments, the front faces (door) of the boxes were facing the centre of explosion. According to Section 2.3.2, the front faces of the boxes were then subjected to reflected overpressure loadings, while the side faces (both top and bottom) would experience something similar to the side-on (free-field) overpressure, and the back faces would be subjected to dynamic loadings slightly less intensive than the side-on overpressure. Considering the dimensions of the boxes, the depths were just 0.15 and 0.2 m hence the decay of the peak side-on overpressure across the box would not be significant as the time it takes to travel across the depths is extremely short. It was therefore assumed that all the faces except the front were subject to the side-on overpressure loading rather than the loading curves shown in Figure 2.13, which are more appropriate for large targets. Box faces which were subjected to reflected and side-on (free-field) dynamic overpressure loading are explicitly shown in Figure 4.18.

There are two methods to determine the reflected and side-on pressure loading curves if the incident blast waves are known from an explosion. For the TNT explosion, it can be determined based on the charge weight and stand-off distance, while for a gas explosion then it is necessary to record the actual pressure - time histories during the explosion. When the incident blast wave parameters are known, one method to calculate the dynamic overpressure loads is using Equations 2.5 to 2.11 as shown in Figure 2.12. This method is referred to as Analytical blast in the following paragraphs. Another method is to use the CONWEP func-



(a) Box150 reflected (b) Box150 side-on (c) Box200 reflected (d) Box200 side-on

Figure 4.18: Box faces subjected to reflected and side-on pressure loading in pure Lagrangian approach

tion in ABAQUS to generate side-on and reflected overpressure loading curves by defining a TNT charge and stand-off distance. Taking Box200-7 in the gas detonation test as an example, the blast loading applied to the numerical model of the box as depicted in Figures 4.18c and 4.18d, which determined by Analytical blast and CONWEP methods are presented in Figure 4.19.

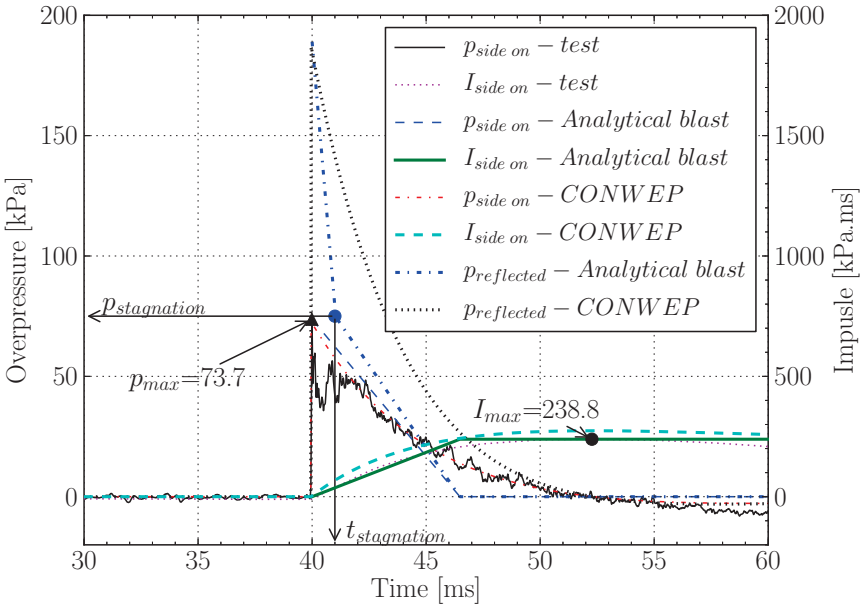


Figure 4.19: Load application in Lagrangian analysis (Box200-7, Transducer B11)

One of the key points in the numerical analysis is that the side on peak overpressure and effective specific impulse must always match between the test

measurements and numerical predictions. The overpressure profiles recorded by the transducer B11 is shown in Figure 4.19. The corresponding impulse time history determined by integration is also shown. The peak side-on overpressure and peak specific impulse were determined to be 73.7 kPa and 238.8 kPa.ms. The first step of the Analytical blast method in order to determine the reflected overpressure loading curve was to match the experimental peak side-on overpressure and impulse by a linear blast profile (right-angle triangle shape) as shown in Figure 4.19.

Using Equations 2.5 to 2.11 with the side-on peak overpressure the peak reflected overpressure was then determined. Subsequently the time $t_{stagnation} = \frac{3S}{U_x}$ and the corresponding dominating stagnation overpressure $p_{stagnation}$ were calculated using the same set of Equations. Finally the overpressure loading on the front face reduced to ambient pressure linearly at time t_d. The side-on dynamic loading curve was simply the matched triangle with the correct peak overpressure and the positive duration t_d.

Since the gas detonation produced ideal blast waves, CONWEP (an **?** function) can also be used to predict the dynamic loadings on the surface of the boxes. It has been determined by trial and error that a TNT charge of 90 kg with a stand-off distance of 14.2 m could produce a free-field (side-on) overpressure blast wave which is reasonably identical to the one registered by transducer B11. Both side-on and reflected overpressure loading curves predicted by CONWEP are shown in Figure 4.19. For completeness, equivalent TNT charges and stand-off distances that produce identical blast waves to the overpressure measurements from the gas explosion are presented below.

Table 4.5: Equivalent CONWEP definition of blast waves in gas detonation test

Box ID	Transducer	TNT weight (kg)	Stand-off distance (m)
Box200-1	B16	132	5.3
Box200-3	B9	427	11.7
Box200-5	B10	372	14.05
Box200-7	B11	90	14.2

It is worth noting that the CONWEP function was intended to be implemented as an automatic tool to apply blast load on the specified surface. In the

present study the blast load curves predicted by CONWEP were explicitly obtained by a simple model consists of one rigid element (with the same distances and TNT charges), and then applied manually to the surfaces of the box model. In such a way, the actual profiles of the dynamic loadings were known, which could contribute to a better understanding of the response of boxes.

4.2.2.1 Consideration of internal pressure

It has been observed in the experiments that in some cases the back face of the box was pushed outward due to the adiabatic compression of the air inside the box. The increase of the internal pressure caused deformation of the back face in the outwards direction. In addition, the interior face of the door was attached with polyurethane sealing gasket which would provide a good seal condition during the explosion. The internal pressure was then modelled to examine its effect on the response of the box to blast waves. In order to simulate the internal pressure

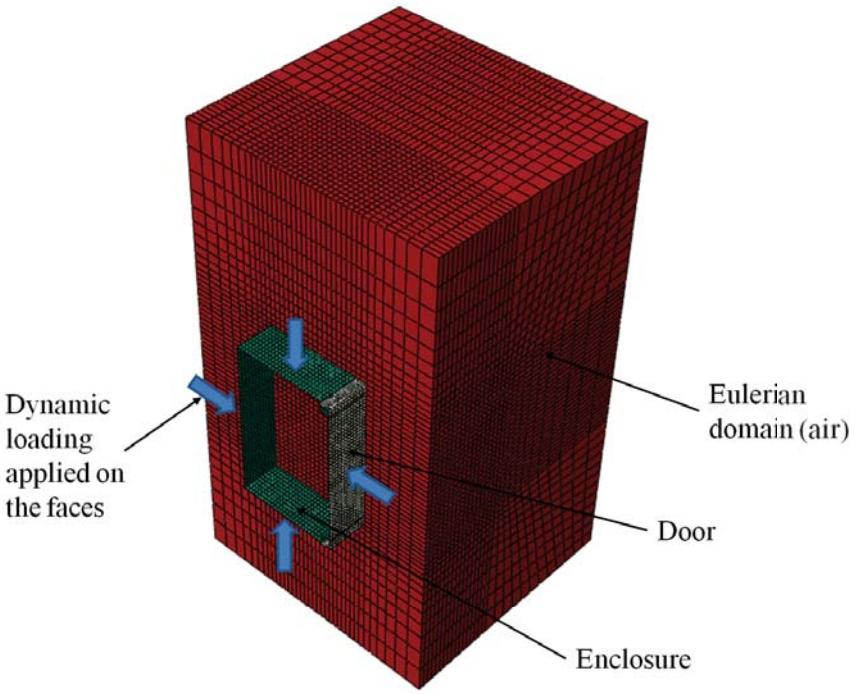


Figure 4.20: Modelling of internal pressure

in the Lagrangian approach, an Eulerian part representing the air inside and

around the box was added to the Lagrangian box model, as shown in Figure 4.20. ABAQUS general explicit contact algorithm will automatically implement the interaction between the box shell and the air Eulerian materials. Therefore the air inside of the box would be compressed by deformation of the box under the blast loading which was applied as uniform dynamic pressure directly on the surface of the box model.

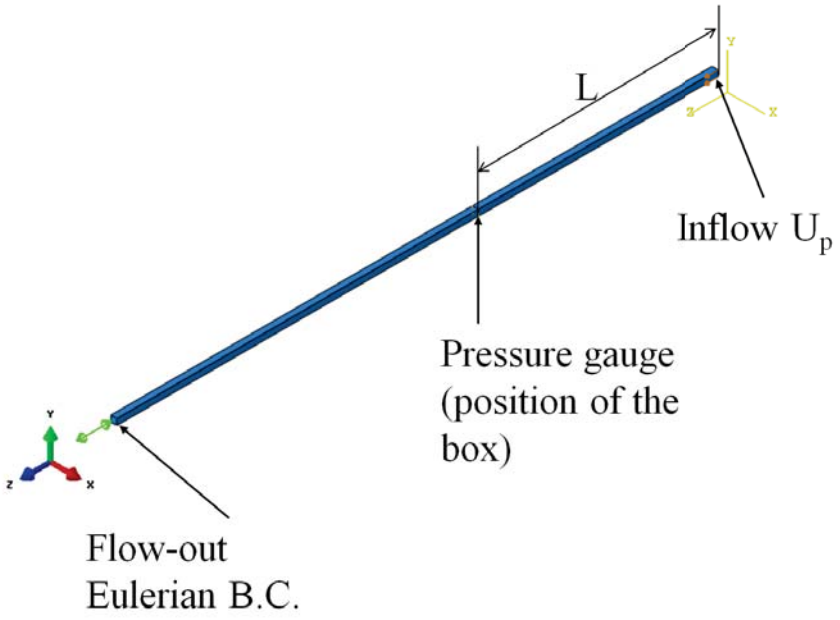
4.2.3 Uncoupled Eulerian - Lagrangian analysis

The Uncoupled Eulerian - Lagrangian approach has been briefly introduced in the previous section. This section presents the details of performing this type of analysis using Box200-7 in the gas detonation test as an example. As discussed above, this uncoupled analysis consists of two steps: (1) using a pure Eulerian model to determine blast loading on the surface of the target by treating it as rigid body; (2) performing a pure Lagrangian analysis to study the response by applying the previously determined blast loading on the surface of the flexible body.

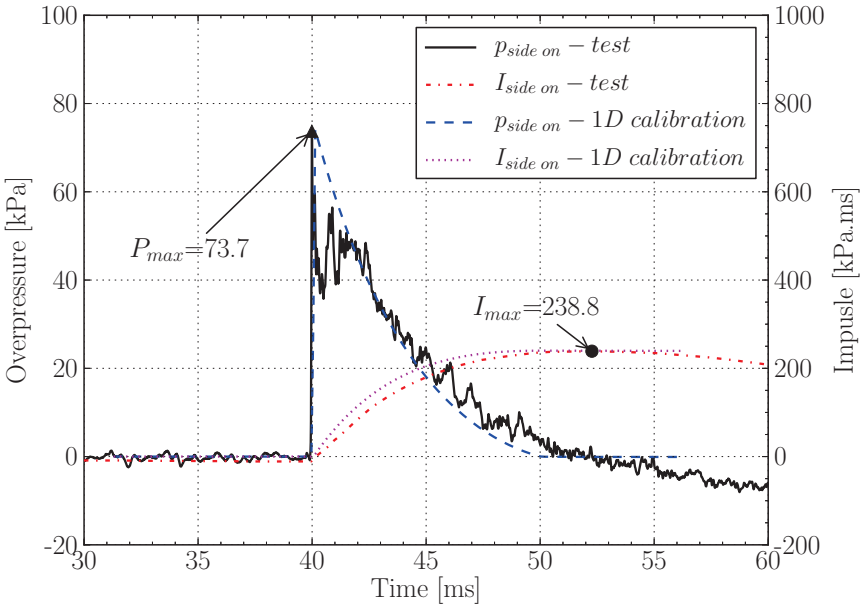
It was necessary to create a blast wave with desired parameters in the Eulerian domain which can be used in the Step 1. It was most efficient to performed this task with a one dimensional Eulerian model. The 1D calibration model is shown in Figure 4.21a. Length L was the distance that the created blast wave would travel and fully develop before reach the location of the target, it was defined as $L = local\ speed\ of\ sound \times positive\ duration\ of\ blast\ wave$. This can be briefly interpreted as the length of the blast wave. A numerical pressure gauge recording the incident overpressure wave was placed at the end of the length L, where is the location of the target. The blast wave was implemented by applying a flow particle velocity - time curve $U_p(t)$ at the inflow boundary, according to Equations 2.9. The applied inflow velocity has a similar form to the blast wave as shown in the Equation below:

$$U_p(t) = U_p \left(1 - \frac{t}{t_d}\right) \epsilon^{-\alpha t/t_d} \tag{4.1}$$

By varying the peak particle velocity U_p, positive duration t_d and the shape pa-



(a) 1D calibration model



(b) Comparison of results

Figure 4.21: Calibration of blast wave in Eulerian model

rameter α, i.e. trial and error, an overpressure blast wave with desired parameters can be created. Figure 4.21b shows the numerical blast wave created for Box200-7 (Transducer B11). It compares favourably with the test recording, both the peak overpressure and impulse values match well with the test data.

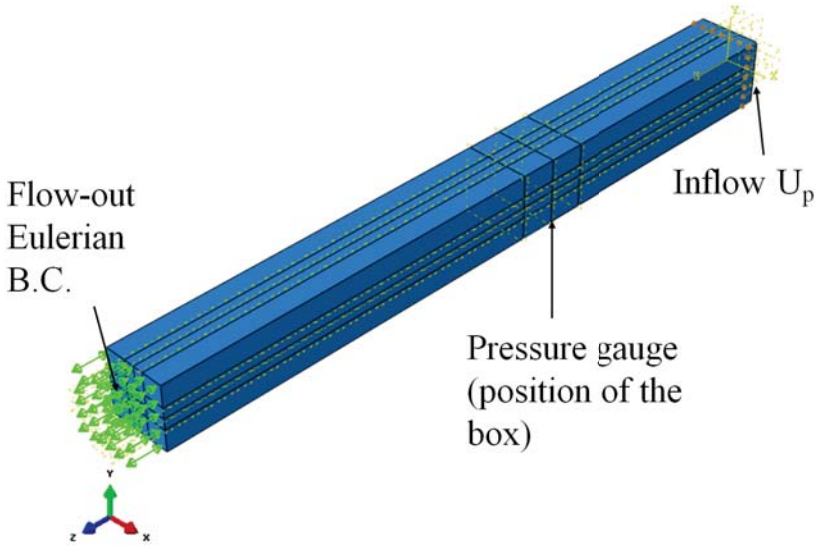
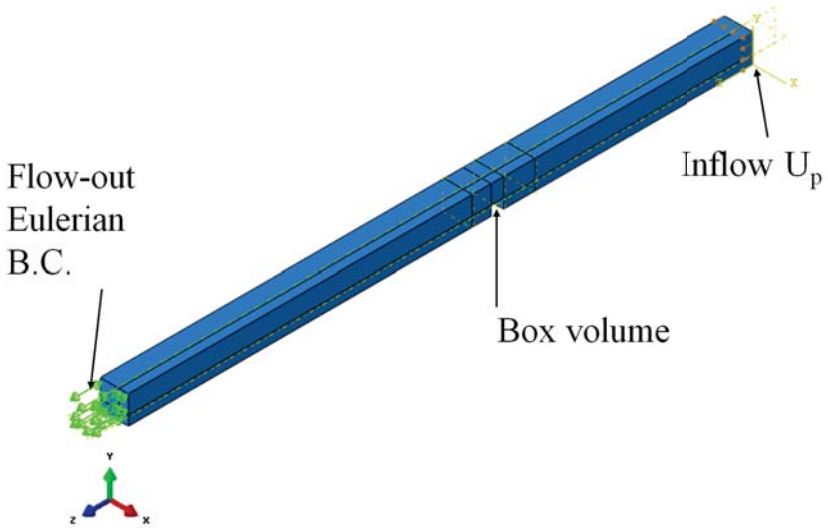


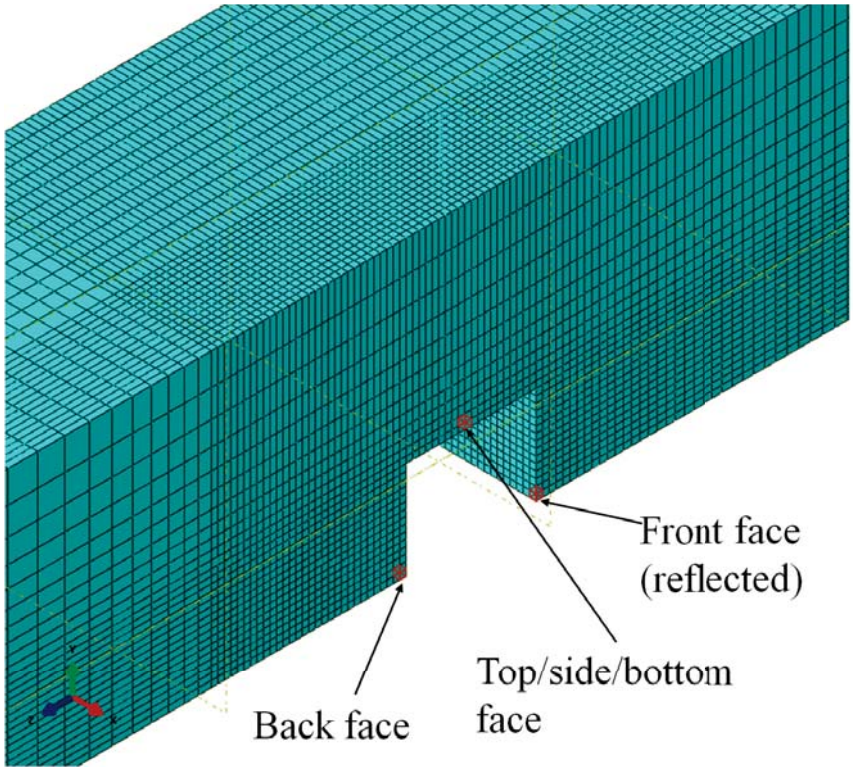
Figure 4.22: 3D Eulerian model

Then the step 1 of UEL analysis was commenced. The same inflow boundary condition was used in a full size 3D Eulerian model as shown in Figure 4.22. The incident overpressure blast at the location of the pressure gauge, as expected, was almost identical to 1D model and plotted in Figure 4.24 tagged with "side on (incident)". The 3D Eulerian model was then reduced into a quarter model by taking advantages of the symmetry and a empty volume was created at the position of the box to represent a "rigid" box, as shown in Figure 4.23a. Pressure gauges were then placed at the centre of the "rigid" faces as depicted in Figure 4.23b to record the overpressure histories and the results are shown in Figure 4.24.

In step 2 of the uncoupled analysis the previously determined overpressure loading curves shown in Figure 4.24 were then applied on the designated surface of the box model (shown in Figures 4.14 and 4.17) and the response were obtained in the same way as in a Lagrangian analysis. In UEL analysis the side-on (incident) overpressures was not used and only served as a reference. The internal pressure



(a) Model for pressure analysis



(b) Pressure gauges

Figure 4.23: A quarter of 3D Eulerian model for UEL analysis Step 1

has also taken into consideration in for Box200-7 by using the model described in Section 4.2.2.1.

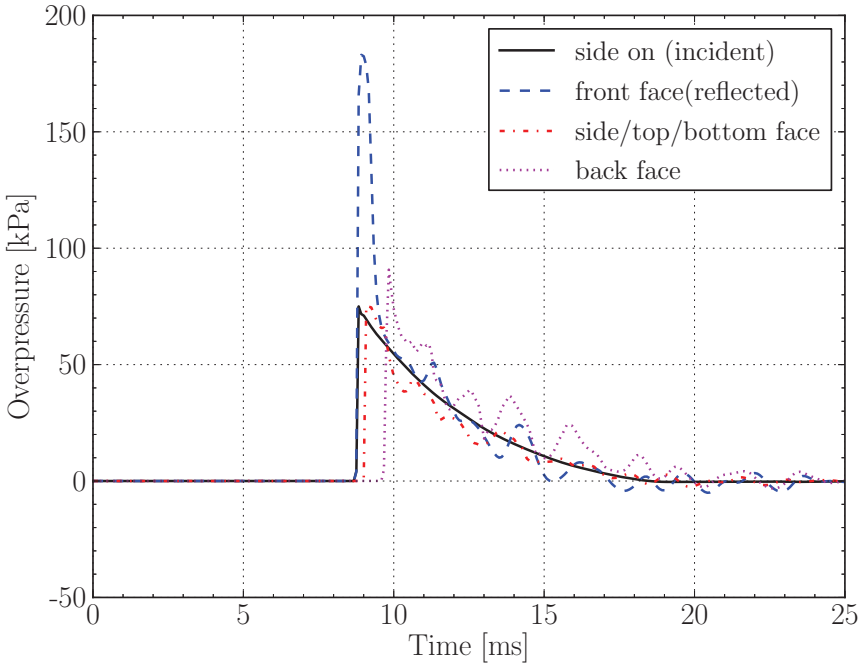


Figure 4.24: Overpressure loading curves for UEL analysis

4.2.4 Coupled Eulerian - Lagrangian analysis

Coupled Eulerian - Lagrangian analysis is the most complex method. The numerical model was created by adding a Lagrangian box model with correct support boundary conditions to the 3D Eulerian model shown in Figure 4.22. The box model was placed at the correct position so that it was exposed to the desired blast wave calibrated in the 1D model. Interaction between the Lagrangian shell elements and Eulerian air material was automatically implemented by the general explicit contact definition of **?**. A coupled Eulerian - Lagrangian model is shown in Figure 4.25, half of the Eulerian part is removed in order to show the box model placed within the Eulerian domain.

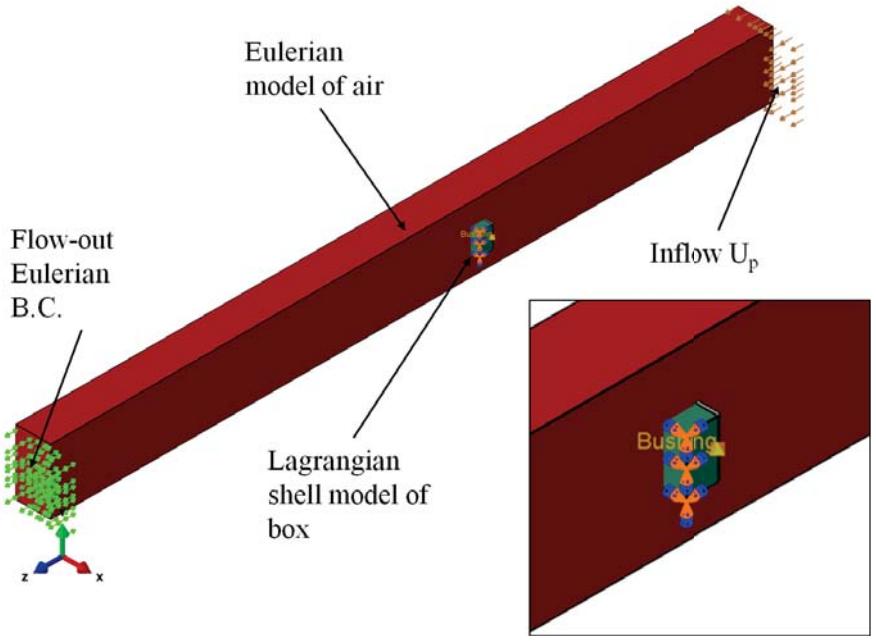


Figure 4.25: CEL numerical model

4.2.5 Comparison of computational demands

It was known that the coupled method (CEL) is much more computationally demanding than UEL and Lagrangian approaches. By taking Box200-5 in the gas test as an example (owning to the moderate damage on the front face), a brief comparison of simulation time for the three types of analysis discussed above is presented here. The simulation running times of a 30 ms numerical analysis for different approaches are listed in Table 4.6.

Table 4.6: Comparison of running time for different numerical approaches

Analysis type	Numerical model[1]	Running time[2]	Total time[2]
Lagrangian	Lagrangian	00:02:02	00:02:02
	Lagrangian with ip[3]	00:49:46	00:49:46
UEL	Step 1 Eulerian	00:45:01	-
	Step 2 Lagrangian	00:02:21	00:47:22
	Step 2 Lagrangian with ip[3]	00:45:19	01:30:20
CEL	Fully coupled	14:57:13	14:57:13

The Lagrangian approach only took 2 minutes for one analysis. It can be seen in Table 4.6 that by considering the internal pressure the running time was increased by 24 times. The Lagrangian step of the UEL approach took only 2 minutes but the Eulerian step required about 45 minutes, hence the total time for a UEL analysis was about 47 minutes which is 23.5 times the pure Lagrangian analysis (without internal pressure). Including the internal pressure in the UEL analysis would roughly double the running time. Apparently CEL approach was the most demanding, it required 897 minutes (15 hours) for one numerical analysis, which is more than 400 times the pure Lagrangian analysis and 19 times the UEL analysis, when internal pressure is not considered.

4.3 Comparative assessment

In the previous section, the numerical models used in different simulation approaches were presented. In this section, data from the experiments was used to study and validate the numerical models so that the most efficient and accurate approach can be used for the parametric studies.

In the following sections, numerical models are used to reproduce the overpressure blast waves recorded in the detonation tests. Numerical results of model Box200 are compared with the gas detonation test to validate the numerical models. Although only limited data were available from the TNT detonation test, the numerical results of Box150 can complement the study of the numerical approaches.

4.3.1 Comparison of numerical results

In order to validate the numerical models, results of simulation of Box200 were compared with the experimental data. Overpressure - time histories predicted by different approaches were compared with the recording from the four transducers to ensure that the numerical boxes were subjected to correct overpressure loading.

[1] all numerical models were implemented on High Performance Computers with 12 2.66 GHz Xeon cpus with total 12 GB Memory

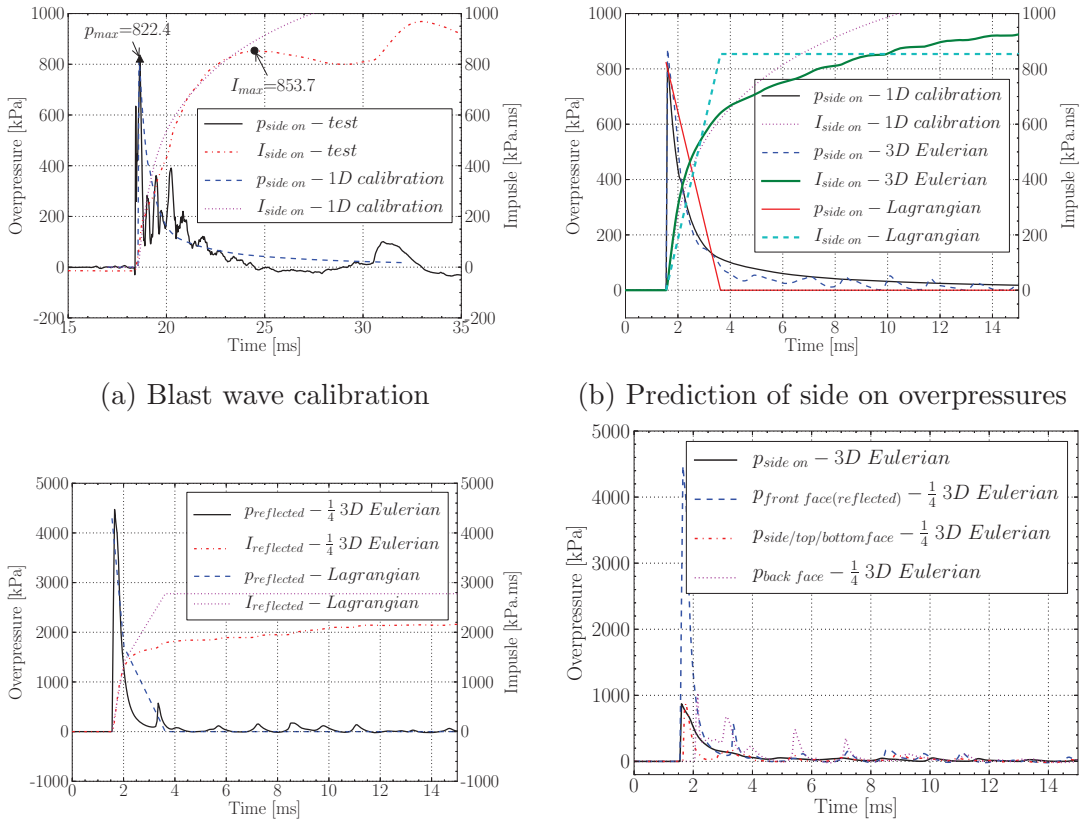
[2] time format hh:mm:ss

[3] "ip" for internal pressure

Deflections at the door centre were compared with the permanent deformation of scanned boxes and overall residual shapes were examined qualitatively.

4.3.1.1 Blast wave and dynamic loading

Three numerical approaches were used: Lagrangian, Uncoupled Eulerian - Lagrangian (UEL) and Coupled Eulerian - Lagrangian (CEL). In the Lagrangian model the overpressure blast load was predicted by empirical equations and referred to as Analytical blast. Since **?** includes the CONWEP function, it is worthy to study the accuracy of the numerical model using CONWEP load. The CONWEP load was only used in the study of response of Box200-7.



(a) Blast wave calibration

(b) Prediction of side on overpressures

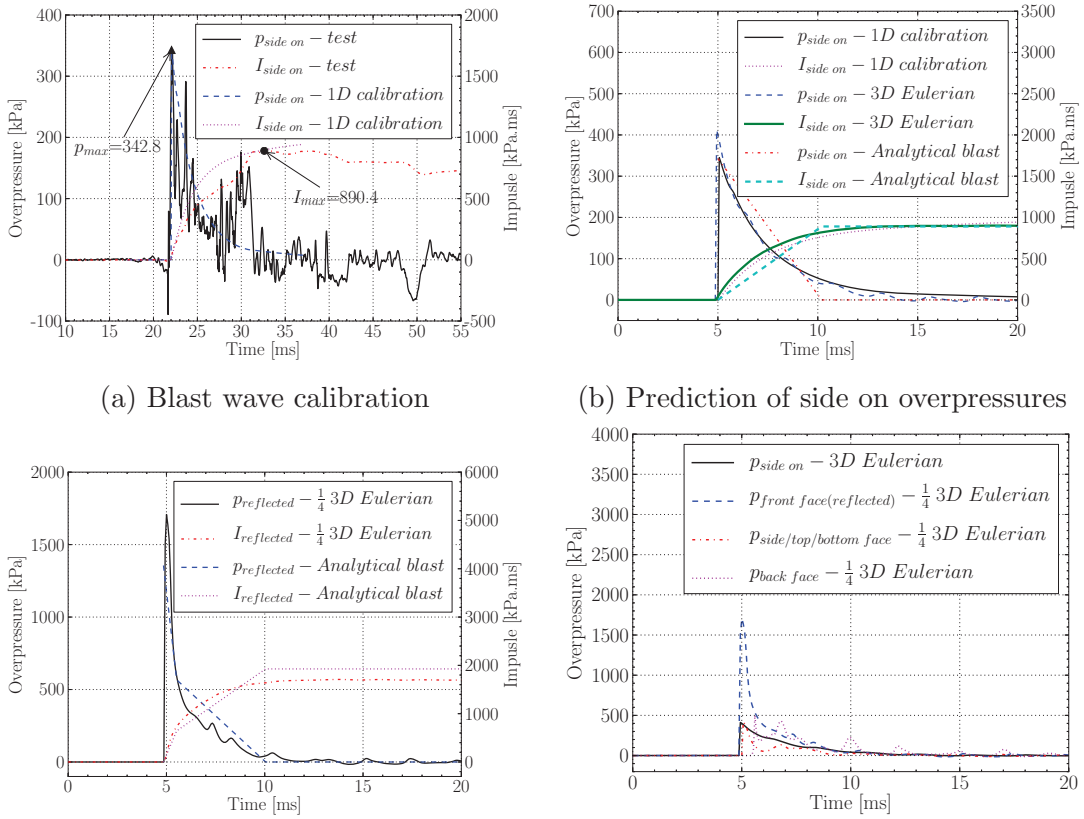
(c) Prediction of reflected overpressure

(d) Pressure loadings of UEL analysis

Figure 4.26: Numerical blast wave and loading results for Box200-1 (Transducer B16)

Numerical overpressure - time history and the corresponding dynamic load

for Box200-1 are presented in Figure 4.26. The calibrated side-on blast wave using the 1D Eulerian model (shown in Figure 4.21a) is compared with the test measurement in Figure 4.26a. The goal was to reproduce a numerical blast wave which has the same peak side-on overpressure and specific impulse at the correct location. However as it can be seen in the figure the experimental data had lots of noise so only the effective maximum impulse, which is shown in the figure, was matched by the numerical 1D blast wave.



(a) Blast wave calibration

(b) Prediction of side on overpressures

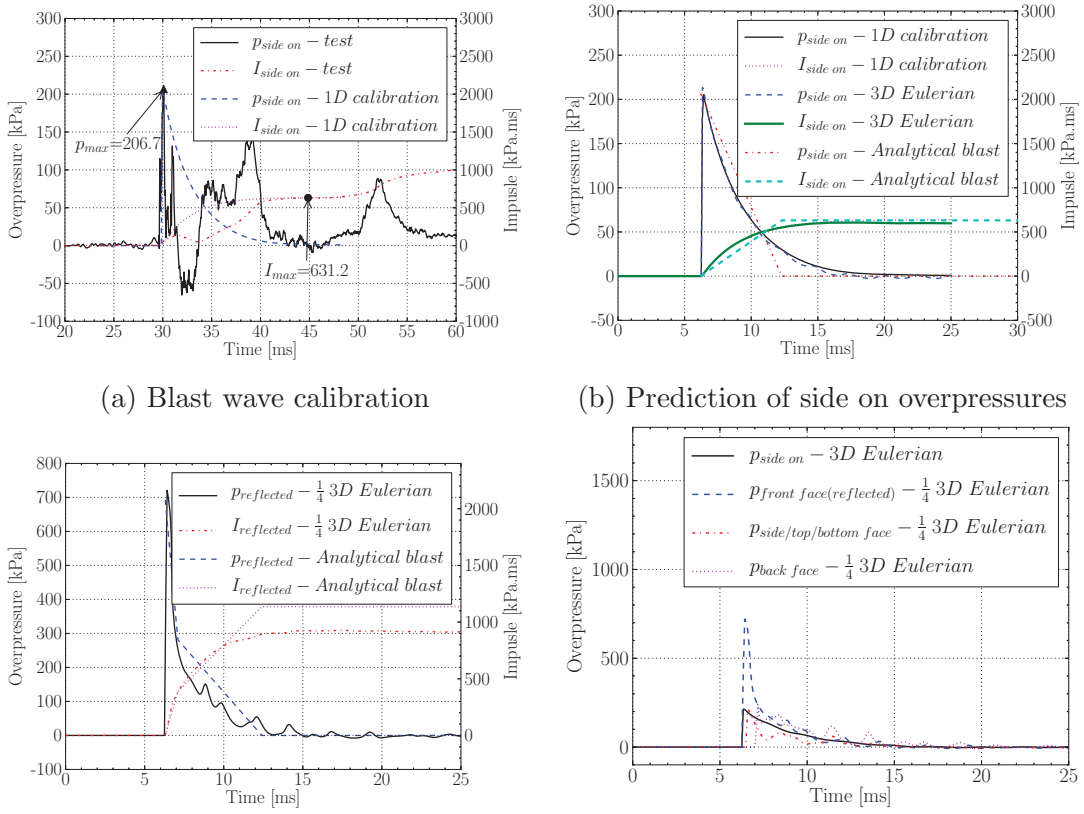
(c) Prediction of reflected overpressure

(d) Pressure loadings of UEL analysis

Figure 4.27: Numerical blast wave and loading results for Box200-3 (Transducer B9)

Once the 1D blast wave was determined, the inflow velocity boundary condition was then applied on the larger 3D Eulerian model (as seen in Figure 4.22). The results are shown in Figure 4.26b, in which the side-on overpressures predicted by 1D, 3D Eulerian model and analytical method (Analytical blast de-

scribed in Section 4.2.2) are compared. The comparison shows that the peak overpressures are almost identical between the different approaches and the corresponding impulses are well preserved.



(a) Blast wave calibration

(b) Prediction of side on overpressures

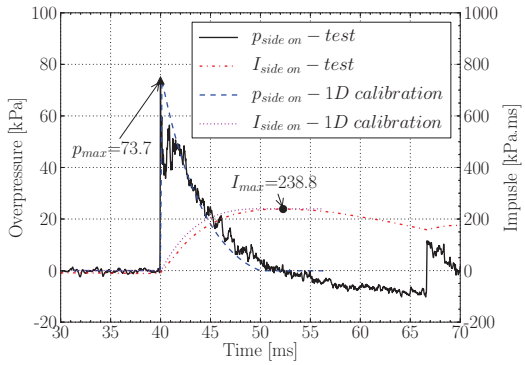
(c) Prediction of reflected overpressure

(d) Pressure loadings of UEL analysis

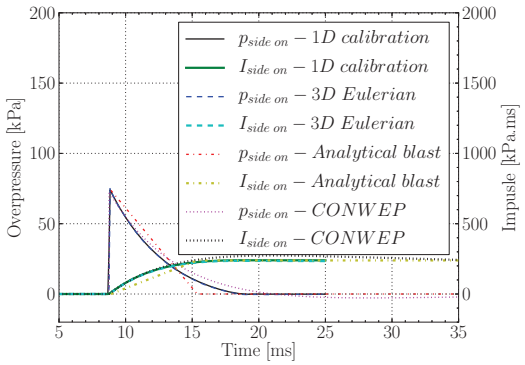
Figure 4.28: Numerical blast wave and loading results for Box200-5 (Transducer B10)

Figure 4.26c compares the reflected overpressures predicted by the one quarter 3D Eulerian model (shown in Figure 4.23) to the analytical method. Although the predicted peak reflected overpressure compare well, the impulses are different. The analytical blast produced greater impulse. This is attributed to (a) the time $t_s = 3S/u_x$ was approximate and (b) the stagnation pressure curve is assumed to be linear and conservative (i.e. based on the side-on overpressure curve using Equations 2.9 and 2.10). Figures 4.26b and 4.26c present the blast loadings used in the Lagrangian analysis (side-on and reflected loads of the Analytical blast).

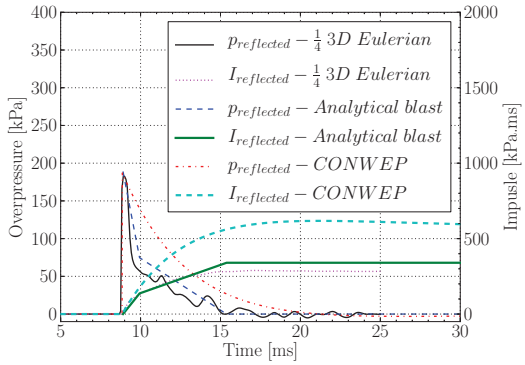
Figure 4.26d presents the blast loadings applied on the box model in the second step of the UEL approach. These curves were obtained by the pressure gauges depicted in Figure 4.23b. The side-on overpressure curve is shown here for reference. The other blast loading curves were assigned with subscripts to indicate which surface they were applied on as depicted in Figure 4.14 and 4.17. It can be noted that in the last figure there are small reoccurring peaks, these was due to the small dimension of the Eulerian domain which caused the reflection from the boundaries. Fortunately their magnitudes were relatively small and can be neglected.



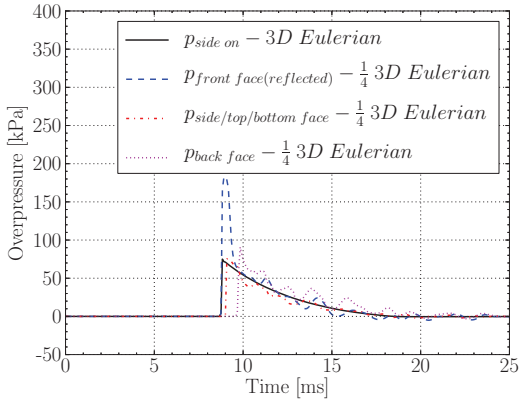
(a) Blast wave calibration



(b) Prediction of side on overpressures



(c) Prediction of reflected overpressure



(d) Pressure loadings of UEL analysis

Figure 4.29: Numerical blast wave and loading results for Box200-7 (Transducer B11)

Similarly, overpressure loading of model Box200-3 and Box200-5 are shown in Figures 4.27 and 4.28, respectively. It can be seen that the impulses were

preserved better at lower level of overpressures, while peak pressure values were matched reasonably well too. One exception is that for Box200-3 3D Eulerian model over-predicted the peak side-on and reflected overpressure values by 20% and 26% respectively compared with the analytical blast. Nonetheless, both side-on and reflected impulses did not differ significantly.

Table 4.7: Overpressure and impulse results of Box200 models

Unit $[p : kPa]$ $[I : kPa.ms]$		Box200-1	Box200-3	Box200-5	Box200-7
Test	$p_{side\ on-test}$	822.4	342.8	206.7	73.7
	$I_{side\ on-test}$	853.7	890.4	631.2	238.8
1D calibration	$p_{side\ on-1D\ calibration}$	816.3	344.9	205.3	74.1
	$I_{side\ on-1D\ calibration}$	890.3	897.8	637.1	239.9
CEL	$p_{side\ on-3D\ Eulerian}$	871.7	412.0	213.5	75.0
	$I_{side\ on-3D\ Eulerian}$	802.8	901.2	604.5	235.9
UEL	$p_{side\ on-3D\ Eulerian}$	871.7	412.0	213.5	75.0
	$I_{side\ on-3D\ Eulerian}$	802.8	901.2	604.5	235.9
	$p_{reflected-\frac{1}{4}\ 3D\ Eulerian}$	4472.5	1707.7	720.7	183.1
	$I_{reflected-\frac{1}{4}\ 3D\ Eulerian}$	2160.2	1709.2	927.3	289.2
	$p_{s/t/b\ face-\frac{1}{4}\ 3D\ Eulerian}$[1]	882.6	421.9	212.3	75.4
	$I_{s/t/b\ face-\frac{1}{4}\ 3D\ Eulerian}$[1]	404.8	483.6	374.9	201.9
	$p_{back\ face-\frac{1}{4}\ 3D\ Eulerian}$	1010.2	498.8	240.9	90.8
	$I_{back\ face-\frac{1}{4}\ 3D\ Eulerian}$	738.9	1008.7	692.3	256.9
Lagrangian Analytical blast	$p_{side\ on-Analytical\ blast}$	822.4	342.8	206.7	73.7
	$I_{side\ on-Analytical\ blast}$	853.7	890.4	631.2	238.8
	$p_{reflected-Analytical\ blast}$	4294.2	1355.8	693.3	189.0
	$I_{reflected-Analytical\ blast}$	2776.9	1926.7	1136.1	340.0
Lagrangian CONWEP	$p_{side\ on-CONWEP}$	-	-	-	72.6
	$I_{side\ on-CONWEP}$	-	-	-	274.1
	$p_{reflected-CONWEP}$	-	-	-	186.9
	$I_{reflected-CONWEP}$	-	-	-	617.7

Another issue which has already been pointed out is the distorted test overpressure profile shown in Figures 4.27 and 4.28. Since they are placed near the small car in the explosion, the overpressure might been affected by the turbulence and reflection generated from the car. As a result, the overpressure profiles had shock front leading the blast wave but the shapes were not typical of an ideal

[1] $p_{s/t/b}$ is abbreviation for $p_{side/top/bottom}$

blast wave. Although the peak effective impulses were well preserved, the impulse - time histories significantly differed from the numerical prediction, particularly for the model Box200-5.

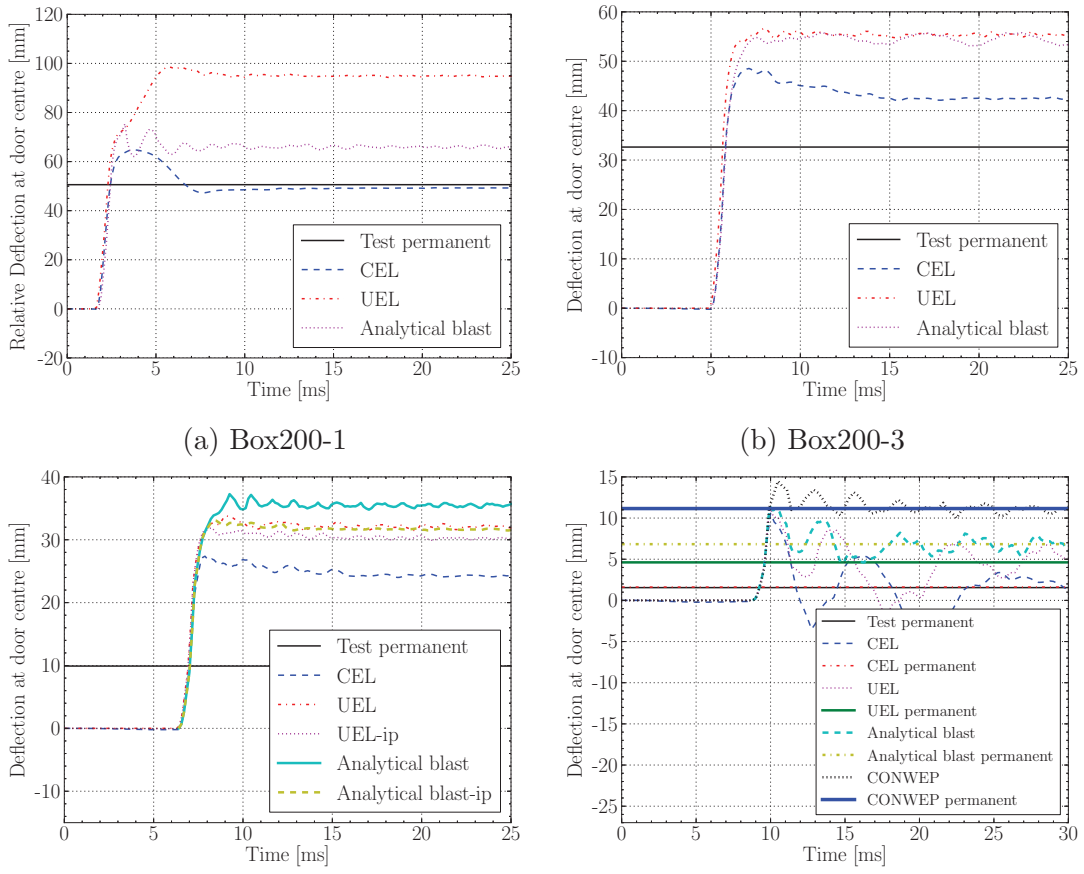
Numerical overpressure loading in the simulation of the mode Box200-7 is presented in Figure 4.29, including the blast curves predicted by CONWEP. Similar to the other boxes, the peak side-on overpressures were matched and impulses were preserved for all three numerical approaches. Here two box models were used in the pure Lagrangian analysis, one was subjected to the analytical blast load and the other was subjected to the CONWEP blast load.

As already shown, using trial and error the detonation blast curve recorded at the location of Box200-7 can be related to a TNT charge with a specific stand-off distance (refer to Table 4.5). The CONWEP load therefore is compared with results from 3D Eulerian and analytical blast in Figures 4.29b and 4.29c. All predicted side-on overpressure curves have identical peak pressure values and the impulses are well preserved. For the reflected overpressure curves, peak reflected values were compared favourably but impulses differed significantly. Analytical method over-predicted the reflected impulse by 17.6% comparing to the 3D Eulerian model, while CONWEP over-predicted twice the reflected impulse of the Eulerian model. This substantial difference was due to that the CONWEP function in **?** did not consider the pressure relief effect caused by the rarefaction wave propagating from the edge of the faces. It effectively treated the target reflection face as an infinite surface.

Overpressure and impulse time histories from numerical models were presented above. The blast loading results were discussed in detail and compared with experimental data. In order to have an overview of all the pressures and impulses, the peak overpressure values and effective maximum impulses corresponding to each curve shown in the Figures 4.26 to 4.29 are listed in Table 4.7. This table allows direct comparison of overpressure and impulse between the test and the numerical approaches. It also includes the peak overpressure values and maximum impulses applied to the surfaces of the box model in the second step of uncoupled Eulerian - Lagrangian (UEL) approach. However, these data were not available for model Box200-1, Box200-3 and Box200-5, as CONWEP load has not been used for the three box models.

4.3.1.2 Box response to gas detonations

Following the discussion of numerical results of the overpressure loading from different simulation approaches, this section presents the response of the box models to the above overpressure loading. Experiment results indicated that the damages are dominated by the crushing of the front face (i.e. the box door), while the enclosure of the boxes were suffered moderate to minor damages. The focus of this study was then placed on the damage to the front face. The displacement - time histories at centre of the door predicted by various numerical approaches are presented in Figure 4.30.



(a) Box200-1

(b) Box200-3

(c) Box200-5

(d) Box200-7

Figure 4.30: Displacement - time histories of box front face centre

As shown in Figure 4.13 the permanent deformation of the front face is mea-

sured from the edge of the door. In order to make meaningful comparison with experimental data, it is necessary to use relative deflections of the door centre. Displacement - time histories at two locations as shown in Figure 4.17a were obtained, thus the time histories of the displacement shown in Figure 4.30 were taken at the centre of the door relative to the middle of the edge of the door. Relative maximum and permanent deformations at the centre of the door are listed in Table 4.8 for a quantitative assessment.

Table 4.8: Displacements of front face centre for Box200 models

disp [mm] (time) [ms]	Box200-1		Box200-3		Box200-5		Box200-7	
	δ_{max}	δ_{perm}	δ_{max}	δ_{perm}	δ_{max}	δ_{perm}	δ_{max}	δ_{perm}
Test	-	50.59	-	32.63	-	9.91	-	1.55
CEL	64.84 (2.0) [1]	49.21	48.54 (2.0)	42.43	27.39 (1.2)	24.28	10.58 (1.0)	1.62
UEL	98.48 (3.9)	94.89	56.66 (2.9)	55.41	33.80 (2.5)	32.09	10.85 (1.0)	4.62
UEL-ip	-	-	-	-	31.91 (1.8)	30.24	-	-
Analytical blast	75.37 (1.4)	65.95	55.82 (2.3)	54.47	37.27 (2.7)	35.48	11.32 (1.1)	6.83
Analytical blast-ip	-	-	-	-	33.12 (1.8)	31.64	-	-
CONWEP	-	-	-	-	-	-	14.49 (1.5)	11.16

It is clearly shown in Figure 4.30 and Table 4.8 that among the three numerical modelling approaches the coupled Eulerian - Lagrangian method is the most accurate one comparing with the experimental permanent deformation. Results of the CEL approach of Box200-1 and 7 are in very good agreements with the test measurements. In the case of Box200-1, CEL approach only under-predicted the permanent deformation by 2.7% and for model Box200-7 the result was over-predicted by 4.5%. However, the error of CEL approach increased to 30% and 145% for model Box200-3 and Box200-5 respectively. These discrepancies, particularly for Box200-5, can be explained by the distorted experimental side-on overpressure blast waves. It has been indicated that the blast waves might be

[1] the time to reach dynamic maximum displacement (δ_{max}), unit: ms

influenced by the presence of the small car near the transducer B9 and B10. The corresponding overpressure profiles are shown in Figures 4.27a and 4.28a.

It is evident that these two experimental pressure curves do not have typical shapes and the corresponding impulse curves differed significantly from the numerical predictions (a typical shape of an ideal blast wave). Although the numerical peak side-on overpressures and maximum effective impulses were the same as the test recording, the time histories were significantly different. Table 4.8 shows that it took 1 - 2 ms for the the centre of the front face to reach maximum displacement. The duration of the side-on overpressure waves are in the range of 10 ms. The blast loadings were dynamic/quasi-static thus the shape of the blast wave profiles are important to the response of the box. It is very likely that these two distorted side-on detonation overpressures in the gas cloud test produced much lower damage to the front face of the boxes (Box200-3 and Box200-5) compared with typical ideal blast waves with the same magnitudes of overpressure and impulse.

In the study of response of the boxes, the reflected overpressure was the most influential factor since the damage is dominated by crushing of the front faces. When presenting the overpressure results in the last section the reflected overpressures were compared only among the numerical approaches. This comparison helped to understand how the front face of the box would respond in different numerical approaches (i.e. under various predicted overpressures). It should be noted that the blast loading determined by the analytical method was more violent than the 3D Eulerian model. With the same level of peak reflected overpressure the analytical blast produced larger impulse. Hence referring to the responses of Box200-5 and Box200-7, it can be seen that the deflections predicted by analytical blast were greater than the UEL method.

However, it was not the case for Box200-1 and Box200-3. In Figure 4.30a the response from UEL approach is greater than the analytical method. The results are misleading since in both approaches the front faces have made contact with the back panel so that the relative deformations at the door centre are meaningless due to the contact, as shown in Figure 4.31. When the front face was not in contact with the back panel in the case of Box200-3, the responses are approximately the same for analytical and UEL approaches. This might be

attributed to that the reflected peak overpressure predicted in the UEL approach by the 3D Eulerian model was 26% higher than the analytical blast but with 11% less impulse. This is due to the combination of the discrepancies in the peak reflected overpressure and the impulse.

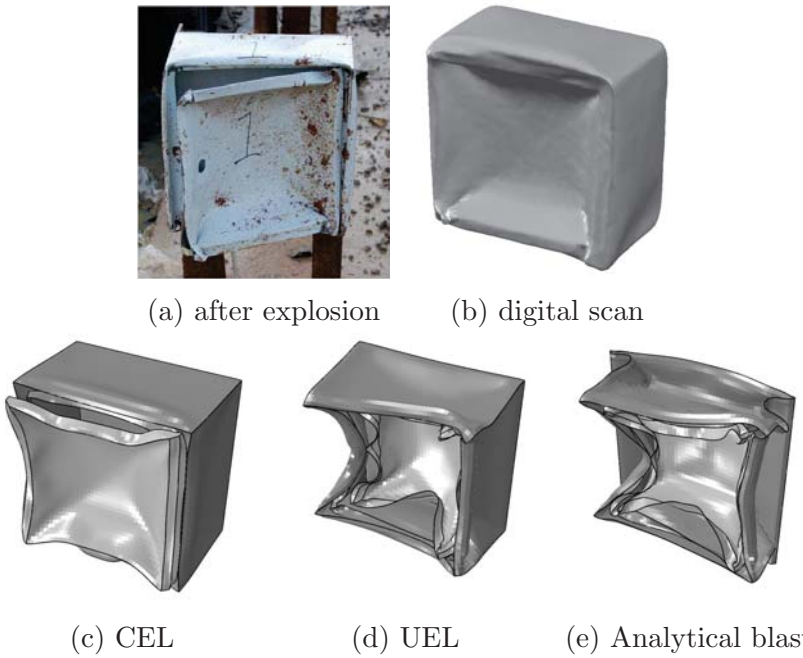
As shown in Figure 4.30c, the response predicted by different approaches has the order: analytical > UEL > CEL. Moreover, in this box model the effect of internal pressure (model depicted in Figure 4.20) was studied in the UEL and analytical approaches. When considering the internal pressure, the permanent deformation was reduced by 5.5% and 11.1% for UEL and analytical approaches, respectively. The reduction was only moderate and there was still about 20% difference compared with the CEL method. This suggests that the method proposed to take into account the internal pressure is not very effective. And the running time increased substantially (25 times longer) when considering the internal pressure in the UEL and Lagrangian approaches, as shown in Table 4.6. Thus to include the internal pressure is excluded for the following parametric studies.

Response of box to blast loadings determined by CONWEP was studied by the model Box200-7 and results are shown in Figure 4.30d. The CEL approach produced the most comparable permanent deformation to the experiment, while UEL and analytical methods over-predicted by 198% and 340%, respectively. However despite the substantial discrepancies in the permanent deformation, the maximum dynamic deflections predicted by the UEL and analytical methods were in good agreement with the CEL approach, where the differences were only 2.5% and 6.9% respectively. It can be observed that the maximum dynamic deflections predicted by three numerical approaches were in good agreement with each other when the damage was minor. However, large discrepancies exist in the permanent deformation. This is partly due to that the permanent deformation is small and any slight different would result in a large discrepancy in terms of percentage. The first rebound of UEL and analytical methods were less than the CEL, this was somewhat similar to the observation in the results from the general validation work of the square plate subjected to close range high explosive loading (first rebound of the UEL approach was much less than the CEL approach). It was also found that the response of the door to CONWEP loading was much

greater than other approaches. Comparing with the CEL results, CONWEP over-predicted the maximum deflection by 37% and permanent deformation by 620%.

The above paragraphs presented a quantitative assessment of the response of the front face of the box to blast loadings determined by various methods. A qualitative assessment of the damages is presented in the following paragraphs. Residual shape of the numerical boxes determined by the three simulation approaches were compared with the digital scan of the experimental boxes. Photos of the test boxes after explosion are also presented.

Residual shapes of the model Box200-1 are shown in Figure 4.31 and compared with the damaged test box. It is evident that the UEL and analytical method are not able to produce qualitatively comparable results, as the front faces were in contact with the back panels. On the other hand, CEL approach produced a rather good residual deformation. The front faces was pushed inwards, while the side walls of the enclosure were slight deformed outwards. The deformation was compared favourably with the damaged boxes in a qualitative point of view.



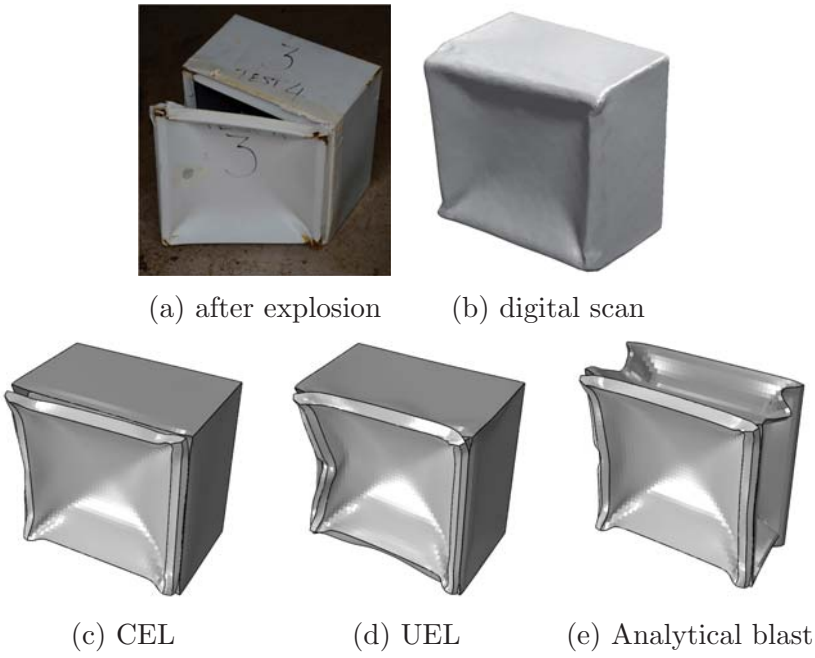
(a) after explosion (b) digital scan

(c) CEL (d) UEL (e) Analytical blast

Figure 4.31: Comparison of residual shapes of Box200-1

Similarly, the residual results of the model Box200-3 are presented and com-

pared in Figure 4.32. The CEL approach produced the most qualitatively comparable permanent deformation as well, and the damage was dominated by crushing of the front face and minor outwards deformation was observed on the side face. Residual deformation from both UEL and analytical approach was less comparable with the actual damaged box, the front face was severely pushed inwards in the UEL approach, while the side walls of the enclosure were buckled under the analytical blast loads. The buckling was actually due to the assumption which was used in the analytical blast. The side-on overpressure curve was applied on the side, top, bottom and back faces of the numerical model in the pure Lagrangian approach (analytical blast). The side-on impulse was determined to be 890.4 kPa.ms while in the UEL approach of Box200-3 the impulse was only 421.9 kPa.ms. With similar peak overpressure values the analytical blast produced more damage to the walls of the enclosure due to greater impulse (refer to Table 4.7 for peak overpressures and impulses applied on the box model faces in different approaches).



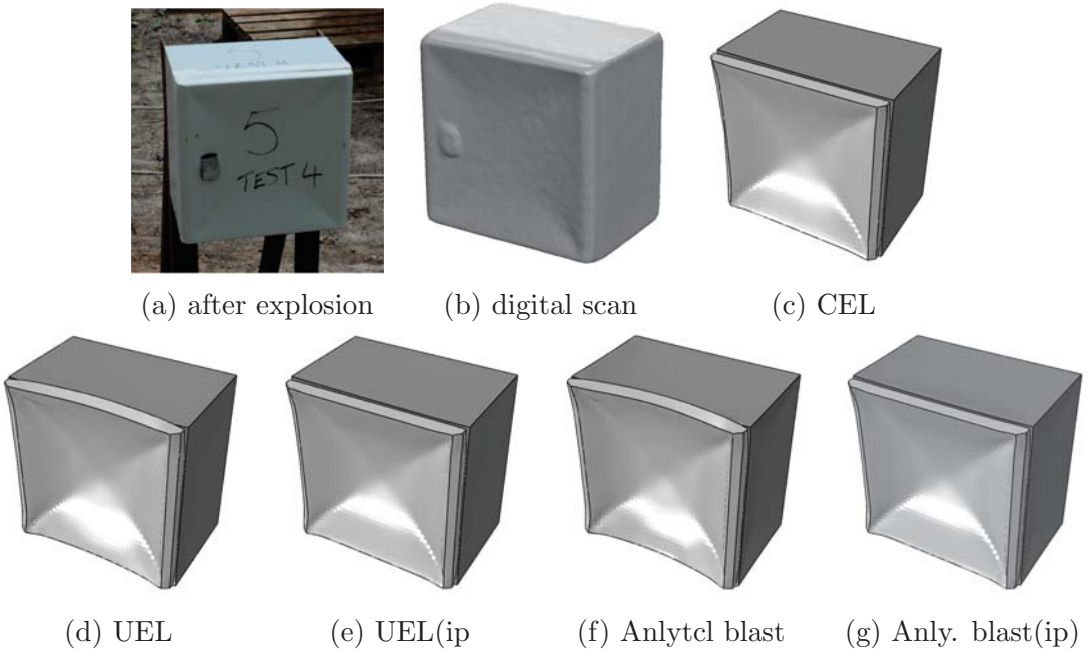
(a) after explosion (b) digital scan

(c) CEL (d) UEL (e) Analytical blast

Figure 4.32: Comparison of residual shapes of Box200-3

Residual shapes of the model Box200-5 and 7 are presented in Figure 4.33 and 4.34. Qualitatively the results were all comparable to the damaged box,

due to the overall minor damage. Only the front face was slightly deformed inwards and no damages were observed at the walls of the enclosure. The only differences between the numerical results were the magnitude of the deformation at the front faces which has been discussed (mainly due to impulses) before and can be observed in the figures.

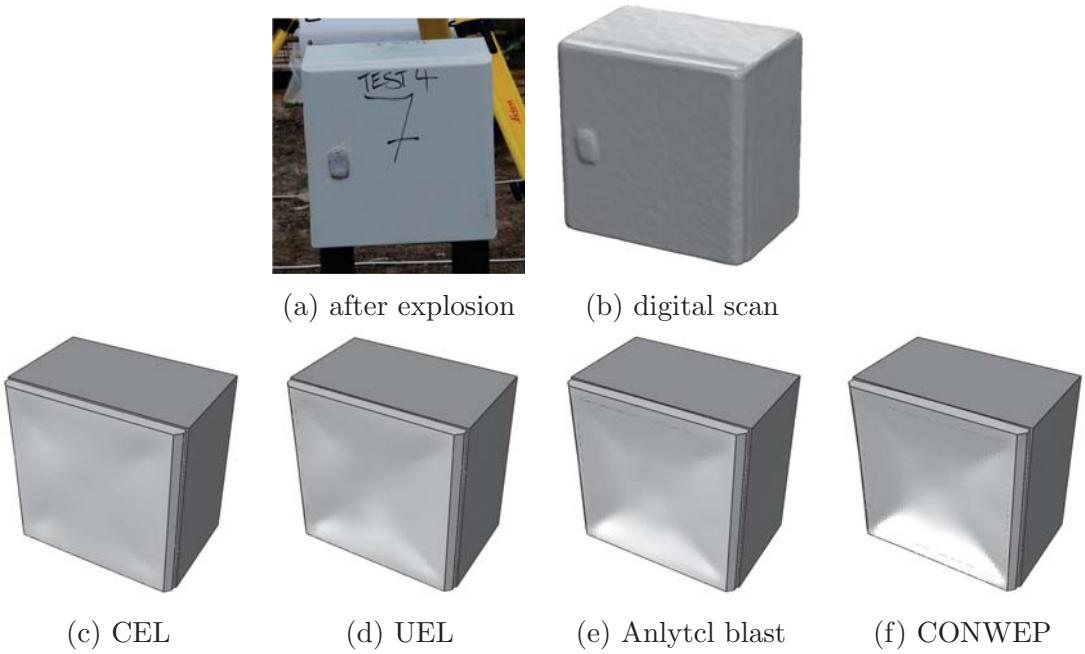


(a) after explosion (b) digital scan (c) CEL

(d) UEL (e) UEL(ip (f) Anlytcl blast (g) Anly. blast(ip)

Figure 4.33: Comparison of residual shapes of Box200-5

In this section, the numerical results from three simulation approaches were discussed in detail. They were compared and assessed quantitatively and qualitatively against available experimental data which were gathered from the gas cloud detonation test. It has been shown that the coupled Eulerian - Lagrangian method can produce accurate results in the analysis of boxes subjected to blast loading, but its application can be limited by the computational demands. The pure Lagrangian (with Analytical blast) method was far more efficient in terms of computation but its accuracy cannot be guaranteed. Based on the coupled Eulerian - Lagrangian method, further studies of the pure Lagrangian method have been carried out to justify its application.



(a) after explosion (b) digital scan

(c) CEL (d) UEL (e) Anlytcl blast (f) CONWEP

Figure 4.34: Comparison of residual shapes of Box200-7

4.3.2 Model selection for parametric studies

It has been reasonably established that the coupled Eulerian - Lagrangian (CEL) approach can accurately predict the responses of the box subjected to high overpressure blast loading. The efficiency of the pure Lagrangian model (with Analytical blast) makes it an ideal candidate for parametric studies. In this section, numerical model Box150 is used in the three simulation approaches based on the TNT explosion test. It is aiming to further study the accuracy of the pure Lagrangian method based on the validated CEL approach. Photos taken from the TNT detonation test are used to qualitatively assess the numerical results. Box150 is more representative of the boxes found in Buncefield site, therefore subsequent results can be used directly to examine the damaged boxes in the Buncefield. Four TNT detonation test have been carried out as described in previous section, two extra cases were defined in order to investigate the response of the box to blast loading with side-on overpressure between 2 and 4.7 bar. The four tests plus two extra cases with overpressure of 3 and 4 bar are presented in Table 4.9.

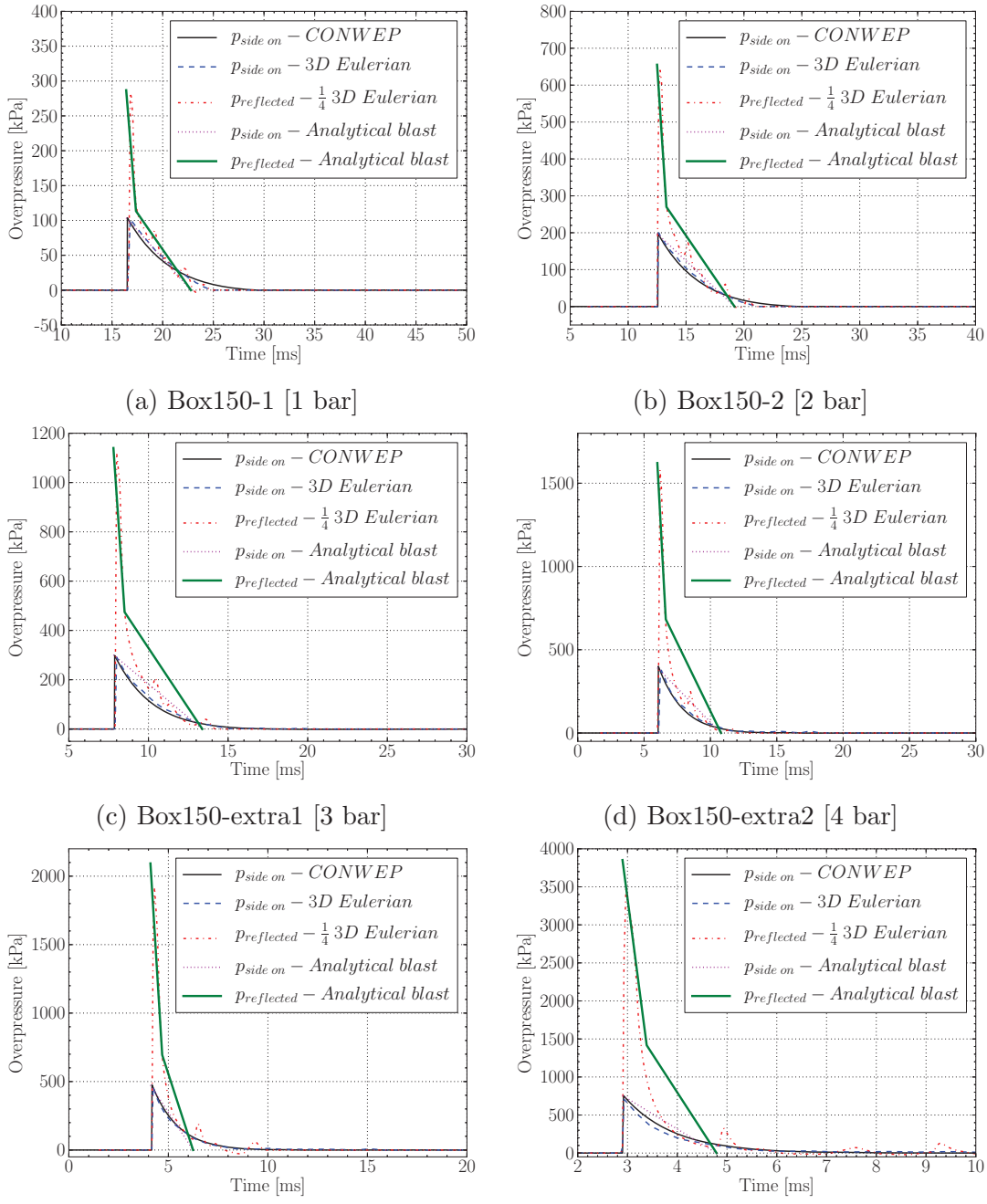
Table 4.9: Model Box150 subjected to TNT explosions

Box ID	W_{TNT} (kg)	Stand-off (m)	Peak $p_{side\ on}$ (kPa)	$p_{side\ on}$
Box150-1	130	13.5	103.8	1 bar
Box150-2	262	13	197.7	2 bar
Box150-extra1	192	9.5	298.5	3 bar
Box150-extra2	183	8.2	400.8	4 bar
Box150-3	90	6.5	475.5	4.8 bar
Box150-4	97.2	5.0	754.5	7.5 bar

Although overpressure - time curves of the blast waves experienced by the boxes during the TNT test were not available, the weight of TNT charge and stand-off distance were adequate for the current analysis. This is because (1) the parameters of blast wave produced by TNT explosive is well characterised by the empirical tools (e.g. CONWEP) and (2) there were no large objects near the charge nor the test boxes thus the overpressure profiles are less likely to be affected. Although it has been shown that the response of the box front face was over-predicted using the reflected overpressure loading determined by CONWEP, the side-on blast wave defined by the CONWEP are well comparable with the experiments. In the absence of experimental incident overpressure profiles, the side-on blast wave predicted by CONWEP based on the TNT charges and stand-off distances were used as the standard of the calibration of the blast wave used in the numerical modelling. It was assumed that all faces other than the front were subjected to side-on blast loadings for simplicity in the UEL approach.

The overpressure blast loading predicted by the three numerical approaches in the six TNT explosion cases listed in Table 4.9 are presented in Figure 4.35. The idea was the same to the modelling of boxes in the gas detonation test. The side-on blast waves of the numerical approaches were calibrated against the CONWEP side-on overpressure curves, in order to match the peak pressure value and preserve the impulse. Then the reflected overpressures were determined by the $\frac{1}{4}$ 3D Eulerian model and Analytical method as described above. The overpressure loading applied to the front (reflected) and other faces (side-on) of the box model (Box150) were all determined.

The time histories of the response of the centre of the box front face under



(a) Box150-1 [1 bar]

(b) Box150-2 [2 bar]

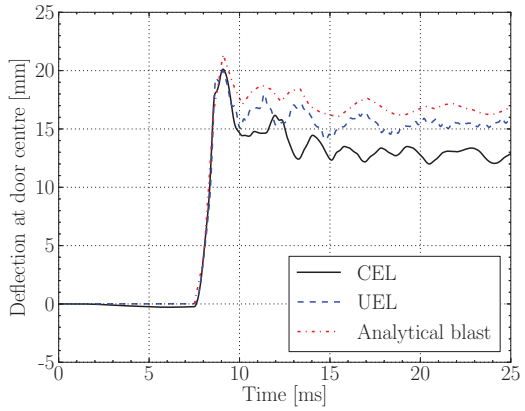
(c) Box150-extra1 [3 bar]

(d) Box150-extra2 [4 bar]

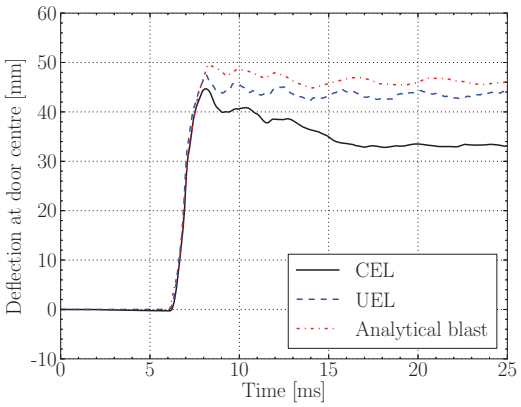
(e) Box150-3 [4.7 bar]

(f) Box150-4 [7.5 bar]

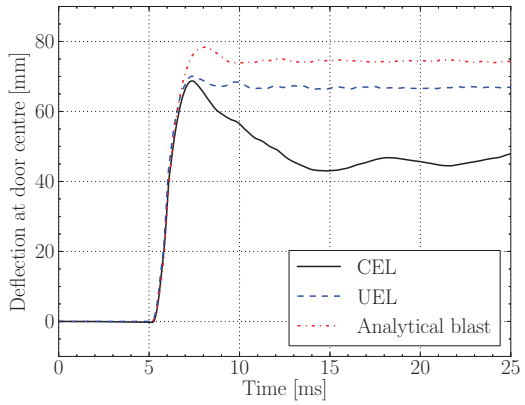
Figure 4.35: Numerical results of overpressures for TNT explosions



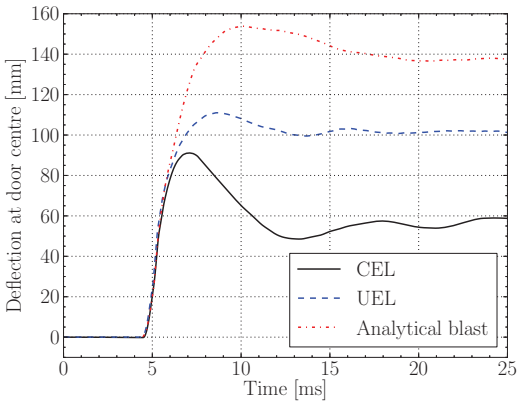
(a) Box150-1 [$p_{side\ on}$=1 bar]



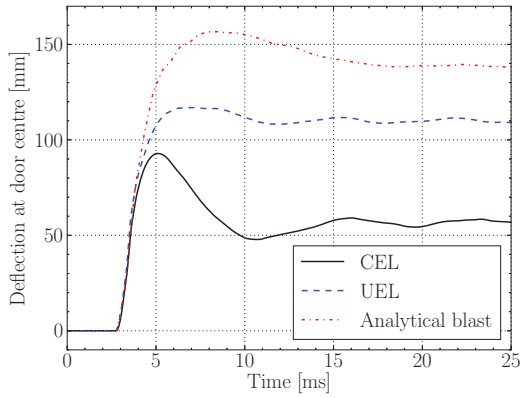
(b) Box150-2 [$p_{side\ on}$=2 bar]



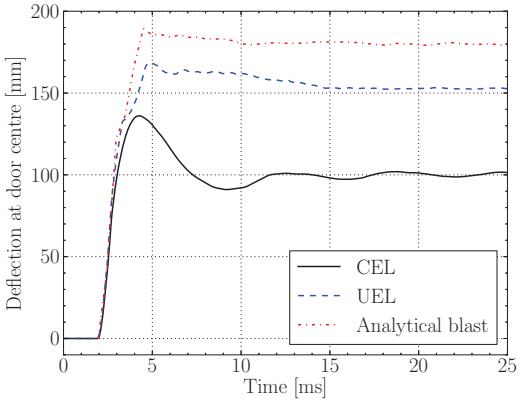
(c) Box150-extra1 [$p_{side\ on}$=3 bar]



(d) Box150-extra2 [$p_{side\ on}$=4 bar]



(e) Box150-3 [$p_{side\ on}$=4.7 bar]



(f) Box150-4 [$p_{side\ on}$=7.5 bar]

Figure 4.36: Numerical results of displacements for boxes in TNT explosions

different blast loadings determined by various approaches are shown in Figure 4.36. It must be noted that the absolute deflections were used for the numerical model Box150, i.e. the deformation was measured from the original location of the centre of the front face, not relative to the edge like the relative measurement taken for Box200. Results of the UEL and Lagrangian (analytical blast) methods were compared with CEL model. The CEL approach has been proved to be reliable in predicting the response of the boxes. The side-on overpressure ranges from 1 to 7.5 bar. Generally, the error of the UEL and Lagrangian approaches increase with the increasing peak overpressures and results of the UEL approach were always better than the Lagrangian model. Maximum deflections of the UEL and Lagrangian (Analytical blast) models were more comparable to the CEL approach than the permanent deformations. It should be noted that at and beyond the side-on peak overpressure of 4 bar, the deflection of front face under analytical blast exceeded 150 mm and made contact with the back face of the box. These are clearly not consistent with the predictions from CEL model. However at lower overpressure levels, Lagrangian and UEL models were compared reasonably well to the CEL model, particularly for maximum deflections.

Table 4.10: Numerical results of displacements of Box150 door centre

Box ID	Displ (mm)	CEL	UEL	Analytical blast	$p_{side\ on}$
Box150-1	δ_{max}	20.12(1.43[1])	20.01	21.39	1 bar
	δ_{perm}	12.98	15.46	16.84	
Box150-2	δ_{max}	44.68(1.85)	47.52	49.6	2 bar
	δ_{perm}	33.99	43.49	46.14	
Box150-extra1	δ_{max}	68.72(2.07)	70.06	78.43	3 bar
	δ_{perm}	45.28	66.77	74.55	
Box150-extra2	δ_{max}	91.08(2.42)	111.03	153.84	4 bar
	δ_{perm}	54.8	101.61	136.94	
Box150-3	δ_{max}	92.87(2.22)	116.95	156.67	4.8 bar
	δ_{perm}	56.45	110.05	138.39	
Box150-4	δ_{max}	136.08(2.23)	168.55	189.27	7.5 bar
	δ_{perm}	99.91	152.54	178.88	

Maximum and permanent deformations at the centre of the front face are listed in Table 4.10. The table also contains the time which took to reach the

[1] The time to reach maximum displacement, unit: ms

maximum deformation at the centre of the front face. The error of the UEL and Lagrangian (analytical blast) approaches relative to the CEL approach are shown in Figure 4.37, including both maximum and permanent deflections. It can be seen that the maximum deformations were compared reasonably well for both UEL and Analytical blast methods up to 3 bar, with maximum error around 60%. Errors in the permanent deflections are always greater than the maximum and became significant at overpressure beyond 3 bar.

It is evident that from both Figure 4.36 and Table 4.10 that in the most cases CEL approach produced less damage compared to UEL and in particular to the pure Lagrangian (analytical blast) model. The Pure Lagrangian model gave the largest response because the reflected impulses were over-estimated by the analytical blast as already discussed. In the UEL approach the blast loading curves were obtained from the Step 1 (model shown in Figure 4.23) by using a empty box volume. This means that the reflected pressure blast loading was determined on the stationary, non-moving front face of the "rigid" box. In the fully coupled approach, the reflected pressure at the front face was however influenced by the movement of the deformable front face of the box. Borvik (Borvik et al., 2009) conducted a study using one-dimensional Eulerian model coupled with a moving rigid Lagrangian element to illustrate the influence of a flexible blast loaded surfaces on the magnitude of the reflected impulse. In this simple model he varied the velocity condition at the reaction end (i.e. the Lagrangian element), which is opposite of the inflow end. The results showed that at velocity of 10 m/s, the reflected impulse was reduced by 23% compared to a stationary reaction end (with zero velocity). In the present study, the average velocities of the box front face centre to reach the maximum deformations were shown in Figure 4.37. At the lowest overpressure level of 1 bar the velocity was 14 m/s and it increases to 60 m/s at overpressure of 7.5 bar. This is a clear indication of why the CEL approach predicted less response than the UEL model and the discrepancy is increasing with higher overpressure levels.

For completeness, numerical residual shapes in various simulation approaches are shown in Figure 4.38 and 4.39. Although there were no detailed data available from the tests, photos shown in Figure 4.6 are used to compare with the numerical results qualitatively. It can be seen that the CEL approach produced

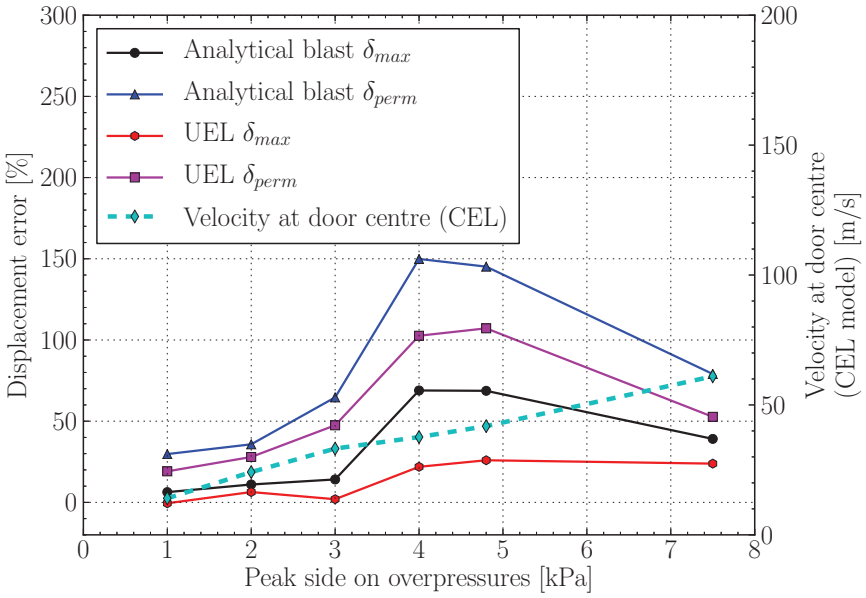
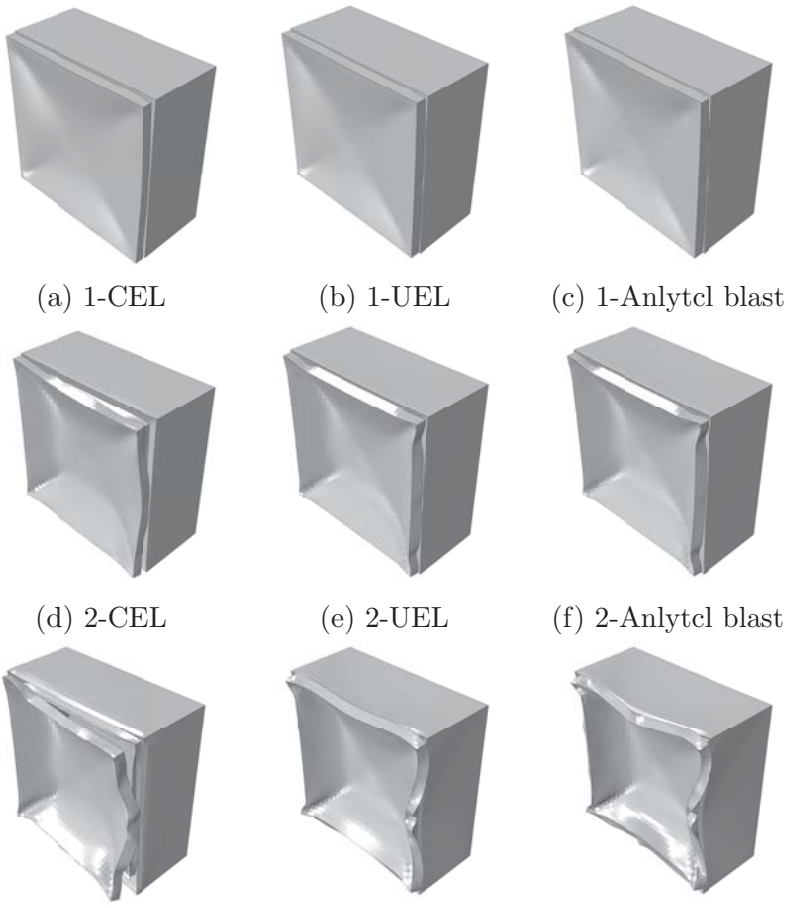


Figure 4.37: Numerical displacements error compared with CEL model

the most qualitatively comparable residual shapes compared to the test photos, i.e. damages are focused at the front face and enclosure walls had no significant inward deformations. More importantly the crushed front face did not made contact to the back faces in all cases. On the other hand, the UEL and Lagrangian (analytical blast) models showed reasonably comparable results to the CEL approach up to 3 bar. Beyond this the differences can be clearly identified that the front faces were in contact with the back panels and the side walls of enclosure significantly deformed inwards.

Both quantitative and qualitative assessment of the numerical results suggested that the coupled Eulerian - Lagrangian approach should be used to accurately predict the response of switch box exposed to blast wave loading. However the high computational demands limited its application and in order to perform a parametric study which covers a wide range of overpressures and impulses, the Lagrangian model(analytical blast) is a better choice in terms of efficiency. According to the above discussion, it was decided that the pure Lagrangian model (analytical blast) can be used for the parametric study but with the overpressure level limited to 4 bar, so that the accuracy of the Lagrangian model is acceptable. According to the Section 2.2.2, overpressures occurred in most of the previous ma-

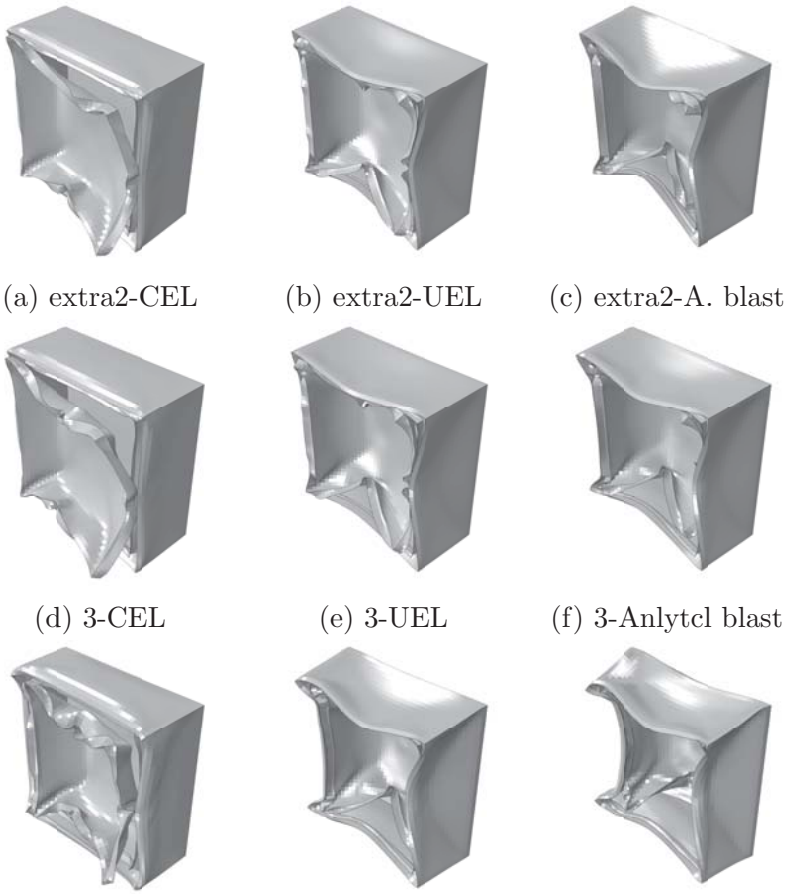


(a) 1-CEL (b) 1-UEL (c) 1-Anlytcl blast

(d) 2-CEL (e) 2-UEL (f) 2-Anlytcl blast

(g) extra1-CEL (h) extra1-UEL (i) extra1-A. blast

Figure 4.38: Numerical residual shapes for Box150 in TNT explosions. Peak side-on pressure: 1 bar, 2 bar and 3 bar



(a) extra2-CEL (b) extra2-UEL (c) extra2-A. blast

(d) 3-CEL (e) 3-UEL (f) 3-Anlytcl blast

(g) 4-CEL (h) 4-UEL (i) 4-Anlytcl blast

Figure 4.39: Numerical residual shapes for Box150 in TNT explosions. Peak side-on pressure: 4 bar, 4.8 bar and 7.5 bar

jor incidents were less than 2 bar. Therefore, the overpressure limit of 4 bar would be adequate for most cases.

4.4 Parametric study and discussion

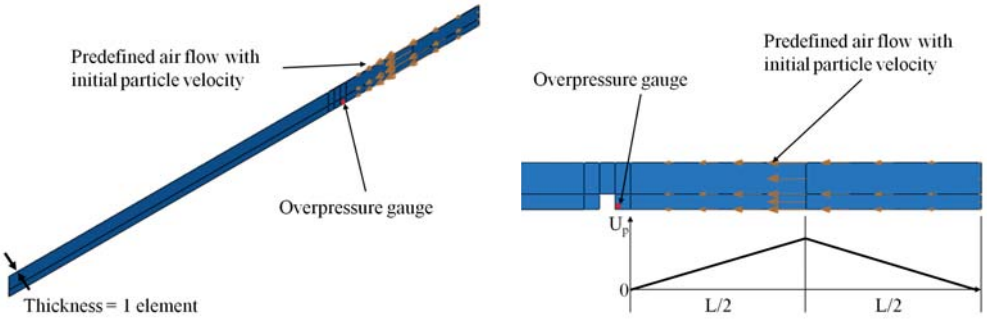
In the parametric study, the Lagrangian box model was subjected to analytical blast loading covering a wide range of side-on overpressures and impulses with peak value limited to 4 bar. The type of blast loadings included detonation and extended to deflagration and quasi-static load (rectangular shape). Results are summarised in the form of pressure - impulse diagrams (iso-damage curves of box front face centre) and selected residual shapes are presented for overall assessment.

4.4.1 Reflection of deflagration blast waves

It has been indicated in the literature review that the deflagration produced a non-ideal blast wave with a compressive wave of finite rise time followed by a rarefaction wave, as shown in Figure 2.1b. The overpressure blast wave from the deflagration can be idealised into a triangle as depicted in Figure 2.9b. It has been discussed that the dynamic pressure loadings from the non-ideal blast waves can not be readily calculated since the first arrival at the reflection surface is not a shock front hence the Rankine - Hugniot relations are not applicable. Thus, an Eulerian analysis has been carried out in the current work to study the reflection effect of the deflagration blast wave.

A pair of two dimensional Eulerian models have been created as shown in Figure 4.40. One model (Figure 4.40b) has a empty box volume so that the reflected overpressure can be determined at the reaction face, while the other (Figure 4.40a) was used to determine the side-on deflagration overpressures. Since Eulerian analysis must be considered in three dimensions (using brick Eulerian elements), this two dimensional model was approximated by a thin three dimensional model with one element throughout its thickness. The non-ideal blast wave was implemented by predefined particle velocity field of a triangular shape which is distributed over the total length L as shown in Figure 4.40, the first half is the compression wave

and the second half is the rarefaction wave. It was assumed that the finite rise time is half of the total positive duration, i.e. $t_r = \frac{1}{2}t_d$. There are no codes or industry standards for determining what shape should be used, and in most cases this should be dependent on the individual deflagration explosions.



(a) side on (b) reflection and predefined velocity

Figure 4.40: Numerical Eulerian model for reflection of deflagration

Design code such as UFC-3-340-02 (USDOD, 2008) provides plots of shock front velocity versus scaled distance for high energy TNT explosives. The shock front u_x and particle u_p velocity of an ideal blast wave can also be calculated according to Equations 2.4f, 2.5 and 2.9c. There are no similar plots nor equations available for non-ideal blast waves from deflagration. However, for design purpose it can be conservatively assumed that a non-ideal blast wave travels at the same velocity as an ideal blast wave (ASCE, 1997). Each portion of the deflagration blast wave travels at its own local speed of sound (determined by the corresponding overpressure). Therefore, the particle velocity u_p of the deflagration can be readily determined in the same way as the detonation and assigned to the velocity field to predefine the deflagration blast wave in the two dimensional Eulerian analysis.

Five deflagration reflection studies have been carried at peak side-on overpressures of 10, 100, 200, 300 and 400 kPa. The finite rise time varied from 1 to 100 ms. Reflection coefficients Λ of the non-ideal blast waves determined by the 2D Eulerian numerical model are shown in Figure 4.41. For comparison, the theoretical reflection factors of ideal blast waves with the same peak overpressures were presented as circular markers in the same figure. The results suggests that the reflection coefficients of the non-ideal blast waves were reduced due to increase

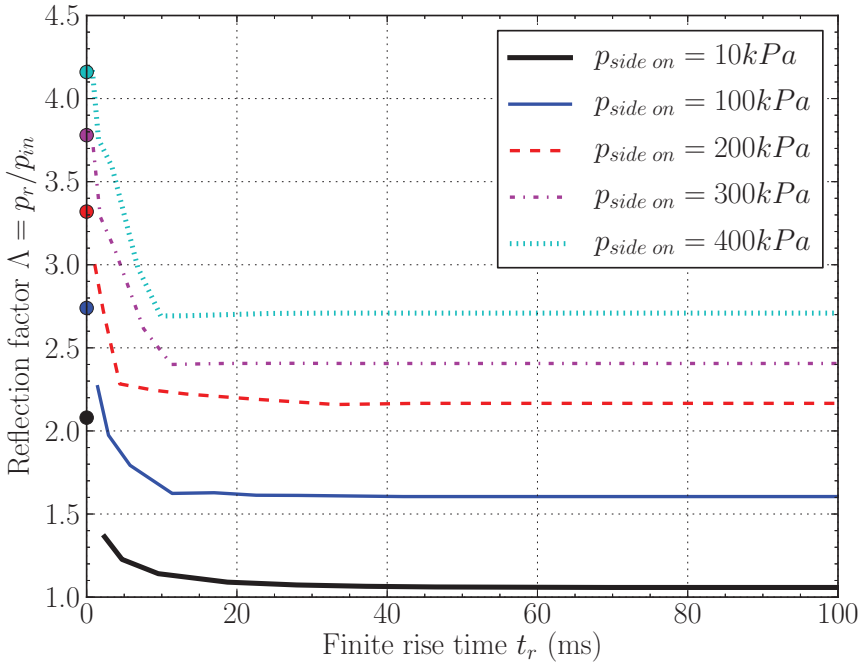


Figure 4.41: Reflection coefficient for deflagration(non-ideal blast wave)

of the finite rise time. It can be observed that the reflection factors reduce dramatically as the finite rise time become longer, but there is no further significant reduction beyond approximately 40 ms. The reductions in the reflection coefficients are 35% and 50% at the side-on peak overpressure of 400 kPa and 10 kPa, respectively.

In addition, the reflection factors are increasing as the finite rise time decreased and they gradually approach to the theoretical values for ideal blast wave at zero finite rise time. It should be noted that this study was based on the switch box which is much smaller than building structures. Due to the fact that reflection of the non-ideal blast wave is dependent on the dimensions of the target, so the reflection factor determined in this study might not be suitable for other structures. However, the same Eulerian analysis can be readily carried out on any other targets so that more appropriate reflection coefficients can be obtained.

4.4.2 Pressure - Impulse diagram and residual shapes

In the two detonation tests described above, data were only available at high overpressure - short duration regions. It is the objective of this parametric study to extend the experimental study into a wider range of overpressures and durations covering both detonation and deflagration. Results are presented in the form of pressure - impulse diagrams, the range of the side-on overpressures is defined from 10 to 400 kPa (reflected 20 - 1665 kPa and the 400 kPa is defined as the limiting overpressure level) with 29 non-uniform increments. The impulse varies from 10 to 10000 kPa.ms (overall covers duration from 0.05 - 2000 ms) with 27 non-uniform increments as well. A total of 840 models were used in one parametric study.

The study considers three overpressure blast loadings: detonation, deflagration and quasi-static (rectangular shape), as shown in Figure 4.42. The reflected blast loading is calculated according to the detonation side-on overpressure wave and the pressure relief effect is taken in account. In all the cases of a box subjected to blast loading, it was assumed that the front face of the box is facing the explosion, thus for detonation the reflected loading was applied to the front face (door) and all other faces were subject to side-on overpressure loading. Both boundary conditions were considered as boxes were supported at the back vertically in the experiments and at the bottom in Buncefield. Both supporting conditions are common in practice.

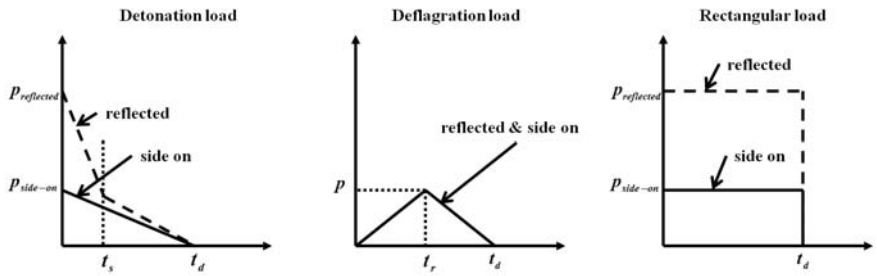


Figure 4.42: Overpressure dynamic loadings for parametric study

In the last section, the reflection enhancement of the deflagration on the switch box was studied. It was found that the deflagration did not have a significant enhancement as expected from an ideal blast wave of the same overpressure level.

Thus for simplicity the reflection enhancement was neglected for deflagration loads in the parametric study. Therefore, the reflected and side-on overpressure loading are identical for deflagration as shown in the figure.

A quasi-static load of a rectangular shape shown on the right of Figure 4.42 is not common in chemical explosions. It is assumed that the quasi-static blast wave is leading by a shock front, which is the same as the detonation but with constant magnitude throughout the duration. As depicted in the figure, the reflected blast loading was obtained by multiplying the side-on overpressure wave by the reflection coefficient for the shock wave of the same level of overpressure.

Parametric studies were performed for each of the three types of blast load. Maximum and permanent deformations at the box front face centre under every combination of side-on overpressure and impulse were obtained. Then the iso-damage curves were constructed based on the maximum and permanent deformation over the corresponding overpressure and impulse ranges. It should be noted that in the pressure - impulse diagrams, the overpressure and impulse were reflected values, which were calculated based on the side-on overpressures and impulses (the actual load input). The deflection results were also converted accordingly so that they were corresponding to the reflected pressure and impulse. This was because the iso-damage curves are obtained at the centre of the front face of the box model which was subjected to the reflected loadings. In addition, since it has been assumed that the reflected and side-on overpressures loads are identical for deflagration, it was necessary to extend the overpressure range of deflagration from 400 to 1665 kPa so that it can be consistent with other types of loads.

The structural responses of model Box150 are summarised in a series of pressure - impulse diagrams shown in Figures 4.43 and 4.44, for back and bottom support respectively. In order to have a visual assessment of the response of boxes, a group of residual shapes in the impulsive and quasi-static regions were presented in Figures 4.45 and 4.46. Since the damages were dominated by crushing of the front face of the boxes, the iso-damage curves were plotted based on the maximum and permanent deformation at the centre of the front face of the box.

For detonation and quasi-static (rectangular) loads, the front face of the box

model was subjected to the reflected overpressure blast loading. Therefore, reflected values are used for the pressure - impulse diagrams. Using the results presented in Figures 4.43 and 4.44 it is straight forward to calculate the response of the box front face based on the side-on overpressure blast wave. One only needs to determine the corresponding reflected overpressure and impulse and then read the damage from the diagrams. The pressure - impulse diagrams can also be used in forensic investigations to determine the side-on overpressure blast wave based on the known damages to the front face of boxes. This involves converting the reflected values to the side-on overpressures and impulses. For deflagration, the reflection coefficients presented in Figure 4.41 can be used to determine the side-on blast waves but bearing mind that as a result the deformations at the faces other than the front thus become conservative since the blast applied are reflected and not side-on as they should be.

Figure 4.43 presents the iso-damage curves at the front face of the box model vertically supported at the back. Figure 4.43a shows the maximum deformation curves while Figure 4.43b shows the permanent deformation curves. For both diagrams the damages levels are set as 0.01, 0.05, 0.1 and 0.15m. The maximum damage level suggests that the front face was in contact with the back panel (0.15m). It can be seen that the iso-damage curves in Figure 4.43a are shifted slightly towards upper-right direction comparing with Figure 4.43b. This indicates that the maximum dynamic deflections are close to the residual deformations (small overshot). It can be observed that the quasi-static asymptote of 0.01 iso permanent damage curve approximately ranged from 100 to 240 kPa for the three types of blast loads. This was a relatively wide range. The impulsive asymptote ranged from 137 to 144 kPa.ms, which was a relatively small range. This suggests that the iso-damage curve of 0.01 m was relatively sensitive to the impulse and relatively insensitive to the peak overpressure. The same observation can be made to other iso-damage curves as well but overall the sensitivity was reduced with increased damages.

In Figure 4.43b, there is a noteworthy feature of the response in the dynamic and quasi-static region of the 0.01 m iso permanent damage curve. The quasi-static asymptote of the iso-damage curve of deflagration was slightly shifted upwards compared to the other two load types. This is a well known phenomena

due to the resonance of the box front face caused by the finite rise time of the deflagration load curve. In the dynamic and quasi-static region the rectangular loading produces more damages than the other two loads. Beyond the damaged level of 0.05 m it can be seen that in the quasi-static region the deflagration produces the worst damage to the front face. This can be explained by referring to Figure 4.45 that among the residual shapes corresponding to quasi-static deflagration load the enclosure wall started to buckle when the applied overpressure exceeded 400 kPa. This significantly promotes the deformation at the centre of the box front face. It is also the reason that the iso-damage curves of deflagration positioned very closely in the quasi-static region while the curves for other load cases spread relatively wider over the overpressure range.

The pressure - impulse diagrams of the model Box150 with bottom support are presented in Figure 4.44. Iso-damage levels are set to various values as shown in the diagram. With the defined boundary conditions the back face can deform significantly under blast loads, so the iso-damage levels at the front face centre would not be able to reach the same depth as the box with back support. The front face were frequently in contact with the back face and this made it impossible to construct clear iso-damage curves at large displacement. Therefore, for deflagration the maximum dynamic iso damage level was set to 0.75 m which is half of the box depth and the permanent iso damage level was set to only 0.5 m.

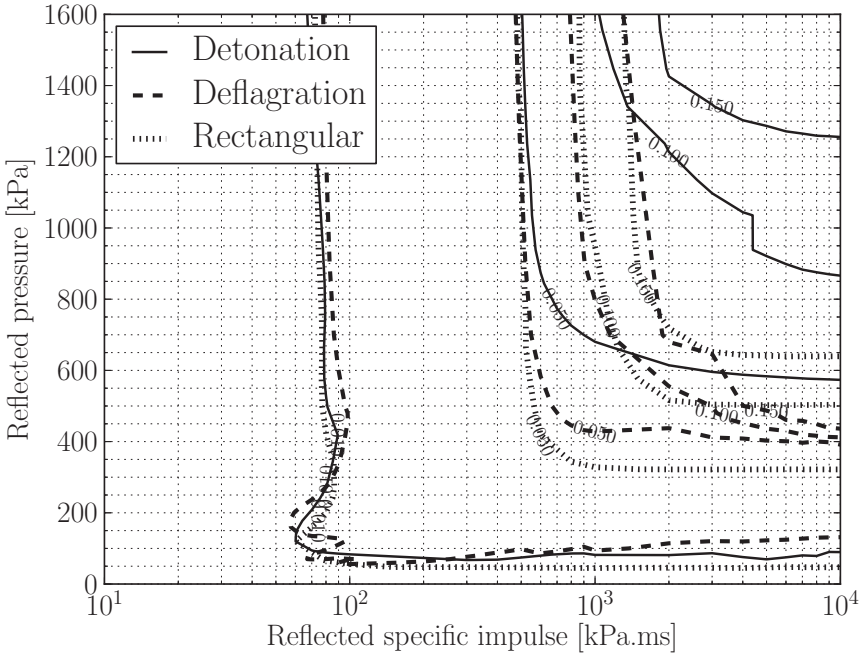
The general features of Figure 4.44 are similar to Figure 4.43 discussed above. The peak dynamic deflections are close to the residual deformations and the upward shifting quasi-static asymptote of 0.01 m iso permanent curve of deflagration is clearly visible as well. Response of the box front face is sensitive to peak applied overpressures in the quasi-static region for deflagration loads, due to the buckling of the enclosure wall which promotes the deformation at the front face centre, as shown in Figure 4.46. In addition, the buckling of the enclosure wall near the bottom occurs when the box is subjected to rectangular loading in the quasi-static region. This also promotes the deformation at the box front face centre and make the iso-damage curves of rectangular loads closely positioned in this region, for both maximum and permanent curves. In the contrary, no buckling occurs in the impulsive series of the residual shapes in Figure 4.46, hence in the impulsive region the iso-damage curves are positioned relatively wide and evenly

over the full range of the impulses.

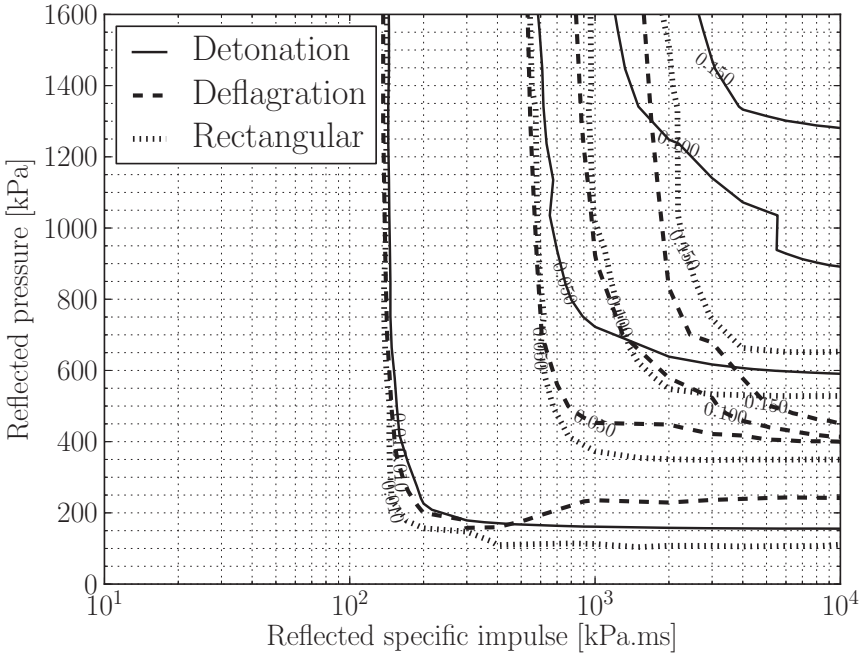
Deflections at the centre of the front face of box models were summarized in the form of pressure - impulse diagrams and discussed in the above paragraphs. In order to provide a visual assessment of the response to three different blast load types, a group of selected residual shapes of the numerical box are presented in Figure 4.45 and 4.46, for different supporting conditions respectively. Residual shapes of the numerical models are selected for each load type in the impulsive and quasi-static regions from the pressure - impulse diagrams. It can be seen from these two figures that for every load type there are two series of residual shapes. One is corresponding to a fixed overpressure value (1665 kPa [reflected value at the front face]) and residual shapes were selected at various impulses (i.e. in the impulsive region). And the other one is corresponding to a fixed impulse value (10000 kPa.ms) where the residual shapes are selected at various pressures (i.e. in the quasi-static region). Permanent deformations at the centre of the front face are shown in the figures as well. It should be noted that side-on and reflected values are both shown for detonation and rectangular loads, with side-on values in the parentheses.

The impulsive series of the residual shapes show the response of the final deformation to impulses where peak pressures were less decisive. In the opposite, the quasi-static series present the box final response mainly related to the peak overpressures rather than impulses. It is evident from these two figures that impulsive residual shapes were different to those in the quasi-static region, particularly for deflagration. In Figure 4.45, it can be seen that the differences for detonation and rectangular loads are dominated by the buckling of the front face. In the case of deflagration, the difference is more clear. Buckling of the enclosure wall occurs at the four corners for impulsive response while for the quasi-static response the buckling occurs at the mid of the edge of front face.

In Figure 4.46, the differences in permanent responses to detonation load are also dominated at the front face. For deflagration load, residual shapes change significantly due to the supporting conditions comparing with Figure 4.45. The impulsive residual shapes look like they have been equally squeezed from all directions, while the quasi-static responses show server buckling at the back (of the enclosure) and the front face was pushed against on the enclosure.

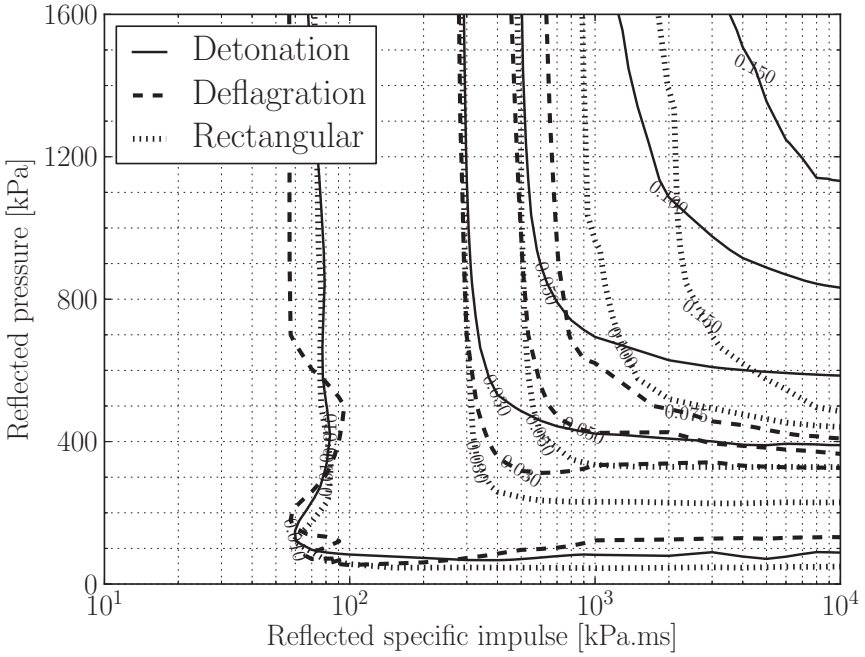


(a) Max. door centre deflection [unit:m]

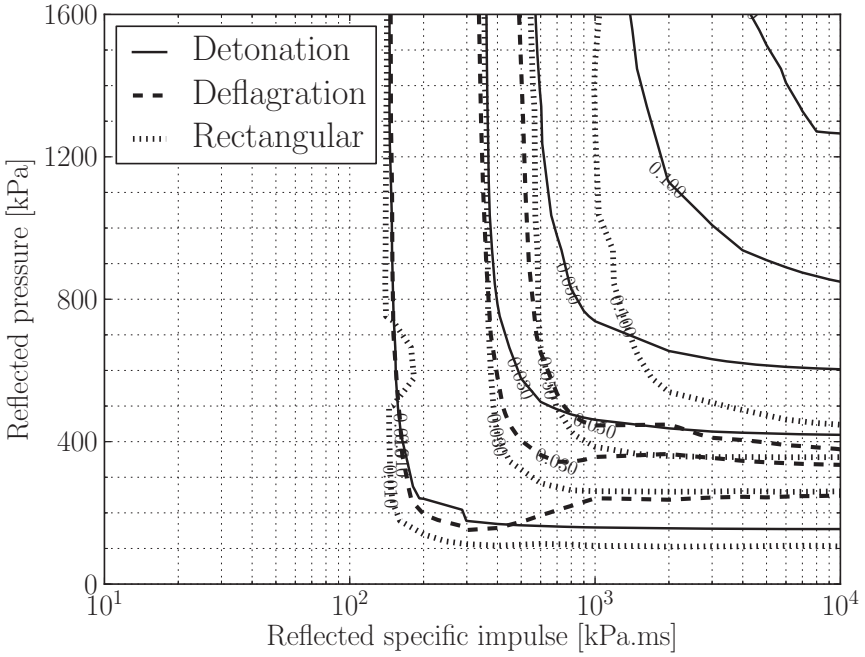


(b) Perm. door centre deflection [unit:m]

Figure 4.43: Pressure - Impulse diagrams for Box150 (back support)



(a) Max. door centre deflection [unit:m]



(b) Perm. door centre deflection [unit:m]

Figure 4.44: Pressure - Impulse diagrams for Box150 (bottom support)

Buckling can be observed in the residual shapes at various locations. It is a clear indication of the minimum overpressure levels which can cause this type of damage feature, particularly for quasi-static loads. In Figure 4.45 the three series of residual shapes related to quasi-static loads indicate that for a box with back supporting conditions the minimum side-on overpressures to initiate a visible buckling are: detonation - 280 kPa; deflagration - 420 kPa and rectangular - 240 kPa. And for boxes supported at the bottom as shown in Figure 4.46 the minimum side-on overpressures are: detonation - 260 kPa; deflagration - 380 kPa and rectangular - 160 kPa.

4.4.3 Comparison with recovered boxes

One of the objectives of the present project is to provide information which can aid the incident investigation. This section presents a brief comparison between the numerical results and the damaged boxes found in Buncefield. Three photos of one damaged box found after the incident are shown in Figure 4.47. The photos were taken from the front ,side and back of the box (shown from top to down in the figure respectively). The immediate investigation after the incident determined the blast directions that the front face (door) of this box was facing the blast wave during the explosion. This was in consistence with the experiments and the numerical simulation in this present work. It can be clearly seen that both the front and back face of the box were significantly deformed in a symmetric way and so did the side faces shown in the middle. The top face had little deformation might be due to the extra plate fixed onto it which protected it from the explosion.

Unfortunately, the actual measurement of the damaged box was not available. It was then assumed that the deformation of the front cover was half of the box depth (75 mm). Among the residual shapes shown in Figure 4.46, four cases with similar deformation at the front cover were chosen to compare with the damaged box. In the quasi-static region, one deflagration and detonation cases were selected as shown in Figure 4.47, and another two cases were selected in the impulsive region. It is fairly easy to eliminate the possibility of deflagration case in the impulsive region and the detonation case in the quasi-static region. Since

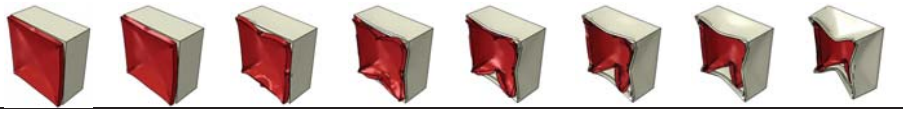
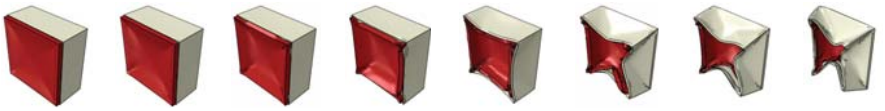
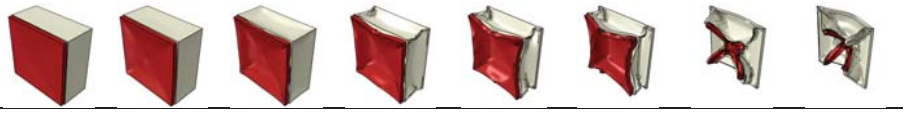
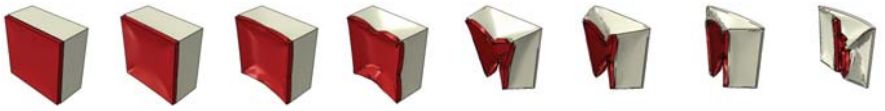
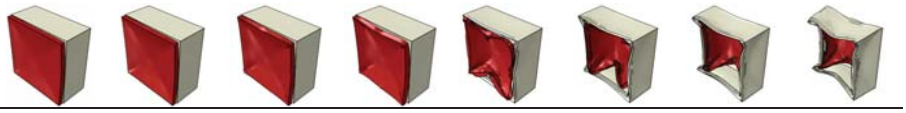
Box150		back support						Reflected(Side-on) residual deflection(m)	
Detonation	Pa.s	333(80)	416(100)	634(200)	824(300)	1027(400)	1236(500)	1447(600)	2301(1000)
	m	0.028	0.035	0.055	0.073	0.093	0.117	0.134	0.149
	Impulsive 1665 kPa								
	kPa	209(80)	344(120)	497(160)	664(200)	844(240)	1035(280)	1237(320)	1341(360)
	m	0.015	0.025	0.038	0.062	0.095	0.113	0.146	0.166
	Quasi-Static 10000 kPa.ms								
Deflagration	Pa.s	100	200	400	600	800	1000	2000	4000
	m	0.005	0.017	0.036	0.058	0.093	0.127	0.165	0.205
	Impulsive 1665 kPa								
	kPa	200	300	360	400	420	440	500	900
	m	0.005	0.019	0.035	0.05	0.121	0.145	0.159	0.183
	Quasi-static 10000 kPa.ms								
Rectangular	Pa.s	166(40)	250(60)	333(80)	416(100)	832(200)	1248(300)	1664(400)	2496(600)
	m	0.013	0.020	0.028	0.036	0.084	0.135	0.148	0.160
	Impulsive 1665kPa								
	kPa	274(100)	344(120)	418(140)	497(160)	579(180)	664(200)	844(240)	1035(280)
	m	0.033	0.050	0.069	0.091	0.112	0.154	0.164	0.180
	Quasi-static 10000 kPa.ms								

Figure 4.45: Numerical residual shapes of Box150 (back support)

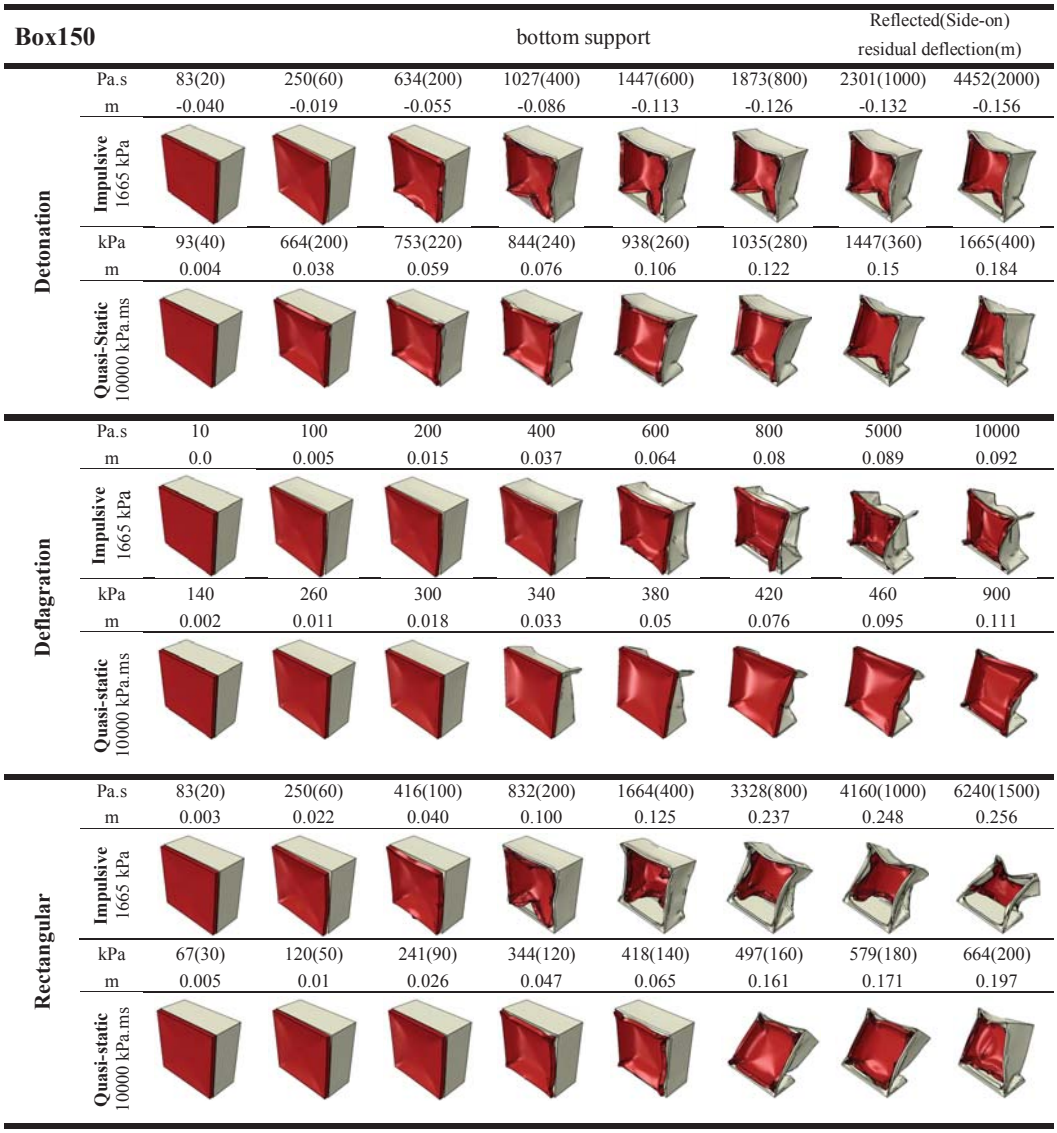


Figure 4.46: Numerical residual shapes of Box150 (bottom support)

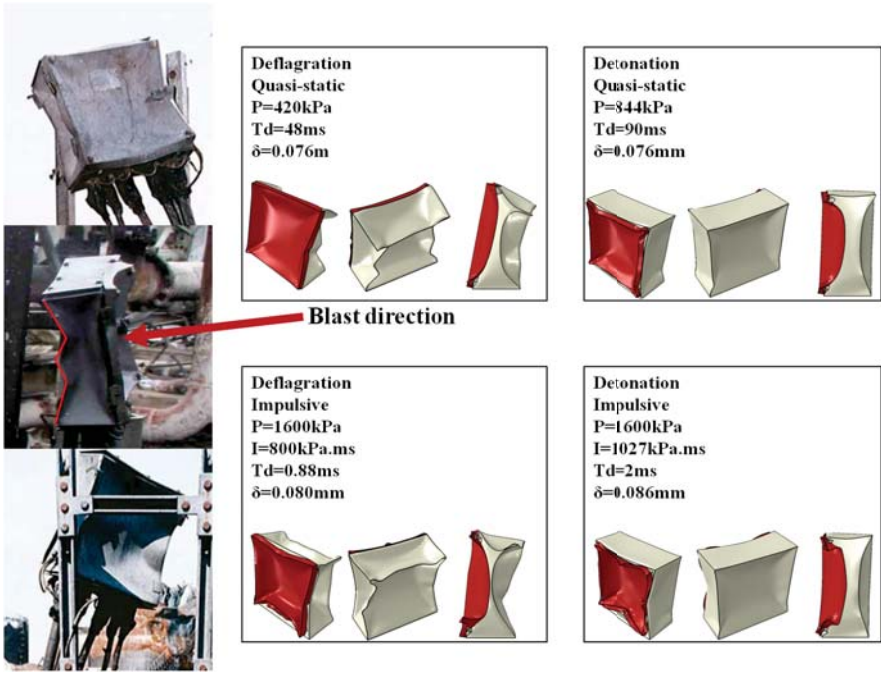


Figure 4.47: Comparison of numerical residual shapes to damaged boxes from Buncefield (SCI, 2009)

the combination of peak overpressures and positive impulses of these two cases did not have typical characteristic for the relevant blast waves.The deflagration blast wave should not be impulsive and the detonation blast wave is unlikely to be quasi-static.

As a result, there are two cases left: a quasi-static deflagration load and an impulsive detonation load. In the case of the detonation load, it can be seen that buckling occurred at the bottom of the front face of the box and the rim of the door was pushed off from the enclosure. This is inconsistent with the observed damage of the box in Buncefield. In the case of the deflagration load, the front face deformed in a similar manner to the damaged box, i.e. no buckling. Moreover, the back and side of the enclosure were buckled in a similar way to the damaged box. From the side view of both cases, it is evident that the deformations of front and back faces in deflagration were more symmetric than detonation. This is consistent with the observation of the damaged box. This comparison suggests that within the vapour cloud the explosion is most likely to be deflagration.

The level of peak overpressure of the deflagration inside the vapour cloud can

be roughly estimated based on the permanent deformation in the quasi-static deflagration case. The applied overpressure loading on the front face was 420 kPa with approximately 48 ms positive duration. Using Figure 4.41 as a guidance the side-on peak overpressure of the deflagration load can be calculated to be around 200 kPa.

4.5 Conclusion

In this chapter, detonation experiments carried out on steel switch boxes by external parties were presented and measurements and observations discussed. Various numerical models used to model response of the boxes to detonation blast loadings were presented in detail. Validation of the numerical models was carried out and it was found that the coupled Eulerian - Lagrangian model has the best accuracy and should be used in blast problems if possible.

However, the high computational demands of the coupled Eulerian - Lagrangian model would limit its application, precluding cases requiring a large number of simulations, particularly for parametric studies. Based on the validated CEL model, the accuracy of the pure Lagrangian approach has been investigated and it has been shown that it is able to produce reasonable results under side-on peak overpressure of 4 bar. With its short running time it is an ideal candidate for parametric studies and therefore a large number of Lagrangian models were analysed subjected to a series of combinations of overpressures and impulses. The range of blast loadings covers both deflagration and detonation for very long and short durations. Results were summarised in the form of pressure - impulse diagrams and selected residual shapes were also presented for visual assessment.

An attempt has been made to compare the numerical results with an actual damaged box from Buncefield. The comparison showed that the parametric study did produce reasonably comparable results to the damaged box. This suggested that the explosion inside the vapour cloud is very likely to be deflagration with a peak overpressure of around 2 bar. Although the comparison was carried out on assumed permanent deformation of the damaged box, the forensic study shown here has given a good insight into the likely loading scenarios.

Chapter 5

Modelling of warehouse structures

During the Buncefield explosion, the steel-clad warehouse located at the south of the site suffered substantial damage and there was serious disruption to business activity. This chapter and following chapter aim to study the response of typical warehouse structures to various blast loading and provide some guidance on the safe siting of industrial type structures in or near oil storage facilities.

5.1 Damages to Buncefield warehouses

There were two warehouses located in the Buncefield site, as shown in Figure 2.3. The high surface area and relatively lightweight construction makes the pressure loading applied by wind a primary design consideration. Typical design pressure forces for the warehouses are shown in Table 5.1 (Atkinson, 2011). These levels are relatively low compared with other types of structure. For example, the criteria for serious damage to a conventional brick building is 5000 Pa (CIA). This is the reason behind the substantial damage to large warehouses that was observed over a large area at Buncefield; because most of the surface components and cladding are potentially at risk, the level of damage to the warehouses may be particularly extensive. Such level of damage could be very time-consuming to repair and increase the level of business disruption.

Table 5.1: Typical design wind pressure for warehouses

Warehouse walls	
Pressure (general zone)	720 Pa
Suction (general zone)	510 Pa
Suction (corners)	720 Pa
Warehouse roof	
Imposed (including snow)	600 Pa
Wind suction (general zone)	1000 Pa
Wind suction (eaves and gable)	1200 Pa

The HSE has participated in the immediate investigation of Buncefield incident, and the damage of the warehouses have been reported (Atkinson, 2011). The nature of damage inflicted on both warehouse buildings can be seen in Figures 5.1 and 5.2. In both cases, the blast wave loading created extensive vents in the front wall of the building (which is closer to the Buncefield site), as shown in Figures 5.1a and 5.2a. These large vents in the front wall allowed formation of a strong internal pressure wave which travelled the length of the fairly empty interior before impacting on the back face (furthest from the side). In both cases, reflection of this internal pressure wave pushed the building cladding outwards over the full extent of the back wall and also part of the side wall close to the back, as shown in Figures 5.1b and 5.2a.



(a) inward deformation at the front face



(b) outward deformation on or near the back wall

Figure 5.1: Damage to Warehouse 1 (Atkinson, 2011)

Most of the cladding of Warehouse 1 on the side wall and roof was undamaged and did not have to be replaced during the repair work. In contrast, the majority

of the cladding on the roof and side wall of Warehouse 2 was significantly damaged and had to be replaced. The difference is due to the type of cladding system and the mechanism of the venting during the blast. Warehouse 1 had a built-up cladding system which remained mostly undamaged at higher pressure loading. The venting started when wind posts along most of the front wall failed, pulling purlins and side rails away from intact primary columns and allowing large sections of cladding (almost undamaged) to swing inwards. Where the secondary frame members did not fail, the strong built-up claddings suffered no permanent damage and were still serviceable.



(a) inward venting of front face and outward cladding damage on the back wall



(b) pressure damage to side wall

Figure 5.2: Damage to Warehouse 2 (Atkinson, 2011)

In the case of Warehouse 2, the cladding panels and supporting side rails were weaker than the structural steel (which mostly remained intact). As the blast wave impacted on the front wall, at first a large portion of cladding and side rails suffered inward deformation without opening up substantial venting area that could allow the interior to be pressurised. When the connections between the cladding panel and side rails or between side rails and column failed hence finally venting the structure, cladding on most of the side wall and roof had already been damaged and needed to be replaced.

The failure mechanism of the warehouse observed in Buncefield incident therefore can be summarised as: (1) if the warehouse is vented by rapid failure of a substantial proportion of the front face, an internal pressure surge is formed. It balances the blast wave loading on the exterior of the side wall and roof, which hence suffers from significantly less damage. The back face and side wall near the back is damaged by the reflection of the internal pressure surge. (2) if the ware-

house has relatively weak cladding and side rails, they will deform significantly before venting of the structure. When the structure is finally vented, claddings on side walls and roof would already be damaged. The internal pressure wave formed by the venting could still be able to cause outward damage to the back face and side walls near the back.

5.2 Typical portal frame configuration

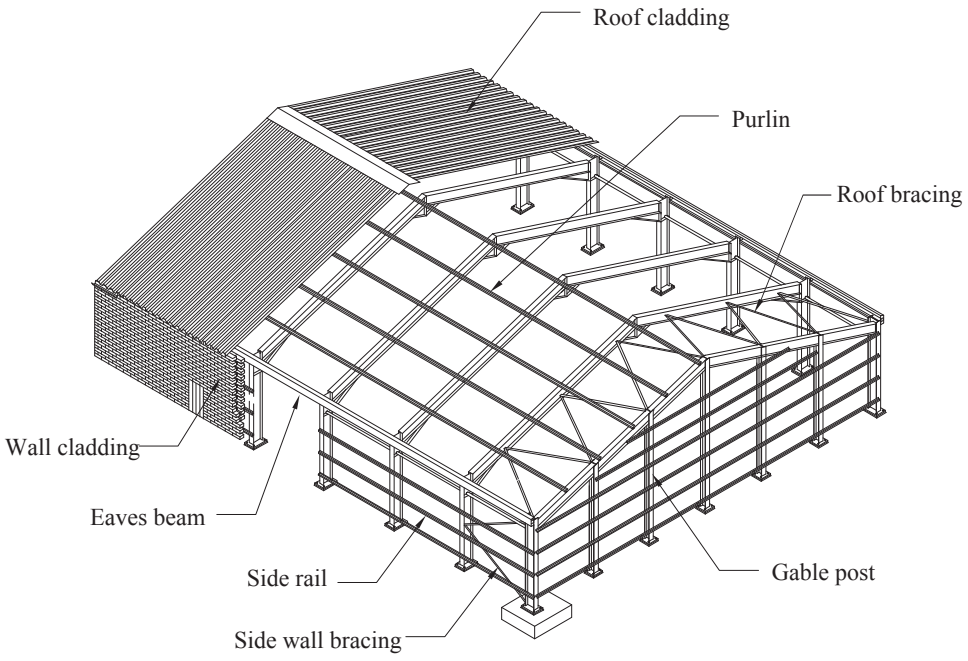


Figure 5.3: Typical warehouse configuration (Burgan and Moutaftsis, 2011)

In the industrial building sector in the UK, steel portal frames with cladding panels are the most widely used structural form (shown in Figure 5.3). Portal frames consist of columns and typically inclined rafters to form a pitched roof, with the columns and rafters normally joined by moment resisting connections. This type of frame relies on the rigidity of the connections, which are stiffened by haunches at the eaves and apex. Frame action provides stability in the plane of the portal frames, while out-of plane stability (orthogonal to the plane of portal

frame) is provided by side wall and roof bracing. Secondary structural and non-structural members do not contribute directly to the overall nominal stability of the structure.

The exterior surface of the warehouse building typically comprises of cold-formed corrugated steel panel with insulation infill, supported by cold-formed purlins on the roof or side rails on the side walls. These secondary components are in turn attached to portal frames, normally using steel brackets.

Industrial buildings are usually designed for dead, live, wind and snow loads. Typical design values for wind and snow loads have already been presented in Table 5.1. The depicted warehouse is for generic illustration purpose and not the one chosen in this project. The design information of the two damaged warehouse in the Buncefield site were not available and a typical but similar warehouse was chosen instead for analysis in the current work.

5.3 Description of warehouse components

The warehouse selected in the present work is typical of portal frame buildings. It is 108.9 m long and 43.6 m wide on plan. The height is 10.45 m at the eaves beam and 11.2 m at the apex. The rafters are inclined at 6^o to the horizontal. Detailed structural design and drawings of the building were provided by Barratt Steel Building Ltd through the Steel Construction Institute (SCI).

5.3.1 Portal frames

The portal frame spans 43.6 m and consist of UB 686×254×140 S355 columns and UB 533 × 210 × 92 S355 rafters. Columns and rafters are connected by moment resisting connections. At the apex, the rafters are stiffened by haunches to provide extra stability and ensure that plastic hinges will be formed in either rafters or columns rather than the connections. Purlins and side rails at approximately 1.8 m centres provide out of plane resistance to the external flanges of the rafter and columns. The main columns have pinned bases to the concrete foundations. The portal frame with the main dimensions is shown in Figure 5.4.

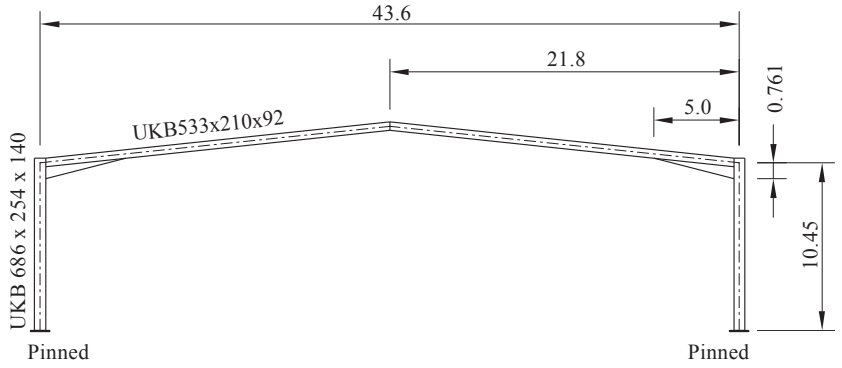


Figure 5.4: Portal frame layout (Burgan and Moutaftsis, 2011)

5.3.2 Gable wall frames

The gable wall frames at the two ends of the building comprise simple rafter and post constructions. The specification of vertical posts are UB $457 \times 152 \times 52$ S355 and corner posts are UB $356 \times 127 \times 33$ S355. Specification of rafters are UB $203 \times 135 \times 25$ S355 and they are joined by simple connection to vertical posts. The K-bracings (SHS $100 \times 100 \times 4.0$ S355) provide the in-plane lateral stability of the gable wall. All vertical posts are pin connected to the base foundation. The structure of gable wall frame is shown in Figure 5.5.

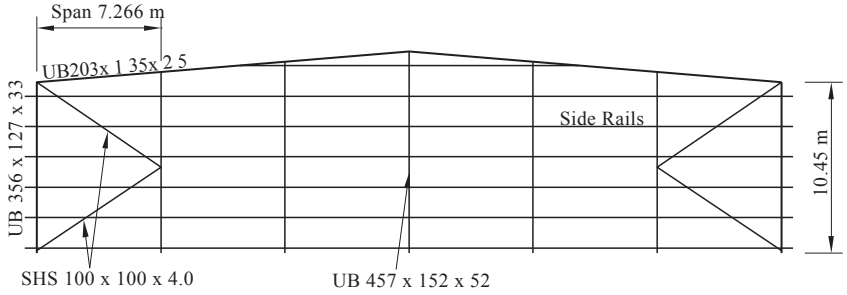


Figure 5.5: Gable wall frames (Burgan and Moutaftsis, 2011)

5.3.3 Roof bracing

Bracing on the roof is used in the two end bays of the warehouse and contribute to the stability in the longitudinal direction of the building (orthogonal to the

plane of the portal frame). The typical span between two main columns is 6.69 m. Figure 5.6 shows a plan view of the building.

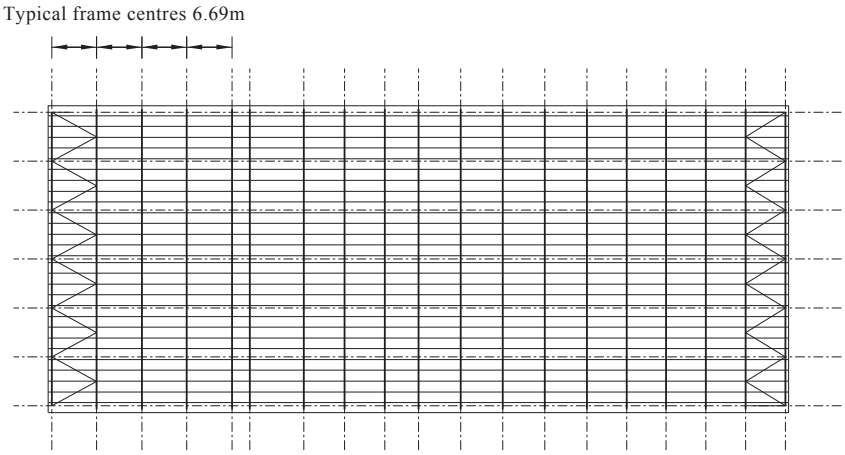


Figure 5.6: Roof plan (Burgan and Moutaftsis, 2011)

5.3.4 Side wall bracing

Wall bracing of K pattern is used in the design at the two end bays to transfer lateral loads acting in the longitudinal directions to the foundations. It consists of SHS $150 \times 150 \times 5.0$ S355 beams. Spacings between columns and side rails are shown in Figure 5.7.

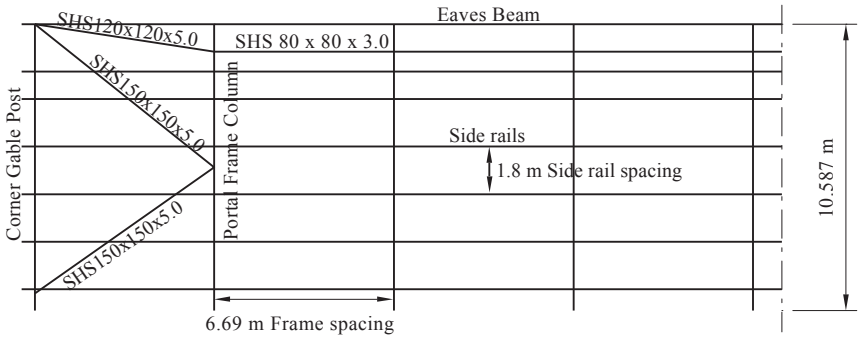
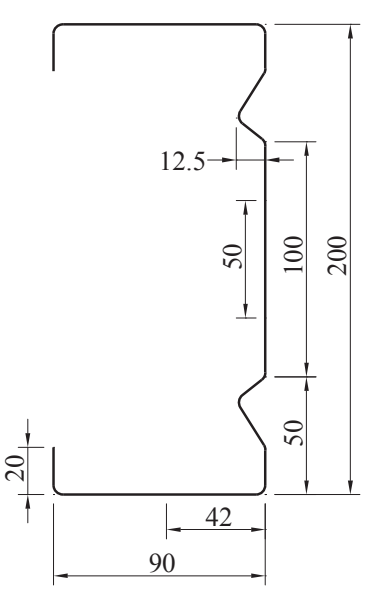


Figure 5.7: Side wall frames (Burgan and Moutaftsis, 2011)

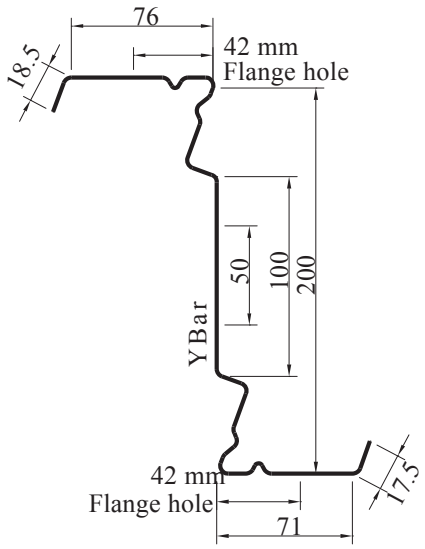
5.3.5 Eaves beam

The eaves beams are used at the top to support wall claddings and gutter corner detail. They consist of cold-formed galvanised channel sections. The Ultra beam S390 ,provided by Hadley Group (Hadley, 2004), is used in various sizes. The cross section is shown in Figure 5.8a. The eaves beams are typically continuous over double-span and connected to rafters with M12 bolts through S275 steel cleats. The eaves beams provide support to the roof and wall system as well as restraint to the external flange at the top of the columns.

5.3.6 Purlin and side rail



(a) Eaves beam (t=1.8mm)



(b) Purlin (t=2mm) and side rail (t=1.2mm)

Figure 5.8: Cross-sectional details of eaves beam, purlin and side rail [units:mm] (Hadley, 2004)

The purlins are used to support the claddings on the roof. They are cold-formed galvanised Z sections (Ultra Zed S390 200180), provided by Hadley Group (Hadley, 2004). The flange is formed with lips to provide additional stiffness to the section. The purlins are continuous over double-spans as well, using overlaps

or sleeves, and connected to the rafter by M12 bolts through 6 mm thick S275 steel cleats. Side rails on the building wall have the same cross-sectional details as purlins but have thickness of 1.2 mm. They are joined to the columns of the portal frame by two M12 bolts through S275 steel cleats. Details of the sections of purlins and side rails are presented in Figure 5.8b.

5.3.7 Cladding

A built-up cladding panel system is used for the roof and side walls of the warehouse. They consist of two layers of cold-formed corrugated sheeting with a mineral wool infill between them. Cladding panel CA 32 1000R (provided by CA Building Systems) is used, with sheeting thickness of 0.7 mm. The cladding is double-span continuous over three purlins or side rails. For every meter width of sheeting there, are six self-tapping fixing screws used at the end of the sheet and three screws at the middle support of the two-span length of the panel. Figure 5.9 below shows the cladding configuration. The external (upper) sheet is connected through a bracket (not shown) to the purlins/side rails to resist the externally applied loads.

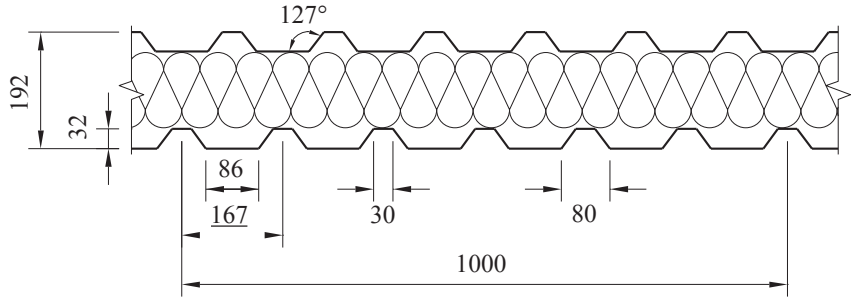


Figure 5.9: Built-up cladding details (Burgan and Moutaftsis, 2011)

5.3.8 Self-tapping screw fasteners

Claddings are fixed to purlins and side rails by self-tapping screw fasteners. In this selected warehouse, screws of type CSC 32/16 (provided by CA Building Systems (CA, 2008)) are used, as shown in Figure 5.10. The diameters are 12.7

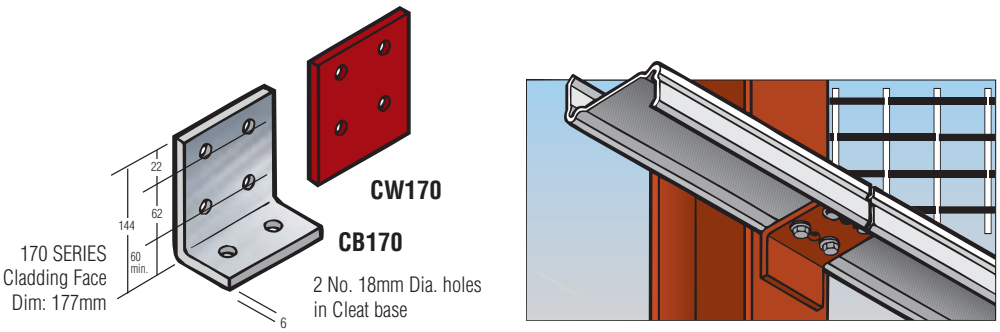
and 5.5 mm for the head and screw shaft, respectively. The length of the shaft is 16 mm. The material of this screw is equivalent to that of a grade 8.8 stainless steel bolt.



Figure 5.10: Self-tapping screw (CA, 2008)

5.3.9 M12 Bolt-Cleat connections

The connection between the purlin/side rails and the columns comprises of two M12 bolts and one steel cleat, as shown in Figure 5.11. The cleat is manufactured with steel S275 and its dimensions are presented in the Figure 5.11a. The cleat can be either bolted or welded to the column. Figure 5.11b shows the discontinuous end of the side rail; the end of one side rails is fixed onto the cleat by two M12 bolts and next to it is the fixed end of another side rail on the adjacent span.



(a) Steel cleat (b) Connection

Figure 5.11: M12 Bolt-Cleat connection (Hadley, 2004)

5.4 Material properties

The constituent materials of various warehouse components were indicated briefly in the previous sections. The summary in Table 5.2 below presents the material used for each component introduced before. These material properties are adopted in the structural analysis carried out in the present work.

Table 5.2: Material types of structural components

Component	Type of steel
Rafter	S355
Column	S355
Bracing	S355
Eaves beam	S390
Purlin	S390
Side rail	S390
Cladding	S220
Self-taping screw	Grade 8.8 stainless steel
M12 bolt	Grade 8.8 stainless steel
Cleat	S275

Limited data on the strain hardening of the actual materials used are available. It was therefore assumed that materials S355, S220 and S275 all have elastic-perfectly plastic behaviour, therefore the yield stresses are 355, 220 and 275 MPa respectively. Plasticity definitions for steel S390 and Grade 8.8 stainless steel are shown in Table 5.3.

Table 5.3: Plasticity of materials

	S390	Grade 8.8 Stainless steel
ϵ_p	σ_p	σ_p
0	390 MPa	640 MPa
0.2	470 MPa	800 MPa

5.4.1 Strength increase factor (SIF)

The yield strength of steel in practice is usually higher than the minimum guaranteed value in design standards. The ratio of actual yield stress to the specified

value in standard is known as the strength increase factor (SIF). The realistic component capacity can be estimated by taking this into account. In addition, this also ensures forces transferred to the connections and supporting members are not under-estimated.

The strength increase factor depends on the grade of steel and manufacturing process. Recommended values for different structural steels are presented in Table 5.4 (USACE, 2008a),(USDOD, 2008) and (ASCE, 1997). It can be observed that the strength increase factor tends to reduce for steels with higher yield stresses.

5.4.2 Dynamic increase factor (DIF)

The mechanical material properties under static loads are different to high speed loads, as depicted in Figure 2.20. The strength of the material will increase at higher strain rate. Strain rate effects were taken into account in the present studies to analyse the response of warehouse structures. The ideal method is to used Cowper-Symonds (Cowper and Symonds, 1957) or Johnson-Cook strain (Johnson and Cook, 1983) rate models, as described in Section 2.4.2, in material definition in the finite element model. Typical dynamic increase factors were used as recommended for the type of steel used in the warehouse structures. The experimental strain rate data of the actual material of the components in the warehouse structure are not available. Typical hardening values at relatively lower strain rate were suggested by our collaborator and used instead.

The dynamic increase factor defines the increase of material strength at high strain rate, which depends on the instantaneous strain rate and material properties. Recommended values of DIF for various structural steels are presented in Table 5.4. The data are based on an assumed strain rate of average 0.01 1/s (USACE, 2008a).

Table 5.4: Stength increase factor for structural steels

Material	Specified static yield stress	SIF	DIF
Cold formed members and sheeting	200 - 400 MPa	1.21	1.1
Hot rolled steel	200 - 240 MPa	1.1	1.29
Hot rooled steel	290 - 400 MPa	1.05	1.19
Hot rolled steel	515 - 690 MPa	1.0	1.09

5.5 Numerical models of warehouse

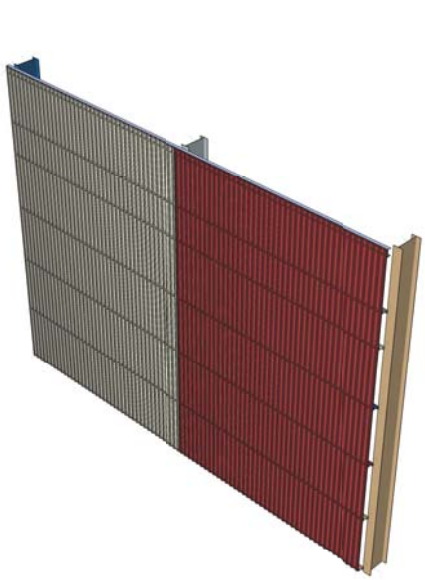
In the previous section, the configuration and components of a typical warehouse building were described in detail. In this section, the creation of a numerical finite element model of the warehouse in the non-linear finite element analysis program **?** is described.

In order to simplify the problem, it was assumed that the side wall (either side) of the warehouse is facing the explosion (i.e. perpendicular to the propagation path of the blast wave). The side wall, which is subjected to the most severe loading in the explosion, was chosen to be analysed in the present work.

It is prohibitive to model the whole side wall from end to end of the warehouse due to the substantial size and the large number of components. It was noted before that the side rails are continuous over a double span, hence it is reasonable to model only two typical spans of the side wall, which preserves the continuity of the side rails. The objective in this section is to select a suitable numerical modelling level which is efficient to run whilst retaining sufficient accuracy.

5.5.1 Double span full model

The double span model of the side wall is shown in Figure 5.12a. This model comprises three columns over two spans including the side rails and eaves beams according to the building design. The cladding system has been simplified to where only a single corrugated sheeting was used and fixed on the side rails by self-tapping screws. The mineral wool infill and the other sheeting were simplified as non-structural mass and added to the modelled cladding panels. It is important to note that the complete cladding system has a self weight of 0.301 kPa according to the building design, while the non-structural mass used in the numerical model was determined to be 0.237 kPa (including one sheeting and the mineral wool infill). As these are only for preliminary purposes, the fasteners and cleat connections were all assumed rigid in this initial study. The claddings were fixed to the outer flange of the supporting frames by tie constraints. In a similar way, the end of the supporting frames were rigidly constrained and connected to the flange of the main columns using tie constraints.



(a) Double span full model



(b) Single span model



(c) Sub-assembly model



(d) Component model

Figure 5.12: Numerical modelling levels

5.5.2 Single span full model

The single span model was simplified from the double span full model and only half of the claddings and supporting frames were considered. The columns were removed for simplicity based on observation after the Buncefield incident that all primary structural components remained intact during the explosion. The single span model is shown in Figure 5.12b, in which the far end of the supporting frames was fully constrained to represent the continuity over the double span and the near end were simply supported. Fasteners were assumed rigid for this initial model and the cleat connections were replaced by boundary constraints at the end of the frames.

5.5.3 Sub-assemblage model

The sub-assemblage model shown in Figure 5.12c was the result of further simplification of the numerical model. It only comprised three side rails and the claddings over double span (two spans of side rail). Fasteners were rigid and the same boundary constraints of single span full model were applied at the end of the side rails. Additional loads were applied directly on the outer flanges of the upper and lower side rails. This was used to take account of the pressure loads from the neighbouring claddings (half span). Accordingly, the additional masses of the neighbouring half span claddings were added to the side rails as well.

5.5.4 Component model

The final simplified model is shown in Figure 5.12d. This component model consists of only the middle side rail in the sub-assemblage model. The weight of half the span of the complete cladding system was added to the side rail and the equivalent pressure loads applied on the outer flange were calculated based on the tributary width of 1.8 m (half span of side rails). Boundary conditions were the same as in the other two simplified models.

5.5.5 Comparison of displacement histories

Claddings of all the numerical models were subjected to a uniformly distributed blast pressure loads with a peak reflected overpressure of 7 kPa and a duration of 150 ms (linear decay). It is important to note that the masses of the relevant components were always preserved in the simplified models and so were the pressure loads.

The analysis time was set to 300 ms. The actual wall clock time used by double, single, sub-assemblage and components models were approximately 20, 15, 10 and 0.5 hours, respectively. All simulations were performed using high performance computers as noted in Chapter 4.

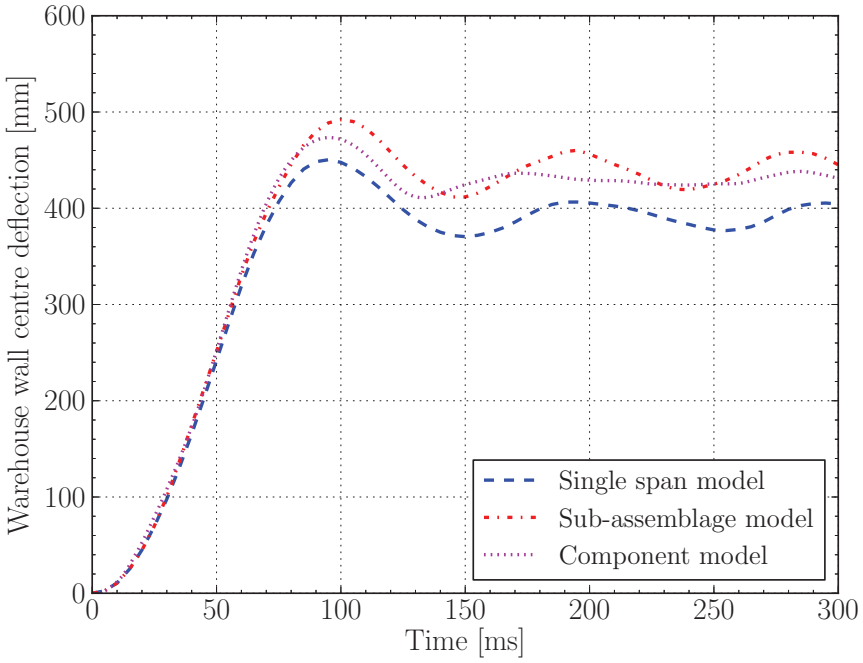


Figure 5.13: Comparison of displacement histories of side wall models

The predicted displacement time histories at the middle of the central side rail are shown in Figure 5.13. It can been seen that the numerical models produced very similar displacement time histories. Results from the double span full model were not included here. It is because the rigid M12 bolt-cleat connection assumption made in this model caused substantial deformation and rotation of the column flange. This is not typical in reality since the connection would fail

before significant deformation or rotation of the flange occurs.

Among the presented three numerical models, the sub-assemblage model offers the most advantages. It requires ten hours to run the simulation which makes validation and parametric studies viable. Moreover, it considers the cladding and side rails at the same time and could provide additional failure information regarding the self-tapping screw fasteners and cleat connections as well. The sub-assemblage model therefore has been chosen as a representative sub-structure of the warehouse building to be used in subsequent studies.

5.6 Validation of sub-assemblage model

The sub-assemblage model has been shown to be at a suitable level for the present work. Validation of the model was performed against a series static tests carried out as part of separate project at Imperial College (Elghazouli et al., 2014).

5.6.1 Tests on cladding-side rail assemblage

The corrugated sheeting and side rails used in the full scale test are very similar to those used in the selected warehouse building described previously. The configuration is exactly the same, and the assembly consists of three side rails and single layer claddings which are continuous over two spans. The test assemblage has dimension of 2.69 $\times$ 4.17 m. The set-up of full scale test is shown in Figure 5.14. It should be noted that in the test only six actuators were used to apply the load. The three actuators shown in the middle of Figure 5.14 were deactivated. In the full scale static test, multi-point loadings were as an approximation of uniformly distributed pressure loads.

Self-tapping screws S-MP 52 Z 6.3 $\times$ 25 supplied by Hilti were selected for the test program. The screw shaft has a length of 25 mm and diameter of 6.3 mm. The screw head diameter is 10 mm. European standard channels UPN 100 $\times$ 50 were selected for the side rails. Its cross-section is 100 mm high and 50 mm wide. The thickness of the web and flange are 6.0 and 8.5 mm, respectively. Corrugated panels TR35/207 (provided by Taborsky roof and wall systems) were used in the test assemblage. The profile of the cladding is shown in Figure 5.15.

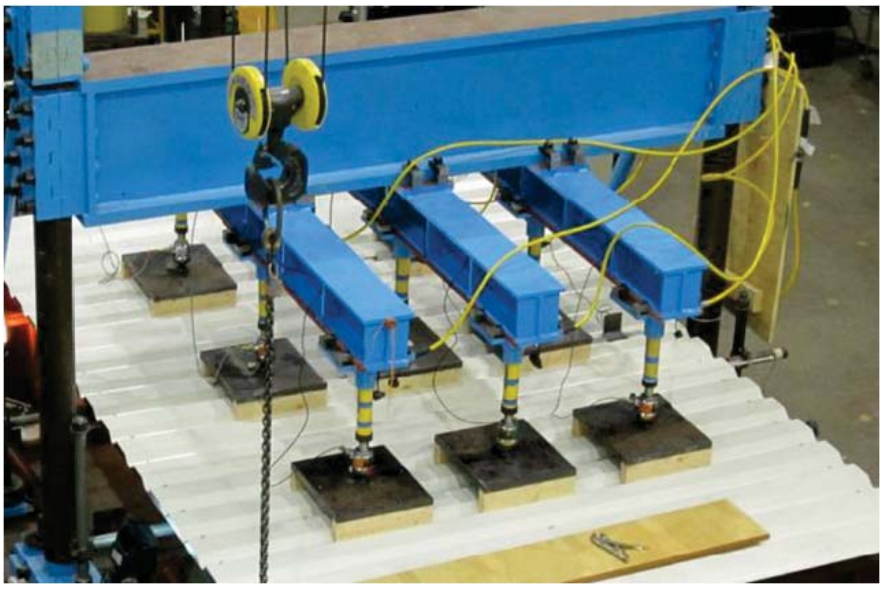


Figure 5.14: Full scale test configuration of cladding-side rail assembly (Elghazouli et al., 2014)

The sheeting has a thickness of 1 mm. The side rails were connected to HEB-200 columns by angles of size L 80 × 80 × 7 mm.

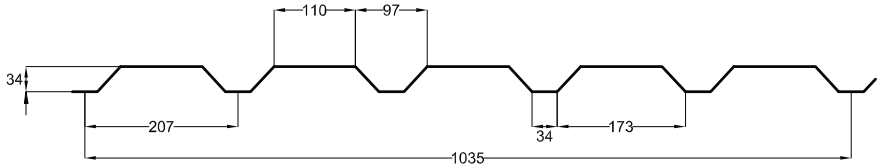
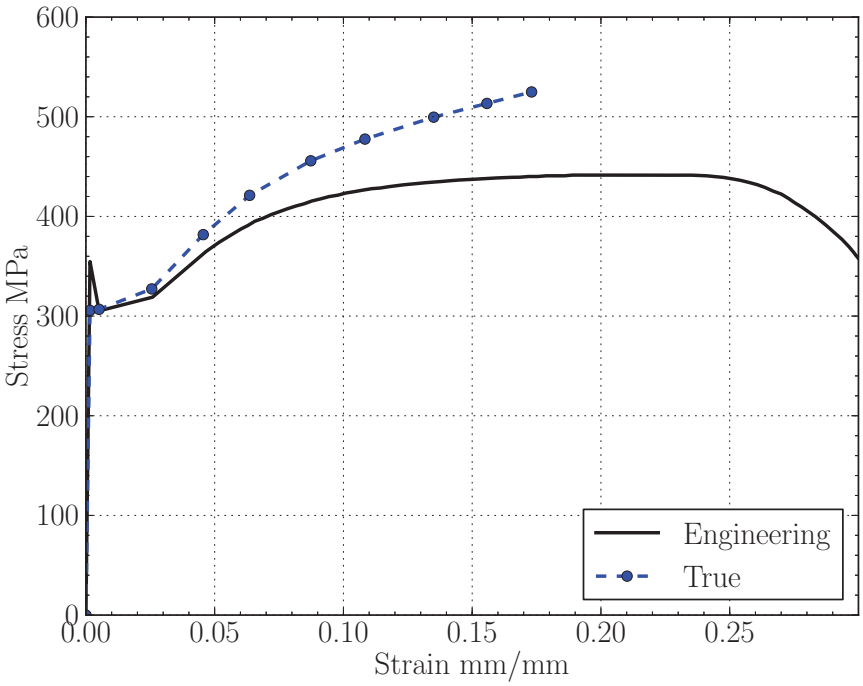


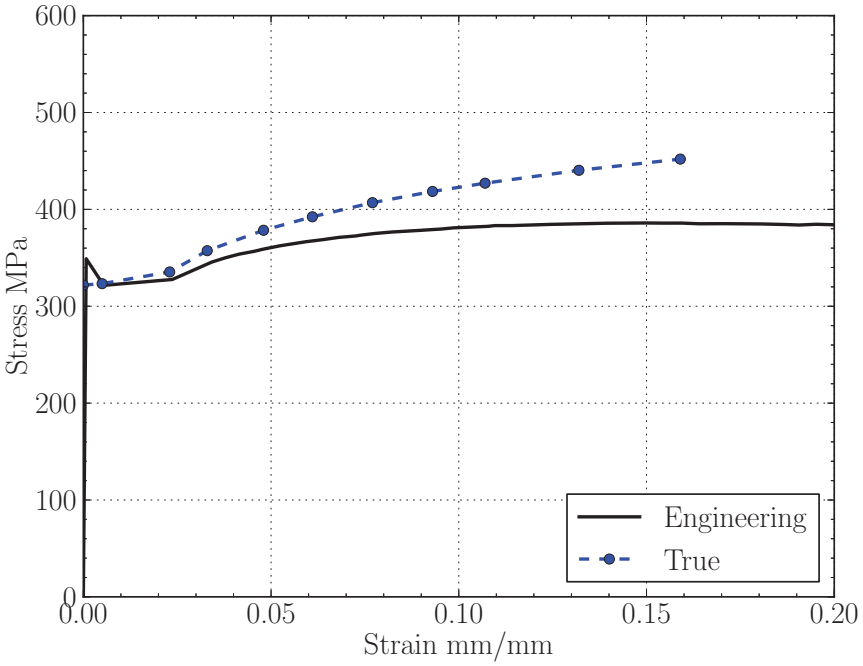
Figure 5.15: Profile of cladding TR35/207 (thickness=1 mm) [unit:mm]

Tensile coupon tests on specimens from the sheeting and side rails were carried out to determine the material properties of the components. The stress - strain curves obtained from the tensile tests are shown in Figure 5.16. True stress and strain curves which have been used in the non-linear finite element model were subsequently determined and compared with the engineering stress-strain curves from coupon tests in the same figure. The material properties of self-tapping screw used in the test were assumed to be equivalent to Grade 8.8 steel.

Figure 5.17 shows the set-up of the numerical model using shell elements that was created in **?** for the full scale test, in which there were six actuators used



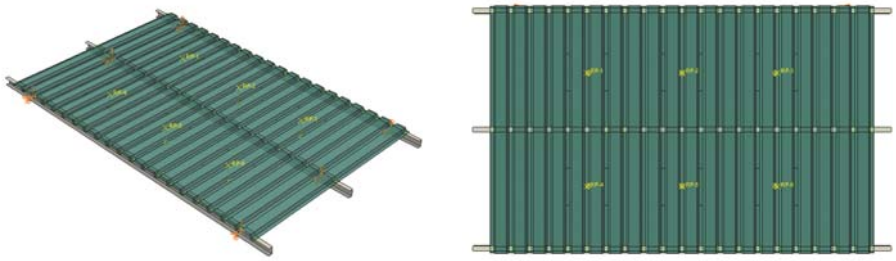
(a) UPN 100 × 50



(b) Cladding TR35/207

Figure 5.16: Material models for cladding and side rail

at the middle position of the cladding. The six actuators were not included in the model for simplicity. Instead, the actual loading areas corresponding to each loading plate (contact area between cladding and plywood in the load distribution unit) were rigidly tied to a reference point (RP) at the location of the loading jack. The load was then applied directly on the reference point and transferred uniformly to the relevant areas of the cladding. Fasteners were modelled by connectors and assumed to be rigid. The connections betweens the side rails and the main frame are semi-rigid, thus for simplicity in the numerical model simply supported boundary conditions with axial constraints were used.



(a) General view (b) Plan view

Figure 5.17: Numerical model used for validation

A uniform mesh consisting of shell elements of type S4R with 5 mm size was used for this finite element model (as shown in Figure 5.18). Rigid connectors (with local coordinates) used to model the self-tapping screws are also shown in the figure.

The loads were applied directly (force control) and the displacement response of the model was determined by static (Newton-Raphson), modified Riks (arc length method) and explicit methods.

5.6.2 Numerical simulations

Two displacement results were obtained from the numerical models for the test. One was obtained at the centre of the cladding assembly. The other was the displacement of the Actuator 1 (RP-1 as shown in Figure 5.17b).

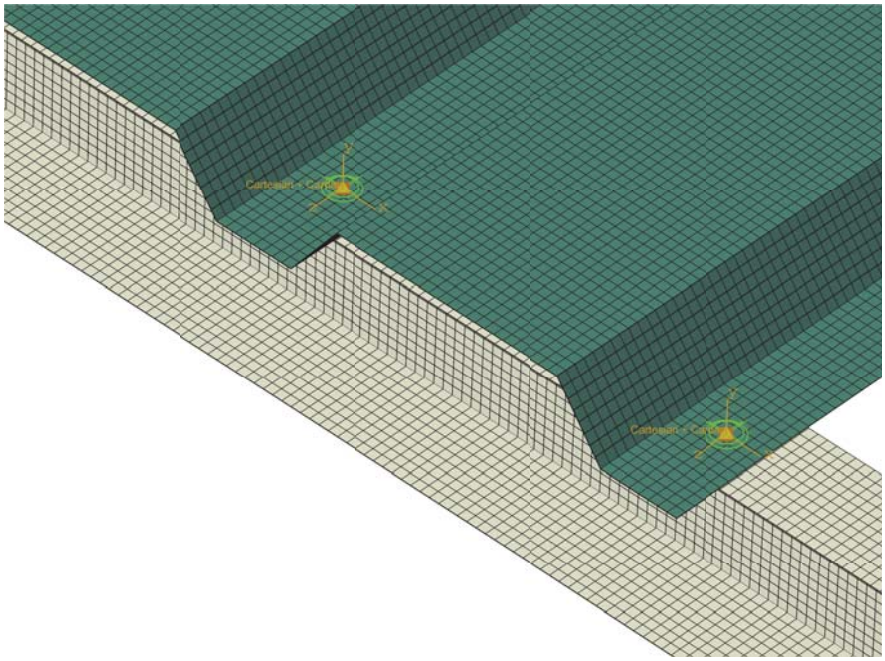
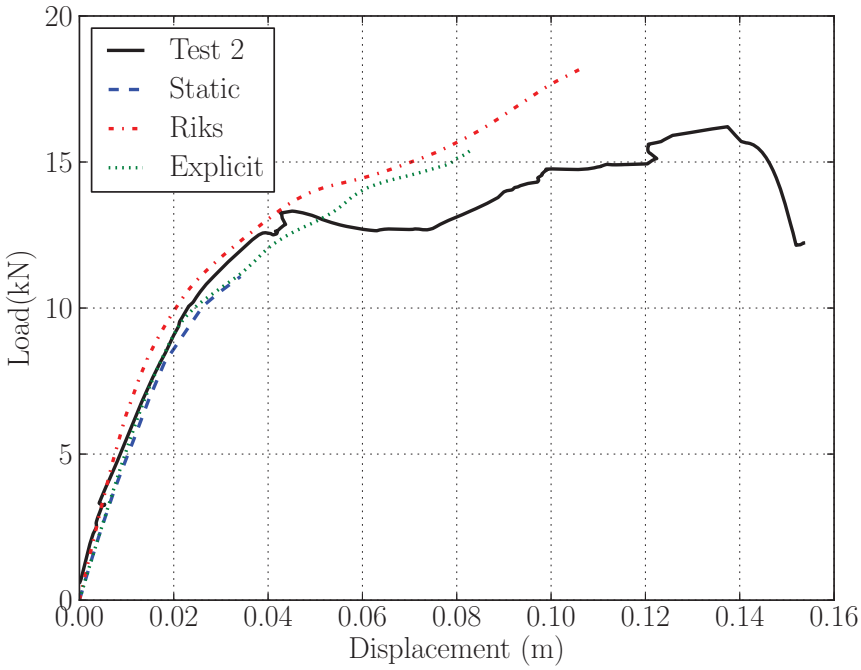


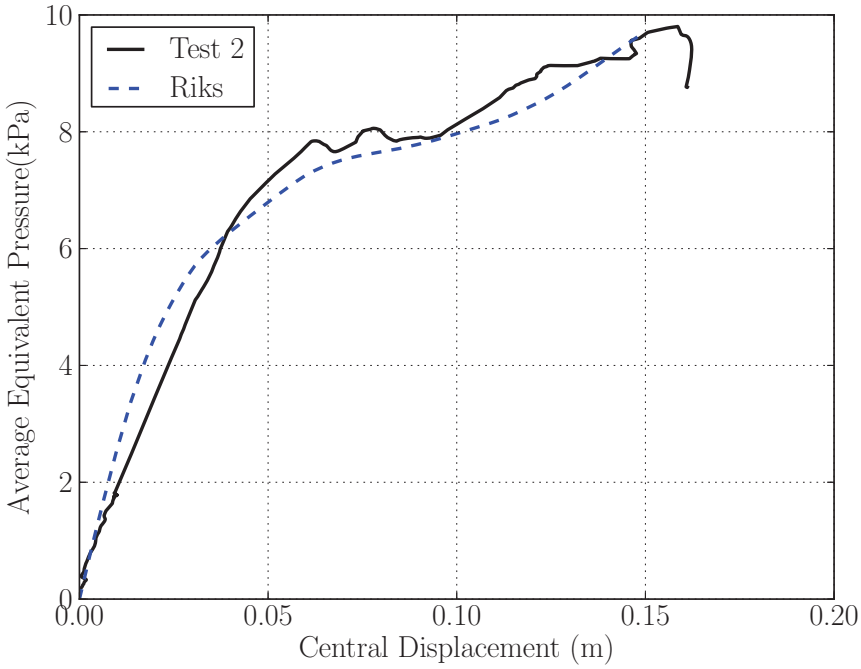
Figure 5.18: Mesh of test assembly numerical model

Figure 5.19 shows comparison between the numerical results and the test measurements. The numerical load - displacement responses of one actuator located at the corners (either RP-1, RP-3, RP-4 or RP-6 in Figure 5.17b) are compared with the experimental data in Figure 5.19a. It is evident that all three solution methods are able to accurately capture the stiffness of the cladding at the location of the Actuator 1. However the static method was interrupted just before local buckling occurred due to convergence difficulties. Although the Riks and explicit methods advanced beyond the buckling point, the loads predicted were much higher than the test (there was no softening in the numerical models). This is mainly due to their inability to capture exactly the local buckling that occurred in the cladding panels locally around the actuators. Also, the rigid fasteners used in the numerical model might affect the local responses as some fastener failures occurred during the loading in the test.

Ideally, the assemblage should be subjected to a uniformly distributed load over the surface, thus the total loads applied by all the actuators were divided by the area of the assembly to determine an equivalent pressure load for both the numerical model and the experiment. These equivalent pressure loads are

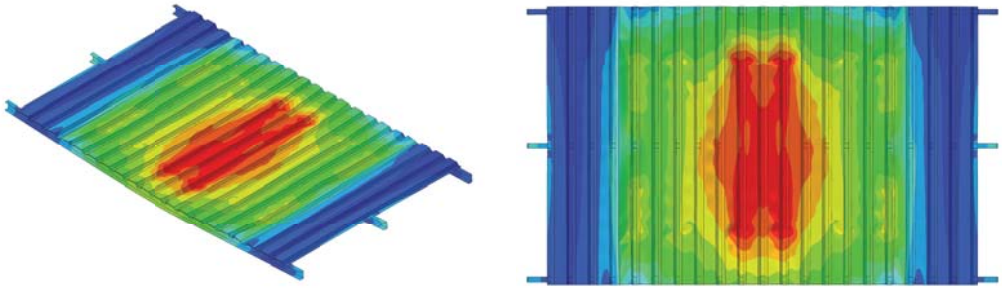


(a) load - displacement of Actuator 1



(b) total pressure - displacement

Figure 5.19: Comparison of numerical results and experimental measurements



(a) isometric view (b) plan view

Figure 5.20: Deformed shapes of test assembly (Riks method)

plotted versus the displacements obtained at the centre in order to examine the global response of the assemblage. A comparison of the global response between numerical model (Riks method) and the test is shown in Figure 5.19b. It can be seen that the overall response predicted by the numerical model compares well with the test. The numerical model had slightly higher stiffness and did not pick up the softening due to localised buckling of cladding panel. The deformed shapes determined by modified Riks method are shown in Figure 5.20.

It has been introduced previously a full scale static test was carried out for the cladding assemblage. The total loads applied by the actuators in the test were converted to equivalent pressures and plotted versus the central displacements as shown in Figure 5.21. A couple of further numerical simulations were carried out in which the multi-points load was replaced by uniformly distributed pressure load. Numerical responses of the models subjected to pressure load are compared with converted test results in Figure 5.21.

As expected, for the static method, the response terminated before the buckling point where the tangent stiffness approaches zero. Both Riks and explicit methods advanced beyond the buckling point and captured some softening response in the plastic regions. The stiffness of the assemblage predicted by these numerical models compares reasonably well with the test. The stiffnesses predicted by the numerical models were slightly larger than the test. This might be due to in the test the actuators acted only on the claddings, hence the resulted stiffness and capacity are both lower than in the numerical model. It is evident from the graph that the overall responses of the numerical models compare

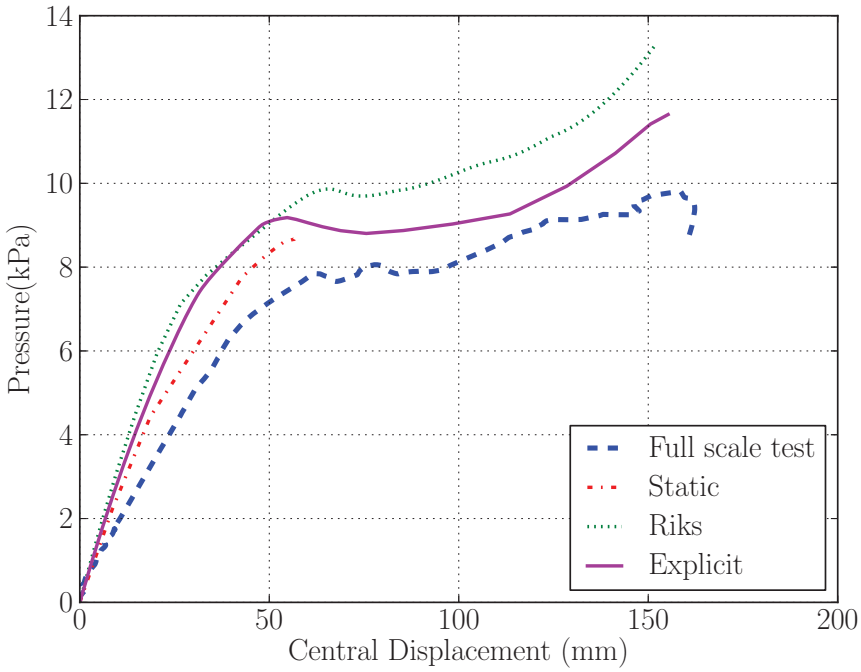


Figure 5.21: Comparison of pressure - central displacement responses

generally well with the full scale test.

After establishing that the sub-assemblage model is able to represent the overall response under static loads, it is important to recall that a number of assumptions were used, as follows: (1) the fasteners were assumed rigid and (2) the side rails were simply supported with axial constraints. The components used in the test were not the same as in the selected warehouse building design and the loads were multi-point rather than uniform pressure. Nonetheless, the work presented in this section indicates the validity of the numerical approach to model a sub-assemblage consists of three side rails and claddings. Further improvements in the sub-assemblage model, particularly with respect to the fasteners and connections are discussed in the following sections.

5.7 Refined sub-assemblage model

In this section, the sub-assemblage model discussed and validated above of the selected warehouse design is refined as illustrated in Figure 5.22. The rigid con-

nectors and simply supported conditions are replaced by connectors with suitable characteristics (represented by translational and rotational springs). The response of the connector models of the fastener is governed by springs k_x, k_y and k_z in three directions, including the stiffness, plastic hardening, damage and failure. Similarly, the response of connector models for the M12 bolt-cleat connections are defined by springs K_x and $K_{\theta y}$, but only including the stiffness and plastic hardening. The following sub-sections describe the procedures adopted to determine the appropriate parameters for these springs.

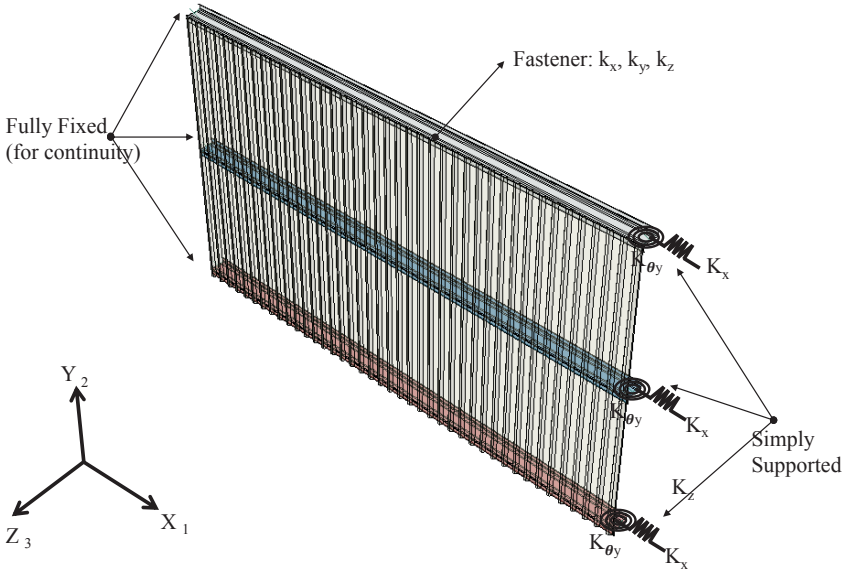
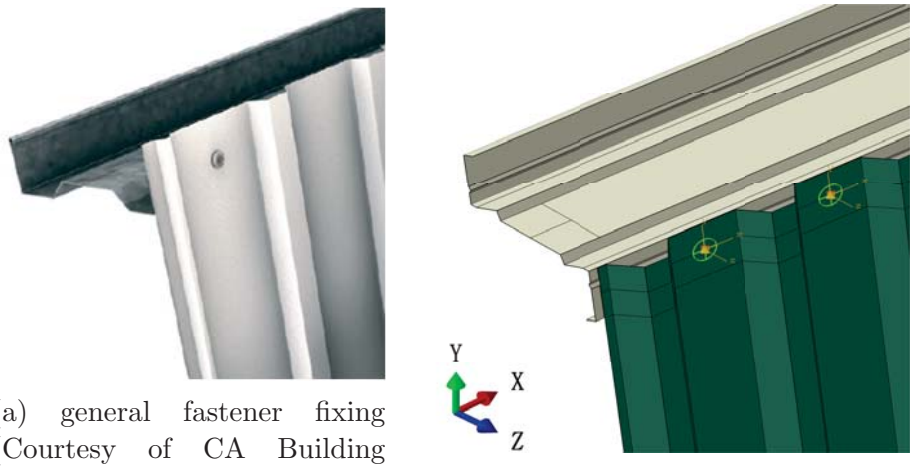


Figure 5.22: Details of sub-assembly model representing the side wall of warehouse

5.7.1 Fastener model and validation

A general fastener fixing is shown in Figure 5.23a, and the numerical connector models which replicate the actual fixings is depicted in Figure 5.23b. Each connector axes has its own local coordinate and in this case it is coincident with the global axes. The connector consists of two inter-connecting nodes, one located at the cladding panel and the other is at the flange of the side rail directly

beneath the first one. Each connector node has an effective radius shown as a green circle in the figure, and the connector forces are uniformly distributed to the nodes of the shell elements within the radius. The effective radius is usually defined to be equal to the radius of the screw head. The connector used here has six degrees of freedom $\{u_x, u_y, u_z, ur_x, ur_y, ur_z\}$ and six corresponding forces $\{f_x, f_y, f_z, m_x, m_y, m_z\}$.



(a) general fastener fixing (Courtesy of CA Building Products)

(b) connector model of fastener

Figure 5.23: Self-tapping screw connector model

There are two types of responses associated with the fastener fixing: one is a shear response in the x-y plane and another is the tensile response in the z-axis direction. The shear behaviour in one direction (along either the x or y axis) is simply equivalent to a lap-joint of two thin steel plates joining the cladding panel and the flange of the side rail. A lap-joint using claddings and fasteners from the full scale static test was used to determine the response of the fastener fixing in an uniaxial tensile test. The test configuration and specimen dimensions are shown in Figure 5.24a. A steel plate of thickness 8 mm was used to represent the 8.5 mm thick flange of a beam of size U100. The tightening torque of the screw was set to 5 Nm (Elghazouli et al., 2014).

Figure 5.24b shows the half finite element model of the lap-joint under uniaxial loading taking advantage of symmetry. Solid elements C3D8R were used to mesh the models. The numerical screws were subjected to an axial pre-tension

determined from the tightening torque, according to the following relationship:

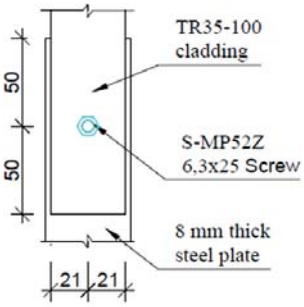
$$T = KDF \tag{5.1}$$

Where T is the tightening torque, D is the diameter of the screw shaft and F is the axial pre-tension in the shaft. K is the torque coefficient ranging from 0.2 to 0.22. Therefore, the axial pre-tension (F) determined with K=0.2 was 3.97 kN. Numerical results from quasi-static analysis (explicit) are compared with the test result in Figure 5.24. Generally, the numerical response compares well with the test measurements particularly at the ultimate shear capacity. The stiffness of the numerical model is greater than the test possibly due to some slip at the pulling head clamping the 1 mm thin sheeting. It was observed from the test that the failure mechanism was dominated by bearing of the clad sheeting and the finite element model showed the same failure mode. No material damage parameters were available, therefore the post-failure behaviour (softening) was not captured by the numerical model. However, it is evident from the comparison that the stiffness and ultimate shear capacity predicted from the lap-joint numerical model are generally reliable.

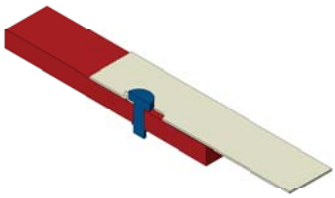
The above validated lap-joint model was then used to obtain the shear response of the fastener fixing for the selected warehouse design in the present project. The thickness of the plates and the diameter of the screw were modified accordingly, and the resulting finite element model is shown in Figure 5.25a. The shear response determined by the numerical model is presented in Figure 5.25b, and an idealised response was assumed based on the numerical response including hardening, damage and failure. The stiffness and the slope of plastic hardening were fitted according to the results shown in the figure.

In the absence of a material damage definition, it was necessary to estimate the ultimate shear capacity and the plastic deformations at which the ultimate capacity (also referred to as damage initiation) and final failure occurs. To this end, Fan (Fan et al., 1997) has carried out a large number lap-joint pulling tests with plate thickness ranging from 0.63 - 8.0 mm and a screw with diameter of 6.3 mm. The experimental results showed that the ultimate shear capacities of lap-joint connections and the plastic deformations where they occurred are dependent

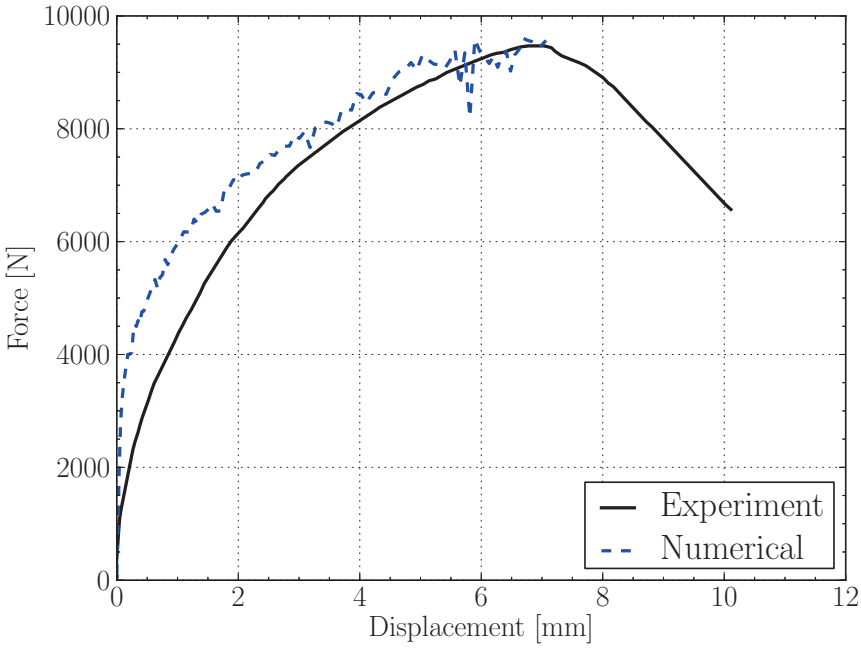




(a) test configuration (Courtesy of Prof Elghazouli,ICL)

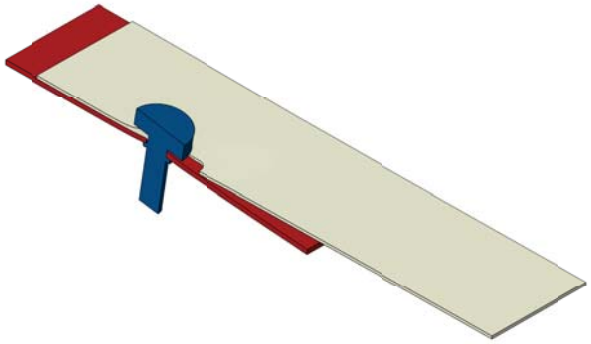


(b) numerical model

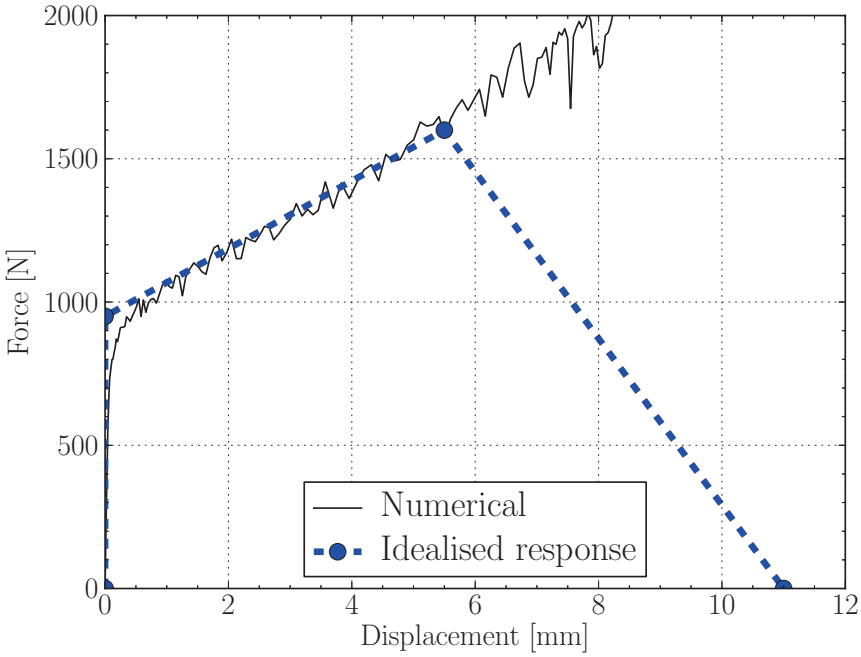


(c) comparison of results

Figure 5.24: Lap joint pulling test using static test components (validation of detailed fastener model)



(a) numerical model



(b) idealised connector response

Figure 5.25: Shear response estimation of the fastener for connector model

on the rotation of the screws, which is in turn dependent on the thickness ratio of the top and bottom plates in the lap-joint. With minor screw rotations (when the ratio of the thickness of top plate to bottom is less than 1), the ultimate capacities usually occur at plastic deformations between 5 - 7 mm. This range is in the proximity of the screw diameter of 6.3 mm. The ultimate shear capacity occurred at a plastic deformation of about 7 mm for the lap-joint test shown in Figure 5.24c, which is also close to the screw diameter of 6.3 mm.

For another study, Lim (Jin-seong et al., 2013) examined the structural behaviour of single shear bolted connections using high strength M12 bolt and 3 mm thickness steel plates. Their results suggested that although the plastic deformations where the ultimate shear capacities occurred can be dependent on the distance from the bolt to the end of plate, the values were still well in proximity of the bolt diameter.

As a result of the observations from tests, it was assumed that for the numerical shear response shown in Figure 5.25b the ultimate shear capacity occurred at 5.5 mm (equivalent to the diameter of the screw). It is difficult to estimate the plastic deformation at total failure of the fastener joint, therefore it was assumed that the failure deformation is twice that of the screw diameter (11 mm). Accordingly the idealised shear response of the numerical fastener lap-joint model can be completely defined as shown in Figure 5.25b. The elastic modulus was estimated to be 9.5 MN/m with a yield shear force of 950 N. The tangent modulus was fitted to be 118.2 kN/m. The connector damage initiation was estimated to be 5.5 mm with the corresponding ultimate shear capacity of 1600 N. Finally, the connector was assumed to fail at a plastic deformation of 11 mm.

5.7.2 Coupled response of fasteners

The uniaxial shear response of the fastener fixing has been defined in the previous section. This response was obtained only in either x or y direction by a lap-joint model. However the fastener joint is indeed axisymmetric, hence the shear response should be identical in any direction in the x-y plane. In this sub-section, a procedure is presented to couple the response in the x and y directions so that the shear response can be identical in any direction in the x-y plane. In

addition, the uncoupled tensile response is also presented to complete the response definition of the connector model for the fastener fixings.

- *Coupled shear response*

The orientation of the connector model for the screw fixings is shown in Figure 5.23b. The connector model has six degrees of freedom, $\{u_x, u_y, u_z, ur_x, ur_y, ur_z\}$ and six corresponding connector forces and moments $\{f_x, f_y, f_z, m_x, m_y, m_z\}$. Uncoupled elastic behaviour was assumed for the connector. The same shear elastic modulus was used for the two shear directions (x and y) based on the assumption of isotropic sheets and isotropic cross section of the screw joints. The elastic behaviour was assumed to be rigid in the axial direction (z-axis) and for the three moment components. The moments exerted in the fastener model were neglected for simplicity.

A connector potential was defined in **?** to describe the plastic behaviour of the connector as shown below, in which F_N is the equivalent tensile (normal) force and F_S is the equivalent shear force.

$$P = \left\{ \left(\frac{F_N}{R_N} \right)^{\beta} + \left(\frac{F_S}{R_S} \right)^{\beta} \right\}^{1/\beta} \tag{5.2a}$$

$$F_N = |f_z| + \frac{K}{r} \sqrt{{m^2}_x + {m^2}_y} \tag{5.2b}$$

$$F_S = \sqrt{{f^2}_x + {f^2}_y} \tag{5.2c}$$

where $\beta = 2$. Assuming $F_N = 0$ (i.e. decouple the tensile force) and ignoring the F_N term in the potential P which can be redefined as:

$$P = \sqrt{\left(\frac{f_x}{R_S} \right)^2 + \left(\frac{f_y}{R_S} \right)^2} \tag{5.3}$$

R_S is defined as the yield force of the connector. Equation 5.3 implies that the redefined shear potential P is a quadratic function of the connector force f_x and f_y, and both of the two forces contribute to the equivalent shear force P

simultaneously. The yield function is then defined as:

$$\Phi(\{f\}, \bar{u}^{pl}) = P(\{f\}) - F^0(\bar{u}^{pl}) \leq 0 \tag{5.4}$$

where $\{f\} = (f_x, f_y)^T$ is the collection of the two connector forces active in the yield function. F^0 is the equivalent yield shear force and defines the yield surface size as a function of the equivalent plastic relative motion $\bar{u}^{pl}$, using a hardening law in **?**.

If yield occurs, the associated plastic flow rule is used to calculate the plastic relative motion as:

$$\left\{\dot{u}^{pl}\right\} = \dot{\bar{u}}^{pl} \frac{\partial \Phi}{\partial \{f\}} \tag{5.5}$$

where $\left\{\dot{u}^{pl}\right\} = \left\{\dot{u}_x^{pl}, \dot{u}_y^{pl}\right\}$ is the collection of plastic relative motion rate in the components active in the yield function. $\dot{\bar{u}}^{pl}$ is the equivalent plastic relative motion rate and is defined as:

$$\dot{\bar{u}}^{pl} = \sqrt{\frac{\left\{\dot{u}^{pl}\right\}^T \left\{\dot{u}^{pl}\right\}}{\frac{\partial \Phi}{\partial \{f\}^T} \frac{\partial \Phi}{\partial \{f\}}}} \tag{5.6}$$

The equivalent plastic relative motion $\bar{u}^{pl}$ is then defined as:

$$\bar{u}^{pl} = \int_0^t \dot{u}^{pl} dt \tag{5.7}$$

And finally the isotropic hardening assigned to the connector as shown in Figure 5.25b is given in Table 5.5 below. The size of the yield surface F^0 is defined as a function of the equivalent plastic relative motion $\bar{u}^{pl}$.

Table 5.5: Isotropic hardening of connector model for fastener joint

F^0(N)	$\bar{u}^{pl}$(mm)
950	0
1600	5.5

A schematic of the equivalent shear response of the connector for the fastener joint is shown in Figure 5.26. The elastic stiffness and plastic isotropic hardening

have been already defined. To describe the failure behaviour of the fastener joint, the connector damage initiation and evolution are defined based on the equivalent plastic relative motion $\bar{u}^{pl}$.

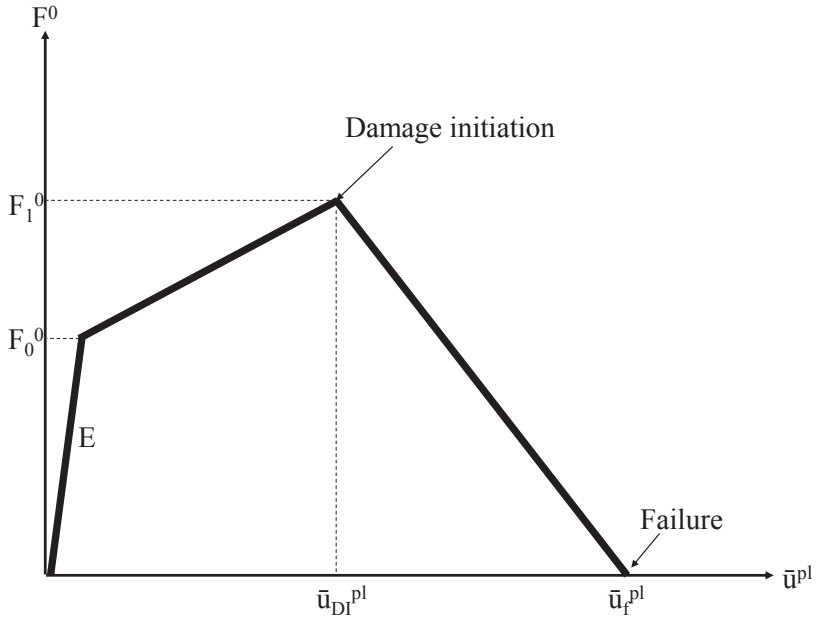


Figure 5.26: Definition of the connector shear response for fasteners

The equivalent plastic relative motion at which damage is initiated $\bar{u}^{pl}_{DI}$ is then defined as a function of the mode-mix ratio Ψ_m in order to consider the dependence of the damage evolution and failure upon the loading direction. The mode-mix ratio is defined in Equation 5.8. It can be seen from the equation that the ratio Ψ_m varies from 0 to 1 depending on the values of f_x and f_y. This is effectively an indication of the direction from 0 to 90 degrees between x and y-axes. $\bar{u}^{pl}_{DI} = 5.5mm$ was then assigned to all values of Ψ_m from 0 to 1 in order to make the damage initiation identical in any direction in the x-y plane. Similarly, the difference between $\bar{u}^{pl}_{DI}$ and $\bar{u}^{pl}_{f}$ the equivalent plastic relative motion at ultimate failure, $(\bar{u}^{pl}_{DI} - \bar{u}^{pl}_{f}) = 5.5mm$, is also assigned for all values of Ψ_m from 0 to 1.

$$\Psi_m = \frac{2}{\pi} tan^{-1}\left(\frac{f_x}{f_y}\right) \tag{5.8}$$

Based on the above, the shear response of the connector model for the fastener joint is fully defined and it is identical in all directions in the x-y plane.

- *Tensile response*

The definition of the uncoupled tensile response in the fastener connector model is relatively simple. The behaviour in the z-axis was assumed rigid and a pull-through capacity was assigned to define a force controlled tensile failure of the connector, in accordance with Eurocode 3 Part 1-3, Section 8:

$$F_{p,Rd} = dwtf_u/\gamma_{m2} = 14 \times 0.7 \times 220/1.25 = 1725N \tag{5.9}$$

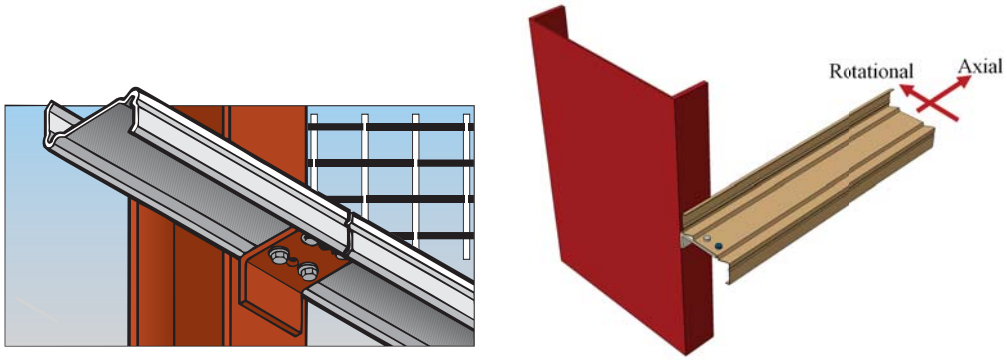
The connector would not fail under a compressive force (negative) and would reach failure once the connector tensile force (positive) exceeds $F_{p,Rd} = 1725N$.

5.7.3 M12 Bolt-Cleat Connection model

Similar approaches have been used to determine the response of the M12 Bolt-cleat connection between the side rails and the primary columns. The configuration of the connection is illustrated again in Figure 5.27a, while Figure 5.27b shows the detailed solid finite element model of the connection. Only half of the column was modelled and fully constrained at the top and bottom. A 1 m length of the side rail was included and connected to the column with two M12 bolts and one steel cleat. The cleat is tied rigidly onto the flange of the column to represent that the cleat is welded onto the flange in the actual structure. The free end of the side rail axial and shear forces were applied to determine the axial and rotational behaviour of the connection.

The axial and rotational responses obtained by quasi-static analysis (explicit) are shown in Figure 6.17. The bearing and shear resistances determined according to Eurocode 3 Part 1-3, Section 8, are shown in Equations 5.10 and 5.11 respectively are plotted in Figure 5.28a as well. The safety factors $\gamma_{\mu 2}$ and γ_{M2} were excluded in order to determine the actual resistances.

The yielding of the numerical model was dominated by bearing of the cladding which is expected due to the high strength of the bolts. However, the approximated numerical yield load is higher than the value determined by codes. This is



(a) design installation (Hadley, 2004) (b) numerical model

Figure 5.27: Finite element model of M12 Bolt-Cleat connection

mainly because the bearing resistance in the design is only based on first yielding of the clad material around the bolt. It can be observed that the numerical axial response is well within the bearing and shear resistances determined from design codes. This suggests that the response obtained from the numerical model offers a good representation.

$$F_{b,Rd} = 2.5 a_b k_1 f_u dt / \gamma_{\mu 2} \quad (5.10a)$$

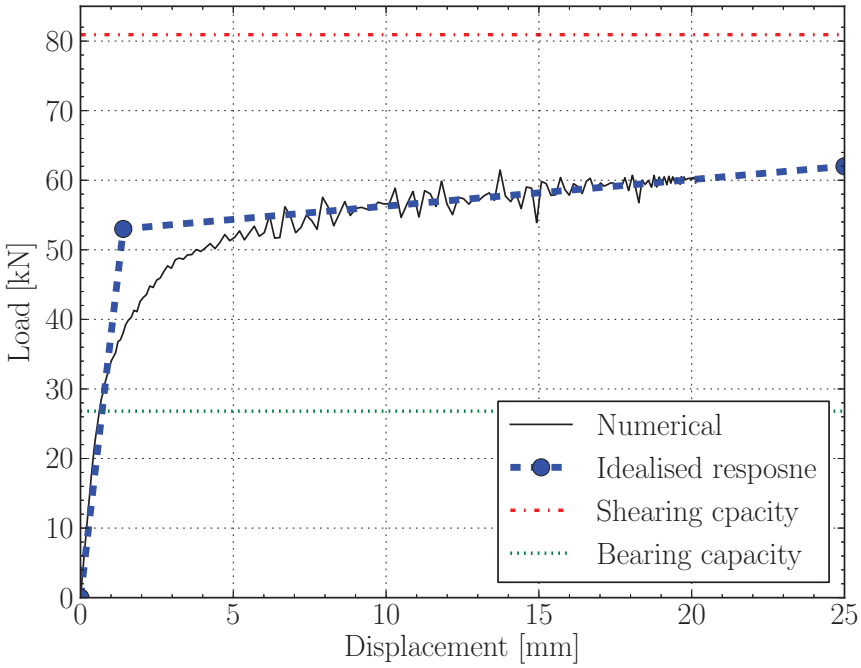
$$k_t = (0.8 \times 1.2 + 1.5)/2.5 = 0.984 \quad (5.10b)$$

$$F_{b,Rd} = 2 \times [2.5 \times 0.833 \times 0.984 \times 470 \times 12 \times (1.2 - 0.04)] = 26.8kN \quad (5.10c)$$

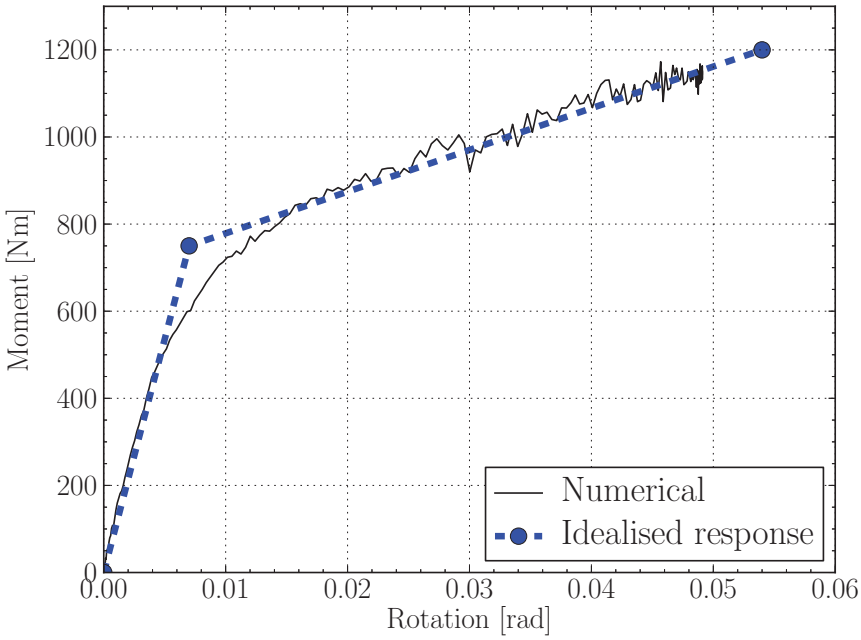
$$F_{v,Rd} = 0.6 F_{ub} A_s / \gamma_{M2} \quad (5.11a)$$

$$F_{v,Rd} = 2 \times [0.6 \times 800 \times 84.3] = 80.93kN \quad (5.11b)$$

Figure 5.29 shows a connector model for the M12 Bolt-cleat connection used in the sub-assemblage model of the warehouse wall. The connector was located on the web of the cladding between the positions of the two M12 bolts. The local orientation of the connector model is shown at the nodes and is coincident with the global coordinates. The connector model also has two inter-connecting nodes; one was rigidly tied to the end cross section of the side rail and the other



(a) axial response



(b) rotational response

Figure 5.28: Response estimation of M12 Bolt - Cleat connection

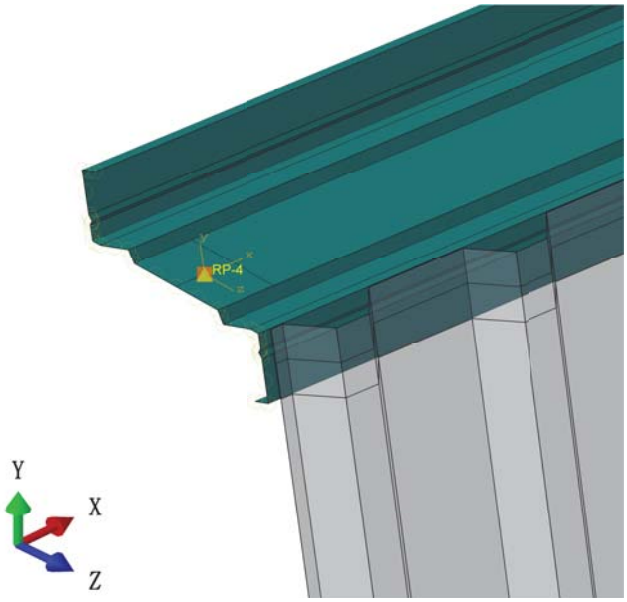


Figure 5.29: Connector model for M12 Bolt-cleat connection

was connected to "ground" (i.e. fully fixed in space at the same position of the first node so that the connector has zero length).

The connector has six degrees of freedom $\{U_x, U_y, U_z, UR_x, UR_y, UR_z\}$ and six forces and moments $\{F_x, F_y, F_z, M_x, M_y, M_z\}$. To simplify the behaviour of the connection, there were only two active degrees of freedoms: axial deformation U_x and rotation UR_y. The behaviour was assumed to be rigid in the translational direction y and z, and for the two rotational components UR_x and UR_z. The rigid response assumption in the z direction of the connector implies that the column supporting the side rails are relatively rigid, which is consistent with the lack of damage in the post-blast observations.

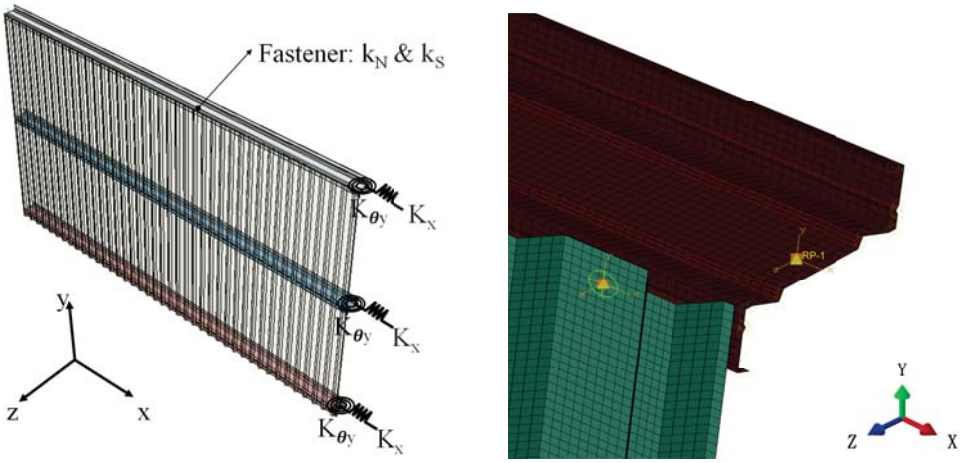
The numerical response in Figure 6.17 was then fitted with a bi-linear curve and assigned to the connector models in the axial and rotational components U_x and UR_y, represented by springs K_x and $K_{\theta y}$ in Figure 5.22. For the axial behaviour, the elastic stiffness was estimated to be 37.85 MN/m and the tangent stiffness as 0.38 MN/m. For the rotational behaviour, the elastic stiffness was estimated to be 107.1 KN.m/rad and the tangent modulus as 9.75 KN.m/rad.

In this sub-section, a sub-assemblage model representing the wall structure of a warehouse building has been presented. The simplified connector models

representing the connection and fastener joints were also described. Validation studies have been carried out against available experimental data in order to ensure the accuracy of the proposed numerical model.

5.8 Complete warehouse sub-assemblage model

The previous section presented details of a typical warehouse design and its components. And Section 5.5 showed all the work that carried out to model a typical wall structure of the warehouse. Various numerical models were developed, validated with available experimental data and simplified for computational efficiency. This section summarises the full sub-assemblage model which was used to study the dynamic response of the wall structure of the warehouse to blast loading.



(a) sub-assemblage model (b) connector models

Figure 5.30: Sub-assemblage model of the wall structure in the warehouse building

The sub-assemblage model is shown in Figure 5.30a again, with translational and rotational springs which simulate the behaviour of self-tapping screw fasteners and M12 bolt- cleat connections between the side rail and column. This sub-assemblage consists of three side rails and cladding panels which are continuous over two spans.

Uniformly distributed dynamic pressure loading was applied on the cladding

panels. The top and bottom side rails were subjected to additional loading accounting for the pressure loads from the neighbouring half-span claddings which were not included in the model. Non-structural masses were used to include the mass of the sheeting and mineral wool infill of the complete cladding panel. Top and bottom side rails were subjected to extra mass as well to take into account the mass from the neighbouring half-span cladding panels. The far end of the side rails were fully fixed to model the continuity of the side rail over a double span. The near end of the side rails were connected to springs which capture the behaviour of the connections (rotational and axial). In the transverse direction, rigid supports were assumed at the ends of the side rails.

In the previous sections, detailed numerical model of the self-tapping screw fastener which fix the cladding panels onto the side rails was created and the shear response was determined. In the sub-assemblage model, the shear response

Table 5.6: Response parameters for connector model of self-tapping screw fastener

	Shear behaviour (k_S)	Tensile behaviour (k_N)
Elastic stiffness	9.5 MN/m	rigid
Tangent stiffness	0.118 MN/m	
Yield capacity	950 N	
Ultimate capacity	1600 N	
Damage initiation	$\bar{u}^{pl}_{DI}$= 5.5 mm	N/A
Total failure	$\bar{u}^{pl}_{f}$= 11 mm	f^{fail}_{z}= +1725 N

was assigned into the connector model as shown in Figure 5.30b. A coupled response was defined so that the shear behaviour in the x-y plane is consistent in any direction. The shear response included elastic-plastic behaviour, damage initiation and final failure, and the defining parameters are presented in Table 5.6. The tensile response of the fastener was decoupled from shear for simplicity. Its behaviour was assumed rigid and failure was triggered by a tensile force (z-axis) criteria set in the same table.

Similarly, a detailed finite element model of the connection between side rails and columns was created, and the axial and rotational responses were determined. The response was assigned to the connector model which represents the connections as shown in Figure 5.30b. The responses were characterised by bi-

linear curves and no damage initiation or failure were pre-defined. The response parameters are summarised in Table 5.7.

Table 5.7: Response parameters for connector model of M12 bolt-cleat connection

	Axial behaviour (K_x)	Rotational behaviour ($K_{\theta y}$)
Elastic stiffness	37.85 MN/m	107.1 kN.m/rad
Tangent stiffness	0.38 MN/m	9.75 kN.m/rad
Yield capacity	53 kN	750 kN.m

In this chapter, observed damages to the warehouse building in the Buncefield incident were briefly reviewed. A typical UK warehouse building was selected as the objective of the current study. Details of the building design and components were described. Non-linear finite element models of the warehouse were developed and a suitable level of simulation was chosen. As a result, a sub-assemblage model representing the wall structure of the warehouse was decided to be used in the study of response of blast loading. Detailed numerical model of fastener and connections were developed and the response was assigned to connector models in the sub-assemblage model. Numerical models have been validated against available test to ensure the accuracy of the numerical results.

A series of simulations have been carried out using the sub-assemblage model to study the dynamic response of the warehouse to blast loading. The results are presented and discussed in the next chapter.

Chapter 6

Response of warehouse structures

In the previous chapter, numerical models of typical warehouse structures were presented and validated with available experimental data. A series of studies were also carried out using the sub-assemblage model. The loading scenarios and numerical results from these studies are presented in this chapter.

6.1 Response measurement and damage levels

It has already been shown that both the component and sub-assemblage models can predict very similar deflections of the side rails. However the sub-assemblage model can provide more detailed information rather than just the displacement at mid-span, as discussed below with reference to Figure 6.1.

The primary output of the model is the displacement history at the mid span of the central side rail. Selected typical deflections of the claddings were recorded. At the mid-span, the deflections of the central cladding are registered by three gauges from top to centre: upper, middle and lower. Similarly, deflections of side cladding to the edge of the model are also recorded by three gauges. Two connectors labelled as central and side fasteners were chosen to be analysed and their locations are shown in the figure. One more connector was also chosen near the support of the central side rail (labelled as the middle fastener). The last connector (labelled as connection) was chosen to study the axial and rotational response of the central side rail.

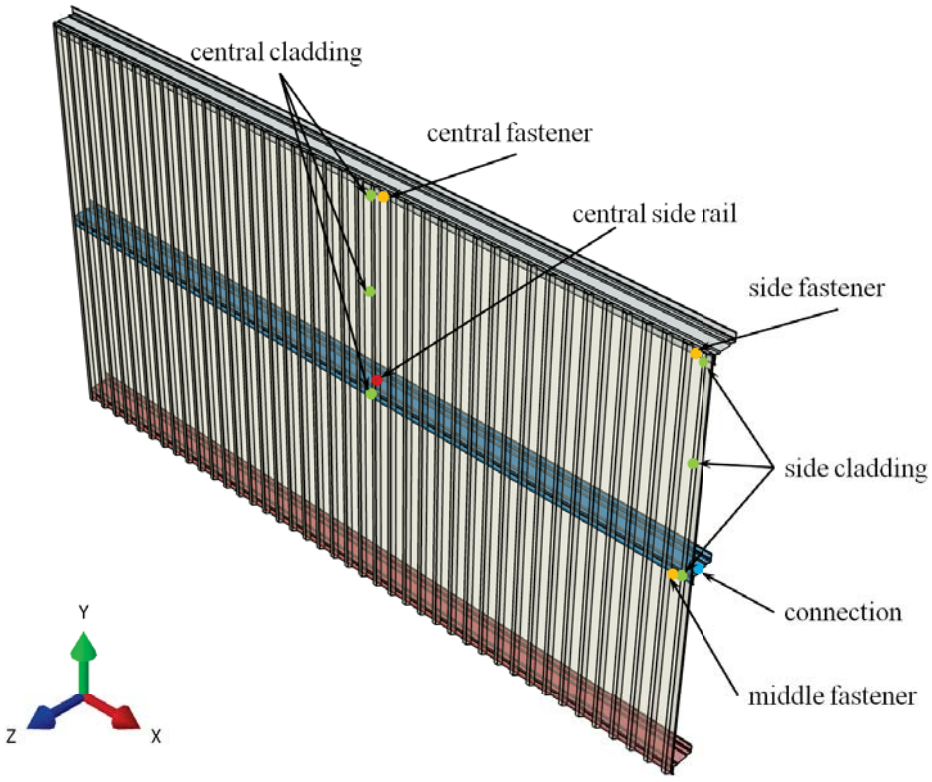


Figure 6.1: Details of sub-assemblage model

In order to restrict the damage to a structure or element which is subjected to incidental dynamic loading, limiting values muse be assigned to appropriate response quantities. These response limits define the performance criteria of the structural components under blast loading. Deformation limits can be defined corresponding to different damage levels. The relationship between the component damage and the response limit are briefly presented below (USACE, 2008b) and (ASCE, 1997).

Deformation limits are defined in terms of the ductility ratio and support rotation for individual structural components. The ductility ratio indicates the component's ability to absorb energy and is defined as the ratio of the maximum mid-span displacement to the displacement at yielding. The support rotation is defined as the tangent of the maximum mid-span deflection over the component's half length. The two response parameters are illustrated in Figure 6.2.

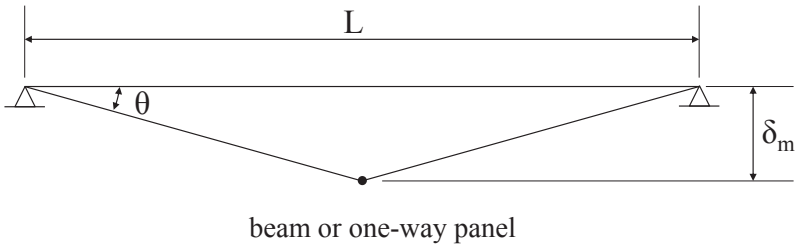


Figure 6.2: Structural component mid-span deflection and end rotation

The ductility ratio μ is defined as $\mu = \delta_m/\delta_e$ where δ_m is the maximum component displacement and δ_e is the deflection at yielding. The support rotation is then defined as $\theta = tan^{-1}(2\delta_m/L)$, where L is the length of the component.

Damage levels of components to a dynamic load are usually defined by reference to a range of ductility and support rotation values to provide upper and lower limits for each damage level. Guidance on response limits for structural components are presented in a number of references (ASCE, 1997), (USACE, 2008b) and (USDOD, 2008). Typical values for cold formed thin wall members are presented in Table 6.1.

[1]TM: tensile membrane

Table 6.1: Response limits for cold formed structural steel members

		moderate		heavy		hazardous	
		μ	θ	μ	θ	μ	θ
side rail and purlin	No catenary action	-	3^o	-	10^o	-	20^o
	With catenary action	-	4^o	-	12^o	-	20^o
corrugated panel	full TM [1] capacity	3	3^o	6	6^o	10	12^o
	some TM capacity	-	1^o	-	4^o	-	8^o
	no TM capacity	1.8	1.3^o	3	2^o	6	4^o

Applying the response limiting values to the components in the sub-assemblage, the limiting values of deflection at mid-span of the side rail and cladding panel are shown in Table 6.2, where $\delta_m = \frac{1}{2}L\tan(\theta)$ ($L = 1800mm$ for cladding and $L = 6690mm$ for side rail). Therefore, the damage levels and limiting response are now based on maximum mid-span deflections.

Table 6.2: Response limits for side rail and cladding panel

damage level	side rail		cladding panel	
	θ	δ_m (mm)	θ	δ_m (mm)
moderate	4^o	234	1^o	16
heavy	12^o	711	4^o	63
hazardous	20^o	1217	8^o	126

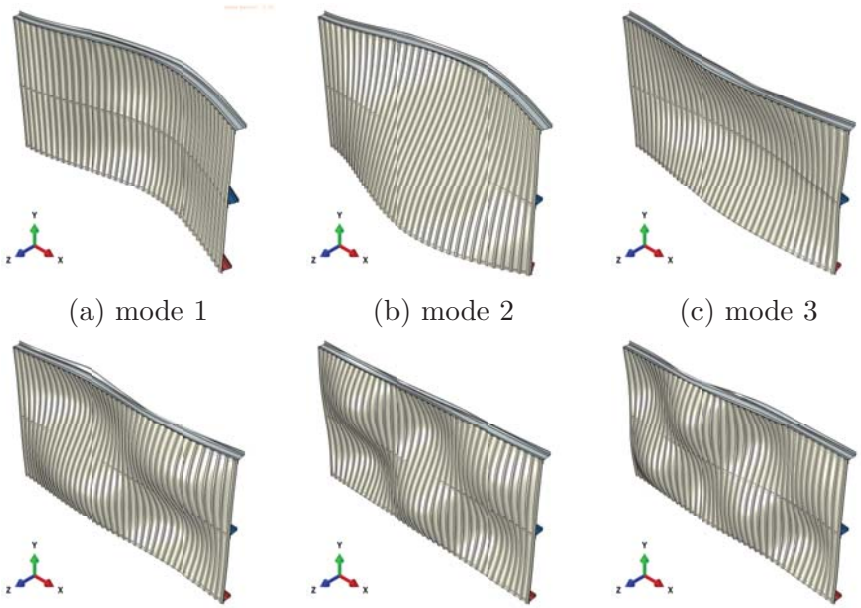
In addition to conventional criteria, the sub-assemblage model can produce two more response parameters: side rail axial displacement and the failure of fasteners. The rotation of the side rail at the support was neglected since the maximum deflection at mid-span is used. For the axial displacement, two limiting values were used: 1.5 mm (connection yield) and 36 mm (connection failure). The yield of the connection occurred at 1.5 mm in the axial direction. The distance between the M12 bolts and end of the side rail is 36 mm, hence the side rail will be pulled out of the connection beyond this axial displacement level.

The ultimate behaviour was also modelled for the self-tapping screw fasteners. During the blast loading, some or all of them would fail at different times due to the structural response and the natural of the loading. The percentage of the fastener failures was defined as the ratio of the number of failed fasteners over the total number of fasteners in the sub-assemblage. This was used as an additional

damage criterion in the current investigation.

6.2 Modal analysis and loading scenarios

Modal analysis was carried out in order to determine the mode shapes and natural frequencies of the sub-assemblage. The highest mode that is relevant to the deformed shape of the structure under blast loading can then be identified. The results of the modal analysis were also used to obtain the natural period of the structure and define the loading scenarios. The first six mode shapes are shown in Figure 6.3. Only the first mode is of most interest since it corresponds to flexural deformation of the sub-assemblage.



(a) mode 1 (b) mode 2 (c) mode 3

(d) mode 4 (e) mode 5 (f) mode 6

Figure 6.3: Sub-assemblage mode shapes

The natural frequencies and periods corresponding to each of the mode shapes in Figure 6.3 are shown in Table 6.3. As already stated, the value for Mode 1 is of most interest given the pressure loading pattern in the current study. The natural periods were used to cover the full spectrum of structural response from impulsive to quasi-static by choosing appropriate blast loading durations.

Table 6.3: Natural frequencies and periods from modal analysis of sub-assemblage model

Model	Natural frequency (Hz)	Natural period (msec)
1	5.6	179
2	5.9	168
3	10.9	92
4	13.5	74
5	14.5	69
6	14.9	67

In the study, the sub-assemblage model was subjected to a series of combinations of blast loadings with varying peak overpressures and impulses. The form of the blast loading is detonation, with linear decay. The peak overpressure value ranged from 1 to 50 kPa. The lower bound is slightly higher than the common wind design value for cladding systems and the upper bound is about 100 times the design value. The duration of the loading ranged from 4 to 20000 ms. Considering that the natural period of first mode of the sub-assemblage is 179 ms, the durations ranged from 0.02 to 110 times the natural period of the sub-structure.

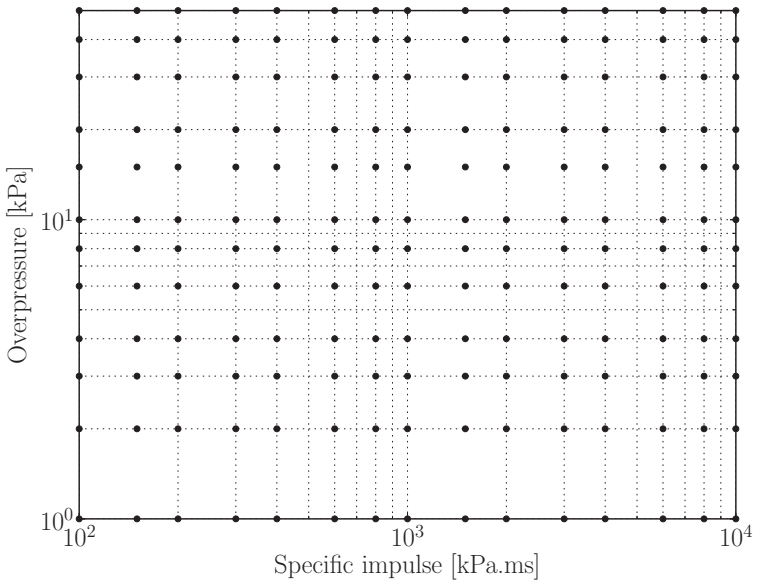


Figure 6.4: Loading scenarios: combinations of overpressure and impulse

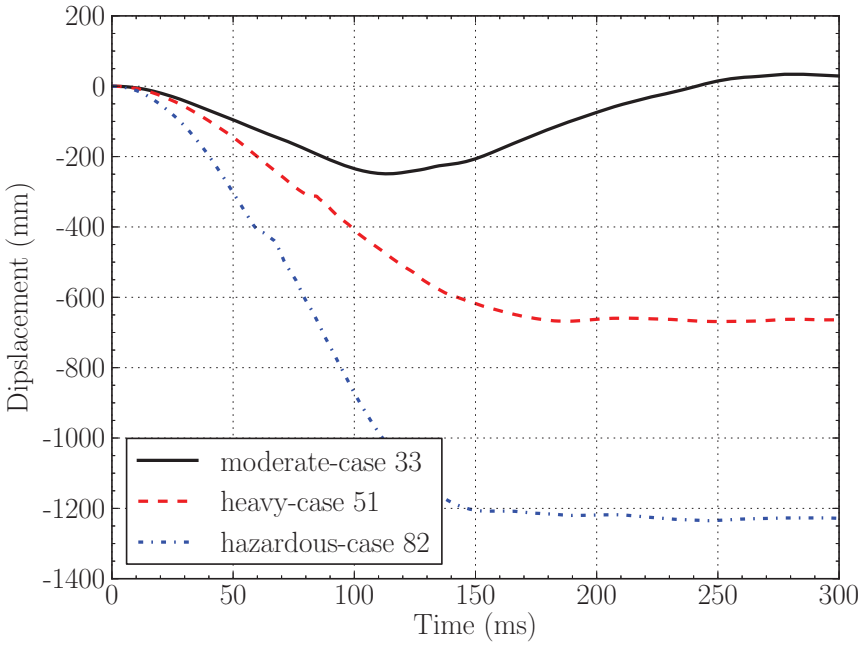
The combinations of overpressures and impulses to define the loading scenarios are presented in the form of pressure - impulse diagrams and shown in Figure 6.4. There were 180 combinations in total. The identification number and corresponding durations for each case are presented in Appendix B for reference.

6.3 Side rail deflection

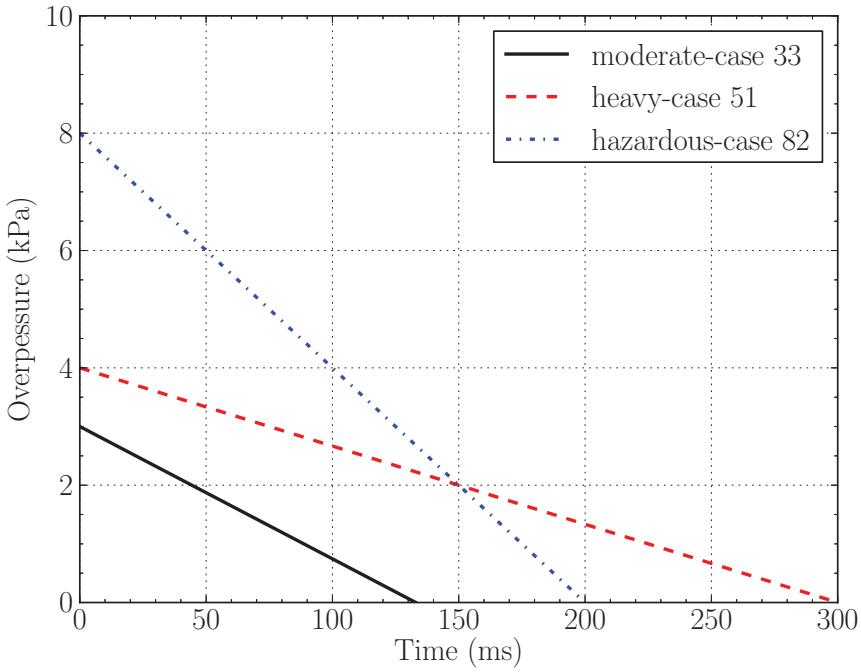
The sub-assemblage model was subjected to combinations of overpressure and impulses as shown in the previous section. An example of the deflection time history at mid-span of the central side rail under three load profiles corresponding to moderate, heavy and hazardous damage is presented in Figure 6.5a. The corresponding load profiles are shown in Figure 6.5b. These three load profiles are corresponding to model Case 33, 51 and 82 (refer to Appendix B).

The three load profiles have durations of 133, 200 and 300 ms, which are in the proximity of the natural period of the first mode of the sub-assemblage, and therefore the loads are in the dynamic response region. The total simulation time was set to 300 ms in order to reduce the running time but still be able to output enough time histories for examination. Each analysis took 12 hours to run on the high performance computer of Imperial College.

Figure 6.6 shows the deformed shapes of the sub-assemblage model at the end of the simulation. This might not be the residual deformations but the maximum dynamic responses available within the simulation time. This numerical analysis took into account the stiffening effect of the membrane action that developed within the connector model of the M12 bolt-cleat connection. The membrane force was controlled by the assigned behaviour of the corresponding connector. However, the model did not include connection failure (the loss of support to the side rail end). Therefore, fictitious failure based on axial displacement was used to interpret the results. In this sub-assemblage model, the side rails were the "primary" components so that the failure at their supports could not be implemented, otherwise the whole model would be lost and the results would be less useful and difficult to analyse.

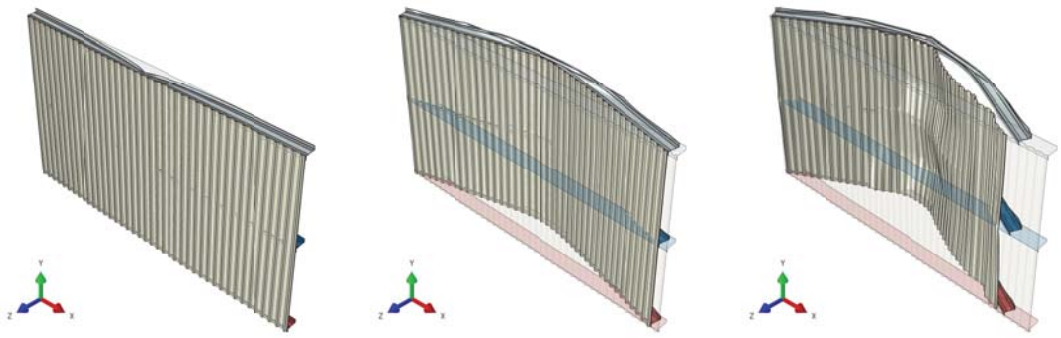


(a) displacement time history



(b) loading profiles

Figure 6.5: Displacement history at the mid-span of the central side rail with loading profiles



(a) Case 33 (b) Case 51 (c) Case 82

Figure 6.6: Deformed shapes of the sub-assemblage

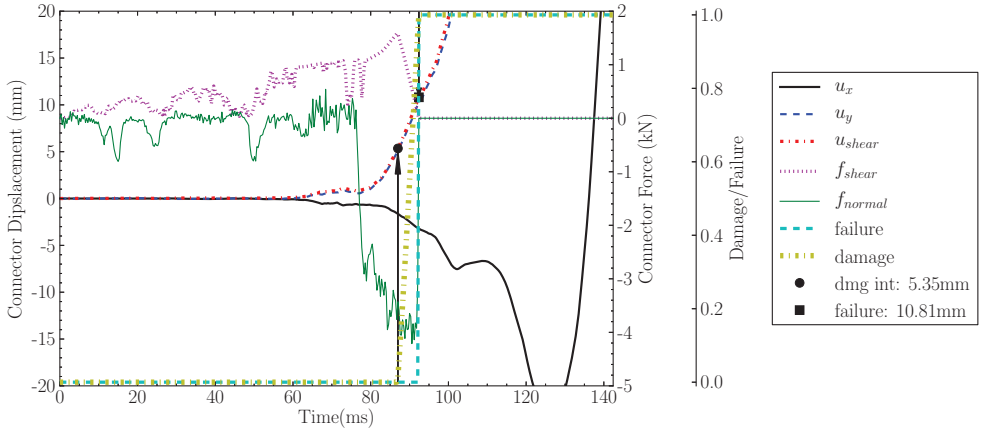
6.4 Cladding and fasteners

The behaviour of fasteners was completely defined in the connector model, including the stiffness, plastic hardening, damage and failure. An example of the detailed response of the central fastener in Case 98 (the blast profile has peak pressure of 10kPa, impulse of 1000kPa.ms and the duration was 200ms) is shown in Figure 6.7. The load defined in this case is dynamic.

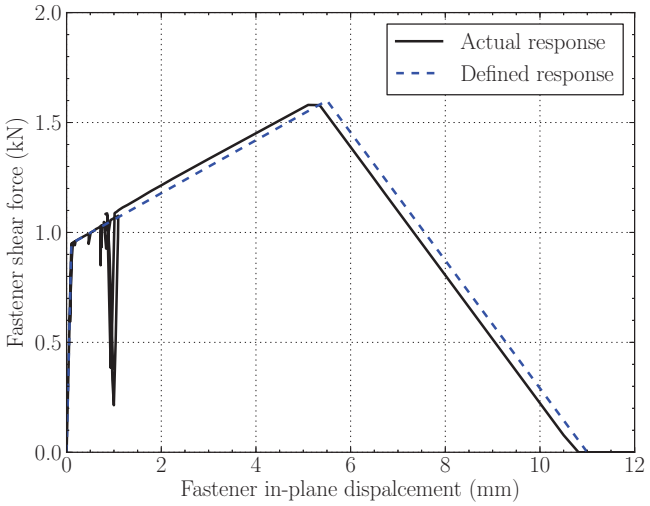
Figure 6.7a presents the details of the time response of the central fastener, which include the displacements, shear and normal forces, damage and failure. The damage history indicates the time of initiation and failure. The resultant displacement (u_{shear}) at the damage initiation and failure were calculated and noted in the figure (5.35 and 10.81 mm). The resultant displacement u_{shear} was defined as $u_{shear} = \sqrt{{u_x}^2 + {u_y}^2}$ by the component displacement u_x and u_y in the x and y direction respectively. The shear force f_{shear} was determined in the same manner, and the numerical relation between shear displacement and force is presented in Figure 6.7b. The numerical shear response is then compared with the pre-defined behaviour of the connector model.

It can be seen that the numerical response of the connector is in good agreement with the pre-defined path except for a short unloading-reloading period. The damage initiated at 5.35 mm and failure occurred at 10.81 mm, and both are very close to the pre-defined values (5.5 and 11 mm). The discrepancies are attributed to the cumulative plastic deformation in the connector during the

variation of shear force, which shifted the hardening curve slightly upwards and subsequently the damage degradation curve to the left. The numerical response path is reasonably clear and the damage initiation as well as failure can be easily identified.



(a) details of fastener time response



(b) fastener response curves

Figure 6.7: Response of central fastener of the sub-assemblage model in Case 98

As shown in Figure 6.7a, the resultant displacement curve u_{shear} is almost identical to the displacement in the y direction u_y, which suggests that the fastener damage and failure occurred in the y direction. The normal force exerted in the connector is also shown in Figure 6.7a, and the results indicate that the

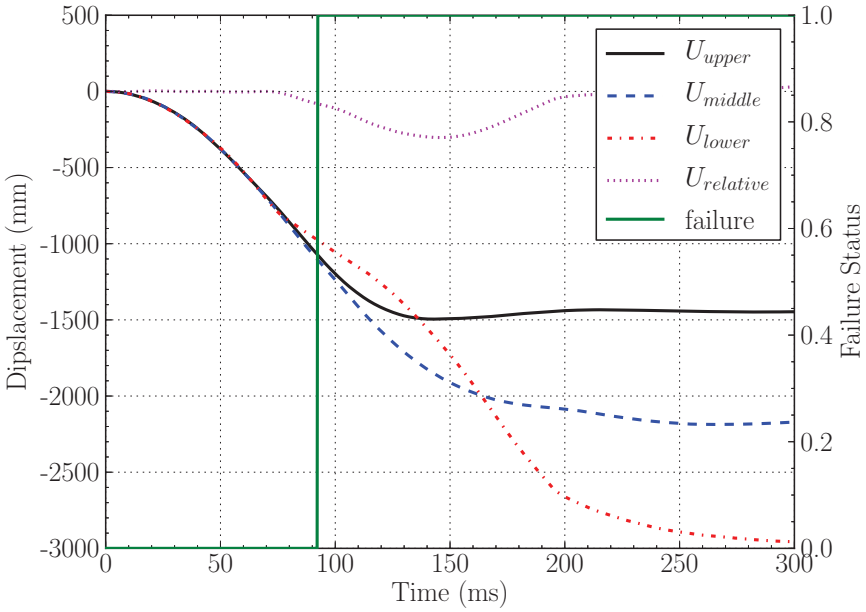
fastener was mainly subjected to compressive force throughout the time history before failure.

The cladding response was measured at three locations as shown in Figure 6.1. An example of the displacement time response of the central cladding subject to blast loading as defined in Case 98 is shown in Figure 6.8. Figure 6.8a shows the displacement time histories at the three locations on the cladding: upper, middle and lower. The displacement at the middle point relative to the average displacement of the upper and lower points, determined as $U_{relative} = \frac{1}{2}(U_{upper} + U_{lower})$, is also shown in the figure. Finally, Figure 6.8a was completed with the failure time history of the corresponding central fastener (presented in Figure 6.7). The relative displacement at the middle of the central cladding was then related to the failure of the corresponding fastener as shown in Figure 6.8b. It can be seen that the shear failure in the y-direction of the fastener occurred at a displacement of -81.66 mm.

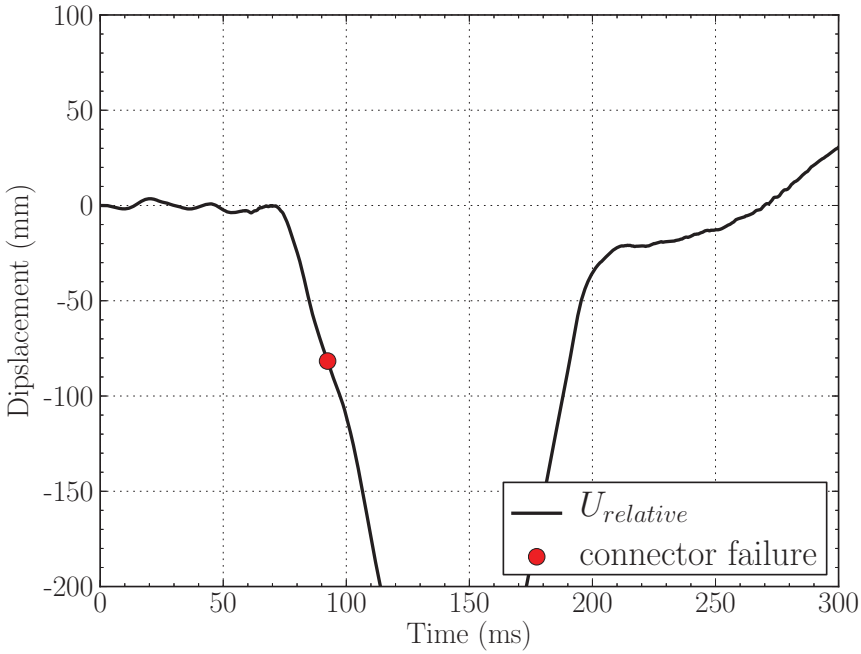
The same analysis was applied to both the side and central claddings of the sub-assemblage in all loading cases. Figure 6.9a represents the relative displacement at the middle of the central cladding with failure of the corresponding fastener for all cases, while Figure 6.9b represents the same results for the side cladding. Thus, these two figures aim to relate the displacement at the middle of the cladding to the failure of end fasteners in the full spectrum of overpressures and impulses.

It is interesting to note that in these two figures the displacement at failure of the fastener varies with the response of the cladding. However, in the Region I of Figure 6.9a, the relative displacement at the central fastener failure was consistently about 81 mm. Similarly, in the Region I of Figure 6.9b the relative displacements at failure of the side fastener was typically about 89 mm. Thus, in general it can be observed that the relative middle displacement at the failure of the corresponding fasteners is approximately $[-81 + (-89)]/2 = -85mm$, although this value only applies to cases in region I in Figure 6.9.

It can be noted that in Region II of Figure 6.9, the results show a very different relation between the cladding displacements and the failure of corresponding fasteners. In Region II of Figure 6.9a the fastener failures occurred much earlier at lower displacements of central cladding. In fact, most of the failure occurred

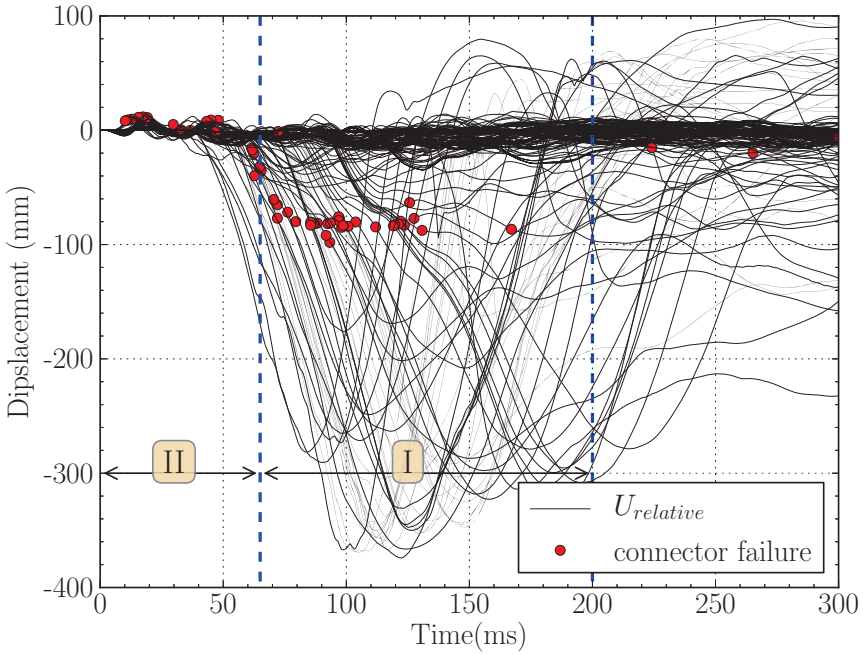


(a) cladding response

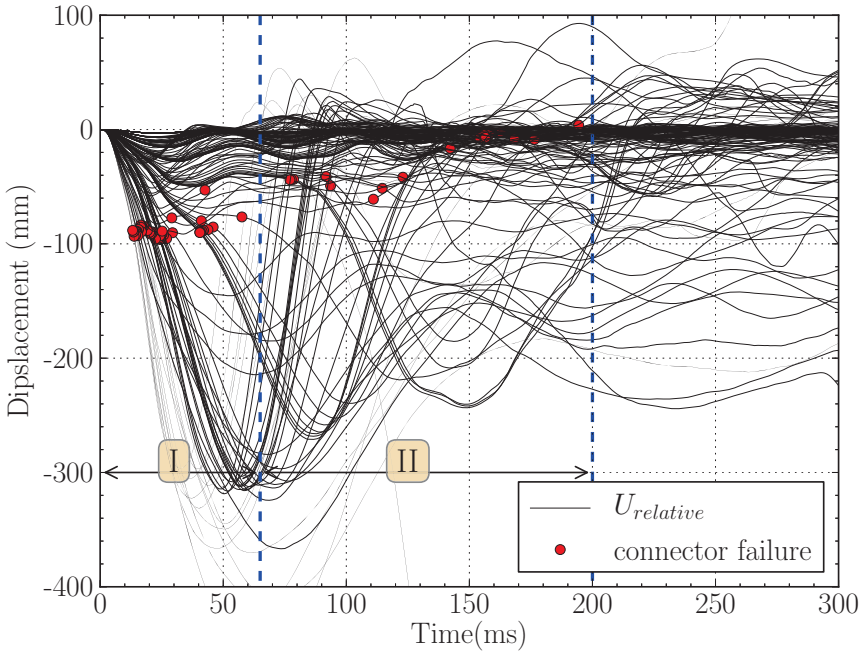


(b) relative displ. with fastener failure

Figure 6.8: Response of central cladding of the sub-assemblage in Case 98



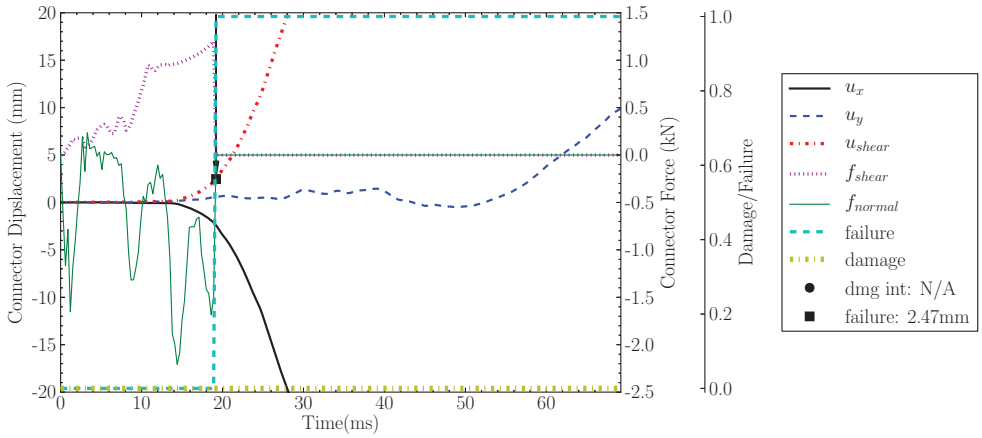
(a) central claddings



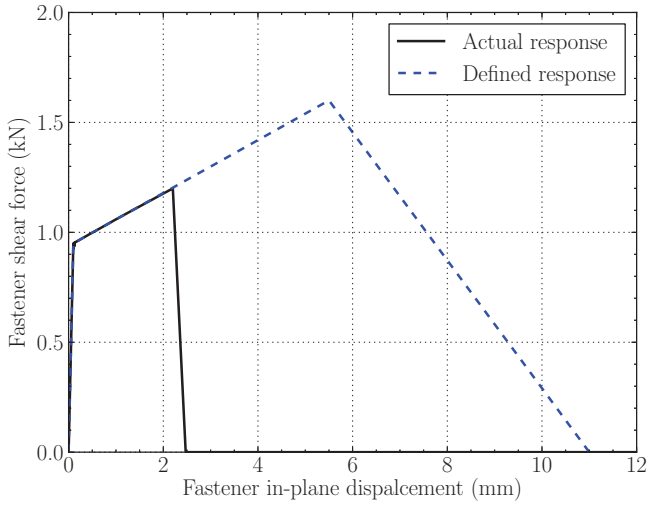
(b) side cladding

Figure 6.9: Relative displacement at the middle of the cladding with failure of the corresponding fastener

when the central cladding deformed in the opposite direction (positive displacement). While in Region II of Figure 6.9b, the fastener failures occurred much later and at smaller middle displacements of the side cladding.



(a) details of fastener response



(b) fastener response curve

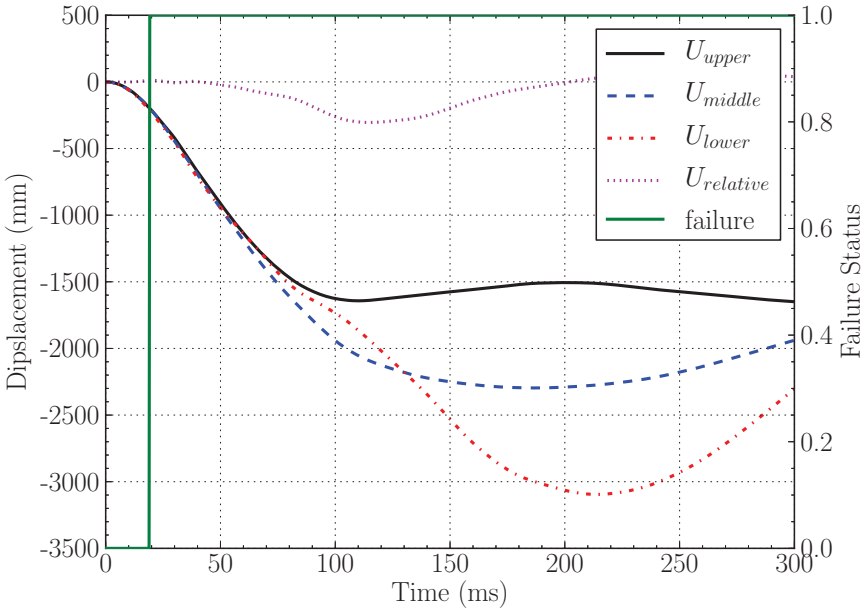
Figure 6.10: Response of central fastener of the sub-assemblage model in Case 157

An example of the central cladding response with failure of corresponding fasteners which occurred in Region II of Figure 6.9a is presented in Figures 6.10 and 6.11. These results correspond to the load profile defined in Case 157 (overpressure: 40kPa, impulse: 800kPa.ms and duration: 40ms). This is an impulsive

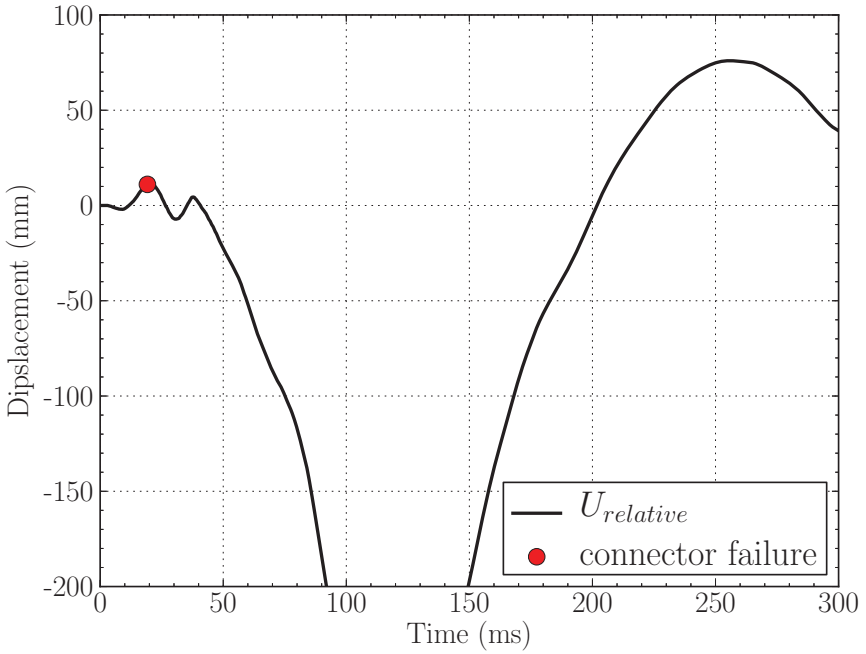
load since the ratio of duration to natural period is only 0.22. The response curve shown in Figure 6.10b indicates that the fastener did not fail by shear since the in-plane displacement at failure is only 2.47 mm. Examining the results in Figure 6.10a suggests that the fastener failed in tension. The sampling rate might not be sufficient to capture the full tensile force histories but this was the only parameter which could activate the failure. The relative middle displacement in Figure 6.11b shows that the corresponding fastener failed when the central cladding deflected at peak in the opposite direction of blast loading.

Similarly, an example of the side cladding response with failure of the corresponding fastener which occurred in Region II in Figure 6.9b, is presented in Figures 6.12 and 6.12b. These results correspond to the load profile defined in Case 75 (overpressure: 6kPa, impulse: 10000kPa.ms and duration: 3333ms). This is a quasi-static load since the ratio of the duration to natural period is 18.5. The response curve in Figure 6.12 shows that the fastener did fail in shear but not as clearly as the central fastener of Case 98 (depicted in Figure 6.7b). This was due to the excessive variation of the shear force in the x-y plane that caused significant cumulative plastic displacements. These plastic displacements triggered the hardening and the damage criteria, although they were not contributing to the advancement on the connector response path. In fact, this fastener failed numerically but in a more realistic interpretation this particular fastener might accumulate considerable plastic deformation around the hole in the cladding rather than fail. As shown in Figure 6.13b, it took a relatively long time for the plastic deformation in the fastener to accumulate, hence the numerical failure would eventually occur but at a much later stage.

Three cases were selected above for examining the cladding and corresponding fastener response: Case 75, Case 98 and Case 157. Some of the results for side or central cladding and fasteners were discussed above. It was estimated that the fastener would fail when the middle displacement of the cladding reached around 85 mm. Table 6.4 presents the time and displacement of the side and central cladding when the failure of the corresponding fastener occurred. It should be noted that for Case 98, the central and side fasteners failed when the cladding middle displacement reached -81.66 and -76.44 mm, respectively. These values are very close to the estimated -85 mm and both lie in Region I (refer to Figure

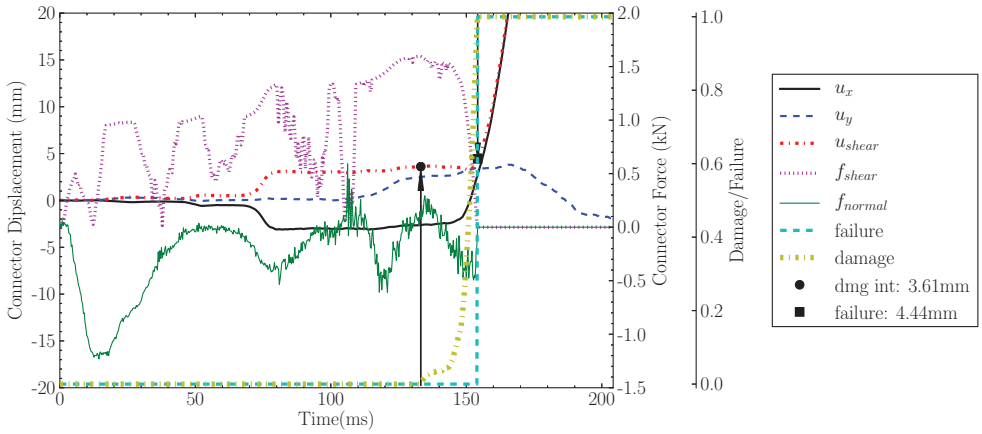


(a) cladding responses

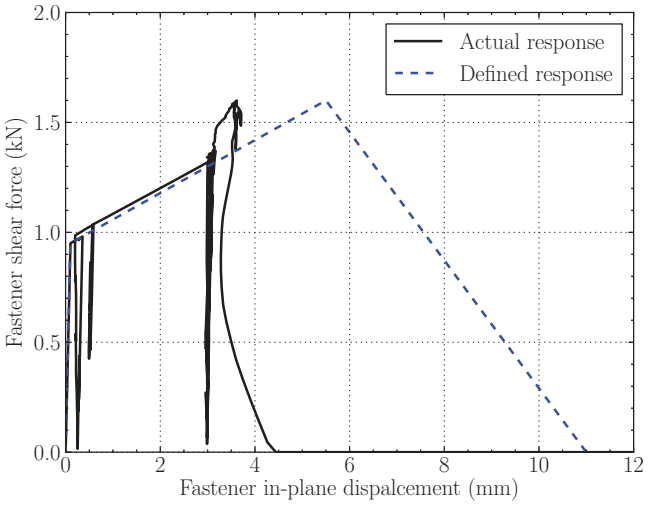


(b) relative displ. with fastener failure

Figure 6.11: Response of central cladding of the sub-assemblage in Case 157

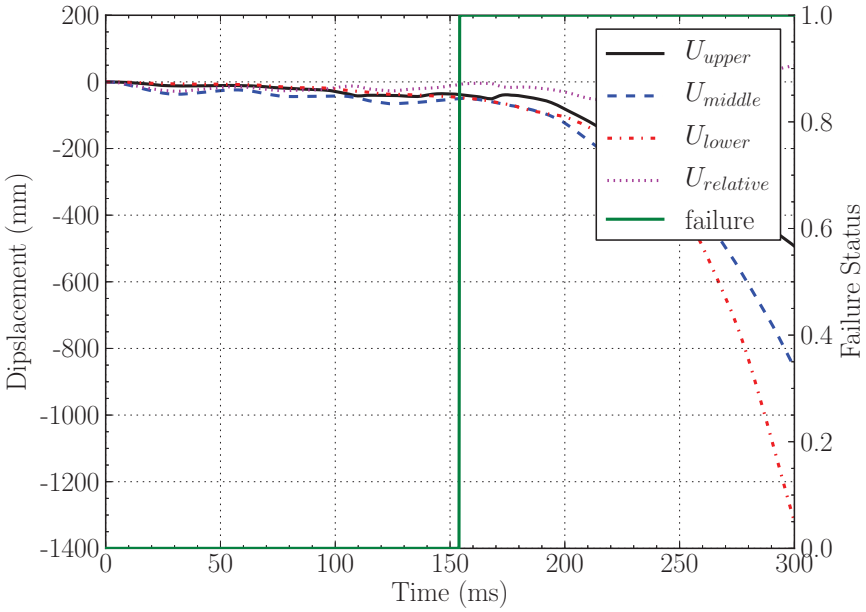


(a) details of fastener response

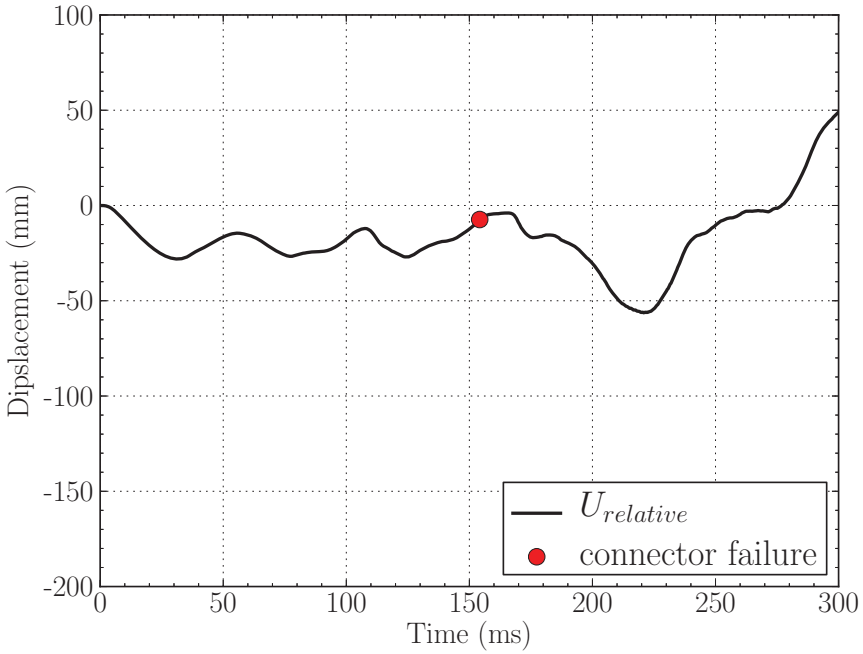


(b) fastener response curve

Figure 6.12: Response of side fastener of the sub-assemblage model in Case 75



(a) cladding responses



(b) relative displ. with fastener failure

Figure 6.13: Response of side cladding of the sub-assemblage in Case 75

6.9).

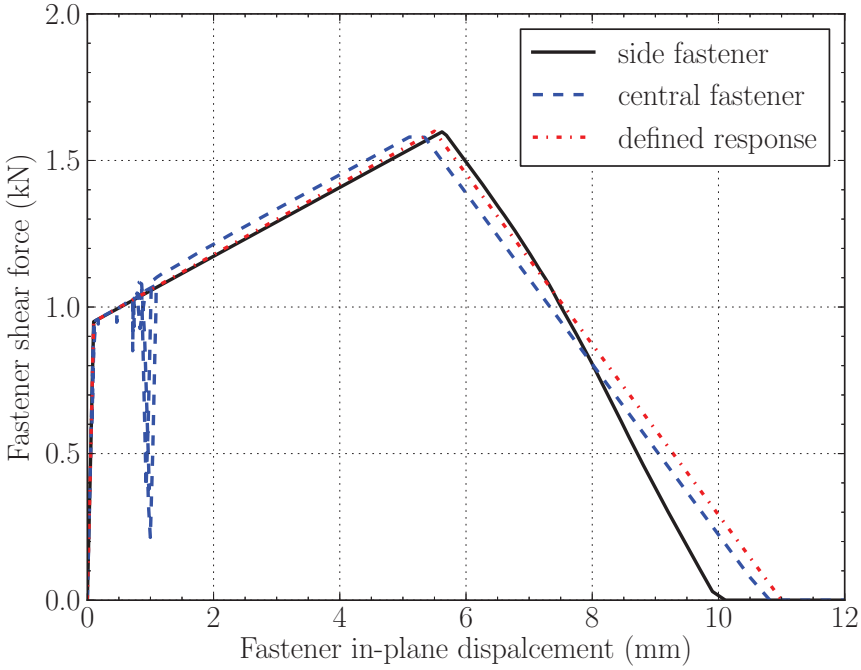
Table 6.4: Selected side and central fastener failures

Case no.	Pressure profile	Fastener	Fastener failure		Region
			$U_{relative}$(mm)	Time(ms)	
75	6 kPa	central	-83.66	119	I
	3333 ms	side	-7.36	154	II
98	10 kPa	central	-81.66	92.4	I
	200 ms	side	-76.44	57.6	I
157	40 kPa	central	+11.08	19.2	II
	40 ms	side	-89.82	15	I

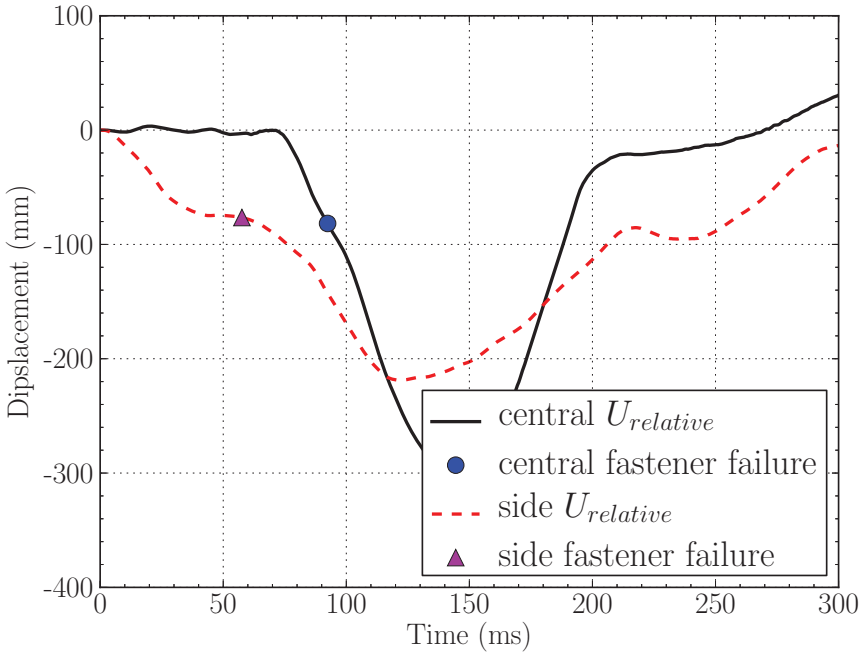
For Case 75, the central fastener failed at a cladding displacement of -83.66 mm and lie Region I. The corresponding side fastener failed by excessive plastic deformation and lie in region II (Figure 6.12 and 6.13). For Case 157, the side fastener failed at a cladding displacement of -89.82 mm and lie in Region I, while its central fastener failed by tension in the opposite direction with a cladding displacement of +11.08 mm and lie in Region II (Figure 6.10 and 6.11). It can be noted that the estimated fastener failure displacement of -85 mm is generally applicable to both the central and side claddings of Case 98 but only applicable to, the central cladding of Case 75 and the side cladding of Case 157.

The above also implies that the behaviour of the side and central cladding in Case 98 are effectively the same, while for Case 75 and 157 these are different. It is evident that in Figure 6.14a, the response of the central and side fasteners are very similar which suggests that they both failed in shear. While Figure 6.14b clearly shows that the failure of the side and central fasteners occurred at a similar relative displacement (-76.44 and -81.66 mm respectively, 6.8% difference) of the claddings. The displacement of the central cladding shown in Figure 6.14b has a delay of about 70 ms. This might be due to the whole central cladding was moving with the deforming side rail as a rigid body and only starting to deform from around 70 ms.

Modelling cases with failed side and central fasteners (either both or only one) are presented in Figure 6.15. The central and side fasteners with clear shear failure close to the y-direction (Region I) or other failure mechanisms (Region II) are clearly labelled. This gives the cases in which the central and side fasteners



(a) connector response



(b) relative displacement of cladding

Figure 6.14: Comparison of failure behaviour of central and side cladding with fasteners for the sub-assemblage model in Case 98

both failed in shear (Region I): Cases 98, 100-105, 111-113, 126, 127 and 141. These cases are labelled as 'identical failure F'. Unfortunately, the increments of overpressure and impulse are not small enough to define precisely a zone in which the failure response of the cladding and corresponding fasteners are identical at both the centre and side locations. Nonetheless, these hilighted cases did provide an indication of the appropriate regions in the pressure - impulse diagrams.

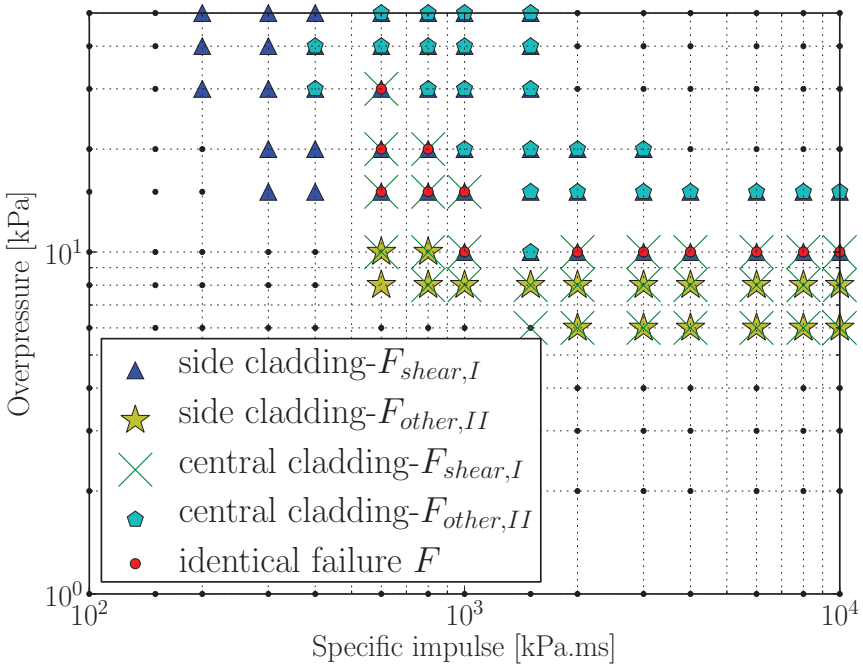
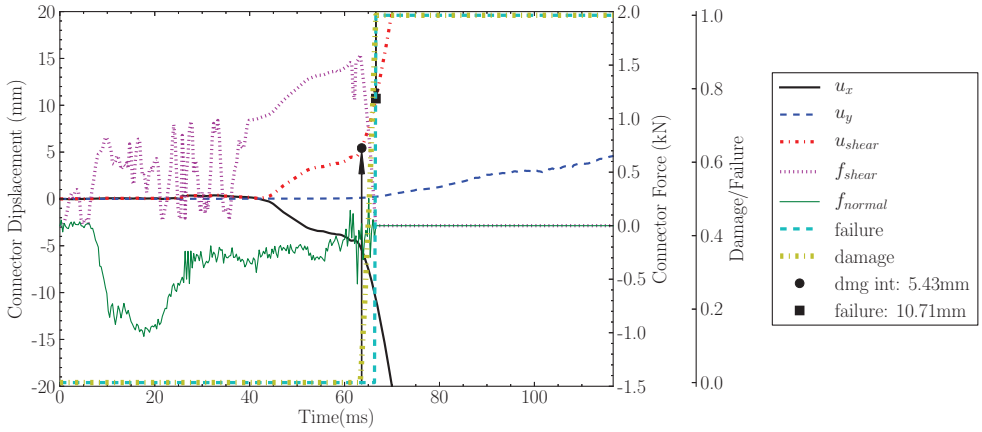


Figure 6.15: Cases with identical failure behaviour of cladding and fasteners at centre and side

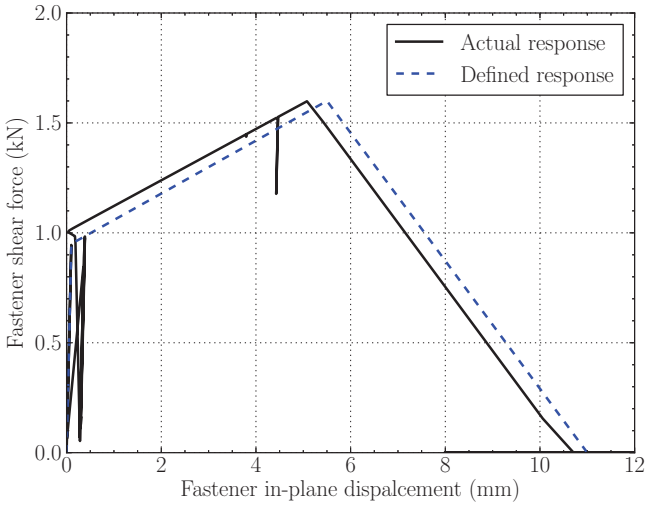
The fasteners shown above all failed mainly in or close to the y-direction. An example of the response of the middle fastener of the sub-assemblage model subject to loads defined in Case 98 is shown in Figure 6.16. The response curve in Figure 6.16b indicates that the fastener failed in shear. A close look at Figure 6.16a suggests that the damage and failure actually occurred in the x direction, since the resultant displacement u_{shear} is almost identical to the displacement u_x. This might be due to the insignificant forces in the y-direction since both the upper and lower claddings were pulling the middle fastener in the opposite direction. However, the shear force generated in the x-direction due to the relative

longitudinal movement of the cladding and side rail (as in a composite beam) was significant and able to fail the fastener.

In this section, the response of typical claddings and corresponding fastener was presented and discussed. Focus was placed on the failure of the fasteners and the relative displacement of cladding at which the failure occurs. The displacement history of the cladding and the maximum dynamic value were not examined in detail here. The reason is that due to the inclusion of the fastener failure in the model, the displacement of the cladding became less important. This is because



(a) details of fastener response



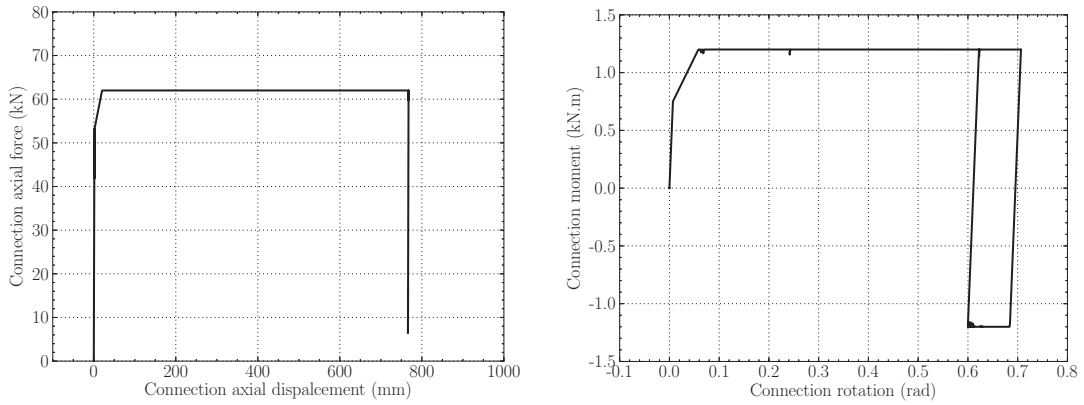
(b) fastener response curve

Figure 6.16: Response of middle fastener of the sub-assemblage model in Case 98

once the fastener fails, the cladding panels would deform significantly without any constraints, hence the displacement after fastener failure becomes rather meaningless. The displacement levels can provide useful information for the cladding damages before fastener failure. However, in view of the overall response in the full ranges of overpressure and impulses, the displacement can be replaced by the failure of fasteners as one of the primary damage criteria used in the present work.

6.5 Side rail axial response and connection behaviour

The connection shown in Figure 6.1 was used to represent the M12 bolt - cleat joint between the side rail and column. In the numerical analysis, it could predict the behaviour of the connection and the axial response of the side rail.



(a) axial response (b) rotational response

Figure 6.17: Numerical response of the M12 bolt-cleat connection

An example of the axial and rotational responses of the connection in the sub-assemblage model subject to the blast load defined in Case 98 is shown in Figure 6.17. It can be seen that significant axial displacement and rotation occurred in the connection. The originally pre-defined axial and rotational behaviour adopted bi-linear curves with yield capacity, elastic and tangent stiffness. The tangent stiffness however caused some numerical problems in the model.

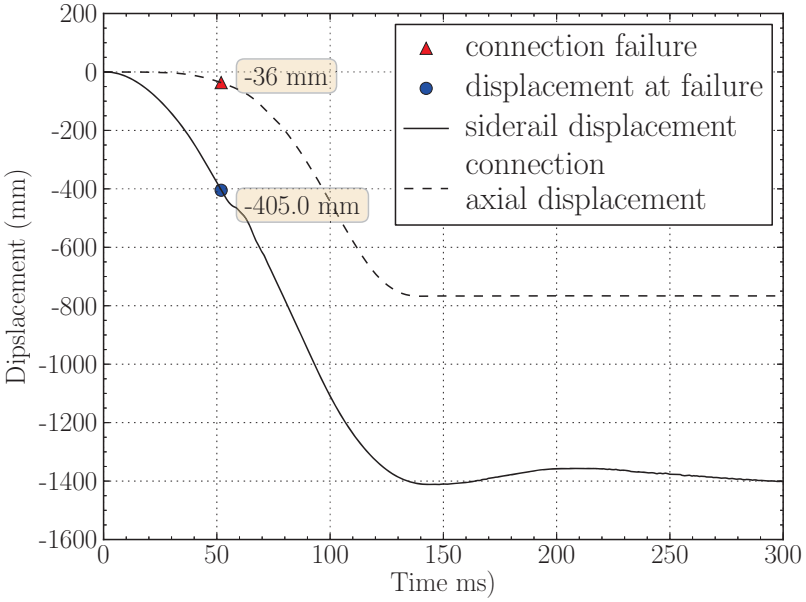
It exerted large axial forces at the support which caused excessive deformation of the shell elements and subsequently terminated the simulation prematurely. In order to overcome this problem, the original bi-linear response curves were modified so that they exhibit perfect-plastic behaviour after the specified level of deformation. For the axial response, the tangent stiffness became zero after an axial displacement of 24 mm was reached at the support (i.e. in the connector). This is twice the diameter of the M12 bolt. For the rotational response, the tangent stiffness became zero after a rotation of 4^o. This corresponds to the heavy damage of the component at the support end. The responses shown in the figure were obtained from the modified behaviour.

An example of the axial displacement of the side rail in the sub-assemblage model subject to load in Case 98 is shown in Figure 6.18a. The transverse displacement of the side rail is shown in the same figure as well for comparison. It can be seen in Figure 6.18a that pull-out failure (36 mm) of the connection occurred a side rail transverse displacement of -405 mm. Failure of the connection was not implemented in the model, so the loss of the side rail would not occur. The side rail would still continue to deform at the pull-out failure but it should be recalled when interpreting the results.

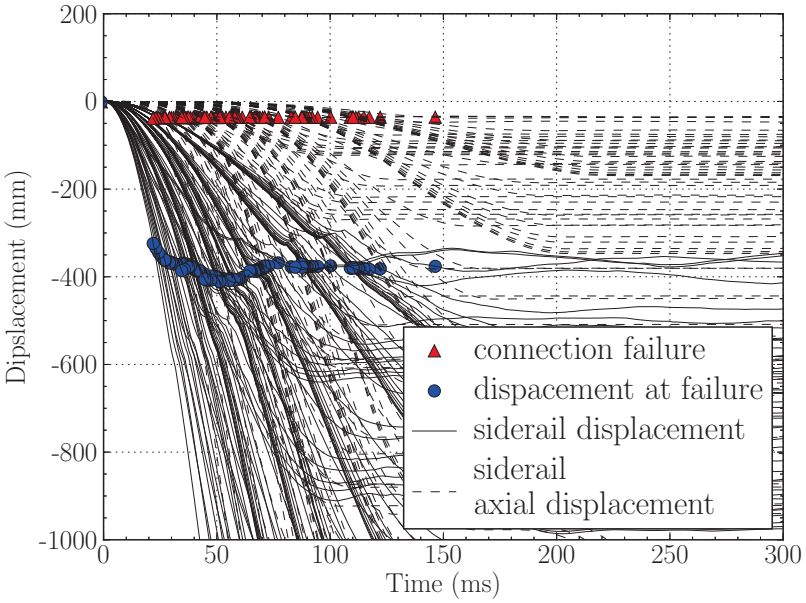
Moreover, all cases which have the axial displacement equal or greater than the pull-out failure were plotted in Figure 6.18b. The relationship of the transverse and axial displacement of the side rail is clear. Under most blast loading cases, the pull-out failure would occur at a transverse displacement of 400 mm. Subject to more intensive load and when the deforming velocity of the side rail increases, the corresponding transverse displacement tends to decrease to 300 mm. This is mainly due to the deformed mode being slight changed under more intensive loads.

6.6 Combined response

In the above sections, the failure of the fasteners has been discussed, and a detailed insight into the response was established. In this section, the aim is to examine the relationship between the failure of fasteners and the displacement of the middle side rail.



(a) case 98



(b) all cases

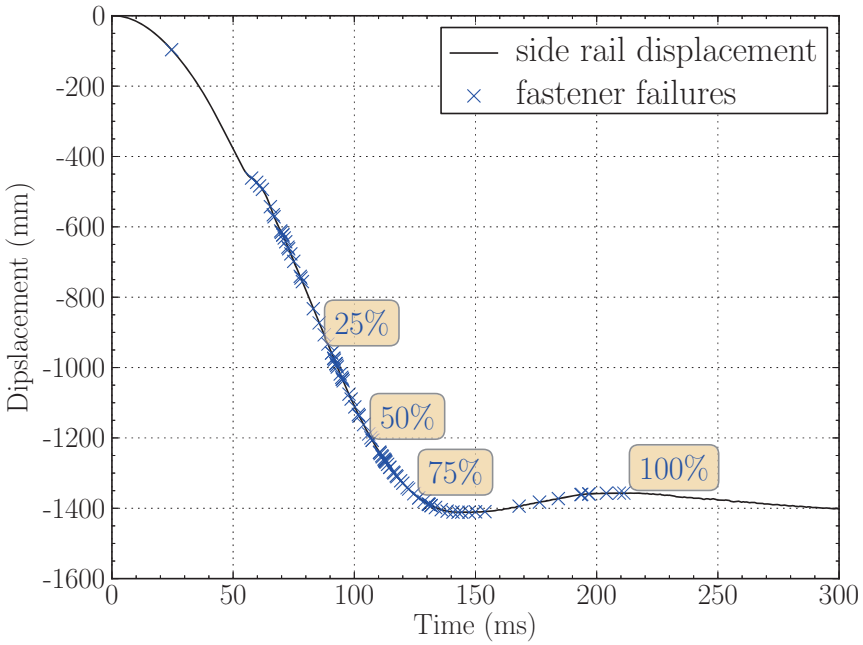
Figure 6.18: Axial and transverse displacement time history of side rail

The side rail transverse displacement from Case 98 is shown in Figure 6.19a. The fastener failure time history is superimposed on the displacement curve. This superposition relates the displacement of the side rail directly to the failure of fasteners. Furthermore, the percentages of fastener failure are also indicated in the figure. For this particular case, it can be seen that 25, 50, 75 and 100 % failure occurred at displacements of 950, 1200, 1370 and 1350 mm, respectively. The majority of the failures occurred after 60 ms and about 75% fasteners failed up to the peak dynamic displacement. The fasteners continued to fail after reaching the maximum displacement.

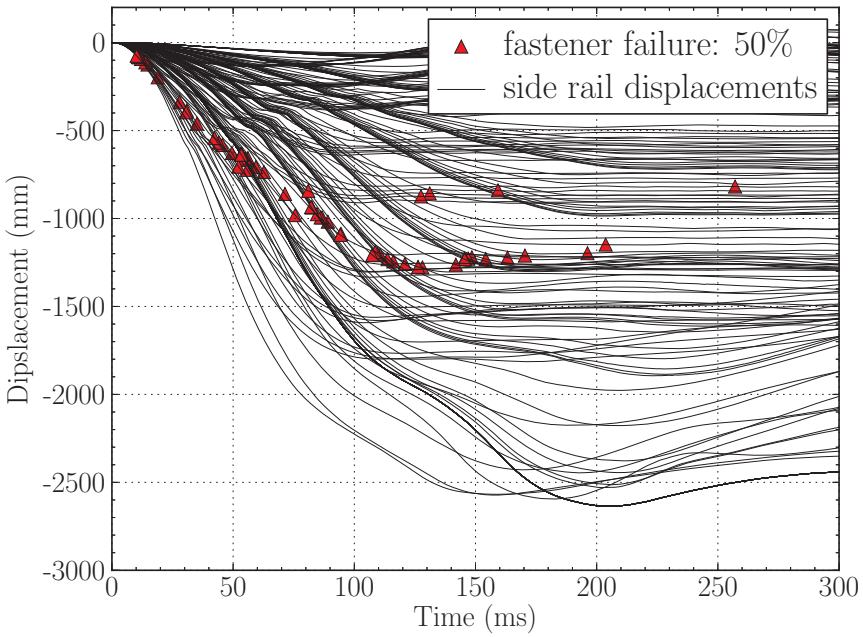
In order to examine the relationship further, as an example, the 50% fastener failure level is plotted against the side rail displacement for all cases and the results are shown in Figure 6.19b. It is clear that a one-to-one relation between the side rail displacement and the 50% of the fastener failure does not exist. The failure varies significantly and is dependent on the actual response of the side rail. It can be seen that when the rate of deformation of the side rail is moderate (i.e. subject to quasi-static or dynamic load), a displacement of -1250 mm can be approximately related to the 50% fastener failure. However, the failure tends to occur earlier and at a lower displacement level once the rate of deformation is increased (under very high intensity or impulsive load).

The above analysis was extended to 25, 75 and 100% failure levels, and results are presented in Figure 6.20. It can be noted that the damage level is scattered over a large range of side rail displacements. The 25% failure level ranges from -68 to -1185 mm; the 50% level ranges from -75 to -1285 mm; while 75% level ranges from -121 to -1380, and finally the 100% level ranges from -715 to -1576 mm. There is no clear one-to-one relation between the displacement and the percentage of fastener failure. Between 100 and 300 ms, the side rail displacement can be roughly related to the percentage level but, as already discussed, this relation breaks down when the rate of deformation increases.

Up to this point, the response of the sub-assemblage model subject to combinations of overpressures and impulses have been examined in detail for a few selected cases. The displacement of the central side rail and the failure of cladding with corresponding fasteners were given particular attention. Efforts were made to relate the failure of fasteners to the response of the cladding and side rails.



(a) Case 98



(b) all cases

Figure 6.19: Side rail transverse response with failure of fasteners

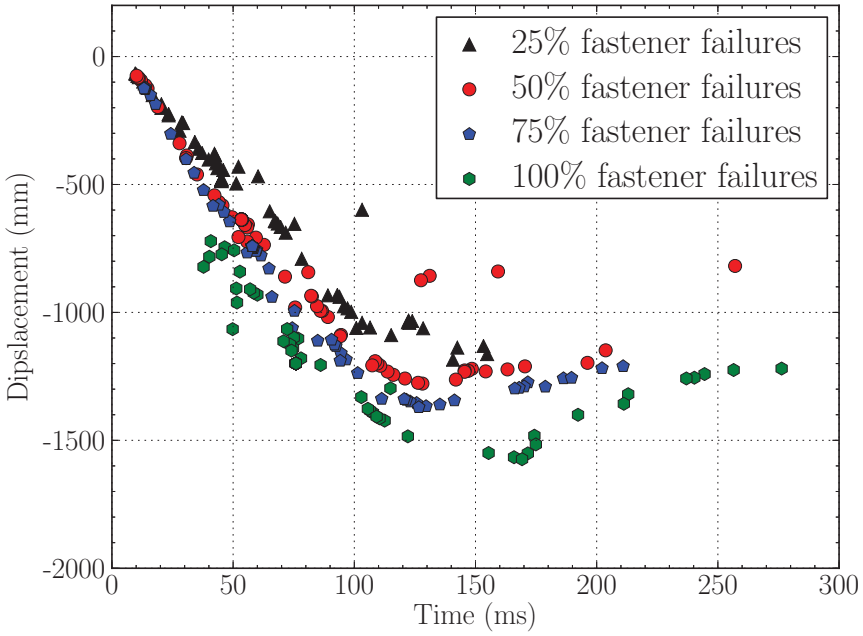


Figure 6.20: Percentage of total fastener failure with side rail displacement

It was shown that for the cladding, the relation between the deformation and the fastener failure conditionally exists under certain loading situations. It was found that for the side rails there is no clear relation between the displacement and percentage of fastener failure. However, a maximum displacement can be established which correlates with a minimum level of fastener failure.

6.7 Pressure - impulse diagrams

The previously discussed displacement and damage parameters are used herein to construct pressure - impulse diagrams of the sub-assemblage. The damage criteria used here are: transverse displacement of side rail, axial displacement of side rail and percentage of total fastener failure. A series of iso-curves for TNT charge were also constructed for ease of identifying the explosion source and safe siting of structures.

The pressure - impulse diagrams have the same range of overpressure and impulse as shown in Figure 6.4. Three damage criteria were used: maximum transverse displacement of side rail, maximum axial displacement of side rail and

the maximum percentage of total fastener failure. All 180 cases defined by Figure 6.4 were used. The maximum value of the time history in each case was extracted and populated over the full range of the pressure - impulse diagram. The iso-damage curves were then determined by interpolating between the points within the grid.

6.7.1 Side rail transverse displacement

The pressure - impulse diagrams of maximum dynamic transverse displacement of the central side rail of the sub-assemblage structure (corresponding to detonation blast scenarios defined in Figure 6.4 and Table 19) are shown in Figure 6.21. The damage levels are defined in Table 6.2. These three iso-damage curves were based on the displacement criteria. The limiting values for the damage levels are summarised and discussed in Section 6.7.5.

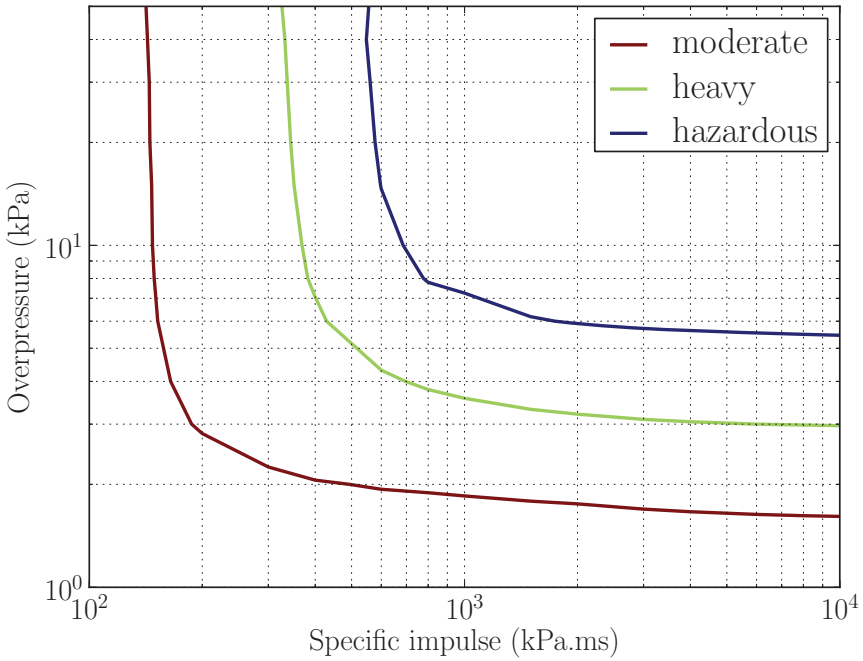


Figure 6.21: Pressure - impulse diagrams: maximum side rail displacement

6.7.2 Side rail axial displacement

The pressure - impulse diagrams of maximum axial displacement of the central side rail of the sub-assemblage structure corresponding to detonation loading scenarios defined in Figure 6.4 and Table 19 is shown in Figure 6.22. Two iso-damage curves are used to represent two damage levels in terms of component axial deformation. The yielding corresponds to axial displacement of 2mm while the failure curve corresponds to 36 mm. Beyond this failure iso-curve, the side rail would be pulled out of the connection and the component would be ineffective. The yielding iso-curve is very close to the lower limit of the overpressure range and it coincides with the line of the lower limit of the impulse range. The limiting values for the damage levels are summarised and discussed in Section 6.7.5.

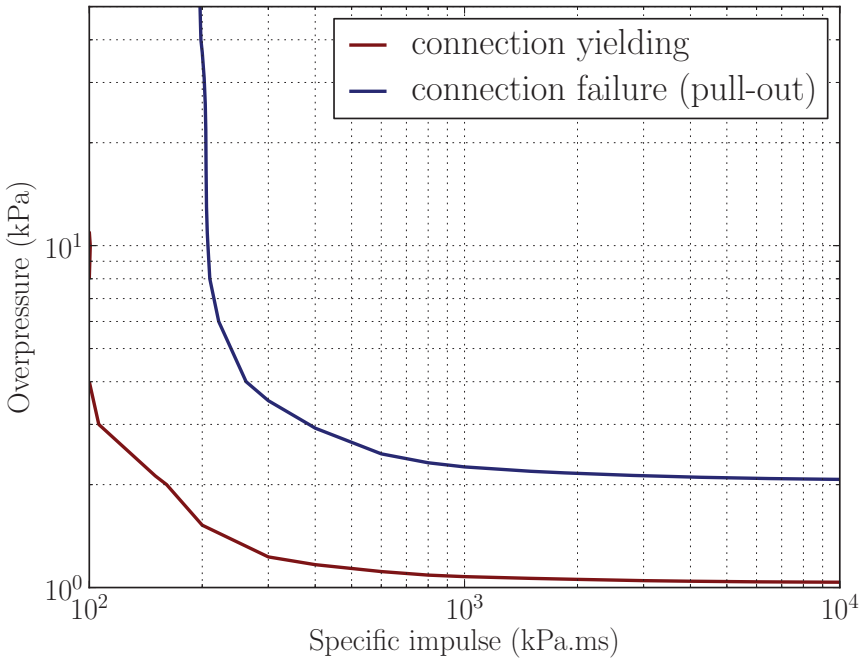


Figure 6.22: Pressure - impulse diagram: maximum axial displacement

6.7.3 Percentage of total connector failure

The pressure - impulse diagrams of total fastener failure of the sub-assemblage structure (corresponding to detonation loading scenarios defined in Figure 6.4 and

Table 19) are shown in Figure 6.23. The failure of fasteners was used in addition to the displacement of cladding as an alternative damage criterion. These iso-damage curves were proposed to help to enable a more direct assessment of the structural damage.

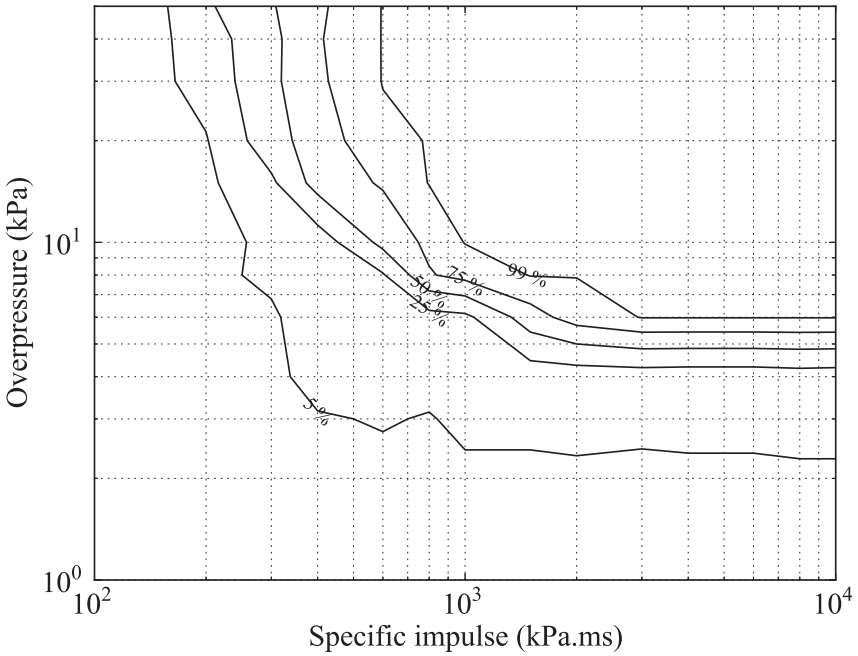


Figure 6.23: Pressure - impulse diagram

Five damage levels were used here: 5%, 25%, 50%, 75% and 99%. It can be seen that the iso-curves are not as smooth as for other damage criteria but the levels of damage are still very clear. Above 25% damage level, in the quasi-static region, the range between iso-damage curves is smaller than the range in the impulsive region. This suggests that the failure of fasteners is more sensitive to the peak overpressure when the damage level is greater than 25%. Also, the failure is less sensitive to impulse loading and can be interpolated very well over the damage range. In the quasi-static region, the blast loading was applied over a long period. Accordingly, once the failure of fasteners started to occur, the neighbouring fasteners would become prone to fail due to the continuously applied load. In the impulsive range, the load could reduce before the failure of connector occurs hence the neighbouring fasteners would not be affected. The

limiting values for the damage levels are summarised and discussed in Section 6.7.5.

6.7.4 Iso-curves for TNT explosive charges

Overpressure and impulse of the blast wave generated by TNT high explosives can be determined by Equations 2.14, 2.15 and 2.17. Iso-distance and iso-charge weight curves can also be constructed by these three equations. The iso-distance curves can be created by keeping the distance R constant at 200, 400, 1000, 6000 and 30000 m while varying the weight of TNT charge W. Similarly, the iso-charge weight curves can be plotted by keeping the weight of TNT charge W constant at 1, 7.5, 150, 2000, and 25000 m while varying the stand-off distances R. The overpressure and impulse presented in the figure are reflected values.

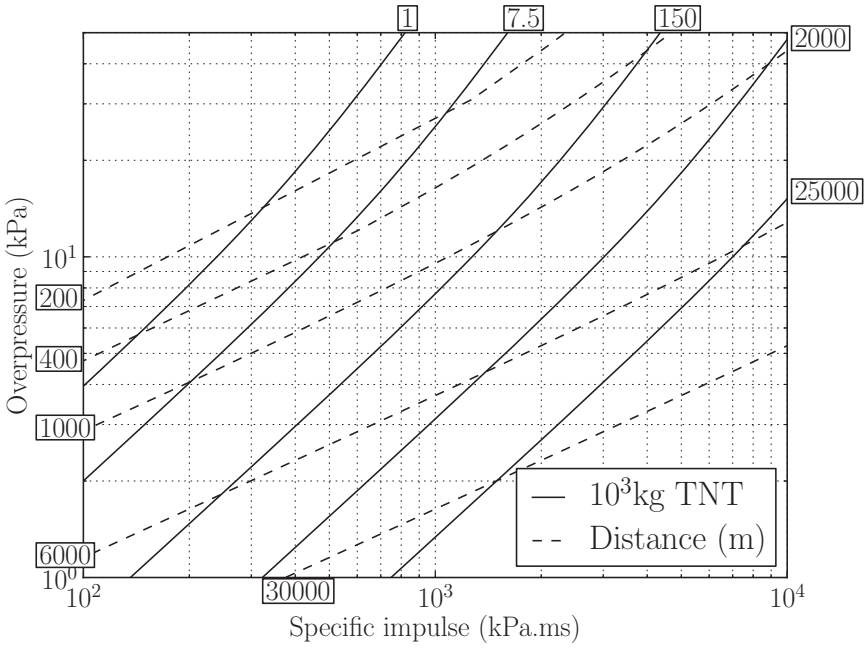


Figure 6.24: Iso-curves for TNT explosive charges

As an example, the intersection of the curve of 1 kg with the curve of 200 m would give the reflected overpressure and impulse of a 1 kg TNT charge at a stand-off distance of 200 m. Interpolating and extrapolating between the iso-curves would define the detonation blast loading for TNT charge sizes from 1 to

25000 kg at stand-off distances from 200 to 30000 m. Combing these iso-curves of TNT charges to the pressure - impulse diagrams of the structure would make the estimation of the expected damage or safe distance more straightforward.

6.7.5 Combined pressure - impulse diagrams

The previously discussed three pressure - impulse diagram plots are combined into one graph as shown in Figure 6.25. The iso-curves of TNT charges are also superimposed. These combined pressure - impulse diagrams can be used to identify the most critical component or parameter which controls the response of the sub-structure. Table 6.5 summarises the limiting pressure and impulse values for the three damage criteria. For better interpretation, three damage levels were selected for fastener failures: 5%(moderate), 50%(heavy) and 99%(hazardous). For the side rail axial response: the yielding and failure criteria were classified as moderate and hazardous levels.

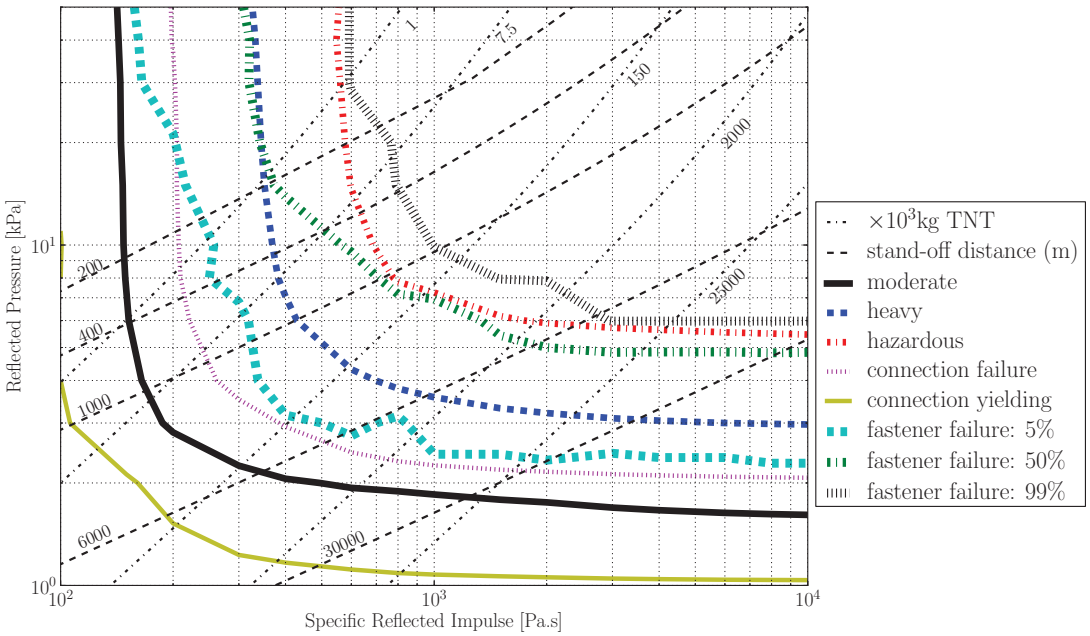


Figure 6.25: Combined pressure - impulse diagrams

The minimum overpressure values for moderate, heavy and hazardous damage levels for the transverse displacement of the side rail are 1.62, 2.95 and 5.5 kPa,

respectively. The corresponding values for fastener failure are 2.33, 4.86 and 6.0. Only two damage levels are available for the axial displacement of the side rail. The minimum overpressure values in this case for the moderate and hazardous damage levels are 1.04 and 2.07 kPa, respectively. Therefore, the axial displacement is the most critical parameter in the response of the sub-assemblage in both the impulsive and quasi-static regions. It is worth noting that the design wind

Table 6.5: Minimum overpressure and impulse for various damage criteria [Impulse: kPa.ms; Pressure: kPa]

	Moderate damage		Heavy damage		Hazardous damage	
	Impulse	Pressure	Impulse	Pressure	Impulse	Pressure
side rail (transverse)	141	1.62	326	2.95	546	5.5
sdei rail (axial)	100	1.04	-	-	197	2.07
fastener failure (%)	158	2.33	308	4.86	591	6.0

pressure for the wall is in the region of 0.5 - 0.6 kPa for this type of structure. The yielding of the connection (axial) would occur at just two times of the wind pressure. The side rail supporting the cladding system would only sustain 3-4 times the wind pressure before the hazardous damage level is reached (pull-out failure and loss of components).

The combined pressure - impulse diagram suggests that for the selected design of warehouse in the current study, the most critical component in the structure is the connection between the side rails and columns. The margin of safety is only around 3-4 times the wind pressure. Increasing the strength of the connection would shift the corresponding iso-damage curves in the upper right direction, which would significantly enhance the blast resistance. It should be noted that once the stiffness and capacity of the connection are increased, the transverse displacement of the side rail would be decreased and the failure of the fastener should occur earlier.

The derived iso-damage curves of the overall fastener failure could be fitted and interpolated as necessary for the design and assessment of such structures. The damage levels corresponding to percentage of fastener failure can be change according to design requirements. In the current work, the three levels were selected arbitrarily for discussion.

6.8 Strain rate hardening of fasteners

The strain rate effect of the cladding and side rail materials presented in the previous chapter was incorporated by a dynamic increase factor (DIF). However, the behaviour determined from the finite element model of the fastener zone was only based on static response, and no strain rate effect was considered. This section examines the possible influence of strain rate in the self-tapping screw fastener so that the rate effect can be incorporated into the connector response through a suitable dynamic increase factor if necessary.

6.8.1 Estimation of local strain rate hardening

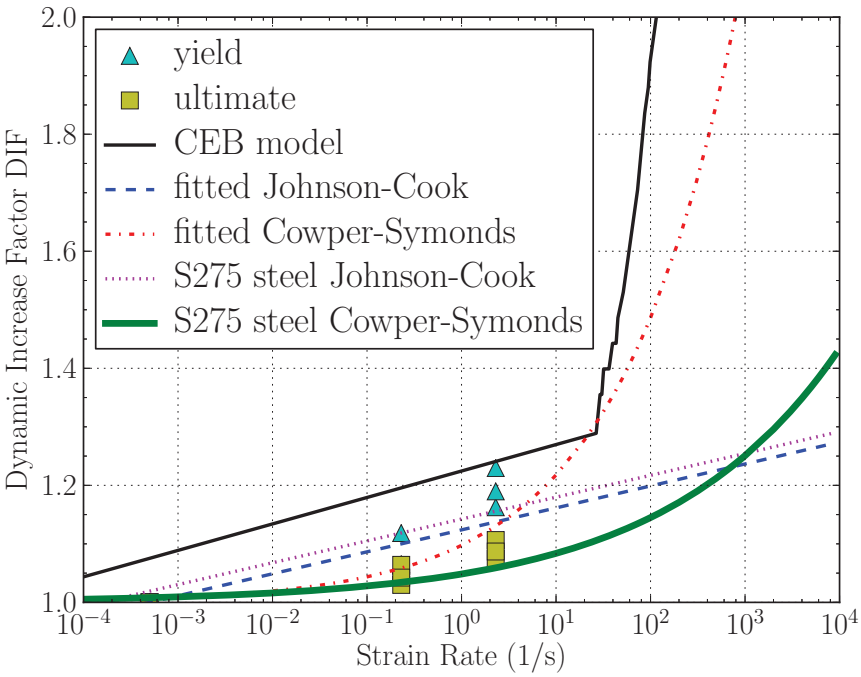


Figure 6.26: Strain rate effect on dynamic increase factor

The dynamic increase factor is used to account for the increase in the strength of the material at high strain rates. The increase depends primarily on the strain rate and material properties. Johnson - Cook (Equation 2.30) and Cowper - Symonds (Equation 2.31) are two commonly used models to estimate the dynamic increase factor. The two models were fitted with available experimental

data on steel materials cut from cladding sheets (Elghazouli et al., 2014). As shown in Figure 6.26, the yield and ultimate factor, were determined from the experimental data and they represent the ratios of yield or ultimate stress at high strain rates to low strain rates (quasi-static). Three strain rates have been achieved in the tests: 0.005(quasi-static), 0.23 and 2.3 s^{-1}. Within the range where test data are available both fitted curves can predict the increase factor reasonably well. However, beyond a strain rate of 2.3 s^{-1} the factors predicted by Cowper - Symonds model are significantly higher than Johnson - Cook model. In fact, the accuracy of neither model can be guaranteed in the lack of test data. The curves of the two models fitted to strain rate data of S275 steel have been included in the figure as well. The mechanical properties of S275 are similar to the material of the cladding panels and the test data covers strain rates from 0.0001 to 3000 s^{-1}. These two curves serve as good compliments to our test data. A curve from the CEB model (Ngo et al., 2007) is also shown here for comparison only since this is typically proposed for reinforcement steel.

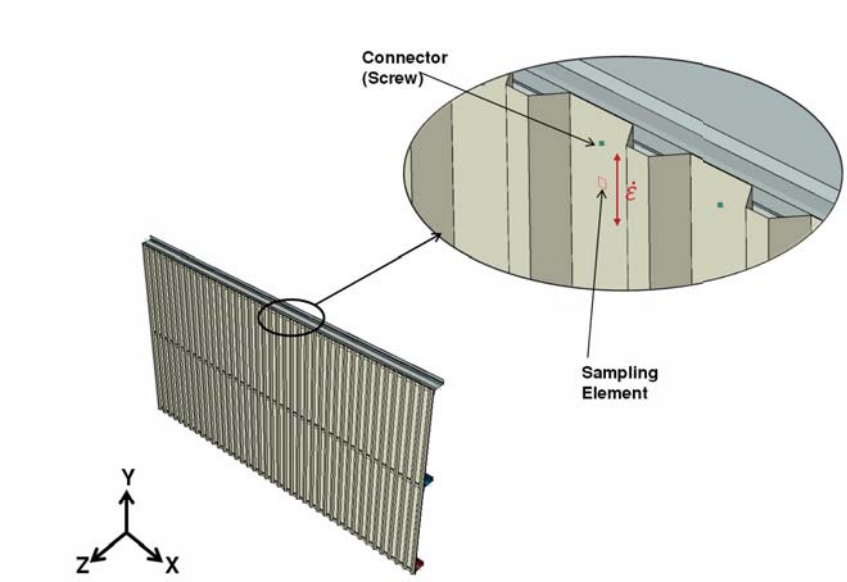
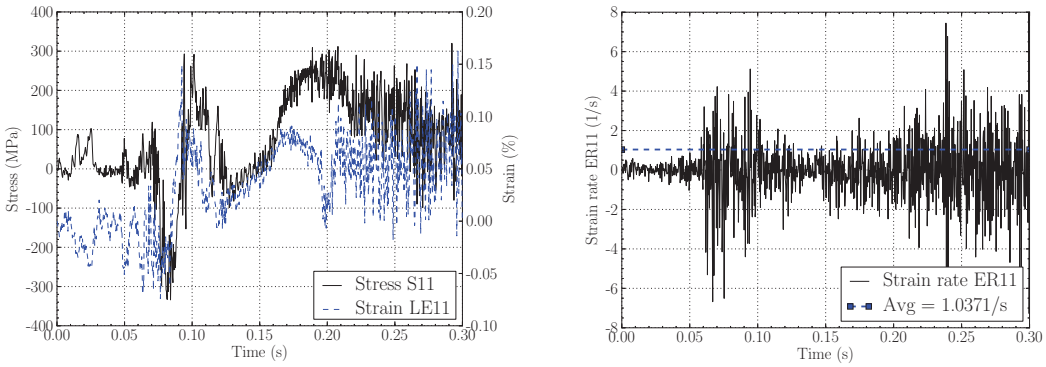


Figure 6.27: Estimation of strain rate in the screw connection

In the sub-assemblage model, the screw connection is modelled as a connector element with two points tied on to a few shell elements of the cladding and the flange of the side rail. Strain rates are available for shell elements in the

cladding but do not account for the stress/strain concentration in the connector model. As shown in Figure 6.27, the actual strain rate in the screw connection can be examined as a function (or a multiplier) of the nominal strain rate from a sampling shell element at a distance away from the connector element. The estimation was only made in the y-direction since it is the failure direction of most of the fasteners.

The sampling sub-assemblage model was subjected to a detonation load of 10 kPa and duration of 200 ms (i.e. Case 98). The stress and strain time histories of the sampling shell element are shown in Figure 6.28a and the corresponding strain rate time history is shown in Figure6.28b. The average of the absolute value of the stain rate history was estimated to be 1.0371 s^{-1}. Thus, the nominal strain rate in the y direction is approximately 1 s^{-1}.

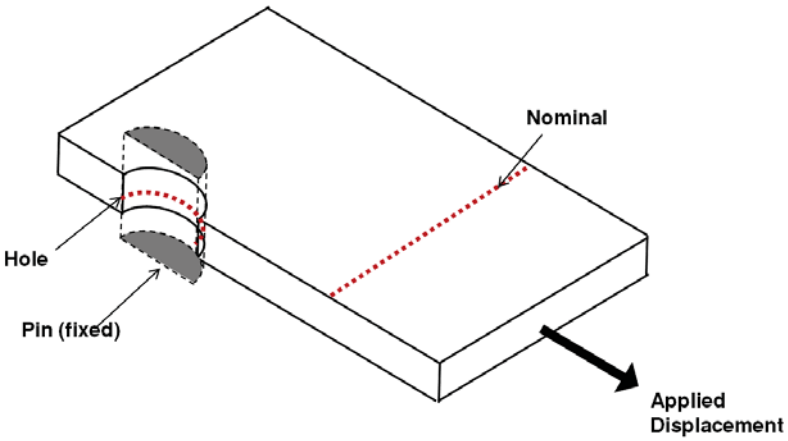


(a) stress and strain (b) strain rate

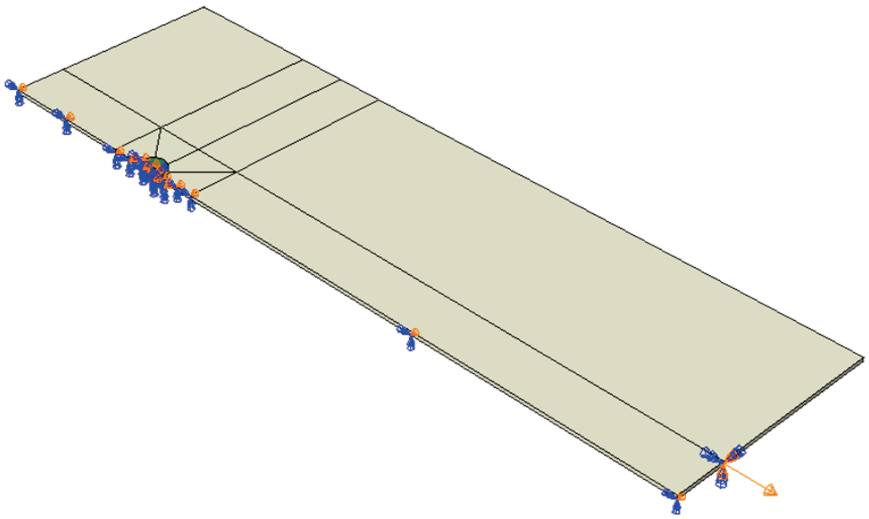
Figure 6.28: Stress, strain and strain rate time histories in the sampling shell element

The yield and ultimate capacities of the self-tapping screw connection is primarily based on the bearing strength of the thin cladding sheet. The screw with the bottom flange of the cladding panel can be idealised by a thin plate loaded with a rigid pin as shown in Figure 6.29a. The pin represents the shaft of the screw and the plate represents the bottom flange. The finite element model is shown in Figure 6.29b.

Similar to the stress and stain concentration around the hole in the pin loaded plate, the stain rate would also concentrate at the screw connection. In the



(a) schematic



(b) finite element model

Figure 6.29: Simplified model to estimate the strain rate in a screw connection

analysis, the explicit method cannot be used due to the transient nature of the problem as the dynamic behaviour would dominate the response. Static analysis was therefore used, but it should be noted that in order to estimate the strain rate the step time now becomes real. A displacement of 0.2 mm was applied over the end of the plate as shown in Figure 6.29a. The displacement was applied linearly so that the velocity is kept constant as shown in Figure 6.30. Six load step times were used to achieve different strain rates: 1, 0.5 ,0.1, 0.01, 0.001 and 0.0001 second.

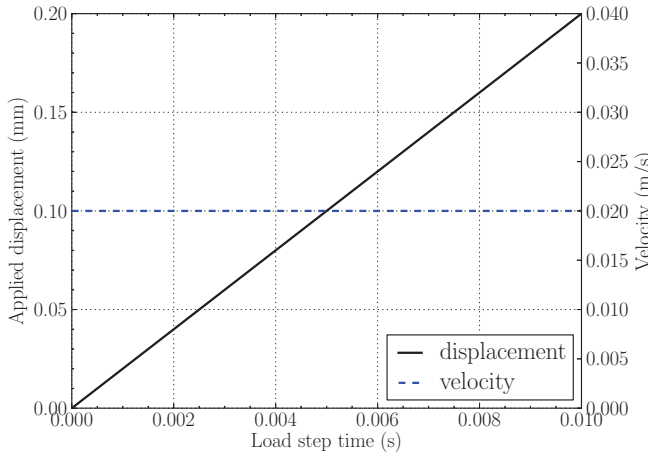
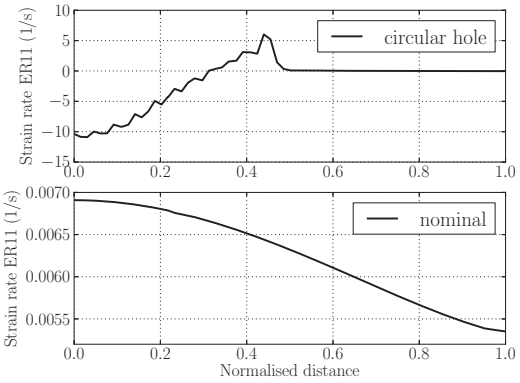


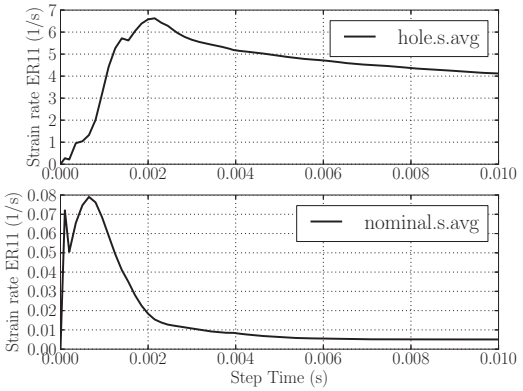
Figure 6.30: Applied 0.2 mm displacement over total time step of 0.01 second

Two sets of strain rate data were measured. The nominal strain rate was measured across the whole plate away from the hole as shown in Figure 6.29a. The other set of strain rate was measured around the hole as also shown in the figure. During the loading process, at an arbitrary time the measured strain rate around the hole and along the nominal section are shown in Figure 6.31a. The normalised distances are presented as dashed red lines in Figure 6.29a. It can be seen from Figure 6.31a that around the hole the first half in contact with the pin exhibited significant negative strain rate (compression) during loading (normalised distance 0.0 - 0.3). In the part where the hole was not in contact with the pin, there was a short length with positive strain rate (tension) and the rest of the hole did not have any strain rate (normalised distance 0.5 - 1.0). The distribution of strain rate corresponds exactly to the stress distribution around

the hole, since both positive and negative values would contribute to the increase of strength. The average strain rate in the hole was estimated based on the absolute values of the distribution around the hole. The variation of nominal strain rate is much smaller and the average can be readily determined.



(a) strain rate spatial distribution



(b) Strain rate time histories with step time of 0.01 second

Figure 6.31: Strain rate analysis around the hole

The spatial average of nominal and hole strain rates have been determined at each step over the loading period. The time histories of the average strain rates are shown in Figure 6.31b. It can be noticed that both the nominal and hole strain rates increased rapidly at early stages of loading. For the model with a time step of 0.01 second, the maximum average strain rate at the hole was roughly $6.5s^{-1}$ while the maximum value for average nominal strain rate was only $0.08s^{-1}$. Extending this analysis to the other five load step times can provide six average nominal strain rates with corresponding strain rates around the hole. Based on this, a relationship between the nominal and concentrated strain rate around the hole can be established, as shown in Figure 6.32.

The average nominal strain rate away from the the connector predicted by the sub-assemblage model as shown in Figure 6.27 is 1.0371 s^{-1}. Thus, the approximate strain rate in the self-tapping screw connector can be estimated by interpolating between the points in Figure 6.32 and the strain rate which was estimated to be 240 s^{-1}. Referring to the fitted Johnson - Cook curve in Figure 6.26, a strain rate of 240 s^{-1} would increase the yield strength of the material by

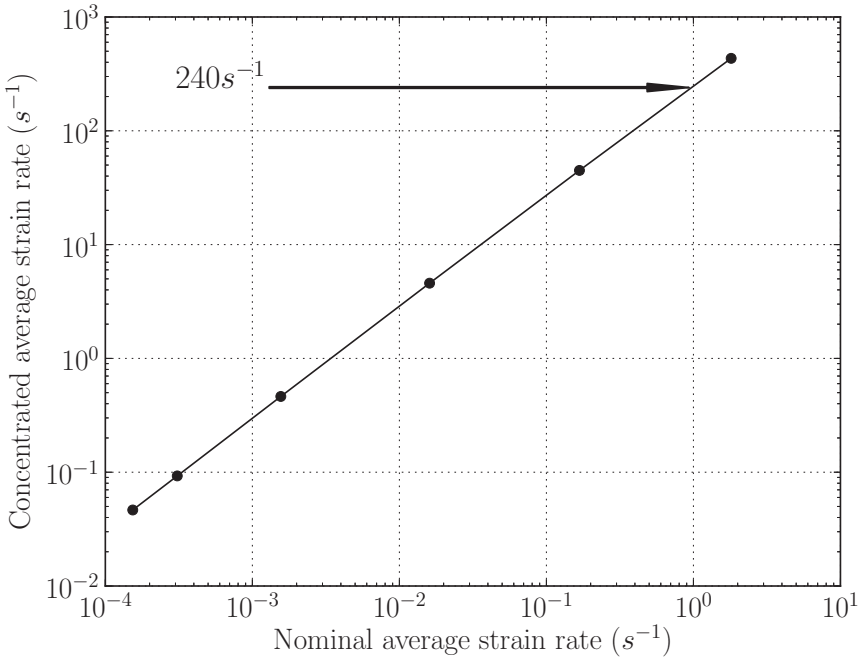


Figure 6.32: Relationship between nominal and concetrated strain rates

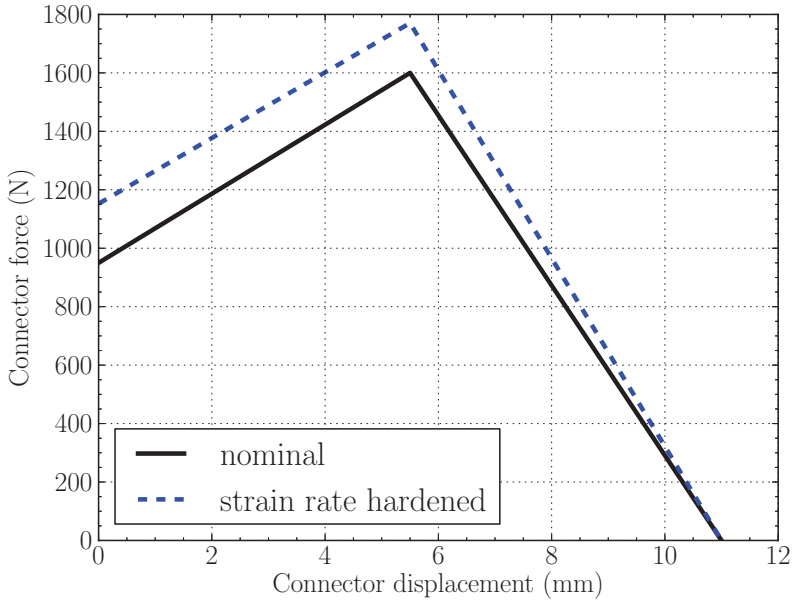


Figure 6.33: Connector response with and without the estimated strain rate effect

21.3%. The increase of ultimate strength is usually lower than the yield strength and it is approximately half as indicated by the test data shown in Figure 6.26. Therefore, the ultimate capacity of the connector was only increased by 10.65%. Nominal and strain rate strengthened response curves of the screw fastener are shown in Figure 6.33. The yield and ultimate capacities are expected to increase by 21.3 and 10.65%, respectively, when the strain rate hardening effect is taken into account.

6.8.2 Influence of strengthened fasteners

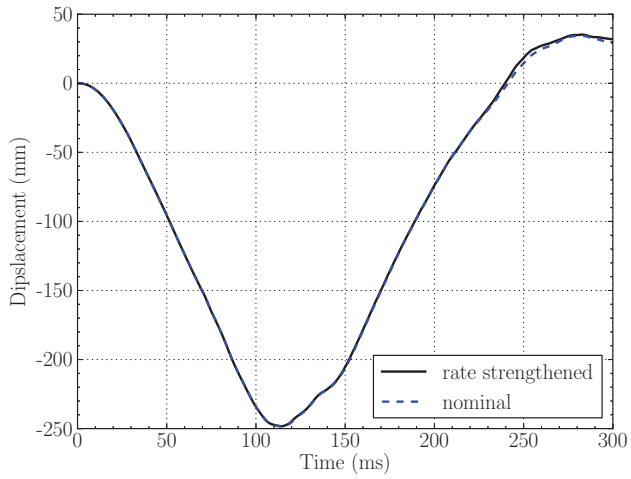
The modified response of fasteners considering the rate effect was then assigned to the sub-assemblage model. A series of analyses were carried out to examine the effect of the stiffened fastener on the response of the sub-structure. In this study, the overpressure ranged from 1.5 to 15 kPa and the impulse ranged from 150 to 1500 kPa.ms.

A comparison of the response of the side rail in the sub-assemblage model with and without the rate stiffened fastener is shown in Figure 6.34. The same cases were selected as in Figure 6.5. It can be observed that the response of side rail was not notably affected by the modified behaviour of the fasteners.

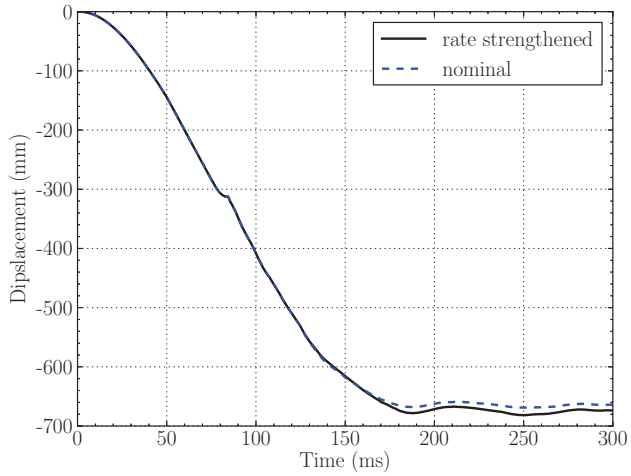
Pressure - impulse diagrams based on the sub-assemblage with stiffened fasteners is compared with the original results with rate effect in Figure 6.35. It is evident that the modified fastener does not have a notable influence on all three damage curves.

In addition to the above, a comparison of the combined response of the side rail with fastener failures is presented in Figure 6.36, corresponding to the load defined in Case 98. Although the response of side rail was not affected, the percentage of fastener failure was influenced to some extent by the strengthened response. It can be seen that the fasteners failure was delayed which also corresponds to a higher displacement of side rail due to the strain rate effect. This is expected since the strength of the fastener was increased hence was able to sustain more load which delayed failure.

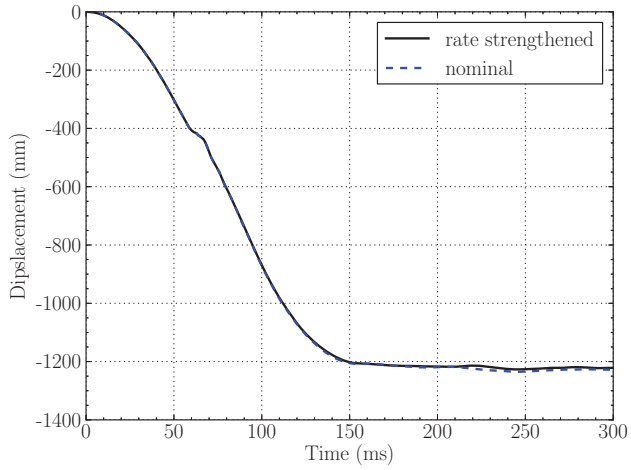
The final analysis was to investigate the influence of the stiffened fastener on the pressure - impulse diagram of the fastener failure (as shown in Figure 6.37).



(a) case 33



(b) case 51



(c) case 82

Figure 6.34: Comparison of response of side rail with and without rate stiffened fasteners

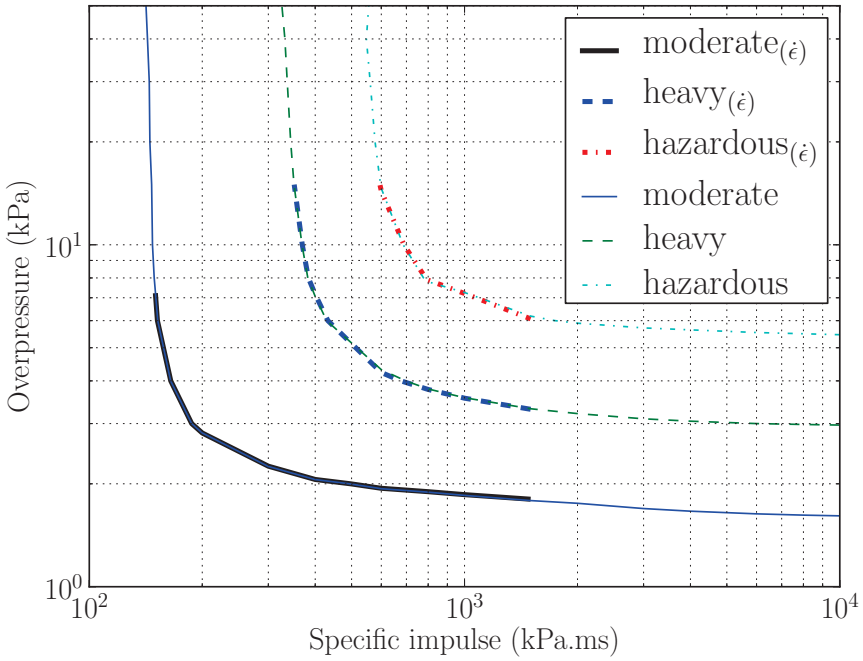


Figure 6.35: Effect of the rate stiffened fastener on the pressure - impulse diagrams of the side rail maximum displacement

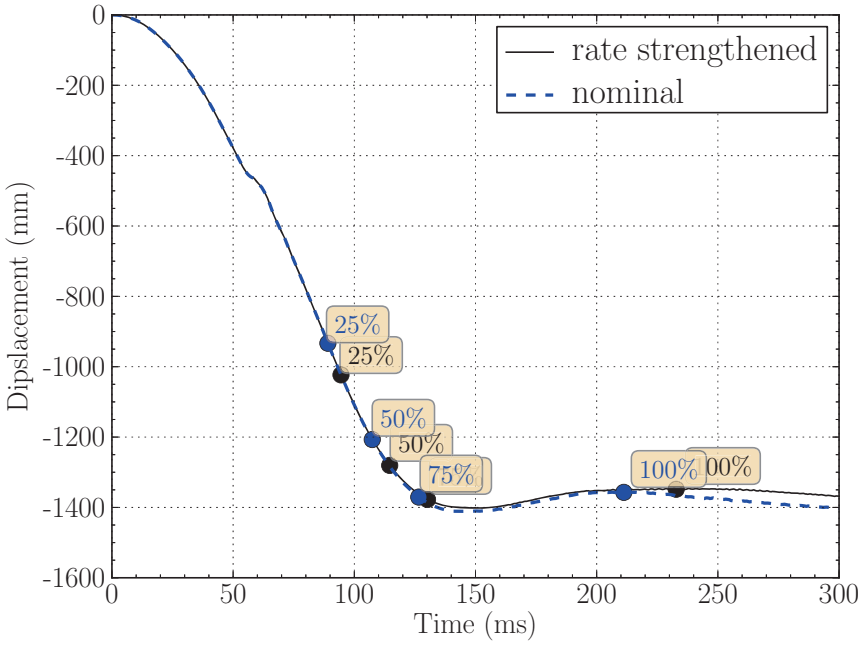


Figure 6.36: Effect of the rate stiffened fastener on the percentage failure of fasteners

The iso-damage curve corresponds to the 50% failure of the fasteners in the sub-assemblage. It can be seen that the iso-damage curve is shifted slight towards the upper and right direction. This increase of resistance of fastener failure is also expected because the iso-curves are directly based on the capacities of the fasteners. However, the effect of the strengthened fastener on the response of the sub-assemblage overall is clearly insignificant.

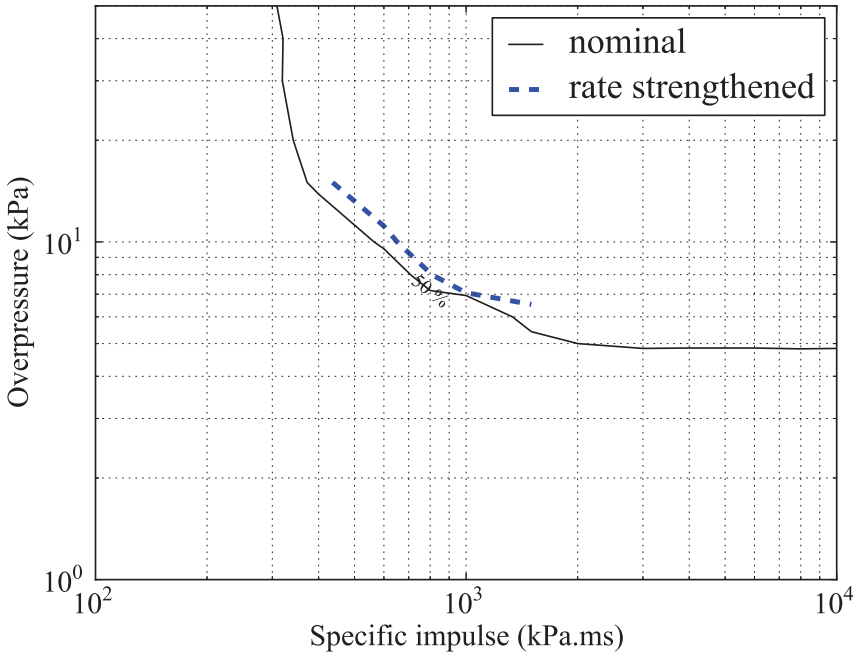


Figure 6.37: Influence of the rate effect on the pressure - impulse diagram of maximum percentage of fastener failure (50% failure)

In this chapter, results from the numerical studies using the sub-assemblage model were presented and discussed. The response of side rail and cladding were examined. The failure of selected fasteners was also assessed in detail. Studies were also performed to relate the cladding and side rail response to fastener failure. It was found that the failure of fasteners was significantly influenced by the response of claddings, but under certain loading conditions the failure can be linked to the displacement of the claddings. It was difficult to relate the overall percentage of fastener failure to the displacement of the side rail. In order to understand the fastener failure under blast loading, the pressure - impulse

diagram using percentage of fastener failure as iso-damage curves was derived. This damage criteria was used to replace the displacement of claddings in this study. Pressure - impulse diagrams using other damage criteria were also created for the sub-structure. The combined pressure - impulse diagrams would serve as a useful tool in blast damage assessment and design of similar structures.

In the next chapter, a simplified approach using a single degree of freedom model is presented and the results are compared with the non-linear finite element results discussed in this chapter. In addition, a blast simulation study is also presented in the next chapter. The pressure - impulse diagrams derived here will be used with the results from the simulation in to highlight key design implications based on the findings of this investigation.

Chapter 7

Simplified approaches and design considerations

7.1 Single degree of freedom approach

The non-linear finite element method is used in this work as the primary tool to study the response of warehouse structures. In addition, simplified single degree of freedom models were used to complement and compare with the numerical analysis tools. SBEDS (USACE (2008a)) was employed here, which is a spreadsheet software implementing explicit numerical step integration. The software accounts for material properties, geometry, boundary conditions, supported mass and connection capacities of the component modelled. It also accounts for tensile membrane action which is limited by the lesser of the connection capacity or the member axial strength. Formulations of the model and tension membrane action were presented in Section 2.4.1.1.

As noted before, the cladding panels are continuous in two-spans over the side rails and which in turn are two-span continuous over the columns. The span of the cladding panel and side rails are 1.8 and 6.69 m respectively. Taking advantage of symmetry, they are modelled as a beam 1.8 or 6.69 m long with one end fully fixed and one simply supported end as shown in Figure 7.1, in which L is the length of the member (L=1.8 for cladding panel and L=6.69 for side rail).

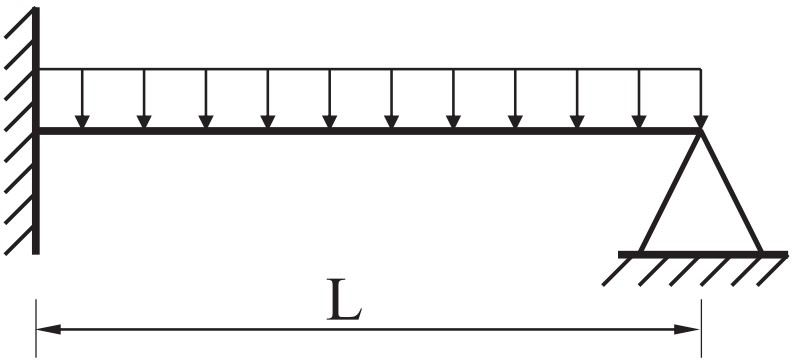


Figure 7.1: Cladding panel and side rail simplified SDOF model

7.1.1 Wall cladding

Cladding panels were described in detail in Section 5.3.7 and the material properties were presented in Section 5.4. Different section modulus and moment of inertia values were used for the inbound and rebound response based on the geometric properties provided by the manufacturer. The values used in the analysis are presented in Table 7.1. It should be noted that in this analysis the total self weight of the cladding panel (two sheeting plus infill) of 0.301 kPa was included. The SDOF model here represents a single layer of the sheeting.

Table 7.1: Geometric properties of wall cladding panel

Positive moment of inertia	119.95 mm^4/mm
Negative moment of inertia	89.02 mm^4/mm
Positive section modulus	5.763 mm^3/mm
Negative section modulus	5.409 mm^3/mm

The cladding panels are fixed to the side rails by six fasteners (Section 5.3.8) at the end of the panels and three fasteners over the middle support. Tensile membrane action is therefore limited by the capacity of the end connections, since they are smaller than the axial capacity of cladding panel. The end connection capacity was determined to be 6.32 N/mm according to Eurocode 3, Part 1-3.

The bearing resistance was calculated as follows:

$$F_{b,Rd} = af_u dt/\gamma_{M2} = \frac{1.14 \times 300 \times 5.5 \times 0.7}{1.25} = 1.053kN \quad (7.1a)$$

$$For\ six\ fasteners\ per\ metre\ :\ \Sigma F_{b,Rd} = 6.32kN/m = 6.32N/mm \quad (7.1b)$$

This will limit the tensile membrane action in the cladding panel when large deflections occurs.

The properties determined for the SDOF model of the cladding panel are shown in Table 7.2. There are two load-mass factors, one for elastic and one for plastic response. The stiffness K_1 is the elastic modulus while K_3 is for tensile membrane action due to the capacity of the end connections. The displacements x_1 and x_2 represent the starting points of the plastic and tensile membrane stages respectively.

Table 7.2: SDOF properties for cladding panel model

Mass, M	30.7 kg/m^2
Load-Mass Factor, K_{LM}	
K_{LM1}	0.78
K_{LM2}	0.66
Stiffness, K	
K_1	0.32 kPa/mm
K_2	0.00 kPa/mm
K_3	0.02 kPa/mm
Resistance, R	
R	5.45 kPa
Yield displacement, x	
x_1	17.12 mm
x_2	20.38 mm

The resistance function of the SDOF model for the cladding panel is shown in Figure 7.2.

7.1.2 Side rail

Details and material properties of side rails have already been presented in Sections 5.3.6, 5.3.9 and 5.4. The geometric properties according the manufacturer

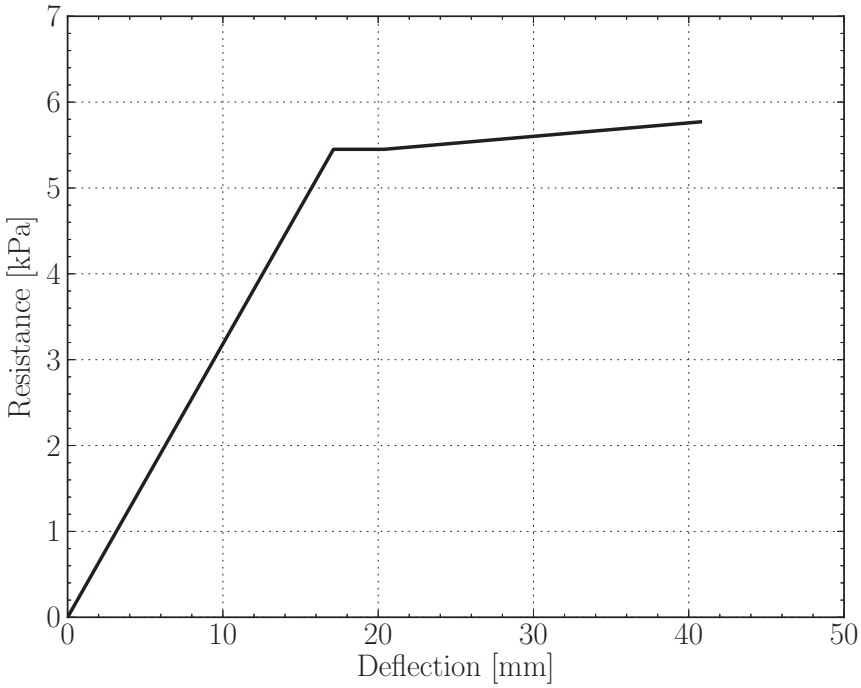


Figure 7.2: Resistance curve of SDOF model for cladding panel

(Hadley (2004)) are shown in Table 7.3.

Table 7.3: Geometric properties of side rail

Self weight	3.7 kg/m
Cross sectional area	4.58×10^2 mm^2
Moment of inertia	2.7475×10^6 mm^4
Section modulus	4.48×10^4 mm^3
Depth	200 mm
Web thickness	1.2 mm
Radius of gyration	28.8 mm

The component has a length of 6.69 m with a tributary width of 1.8 m (for supported cladding panel mass and load calculation). The limiting tensile capacity for membrane action was determined to be 21.45 kN, which is the bearing

resistance of the side rail calculated as follows:

$$F_{b,Rd} = 2.5a_b k_1 f_u dt/\gamma_{\mu 2} = \frac{2.5 \times 0.833 \times 0.984 \times 470 \times 12 \times (1.2 - 0.04)}{1.25} = 10.725kN \quad (7.2a)$$

$$For\ two\ bolts\ :\ \Sigma F_{b,Rd} = 21.45kN \quad (7.2b)$$

This will limit the tensile membrane action in the side rail when large deflections occurs.

The properties of the SDOF model for the side rail are shown in Table 7.4. Similarly, two load-mass factors are used for elastic and plastic response respectively. The stiffness K_1 is the elastic modulus while K_2 is for tensile membrane action due to the bearing resistance of the connection as calculated above. The plastic range begins at x_1 while the catenary stage starts at x_2.

Table 7.4: SDOF properties for the side rail model

Mass, M	32.74 kg/m^2
Load-Mass Factor, K_{LM}	
K_{LM1}	0.78
K_{LM2}	0.66
Stiffness, K	
K_1	0.03 kPa/mm
K_2	0.00 kPa/mm
K_3	0.002 kPa/mm
Resistance, R	
R	2.09 kPa
Yield displacement, x	
x_1	81.66 mm
x_2	145.26 mm

The resistance function of the SDOF model for the side rail is shown in Figure 7.3.

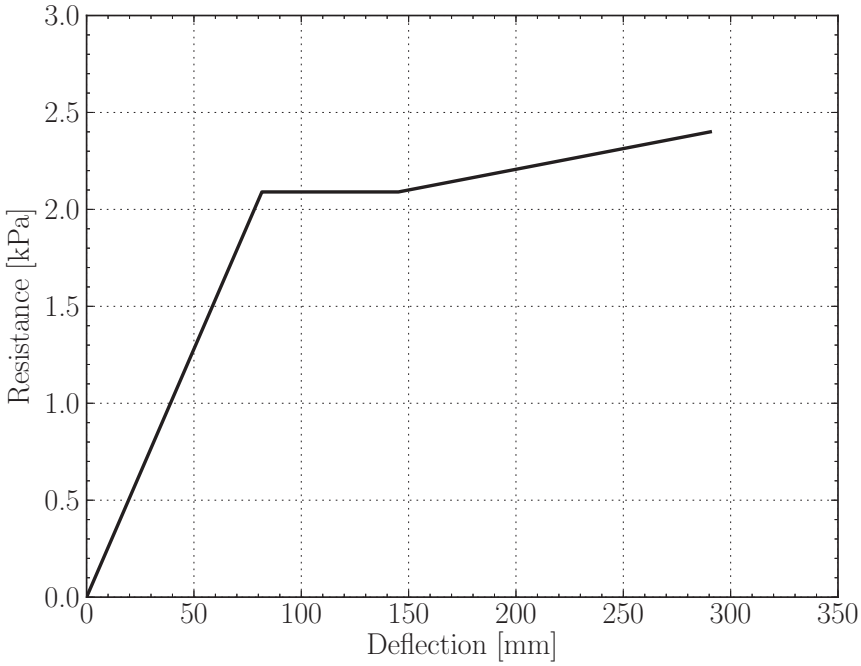


Figure 7.3: Resistance curve of SDOF model for side rail

7.1.3 Component interaction

In the SDOF analysis, each component is modelled individually. The cladding panels were uncoupled from the side rails and then the blast load was in turn applied to each of the component. Each component was analysed independently with the mass of the supported components to account for the the correct inertia and deflections. This method is generally more conservative and was indicated to be appropriate when the ratio of the natural frequencies of the supporting and supported components is greater than two (Biggs (1964)).

The natural period of the equivalent SDOF model for the side rail and cladding panel can be calculated as:

$$T_n = 2\pi\sqrt{\frac{K_{LM1}m}{k_1}} \tag{7.3}$$

Thus for the side rail the natural period is $T_{n(siderail)} = 198.42ms$ and for cladding panel $T_{n(cladding)} = 54.48ms$. The ratio of natural frequencies was determined to be $\frac{115.33\ rad/sec}{31.64\ rad/sec} = 3.64$, and according to Biggs (1964) this approach can be

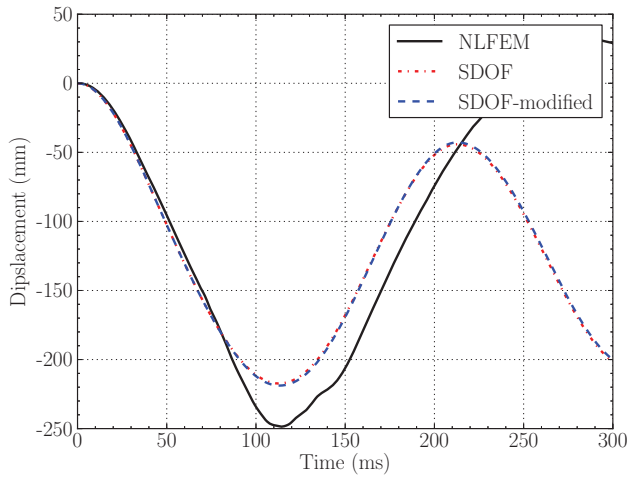
adopted for the analysis of the structural components of the warehouse.

7.1.4 Response of simplified model of side rail

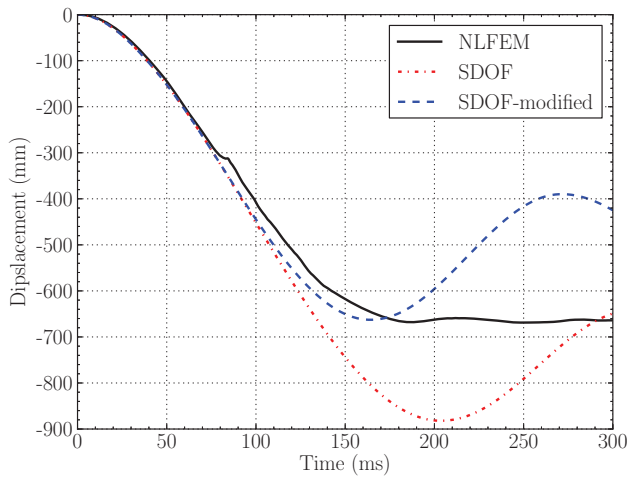
Three examples of the response of the simplified model of the side rail are presented in Figure 7.4. Their responses correspond to the loads defined in Case 33, 51 and 82. These are the same selected cases in the detailed finite element study corresponding to moderate, heavy and hazardous damage levels. It can be noted that at the moderate level, the simplified model compares well with the finite element model. However, in the case of heavy and hazardous damage levels, the simplified model significantly over-predicts the maximum dynamic displacement. The reason behind this is that the tensile membrane stiffness defined in the simplified model was based on the shear capacity of the side rail according to the Eurocode (Equation 7.2), which was 24.15 kN. This is smaller than the axial yield capacity of 53 kN determined by the finite element model of the connection. It can be seen that the responses of the simplified model compares much better with the finite element model when the numerically determined axial capacity was used to define the tensile membrane stiffness.

The pressure - impulse diagram based on the simplified model of the side rail is presented in Figure 7.5 and compared with the iso-damage curves produced by the finite element sub-assemblage model. Generally the iso-damage curves based on the simplified model compare well with that of the finite element model, particularly at the moderate and heavy damage levels. Some discrepancies can be observed at the hazardous damage level.

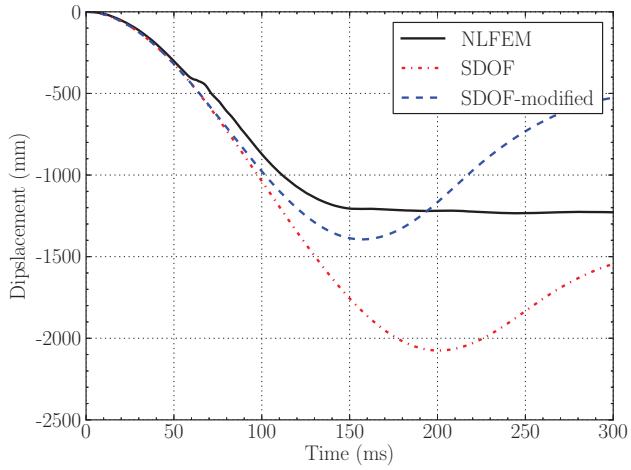
At hazardous damage level, the limiting pressure value of the simplified model in the quasi-static region is lower than the finite element model. This indicates that in this region the simplified model over-predicts the maximum displacement at the centre of the side rails. In the finite element model, the axial behaviour for the end connection of the side rail was defined with plastic hardening; while, in the simplified model, only one constant axial support capacity was used to determine the tensile membrane stiffness. Therefore, at large deformation (e.g. hazardous damage level), the plastic hardening of the connection response results in a higher tensile membrane stiffness than in the simplified model. Hence, the



(a) Case 33



(b) Case 51



(c) Case 82

Figure 7.4: Response of simplified model of side rail

displacement predicted by the finite element model is less than in the simplified model.

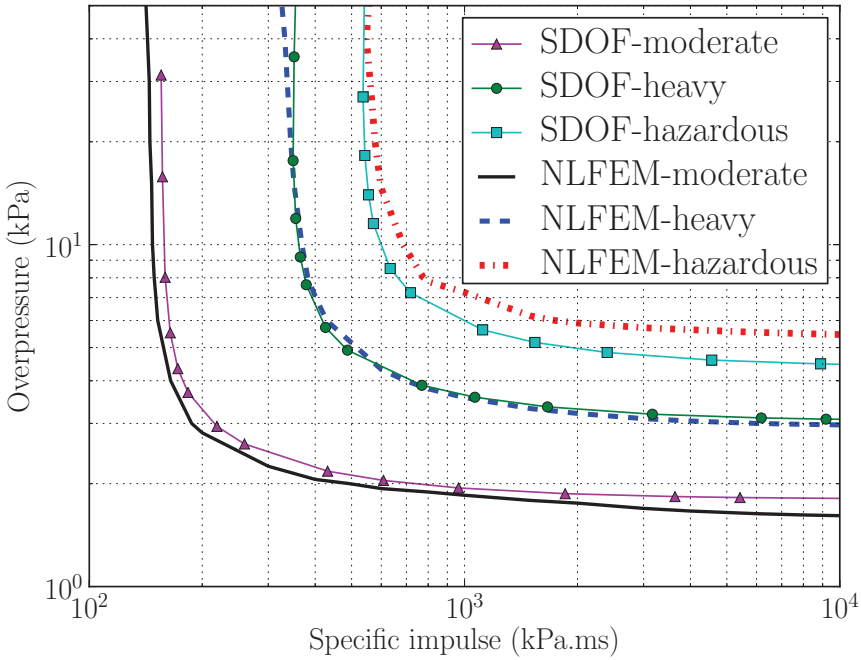


Figure 7.5: Comparison of pressure - impulse diagrams (maximum dynamic displacement)

In the impulsive loading region, the curves corresponding to the hazardous damage level predicted by the simplified model and the finite element model match reasonably well despite the same difference in tensile membrane stiffness. This is attributed to the combination of higher response modes of the side rails that are excited by the impulsive loading and the higher tensile membrane stiffness in the finite element model. Higher modes in the response of side rails increases the maximum displacement at the centre. The simplified approach was based only on the fundamental mode of the component. Based on the above discussion, it can be concluded that both the simplified and finite element model are capable of accurately predicting the response of the side rails in the sub-assemblage. The assumption of analysis of the component in a decoupled manner claimed by Biggs (Biggs, 1964) is valid for the side rails.

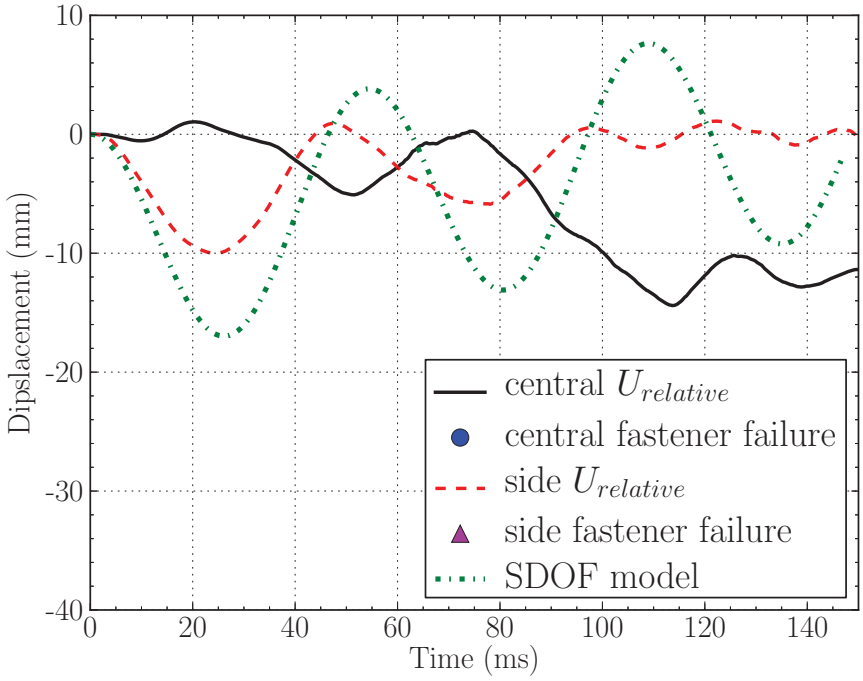
7.1.5 Response of simplified model of cladding

Two selected cases of the simplified model of cladding panel are presented in Figure 7.6. The response corresponds to the load defined in Case 33 and 82, for the moderate and hazardous damage levels of the side rail. It can be seen in Figure 7.6a that the response of the simplified model is only comparable with the side cladding of the finite element model. The maximum displacement of the simplified model is about 16.98 mm while that of the side cladding of the finite element model is 10 mm. This discrepancy is mainly due to the difference in elastic stiffness in the simplified and finite element model.

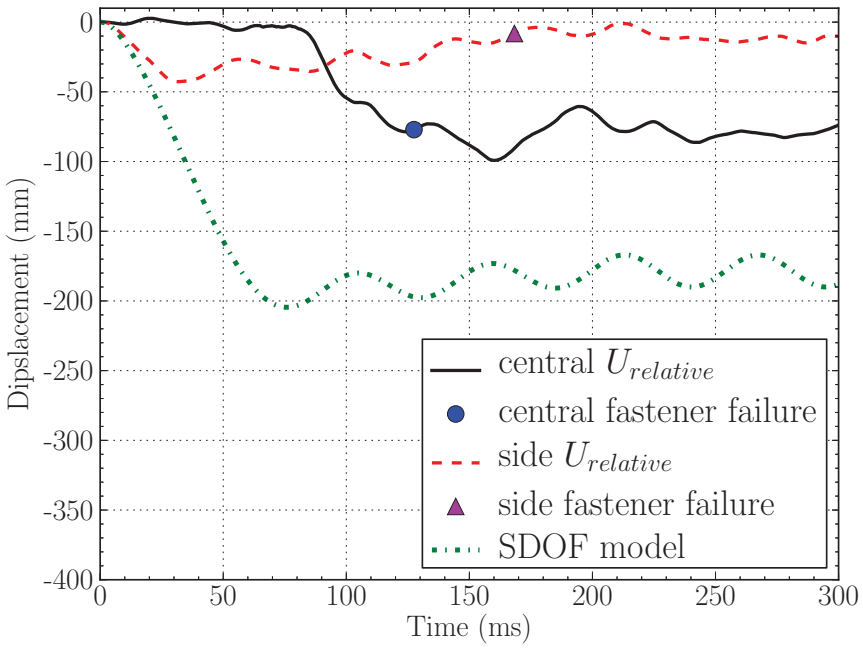
It can be noted that the displacement of 16.98 mm is just within the elastic range depicted in Figure 7.2, hence in Case 33 the response of cladding was elastic. The elastic stiffness determined for the simplified model is 0.32 kPa/mm, and at 16.98 mm displacement the resistance is $0.32 \times 16.98 = 5.41$ kPa. An elastic finite element analysis determined that the elastic stiffness of the cladding is 0.525 kPa/mm, thus at a resistance of 5.41 kPa the elastic displacement is $5.41/0.525 = 10.3$mm, which is approximately equal to the maximum deflection of the side cladding in the finite element model of the sub-assemblage.

It can be seen that the displacement history of the central cladding of the sub-assemblage is significantly different to the side cladding and the simplified model. This is mainly due to the dynamic effect and the response interaction between the central cladding and the side rails. Within the first 30 ms shown in Figure 7.6a, the central cladding deformed slightly inwards and then outwards relative to the side rails, before large deformations occurred. Similarly, as shown in Figure 7.6b, there is a delay in the deflection of the central cladding about 80 ms before it started to deform. These observations suggest that there are strong dynamic interaction between the central cladding and the side rails.

The displacement history of the simplified model corresponding to Case 82 is shown in Figure 7.6b. The simplified model significantly over-predicted the response compared to the displacement of the side cladding in the sub-assemblage model. The maximum displacement predicted by the simplified model was 204 mm. Following the resistance curve in Figure 7.2, it was determined that the maximum resistance at 204 mm was 8.31 kPa. At this level of pressure, in the



(a) Case 33



(b) Case 82

Figure 7.6: Responses of simplified model of cladding

elastic finite element model, the side cladding should displace 8.31/0.525=15.83 mm at the mid-span. The actual maximum displacement of the side cladding was 45 mm, which falls between the elastic value (15.83 mm) and the simplified value (204 mm).

The above indicates that the yielding resistance of the simplified model for cladding was under-estimated. The discrepancies between the simplified cladding model and the side cladding were due to both the stiffness and yielding capacity of the cladding being under-estimated by the simplified approach. Louca (Louca et al., 1996) suggested that in order to achieve better correlation between the simplified and FE model, the resistance curve based on static non-linear FE analysis should be used. However, the correlation between the simplified model and the central cladding cannot be improved by the above suggestion, owing to the strong interactions between the central panel and the side rails.

It has been noted that the displacement of the cladding can reasonably be related to the shear failure of the corresponding fastener. It has been found out that for this type of structure, the major shear failure (closely related to the y direction) of the fastener would occur at a cladding displacement of about 85 mm, which is 5% of the length of the span. In the region defined in Figure 6.15, the simplified model of the cladding can be used to capture the fastener failure based on the maximum displacement at the middle. This is because the simplified approach had the same deformed shape as the cladding (either central or side) only when the fastener failed in shear (close to the y direction). It is not able to capture failure in the tensile or in the x direction (in the middle side rail), nor the excessive accumulative plastic deformation around the screw.

According to Figure 6.15, the simplified model of the cladding should be able to capture the shear failure (close to the y direction) in the impulsive region for the side claddings or in the quasi-static region for the central claddings. For some cases, as highlighted in the figure, it is applicable to both the side and central cladding panels when the failure mechanism of these two are the same.

Based on above discussion, it can be concluded that the simplified approach is not suitable for the analysis of the panels, particularly for the central ones. This is due to the inability of the simplified model to capture the interaction between the central cladding and the side rails. This is inconsistent with the assumption

made by Biggs (Biggs, 1964) in order to use the simplified model to analyse two components in a decoupled manner, the natural frequency ratio of the two components should be more than two. The frequency ratio of the cladding and side rail used in the present work is 3.64. It has been shown that the fasteners failed in different modes, and that simplified model should be able to capture the shear failure close to or in the y direction, where it is unable to capture failure in the tensile direction nor the excessive accumulative plastic deformation around the screw.

7.1.6 Pressure - impulse diagrams of simplified models

A combined pressure - impulse diagram using the simplified models presented above is shown in Figure 7.7. This completes the blast resistance analysis based on simplified models of the sub-assemblage structure of the selected design in this work. The limiting values of overpressure and impulses are shown in Table 7.5.

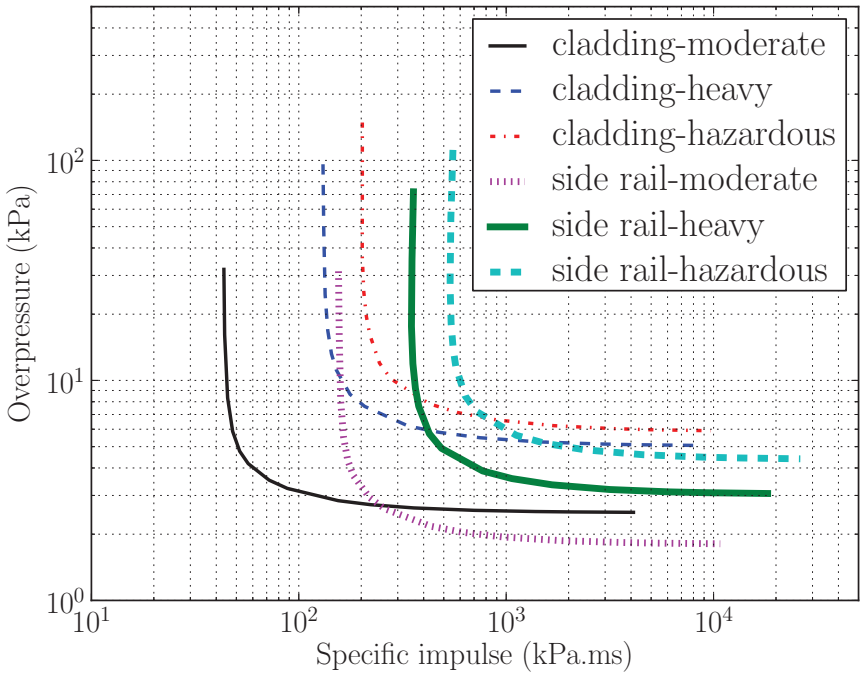


Figure 7.7: Combined pressure - impulse diagram using the simplified approach

It can be seen that in the quasi-static region the critical component are side rails.

In contrast, the claddings become critical in the impulsive region.

Table 7.5: Combined pressure - impulse diagram of simplified model

	moderate		heavy		hazardous	
	P(kPa)	I (kPa.ms)	P(kPa)	I (kPa.ms)	P(kPa)	I (kPa.ms)
side rail	1.8	155	3.0	357	4.4	553
cladding	2.51	43.5	5.06	131	5.9	202

It should be noted that in this pressure - impulse diagram, the iso-damage curves for the side rails match well with the non-linear finite element model. The iso-damage curves of the cladding, on the other hand, were over-predicted due to the smaller stiffness and lower yield capacity. More importantly, the iso-damage curves did not distinguish between side and central claddings, hence information on the fastener failure (based on cladding deformation) is difficult to obtain. No information can be obtained on the total fastener failure from the simplified approach.

In this section, the simplified approach based on Biggs' method (Biggs, 1964) was presented. The results of the simplified approach were compared with the non-linear finite element model. It was found that the results of the simplified approach were comparable for side rails but not in good agreement for claddings, particularly for the central panels. This was mainly due to the inability of the simplified model to capture the strong interaction between the central cladding and the side rails.

7.2 Assessment of blast overpressures

7.2.1 Blast wave simulation on rigid warehouse

Assessment of the structural damage from the Buncefield incident was undertaken by the Defence Ordnance Safety Group (DOSG) of the Ministry of Defence (SCI (2009)). The work covered a range of buildings in or near the Buncefield depot. DOSG has access to a variety of tools for predicting the blast effects from high explosive detonations ranging from simple look-up tables, empirical curves, to full 3D hydrocodes. For this assessment, an empirical tool based on Kingery -

Bulmash curves for TNT detonations (Kingery and Bulmash (1984)) was used to investigate the relationships between peak overpressures and the corresponding damage levels at various distances from the Buncefield explosion.

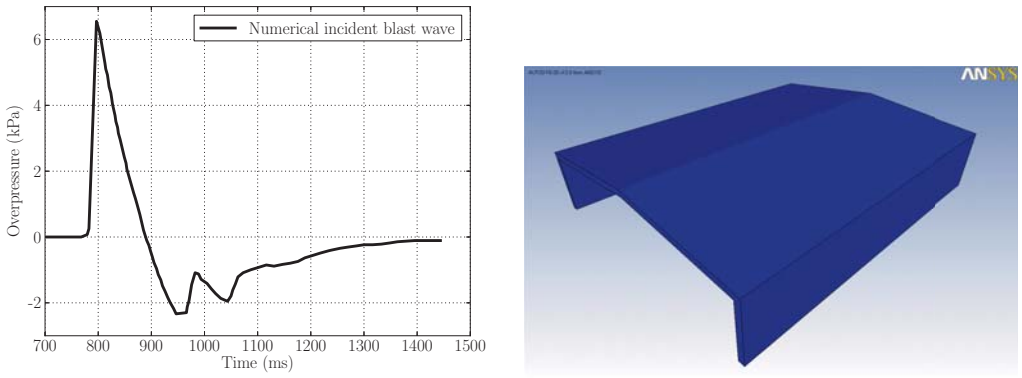
Table 7.6: Peak overpressure of blast wave from 7500 kg TNT charge with 324 m stand-off distance

Blast wave analysis tool	Peak overpressure(kPa)
AUTODYN-1D	6.7
Empirical charts	7
DOSG Assessment	8

Previous assessments suggest that a high explosive semi-spherical charge of 7500 kg of TNT at the centre of Tank 912 (shown in Figure 2.3) would be able to replace the vapour cloud and cause similar damage levels to the surrounding building structures. It has been found that this equivalent method with 7500 kg TNT charge has consistent scaling with direction from the source of explosion (Tank 912) and provide reliable scaling of pressure related damage with distance. Warehouse 2 (WH2) located at the north east of the site is 324 metres away from the centre and Warehouse 1 (WH1) at the south is 414 metres away. Taking the location of Warehouse 2 (WH2) as an example, in the present project the hydrocode AUTODYN (ANSYS) and empirical charts (Baker et al., 1983) were used to predict the overpressure blast wave at 324 metres away from a detonation of 7500 kg TNT charge. The peak overpressures are compared with DOSG results in Table 7.6.

It can be seen that the results from AUTODYN and the empirical charts (Baker et al., 1983) compare well with the DOSG analysis. The difference between the empirical charts and the DOSG assessment deserve some discussion. AUTODYN can only model spherical air burst whose charge weight has to be multiplied by a factor so that it is equivalent to the semi-spherical surface burst used in the empirical charts and the DOSG analysis. The conversion factor usually ranges from 1.5 to 2.0. In the AUTODYN-1D model, a factor of 1.8 was used and this could contribute to the underestimation of the peak overpressure value. Figure 7.8a shows the time history of the blast wave predicted by AUTODYN. The blast wave has a peak value of 6.6 kPa and a positive duration around 100

ms.



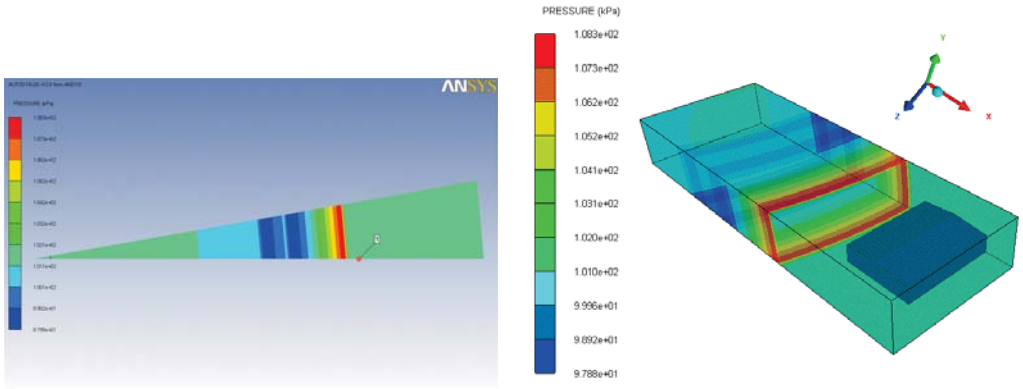
(a) numerical blast profile (b) rigid model of warehouse

Figure 7.8: Numerical modelling of blast wave (semi-spherical 7500kg TNT charge and 324m stand-off) and the rigid warehouse structure

Atkinson (Atkinson, 2011) noted a post-Buncefield investigation that the failure of structural connections (blastward side, close to the explosion) would lead to large venting areas on the wall surface. This would result in pressurising the interior of the warehouse and protect the other side walls and roof from blast damage. It has been therefore decided to carry out a numerical study using AUTODYN (ANSYS) to investigate the warehouse internal pressurisation due to failure of the walls and then examine the blast loading on various surfaces of the warehouse. The study was based on the location of Warehouse 2 (WH2).

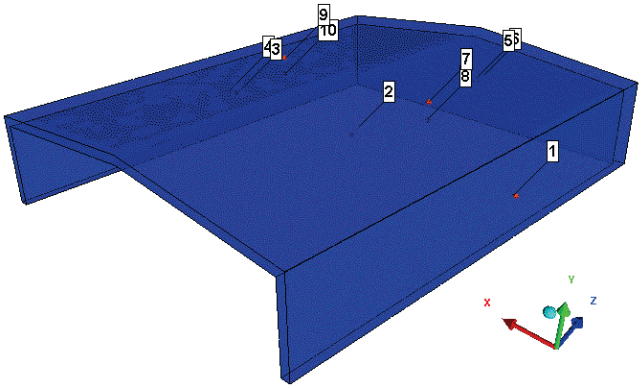
It was impractical to model the whole structure with flexible components and connections. Hence, a rigid solid model was used to represent the envelope of the warehouse and subsequent numerical studies were carried out on a rigid structure. A coupled Eulerian - Rigid Lagrangian model was used in the analysis as shown in Figure 7.9, which shows the one dimensional blast wave which modelled the initial explosion of 7500 kg semi-spherical TNT charge. The 1D blast wave was then remapped into the three dimensional model shown in Figure 7.9b and coupled with a rigid warehouse. Only half of the warehouse was modelled by taking advantage of symmetry.

Pressure gauges were used to record the blast loading experienced by the rigid warehouse model. Their locations are shown in Figure 7.10. Gauge 1 is located at



(a) blast wave Autodyn-1D model (b) coupled rigid warehouse model

Figure 7.9: Coupled model of blast wave with rigid warehouse

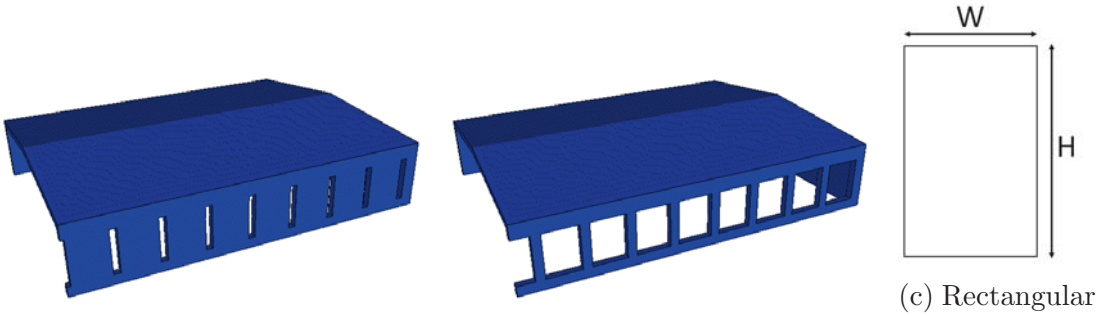


Gauge 1: front wall externalsurface
Gauge 2: centre inside of warehouse
Gauge 3: back wall internal surface
Gauge 4: back wall external surface
Gauge 5: side wall internal surface
Gauge 6: side wall external surface
Gauge 7: front roof external surface
Gauge 8: front roof internal surface
Gauge 9: back roof external surface
Gauge 10: back roof internal surface

Figure 7.10: Location of numerical pressure gauges

the external surface of the front wall (blastward wall, facing the blast wave) which would register the normal reflected overpressure blast wave. Gauge 2 is located at the centre of the building so it would register the internal pressurisation due to failure of the structure. Gauges 3 - 10 were used to record the internal and external overpressure loading experienced by the back wall (leeward), side walls and roof.

Since the warehouse model was rigid, no failure of the structure would be possible hence venting and pressurisation was not allowed. To enable internal pressurisation during the passage of the blast wave, pre-cut rectangular holes were created on the blastward wall of the model, as shown in Figure 7.11. These holes were used to represent the venting area created by failure of the walls.



(a) 10% venting area (b) 50% venting area (c) Rectangular hole

Figure 7.11: Pre-cut holes on the blastward wall of the rigid warehouse model

Table 7.7: Analysis cases with different venting area definition

Case	Venting area (%)	W (m)	H (m)
1	0	0	0
2	10	1.5	6.5
3	20	2.0	6.5
4	30	3.0	6.5
5	40	4.0	6.5
6	50	5.0	6.5
7	30	4.4	4.4
8	30	6.5	1.85

The venting area was defined as a percentage representing the ratio of the area of the rectangular hole to the total area of the blastward wall (front wall).

In this study, the venting area in Cases 1-6 ranged from 0 - 50 % as shown in Table 7.7 by varying the dimensions of the rectangular holes. Cases 7 and 8 had the same percentage of venting areas as Case 4 but the shape of the rectangular holes were different. This was intended to study the effect of the shape of the holes on the internal pressurisation of the building.

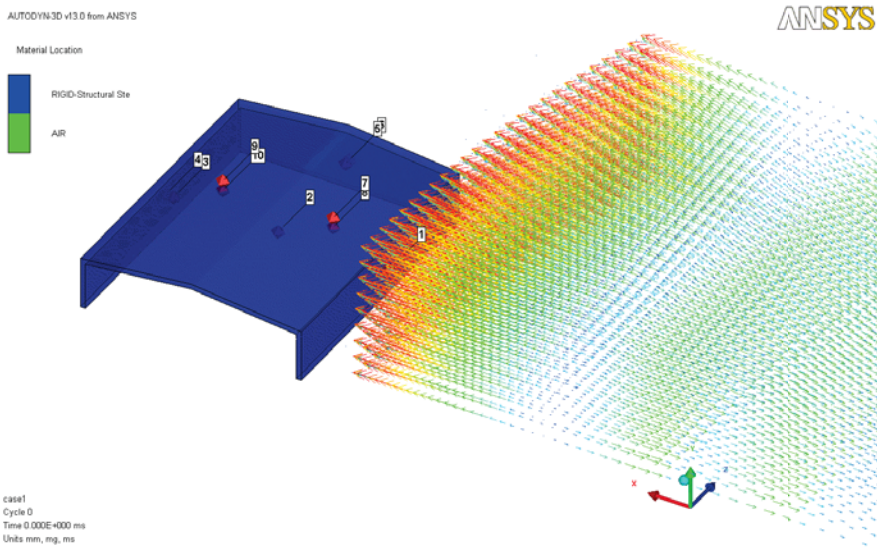


(a) rectangle $W/H = 0.46$ (b) square $W/H = 1$ (c) rectangle $W/H = 3.51$

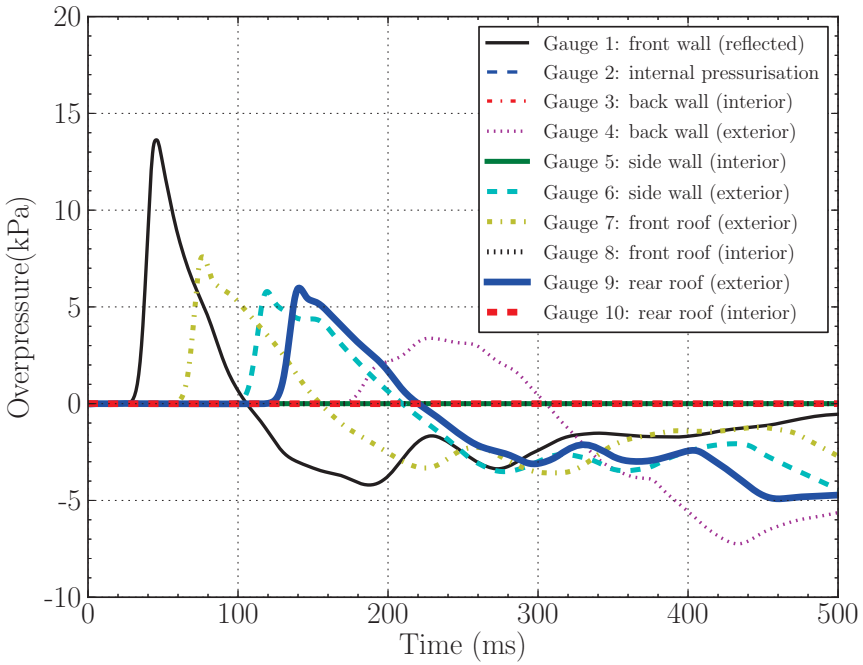
Figure 7.12: 30% venting area with different shapes of holes

7.2.2 Discussion of blast loading results

Blast loading assessment has been carried out as described in Section 7.2.1. The incident wave depicted in Figure 7.8a was coupled with the rigid house as shown in Figure 7.13a. The free-field overpressure blast wave at the distance of the front wall has a peak overpressure of 6.7 kPa and duration around 100 ms. In Case 1 the rigid structure was assumed to be intact and overpressure loadings recorded on the exterior and interior faces of the walls and roofs are presented in Figure 7.13b. It can be seen that all gauges located inside the building recorded zero overpressures since no pre-cut holes were created in Case 1. The peak reflected overpressure recorded by Gauge 1 at the exterior of front face is 13.63 kPa, which compares well with the theoretical value of 13.78 kPa for normal reflection of a rigid surface (only under-estimated by 1.1%). Overpressure loadings on the roof and side show similar characteristics to chose described in the literature. Since the gauges were located at different distances, the arrival time of the pressure waves are different as well. The back face experiences the blast loading last with the lowest peak value as expected, and the overpressure loading has a clear finite rise time. This is attributed to the occurrence of the diffracted wave at the corner between the roof and the back wall. It travels on the back wall with the blast wave and cause the latter to have a finite rise time.



(a) rigid warehouse with blast



(b) overpressure loadings (Case 1)

Figure 7.13: Simulation of blast loading on rigid warehouse model

According to Table 7.7, a few pre-cut holes were created on the front wall to simulate the venting through the area caused by structural failures. The venting area ranges from 10 to 50% in modelling Cases 2 - 6. Figure 7.14 shows the overpressure loading for all gauges in Case 4 with 30% venting area on the front wall. The inside of the warehouse model was pressurised through venting, and pressure gauges located on the interior faces of walls and roofs registered overpressure loadings with various intensities. The pressure loading recorded by Gauge 1 was did not exhibit a normal reflection of the incident blast wave and the peak value was reduced by the presence of pre-cut holes. However since the objective of Cases 2 - 6 was the internal pressurisation, the reflection at the front wall is no longer relevant.

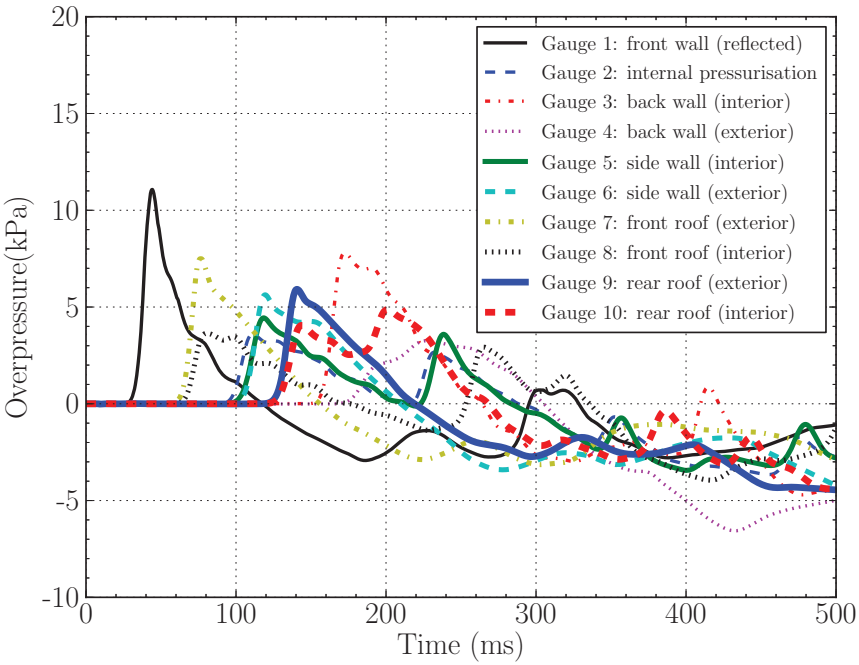


Figure 7.14: Overpressure loading results for Case 4 (30% venting area)

Gauge 2 was used to register the internal pressure in the middle of the rigid building model. The peak internal overpressures recorded by Gauge 2 in Cases 1 - 6 are plotted in Figure 7.15. As expected the peak internal overpressure increases with a larger venting area on the front wall. It approaches the free-field peak value as the venting area increases to 100 %.

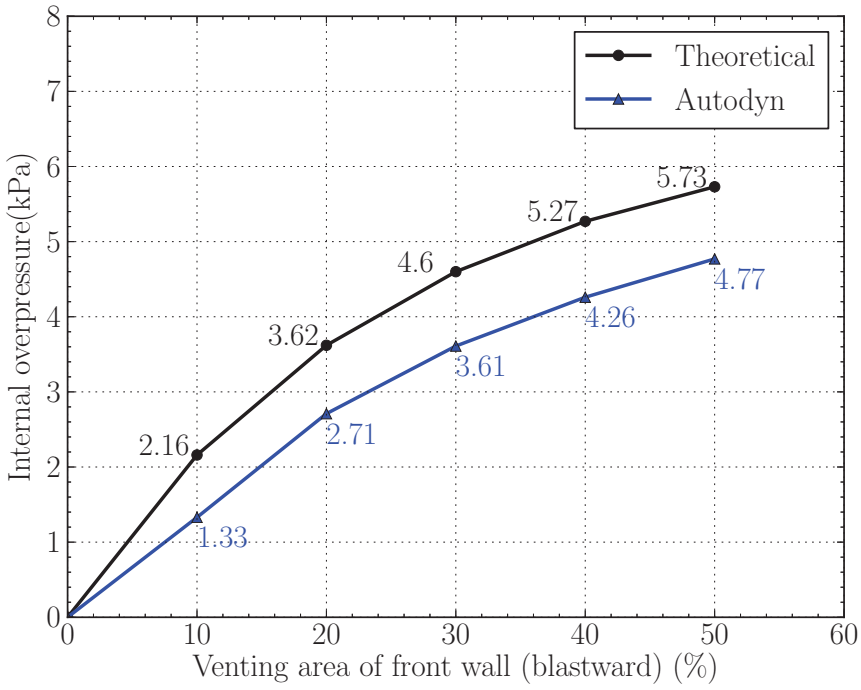


Figure 7.15: Internal pressurisation due to venting area on front wall

The theoretical and numerical results are compared as shown in the same figure. The theoretical values were calculated according to Equation 7.4 for transmission of a weak shock wave through a perforated wall in to a closure (Atkinson, 2011).

$$P_{transmission} = \frac{C}{2}\left\{\sqrt{1+\frac{4P_{incident}}{C}}-1\right\} \; where \; C = 2\frac{F^2}{(1-F^2)}{C_d}^2 \cdot \rho {a_0}^2 \quad (7.4)$$

where $P_{transmission}$ is the overpressure transmitted through the perforated barrier while $P_{incident}$ is the incident overpressure. F is the opening percentage and C_d is the discharge coefficient for flow through the barrier. And ρ is density and a_0 is the speed of sound.

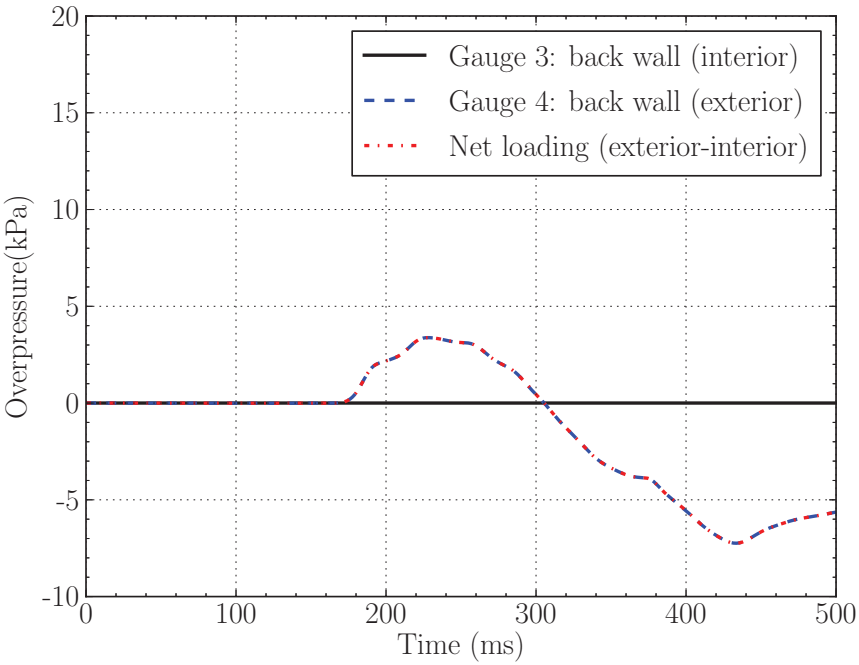
It can be noted that numerical results are all lower than the theoretical values. The simple theory applies to a constant external pressure and the transmitted wave is determined at the location immediately after the perforated barrier. In addition, the short duration pressure waves in the numerical simulation tended

to broaden, and the maximum pressures were decreasing as they propagated.

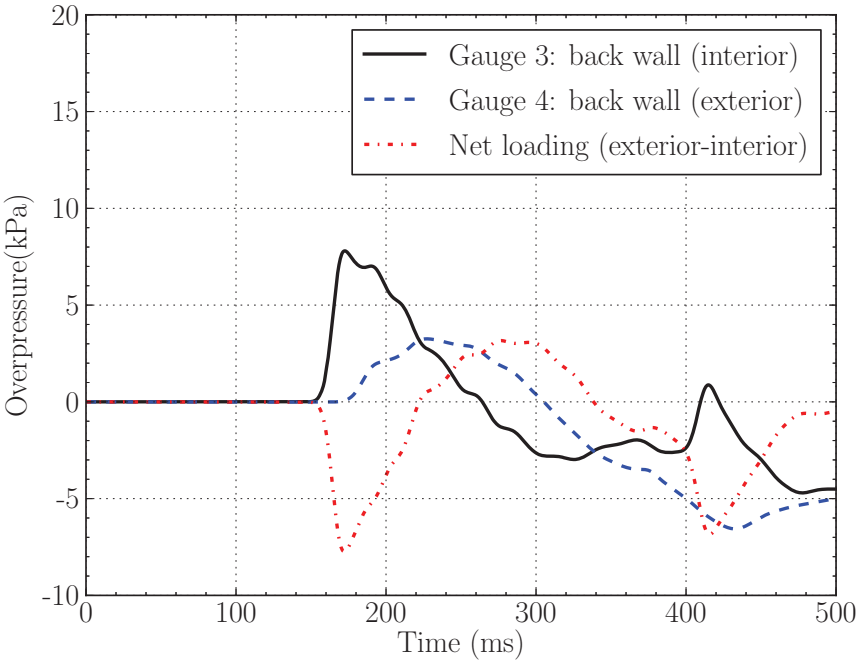
In order to examine the internal pressurisation in detail, the pressure loading at the back and side walls are presented in Figures 7.16 and 7.17. Figure 7.16a shows the pressure loading on the external and internal surfaces of the back wall. Since there was no venting at the front, the overpressure at the interior face was zero and the net loading was equal to the external overpressure measured by Gauge 4. Thus, the anticipated damage of the back wall would be towards the inside. When the venting was allowed at the front, as shown in Figure 7.16b, the overpressure loading at the internal face of the back wall significantly increased (with help from the reflection effect). It can be noted that the slower rate of increase of overpressure on the exterior of the back wall caused the net loading to act outwards (negative value) at the beginning. The peak value of -7.73 kPa (outwards) would be able to cause severe damage to back wall of the structure.

Similar analysis can be undertaken as shown in Figure 7.17. Figure 7.17a depicts the overpressure loading on the side wall when there was no venting from the front wall. There were zero internal overpressures and the net loading was equal to the overpressure on the exterior, which could cause inward damage in the side wall elements. On the other hand, if 30% venting existed at the front wall as shown in Figure 7.17b, the internal overpressures would immediately offset the external pressure loading and could reduce the damage risk of the side wall. Overpressure loading on both the interior and exterior of the side wall have similar rate of increase causing the net loading only has a small negative peak (-0.36 kPa, acting outward). This then acts inwards throughout the positive phase with an offset peak value of 1.83 kPa. In Figure 7.17b, the overpressure loading at the interior of the side wall has two positive phases. The second one was generated by the reflection from the back wall. The width of the warehouse is 43.6 m; assuming the blast wave travels at the speed of sound, then the time it takes to depart and return (after impinging on the back wall) from Gauge 3 would be $\frac{43.6m}{340m/s} = 128ms$. This is approximately equal to the time between the two overpressure peaks at the side wall interior. Therefore, the second positive phase can be ignored during the analysis.

The same analyses have been carried out for all cases as well as the roof. Table 7.8 presents a summary of the peak (both negative and positive) overpressures of

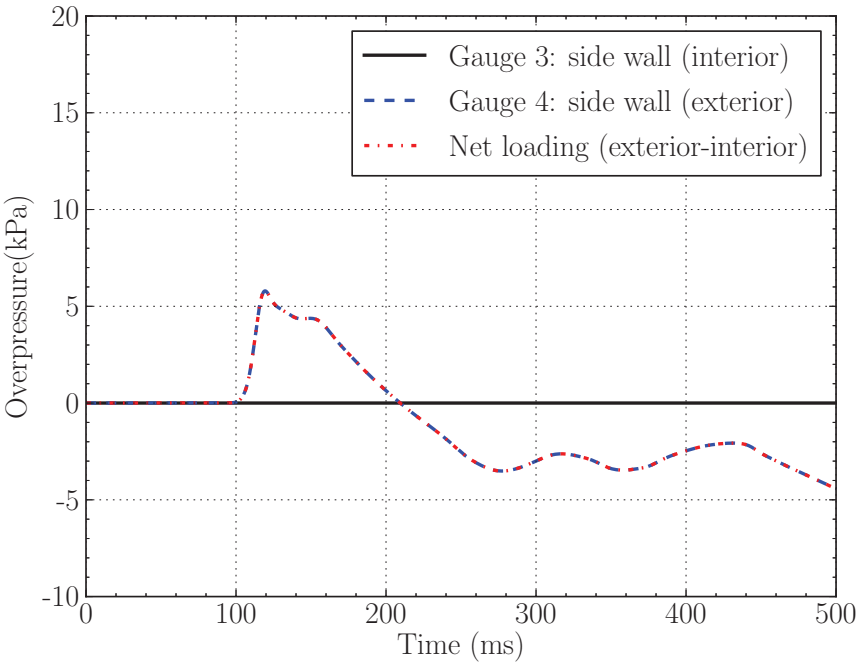


(a) Case 1 (0%) venting

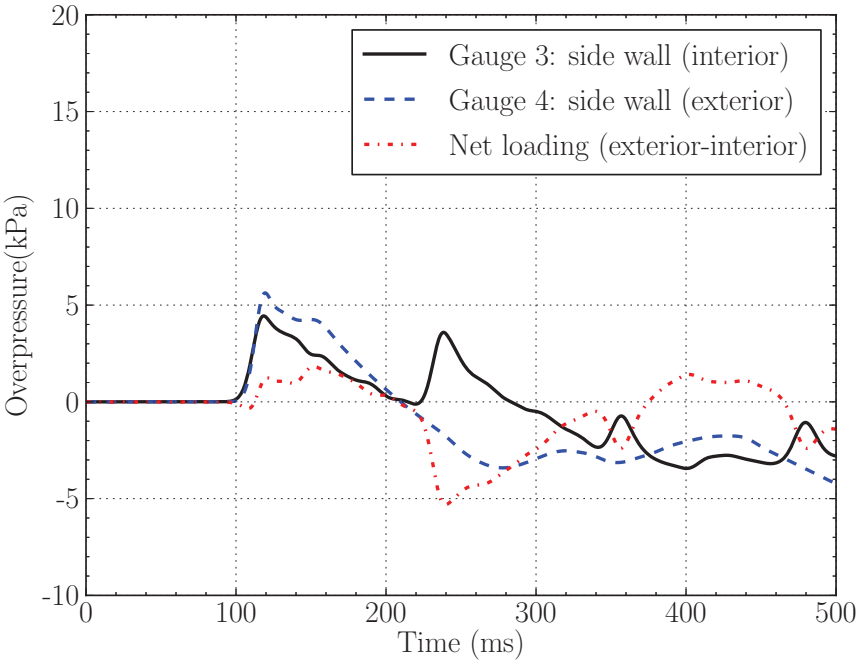


(b) Case 4 (30%) venting

Figure 7.16: Overpressure loadings at the back wall



(a) Case 1 (0%) venting



(b) Case 4 (30%) venting

Figure 7.17: Overpressure loadings of side wall

Table 7.8: Peak overpressures on walls and roofs of warehouse

Case	Venting(%)	Net peak overpressure (kPa)							
		back wall		side wall		front roof		back roof	
		out	in	out	in	out	in	out	in
1	0	0.0	3.38	0.0	5.79	-	7.59	-	5.98
2	10	-2.77	3.46	0	4.13	-	6.25	-	4.68
3	20	-5.82	3.2	-0.09	2.43	-	5.26	-	3.46
4	30	-7.73	3.17	-0.35	1.83	-	4.42	-	2.45
5	40	-9.25	3.27	-0.95	1.57	-	3.69	-	1.61
6	50	-10.33	3.53	-1.38	1.42	-	3.04	-	0.85

the net loading in the positive phase. It is evident that the outward acting loading on the back wall becomes more intensive as the venting area increases. The peak overpressures at the exterior face of the back wall are not affected by the opening area at the front. Since the rate of increase of internal and external overpressure loading on the side wall are similar, the net loading only has a small outward acting peak and is dominated by the inward external pressures. As it can be seen in the table, the net outward peak overpressures are small for all cases. The external overpressure loading is on the other hand significantly offset by internal pressurisation. The net inward peak overpressure was reduced to 1.42 kPa for Case 6 with a 50% venting area. A well designed cladding wall system would prevent fatal damages to the structures under this level of overpressure. There were no outward (negative) overpressures for roofs, therefore only positive peak overpressure loading acting inwards (or downwards) are shown. As expected, the external loading was greatly offset by internal pressurisation because the peak positive (inward) values decreased quite substantially with the increase in the venting area.

The final study in the coupled blast wave simulation was to investigate the effect of the shape of the venting areas. The numerical models of rigid warehouse with same percentage of venting area with different shapes are shown in Figure 7.12. The internal pressures recorded by Gauge 2 in Cases 4, 7 and 8 are shown in Figure 7.18. It is evident that the shape and location of the venting openings on the walls would not affect the blast wave transmitting into the interior of the building.

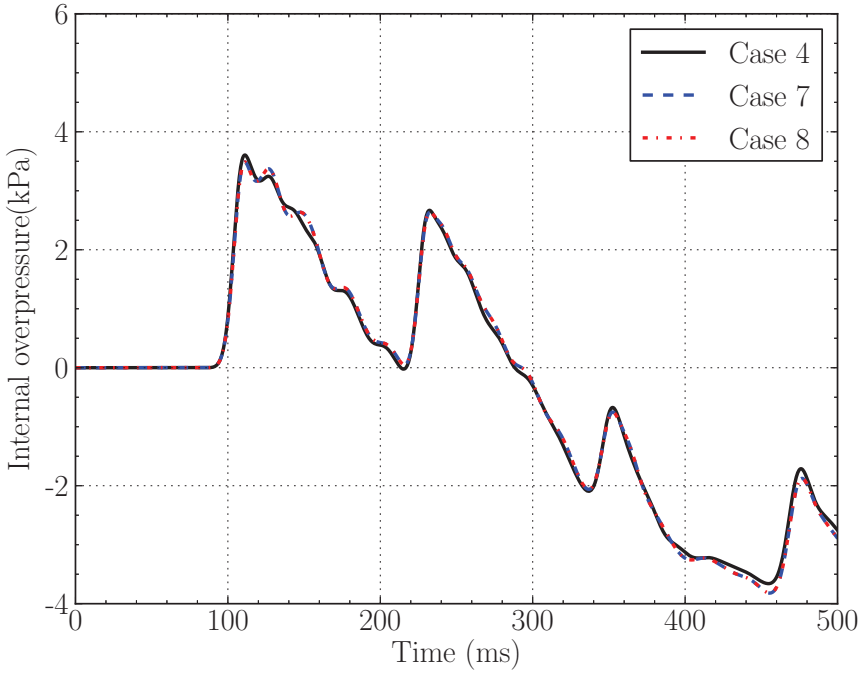


Figure 7.18: Effect of venting area shapes on internal pressurisation

In this section, an assessment of blast overpressure loading based on explosion examination of the Buncefield incident was presented. It was observed that the back wall deformed outwards due to internal pressurisation. The numerical simulation showed that even with only a 10% venting area the reflected overpressure at the interior face of back wall would be 2.77 kPa causing outwards damage to the structure. It was also observed that early failure of the front wall (i.e. opening up large holes) would allow the inside of the building to be quickly pressurised hence the damage of the roof and side walls can be reduced. It was found from the numerical simulations that the peak overpressure loadings on the roofs and side wall were greatly reduced by increasing of the venting areas (hence more internal pressurisation). The loading conditions matched reasonably well the observed warehouse structural damage. All numerical results from the blast wave simulations are presented in Appendix A, which can be referred to for complete loading histories acting on the roof and sides of the rigid warehouse model.

7.3 Design considerations for steel-clad industrial buildings

In the previous chapters and sections, the response of warehouse structures subjected to blast loading was examined in detail, and a series of pressure-impulse diagrams were derived. Non-linear finite element models as well as simplified single degree of freedom approaches were employed in order to construct the iso-damage curves. This section brings into focus some considerations and guidance for the design of steel-clad industrial buildings based on the findings of this research work.

7.3.1 Pressure - impulse diagrams

The previously-derived pressure-impulse diagrams (either based on FE or SDOF models) can be used in the evaluation of similar structural forms subjected to blast loading. This approach combines both dynamic analysis and design evaluation into a single procedure which can be used for a relatively rapid assessment of potential damage levels for this type of structure.

Pressure-impulse diagrams derived for the steel-clad warehouse structure subjected to detonation-type blast waves are presented in Figures 6.25 and 7.7. The Iso-damage curves in Figure 7.7 are based on SDOF models of claddings and side-rails. Damage levels correspond to deformation states at mid-span of the various components. Iso-damages curves of cladding are superimposed to those of the side-rail to provide an overall damage assessment of the structure and identify the most vulnerable components. The abscissa and ordinate values are directly given in terms of overpressure and specific impulse. Knowing the peak overpressure and impulse of the blast wave relative to the blast source, enables designers to extract the damage levels directly from the iso-damage curves.

FE models were used to construct the P-I damage curves in Figure 6.25. The damage levels are related not only to the displacement state (moderate, heavy and hazardous, as defined in Section 6.1) of the side-rail but also to the state of the side-rail connections and the cladding screw fasteners. These superimposed iso-damage curves suggest that, for this type of structure, the most vulnerable part

can be the connection between the side-rails and the primary columns. This P-I diagram omitted the damage to the claddings due to the explicit inclusion of the failure of the screw fasteners. It provides more information than the SDOF based P-I diagram. Moreover, iso-distance and charge curves for high explosive TNT are also superimposed on the diagram. In such a way, the safe siting distance can be determined if the anticipated risks (charge size of TNT or equivalent) are known. These superimposed TNT curves also enable the damage assessment to be carried out purely on the basis of the estimated charge size and stand-off distance.

It is important to note that the abscissa and ordinate values are given in terms of reflected pressure due to the fact that the iso-damage curves were prepared for the front face of the warehouse. Recognising the values as incident (i.e. freefield) enables the user to apply these damage curves to other part of the structure; e.g. side walls, back walls or even the roof, provided that their components are similar to the front wall. Once the blast overpressure and impulse relative to the explosion source are known, designers can obtain directly the damage status of the side-rail, side-rail connection and the failure of the screw fasteners. These damage states are of more direct use to practising design engineers.

7.3.2 Example of application of P-I diagrams

The previous section presented an assessment of the anticipated blast loading scenarios of typical warehouse structures in the Buncefield explosion. Using the blast loading obtained at the surfaces of the assumed rigid warehouse, the damage levels of the warehouse can be identified using the pressure-impulse diagrams derived from the finite element model. In this sub-section, an example of using the pressure-impulse diagrams for damage assessment is presented.

As shown in the blast wave simulation on a rigid warehouse structure (TNT charge of 7500 kg with 324 m stand-off distance), the peak reflected overpressure on the front wall of the warehouse facing the explosion was determined to be 13.63 kPa with a specific reflected impulse of 444 kPa.ms. This blast loading state on front wall is indicated on the pressure-impulse diagrams in Figure 7.19. It can be observed from the damage curves that the damage to the side-rails

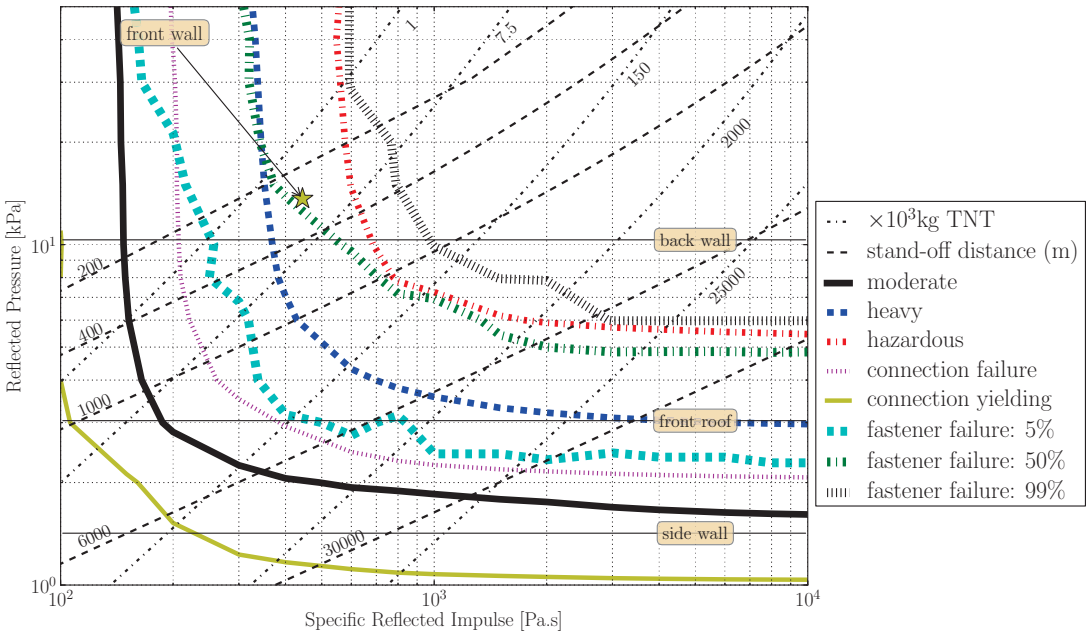


Figure 7.19: Application of pressure - impulse diagram

is between heavy and hazardous, and approximately 50% of the fasteners failed under this loading scenario. The damage to the connection joining the side-rails to the columns is far beyond failure. Referring to Figure 5.1a which shows the damage to the front wall of Warehouse 2 (WH2), the damage identified by the pressure-impulse diagrams fits reasonably well with the observed actual damage to the warehouse. During the explosion, many side-rails were pulled off from the connections and substantial deformation of the side-rails can be observed. Some of the cladding panels were blown off and others were still attached to the damaged side-rails.

Since it is estimated that 50% of the fasteners would fail in the assumed explosion scenario, it can also be assumed that 50% venting exists at the front wall. This can be used as an idealisation in order to determine the overpressure loading on the other walls as well as on the roof. It was found that opening of the front wall due to structural failure would pressurise the interior of the building hence reduce the net overpressure loading. As a result, the actual net overpressure loading on the side/back walls and the roof is not typical of a detonation due to the internal pressure. The exact point on the pressure-impulse diagram

which corresponds to the net loading cannot be determined as the damage curves were based on detonation blast waves. However, in a conservative manner, the maximum overpressure level on the surface can be used to assess the damage to the structure in the quasi-static region, as shown in Figure 7.19. The maximum overpressure on the surfaces of the warehouse as presented in Table 7.8 are therefore 10.33(outward), 1.42(inward), 3.04(inward) and 0.85(inward) kPa for the back wall, side wall, front roof, and back roof, respectively. The corresponding damage levels are indicated in Figure 7.19.

Assessing the damage to the back wall using the limiting overpressures indicates that the level of damage is beyond hazardous and towards the outside of the building. This is consistent with the observations of the damage to the back wall during the explosion. It should be noted that the P-I diagrams were based on the in-bound capacity of the cladding. The resistance of the cladding in the opposite direction might be significantly lower; hence more severe damage could occur to the back wall. It can be seen that the maximum overpressure on the side wall is less than the limiting overpressure of the moderate damage level and the connection failure overpressure. This suggests that the damage to the side wall is minimal, but that yielding would occur in the connections.

Due to the 6^0 incline to the horizontal, the maximum overpressure on the front roof was determined to be 3.04 kPa, which is approximately the same as the limiting pressure value for heavy damage of the side rails. The fastener total failure is more than 5%. However, it should be noted that in the Buncefield explosion, the orientation of the roof was different and the overpressure was similar to the side walls. Therefore, there was no significant damage observed to the roof of the warehouse at Buncefield. The back wall was subjected to a maximum pressure of 0.85 kPa in the numerical simulation, which is almost equal to the design wind pressure of the cladding wall system and below the minimum pressure limit of the pressure-impulse diagram. Therefore, it is expected that no substantial damage would occur at the back roof. It should also be noted that the purlins used in the roof are slightly stronger than the side rails, thus the damage would be expected to be even smaller at the same level of limiting overpressures.

The superimposed TNT curves in the pressure-impulse diagram indicate more severe damage to the structure based on a TNT charge of 7500 kg and 324 m

stand-off distance. The discrepancy mainly depends on the magnitude of the overpressure in the blast wave predicted by the empirical tool and hydrocodes such as AUTODYN/ANSYS. Nonetheless, the iso-curves of TNT charges suggest that the safe siting distance of the warehouse building would be more than half a kilometer to avoid heavy damage to the fasteners or side rails. Additionally, probably more than one kilometer distance would be required to mitigate all damage below moderate; i.e. below moderate for fastener failure and deformation of side rails, with no failure of connections occurring.

7.3.3 SDOF and FE models

The non-linear finite element model of the sub-structure was shown to be capable of providing detailed response information and can faithfully capture the dynamic behaviour of the components. However, the running time and man power required to create such detailed models limit its application in practical design. Such detailed finite element approach can be used at the final stage to perform an overall assessment of the capacity of a structure to resist blast loading. However, in the preliminary design stage, a more efficient simplified approach would be favoured in order to provide a practical assessment as well as an initial insight into the expected key aspects of behaviour and levels of response.

It was shown in this research that the simplified SDOF approach is generally reliable for predicting the maximum response of the side-rails when compared with the detailed non-linear finite element models. It should be pointed out that the tensile membrane action becomes important at large deflection. Therefore, it is important to determine appropriate tensile membrane stiffness and capacity based on realistic response at the support. The yield capacity based on shear behaviour of the side-rail as specified in the Eurocode was shown to be too small. For cladding panels which are supported by the side-rails, the simplified approach tends to over-predict the response. Improvements would be achieved if the resistance curve is obtained from a static non-linear analysis of the cladding. It should also be noted that the simplified model is unable to capture the component interaction between the cladding and the side rails.

It is recommended to use the simplified approach only for the cladding panels

located close to the support of side rails, where the dynamic interaction effect is minimal. For cladding panels at mid-span of the side-rail, the simplified approach must be used with caution or a non-linear finite element analysis should be adopted.

7.3.4 Side-rail connections

From the combined pressure-impulse diagrams of the wall structure of the examined warehouse building, it can be seen that the critical component is the side-rail whose connection axial failure criterion limits the blast capacity of the sub-assemblage. The connection of the side-rails to the column consists of a thin side rail web bolted through two M12 bolts to the cleat. The web thickness is 1.2 mm and the end distance of the bolt connection is 36 mm. As the blast load is applied to the side rails, the end of the side rail may be pulled out easily from the connection due to inadequate bearing capacity. Increasing the end distance of the connection is impractical since the side rails are installed end to end. A possible straightforward upgrade option is the addition of a shear tab bolted or welded to the side rail in order to increase the thickness of the web, hence the bearing capacity (ASCE, 1997).

7.3.5 Cladding connections (fasteners)

Cladding panels are typically formed from thin gauge material, and are therefore prone to local buckling before reaching the ultimate plastic capacity. When premature buckling occurs, the flexural resistance of the cladding diminishes. Post-buckling resistance is subsequently provided by tensile membrane action which primarily results from the stretching of the panel. It is important to adequately restrain the end of the panel in order to provide sufficient in-plane resistance. Self-tapping screws are commonly used to fix the cladding panel onto the side-rails. These screws might not be adequate to develop necessary membrane capacity of the cladding due to bearing failure as well as pull-out over the head of the screw (tensile failure). In order to increase the shear capacity of the screw fixing, it is necessary to increase the edge distance of the screws or the thickness of the cladding around the screw. To avoid the pull-out tensile failure, larger washers

and/or nuts could be used to increase the tensile capacity. These would provide additional capacity to the overall blast resistance of the structure.

7.3.6 Other considerations

It was observed that the opening of the blast-ward wall could protect the elements at the other parts of the warehouse structure due to the internal pressurisation. Therefore, in some cases it could be beneficial to deliberately design the cladding panels which are susceptible to high overpressure blast loading (e.g. reflected blast pressure) to give way at a relatively early stage hence protecting the remaining elements during the explosion. This would be on the basis that protecting these elements would be more important than breaching the inside of the structure. It was also shown that the area and location of the openings have no influence on the internal pressurisation. Therefore, in this way, the rapid failure of cladding at any location would allow the interior of the building to be pressurised quickly hence protect the elements of other sides/roofs. In addition, most of the claddings are continuous over two spans thus strong side rails could prevent the bent cladding from falling off and causing further damage on site.

Chapter 8

Conclusions and further work

The conclusions of the present study are summarised in three parts: blast response of steel boxes, blast response of warehouse structures and blast simulation. The recommendations for future research are also presented herein.

8.1 Blast response of field objects

The blast response of steel field boxes was examined in detail in the current work. Three types of numerical approaches were adopted to study the response of the steel boxes: Lagrangian, Uncoupled Eulerian-Lagrangian and Coupled Eulerian-Lagrangian. The pure Eulerian modelling method was used to reproduce the blast waves that occurred in the test explosions. The numerical blast waves were shown to be in good agreement with the test results. The Eulerian capability in **?** can therefore be used to create blast waves reliably.

Data collected from blast tests carried out independently was used to validate the numerical models adopted in the current study. Both quantitative and qualitative analyses of the response of the test boxes were carried out. The results indicated that the Coupled Eulerian-Lagrangian approach was the most accurate method for analysis of blast problems involving small objects such as the steel boxes, but its running time (more than 10 hours for each model) limits the range of application. The more efficient Lagrangian approach only requires 3-5 minutes for each model, but it becomes less accurate at high overpressures due to impulse reduction effects at the front surface.

An Eulerian study on the reflection of deflagration blast waves was undertaken by using a two-dimensional Eulerian model. This study suggested quantitatively that the reflection enhancement of overpressure loading of the deflagration is not as strong as for a detonation. The reduction in the reflection coefficient ranged from 35% to 50% for deflagration loading with peak overpressure from 400 kPa to 10 kPa, respectively.

Parametric studies covering detonation, deflagration and quasi static overpressure blast loadings cases were carried out to assess systematically the response of the boxes. In the investigation, the Lagrangian model was used and subjected to a series of peak overpressure and impulse combinations. The overpressure range was limited to a side-on pressure of 4 bar in order to retain the accuracy of the Lagrangian model. The results were presented in the form of pressure-impulse diagrams and typical residual shapes were selected for visual assessment.

A few selected results from the parametric studies were compared broadly with an actual damaged box recovered from the Buncefield site. The comparison suggested that the explosion within the vapour cloud that spread over the Buncefield site was likely to be a deflagration with side-on overpressure of 420 kPa or roughly head-on overpressure of 200 kPa (using the derived reflection coefficients of deflagration). This showed that the results can be used for future forensic investigation of explosion incidents.

8.2 Blast responses of warehouse structures

A typical UK warehouse was chosen to study its structural response to blast loading. The strain rate effect of the material was incorporated through dynamic increase factors. Different simulation levels of the structure were investigated and it was shown that a sub-assemblage model is sufficient for representing the response of the wall structures. Validation of the sub-assemblage model was carried out against a full-scale static test conducted at Imperial College (Elghazouli et al. (2014)). This validated the adequacy of the sub-assemblage model in representing the material and geometric properties of the structure.

A refined sub-assemblage model was then developed by using connector mod-

els to realistically represent the behaviour of the self-tapping screw fastener fixings and the M12 bolt-cleat connections. The connector behaviour was also validated against available test data at Imperial. The refined model was then employed in parametric studies to investigate the response of the structure to blast loading with various overpressures and impulses.

The failure of the fastener models was examined in detail and the results showed that the fastener can fail by different mechanisms depending on the characteristics of the blast loading and its location. For example, the central fastener located at the middle of the upper or lower side rail failed by shear (close to the y-direction) when subjected to a quasi-static loading, while it failed in tension when subjected to an impulsive loading. Under some blast loading situations, the failure of the connector can be related to the middle relative displacement of the cladding. It was shown that the shear failure (close to the y-direction) occurs when the middle of the cladding deforms to 85 mm relative to the average of two ends, which is about 5% of the span of the component. However, it was difficult to relate the middle displacement of the side rail to the failure of the fasteners, as it was heavily dependent on the nature of the loading and the response of the structure.

The results of the parametric studies were summarised in the form of pressure-impulse diagrams. The typical criteria used for the construction of the iso-damage curves were the transverse and axial displacements of the central side rail in the sub-assemblage. A new damage criterion based on the failure of the fasteners was proposed and replaced the displacement of the cladding. The new damage criterion provides a more straightforward assessment of the damage to the steel cladding structures. The pressure-impulse diagrams were then superimposed to form a combined diagram in which the axial connection failure was established to be the most critical condition for the structure under study. Design considerations were provided in order to offer guidance for mitigating the extent of damage to the fasteners and connections. Finally iso-curves of high explosive TNT were also superimposed in the combined diagram with the aim of of providing guidance on the safe siting distances of buildings from possible sources of detonation explosions.

Since the response assigned to the fastener model was based on static test

results, a focussed study was carried out to estimate the local strain rate in the self-tapping screw fastener. It was estimated that the fastener had a typical strain rate of 240 s-1, assuming a relatively strong dynamic loading condition. This increased the yield and ultimate capacity of the fastener by approximately 21.3 and 10.65%, respectively. However, in subsequent analyses using strain-rate strengthened fasteners, it was observed that the displacement of the side rails was not affected by the increase in fastener capacity. Nonetheless, the failure of the fastener has been affected slightly. It was suggested that for simplicity the strain rate effect of the fastener could be ignored without significant influence on the accuracy of the results.

To complement the non-linear finite element method, the simplified single degree of freedom approach was also used to analyse the response of the sub-structure. The interaction between the constituent components of the sub-structure is typically considered to be insignificant if the ratio in natural frequency is less than double, which is significantly exceeded in the structure under examination. It was observed that the simplified approach provided reliable predictions for the response of the side rails, provided that the tensile membrane action is properly defined. However, the simplified approach only worked for the side cladding but not for the central cladding. Examining the response histories of the side and central cladding revealed that the dynamic interaction between the central cladding and the side rails was significant. Accordingly, the uncoupled simplified approach might be not applicable even though the ratio of natural period of the system was greater than 2. The comparison of the response between the detailed non-linear FE model and the simplified approach demonstrated the importance of using a realistic resistance function of the component. To this end, according to (Louca et al., 1996), the resistance function is recommended to be determined using a static non-linear finite element analysis.

8.3 Assessment of blast loading

Based on the estimation of the explosion undertaken by DOSG (SCI (2009)), a numerical study was carried out to assess the overpressure loading on the warehouse

selected for the current work. The study adopted a Coupled Eulerian-Lagrangian approach, but in which the Lagrangian warehouse was assumed to be rigid. This study reproduced the overpressure loading levels predicted by DOSG and investigated the effect of the internal pressurisation due to opening areas on the front wall.

The numerical results showed that the internal pressure increased with larger opening of the front wall, and quantitatively the pressurisation level compared reasonably well with theoretical solutions. The overpressure loading on the different walls/roofs of the warehouse building was studied with different levels of opening areas. It was observed that the location and the shape of the opening did not affect the internal pressurisation. It was also shown that even with only a 10% opening area, serious outward damage to the back wall could occur. However, on the other hand, when the opening area was 30% or more the overpressure loading on the side walls and roofs were actually reduced significantly and the structures could effectively be protected from serious damage.

8.4 Recommendations for further work

The work presented in this thesis included various numerical approaches which can be used in future analysis of blast problems. The numerical models were validated against available experimental data where feasible. Detailed assessments of test results and numerical simulations were provided for reference by researchers and practicing engineers. However, there are still many problems that remain to be addressed with regard to the dynamic response of field objects and warehouse structures. This section outlines a number of recommendations arising from this thesis for further research related to the response of structures to vapour cloud explosions, as follows:

- The field objects examined in the current work were limited to steel boxes. Many other objects were also found in the Buncefield explosion site, such as steel drums and iso-containers. The numerical approaches presented in this thesis are readily applicable in further studies involving the steel drums, and could therefore expand the usability of the numerical studies in future

forensic investigations as steel drums are also common on any industrial site. Additionally, iso-containers may occasionally accommodate personnel or valuable contents. Thus, it is also important to understand the behaviour of these objects when subjected to blast loading.

- Thermal effects have been neglected in the current work. Within the cloud, the extremely high temperatures may lead to a reduction in the stiffness and strength of the field objects or structures. In addition, the reacted mixture and high temperature gas behind the wave front could affect the reflected overpressure on the surface, which is different from a blast wave outside the explosion cloud. If possible, it is worth investigating the thermal effects on the structure and the loading within the exploding vapour cloud.

- The side rail-column connection in the warehouse selected in the current work has relatively low capacity due to the shear failure of the thin bolted web. Further work could focus on stronger connections which would be less vulnerable during the explosion, as well as on the effect of using an enhanced connection on the response/failure of the cladding and even the primary columns.

- Decoupled analyses have been adopted for the simplified single degree of freedom approach, based on the criterion that the natural frequencies of the supporting and supported components differ by a factor of more than two. However, with a ratio of 3.64, the non-linear finite element model still showed that there was strong interaction between the central cladding and the side rail. The behaviour of the central and side cladding panels was different. Further investigation might be needed to establish more detailed insights into these aspects of behaviour.

- Finally, the assessments performed in this research can be replicated so that extensive pressure-impulse diagrams are made available for other type of buildings which are commonly present in high risk industrial sites.

Appendix A: Results of assessment of blast overpressure

In the Appendix A, all the numerical results from the assessment of blast overpressure loading on the rigid warehouse model are presented. Results include the pressure loadings recorded by all numerical gauges in every modelling case and detailed plots for blast loadings on roofs ans walls in each case, respectively.

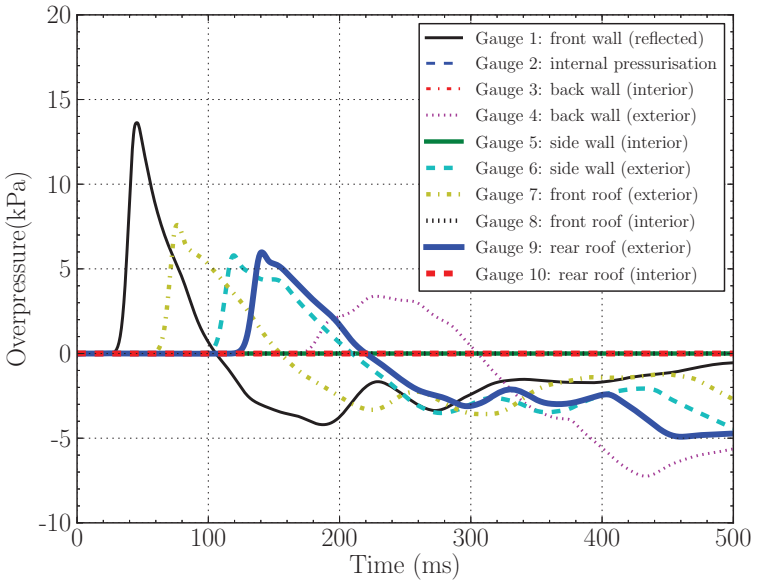


Figure 1: Overpressure loadings on rigid warehouse (Case 1)

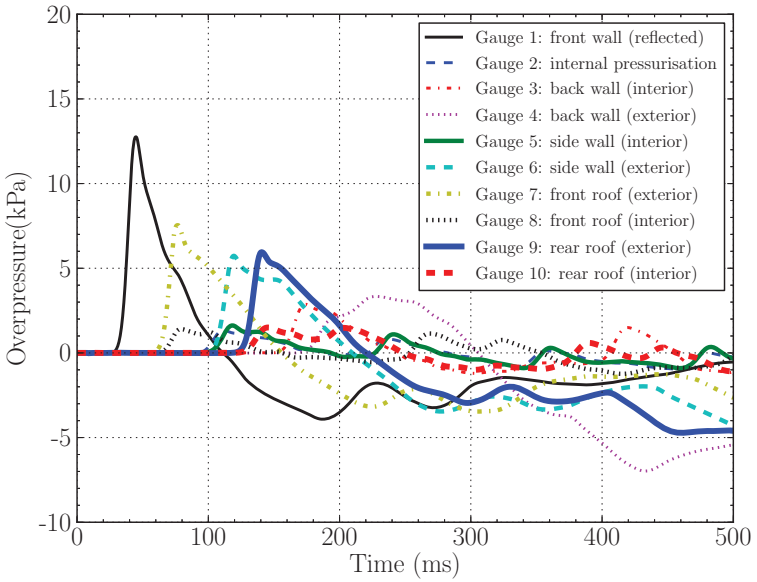


Figure 2: Overpressure loadings on rigid warehouse (Case 2)

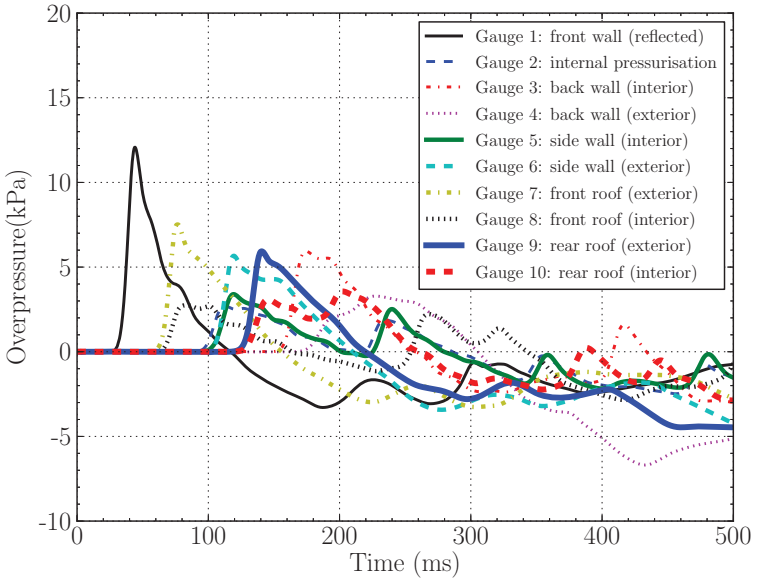


Figure 3: Overpressure loadings on rigid warehouse (Case 3)

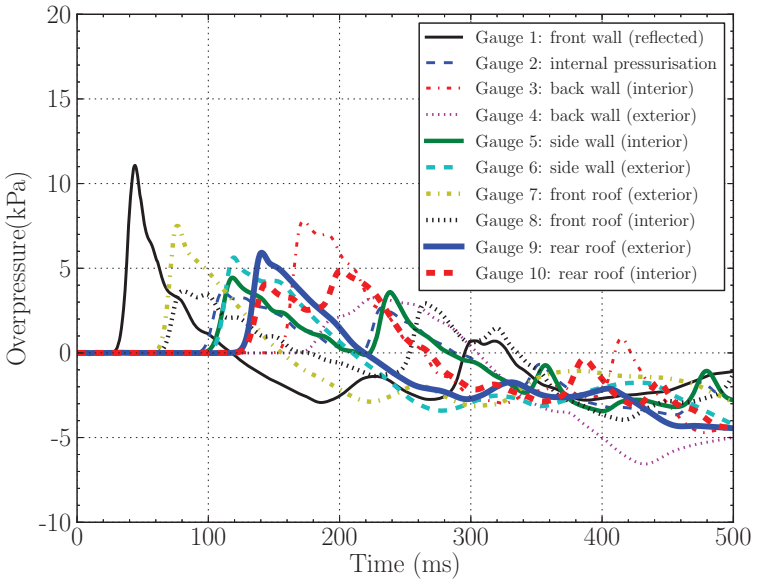


Figure 4: Overpressure loadings on rigid warehouse (Case 4)

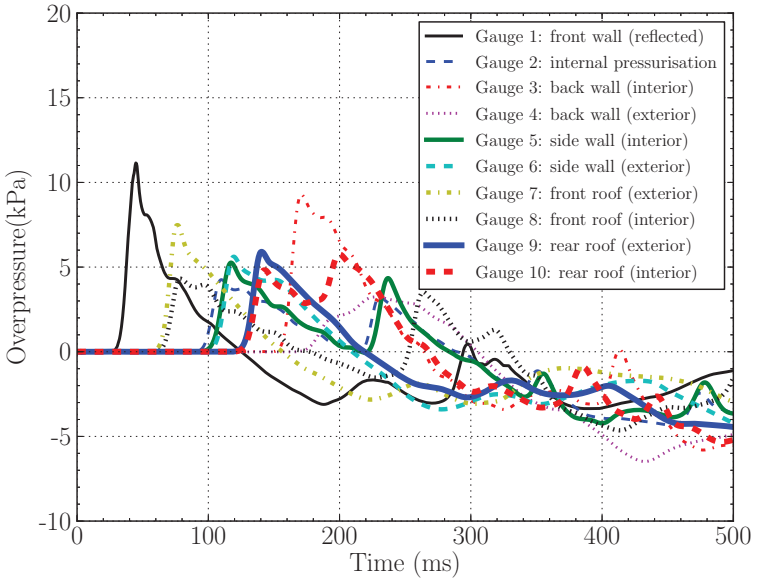


Figure 5: Overpressure loadings on rigid warehouse (Case 5)

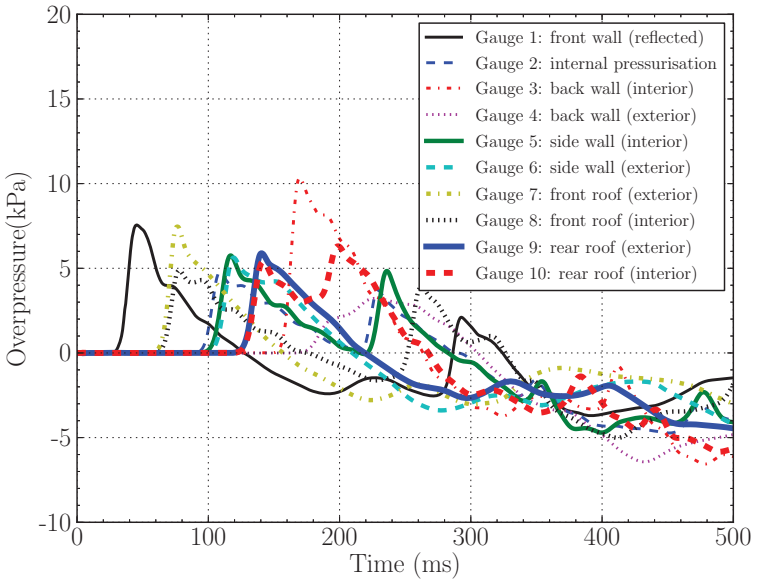
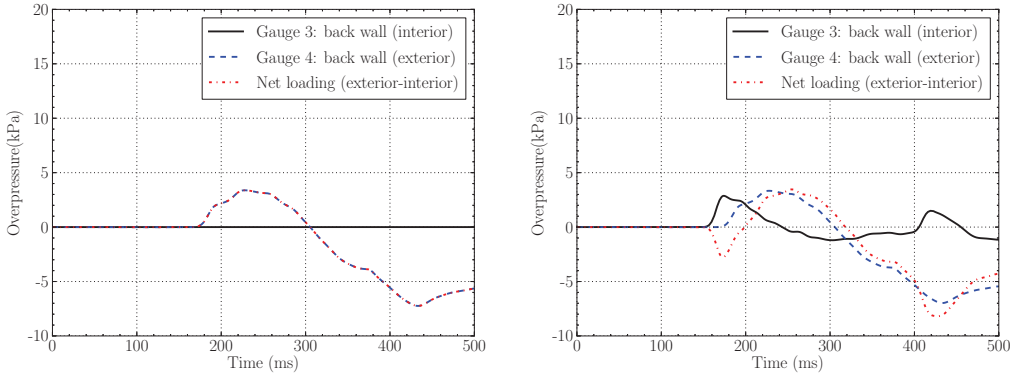
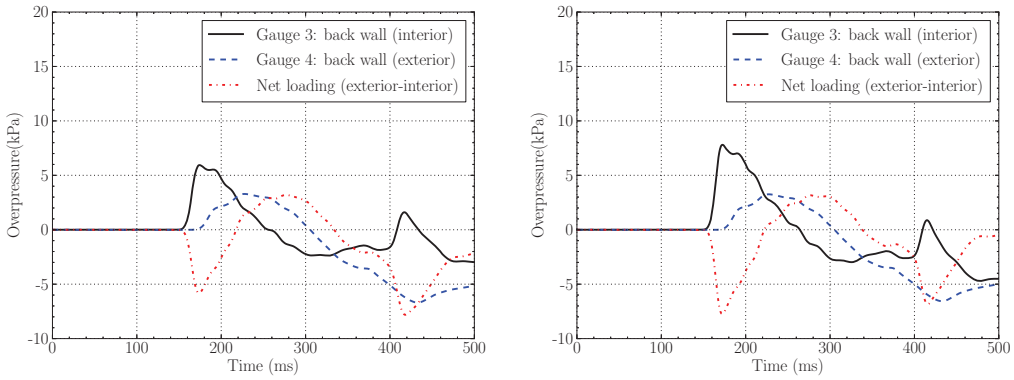


Figure 6: Overpressure loadings on rigid warehouse (Case 6)



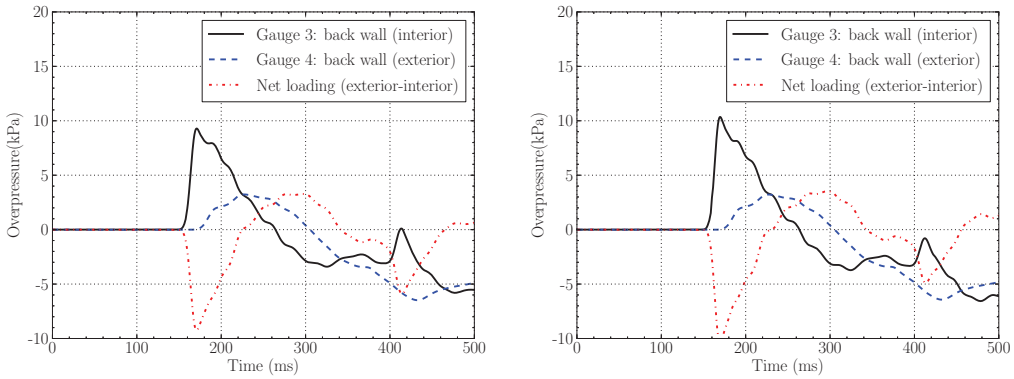
(a) Case 1 (b) Case 2

Figure 7: Overpressure loadings of back wall (Case 1 & 2)



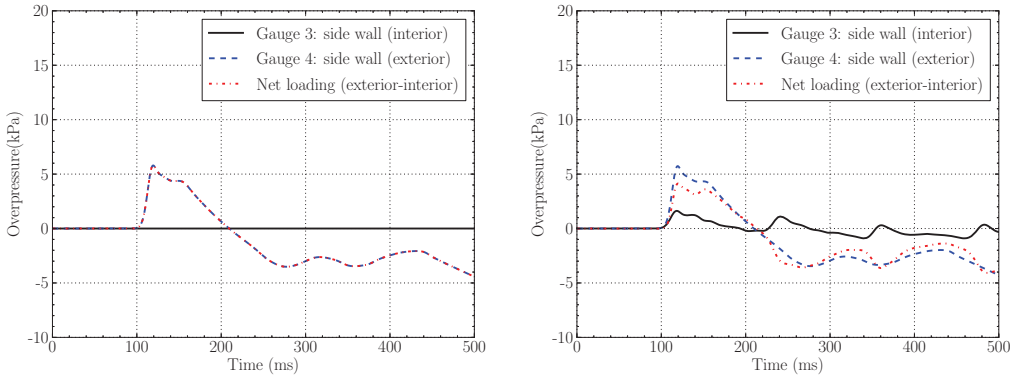
(a) Case 3 (b) Case 4

Figure 8: Overpressure loadings of back wall (Case 3 & 4)



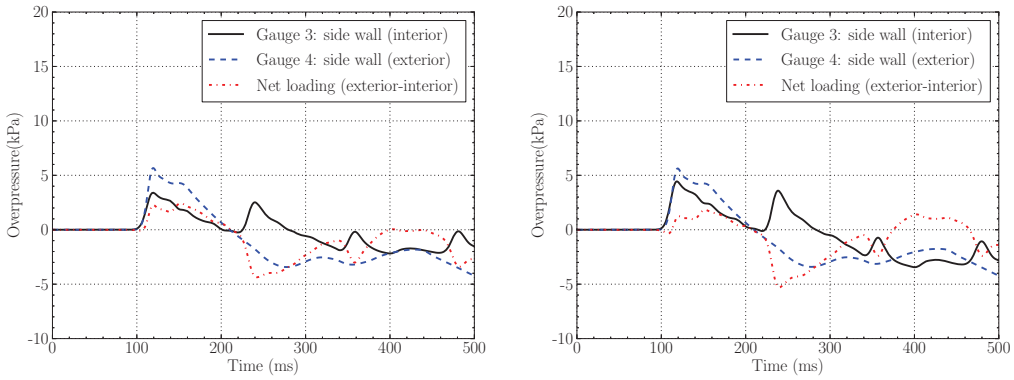
(a) Case 5 (b) Case 6

Figure 9: Overpressure loadings of back wall (Case 5 & 6)



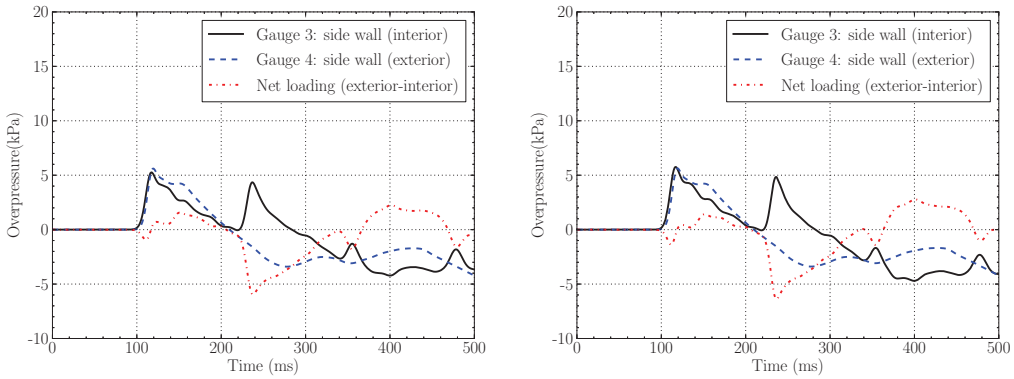
(a) Case 1 (b) Case 2

Figure 10: Overpressure loadings of side wall (Case 1 & 2)



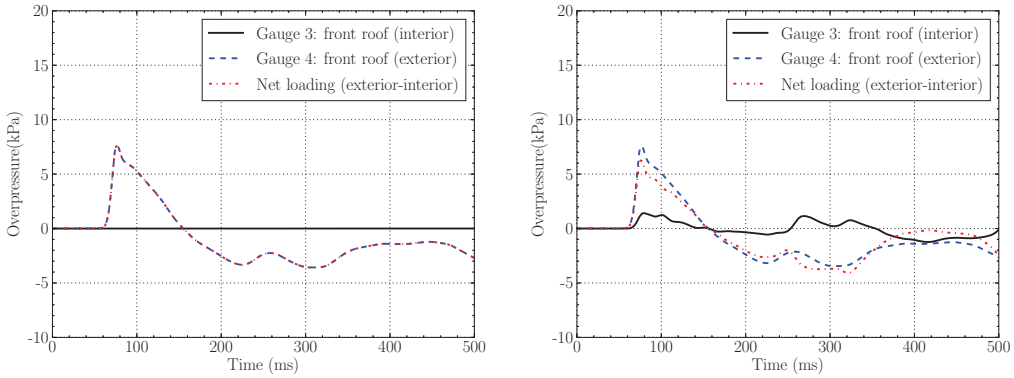
(a) Case 3 (b) Case 4

Figure 11: Overpressure loadings of side wall (Case 3 & 4)



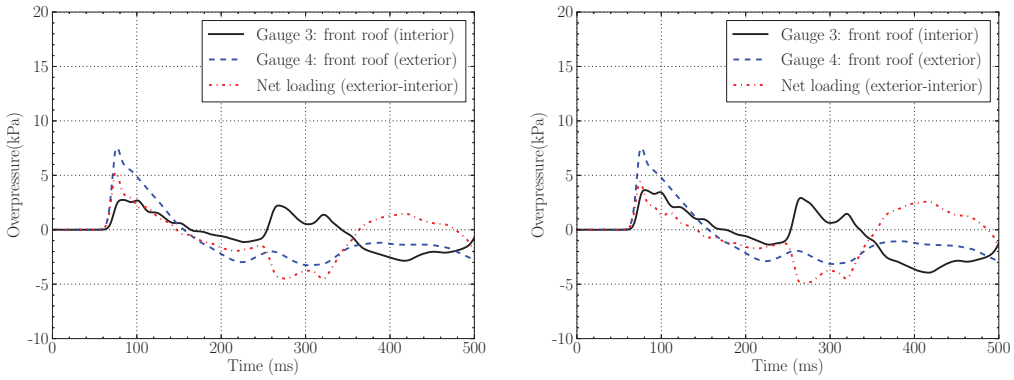
(a) Case 5 (b) Case 6

Figure 12: Overpressure loadings of side wall (Case 5 & 6)



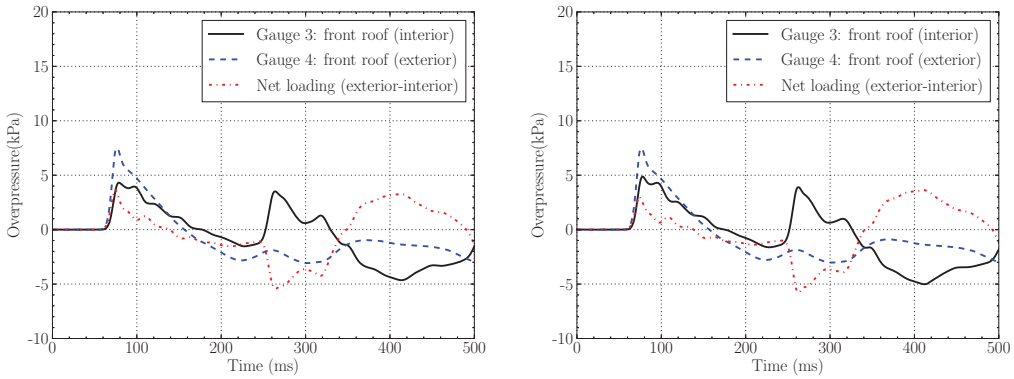
(a) Case 1 (b) Case 2

Figure 13: Overpressure loadings of front roof (Case 1 & 2)



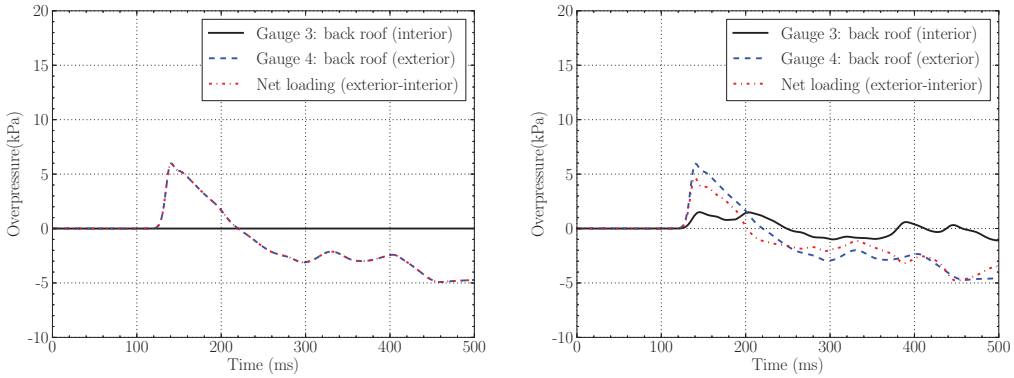
(a) Case 3 (b) Case 4

Figure 14: Overpressure loadings of front roof (Case 3 & 4)



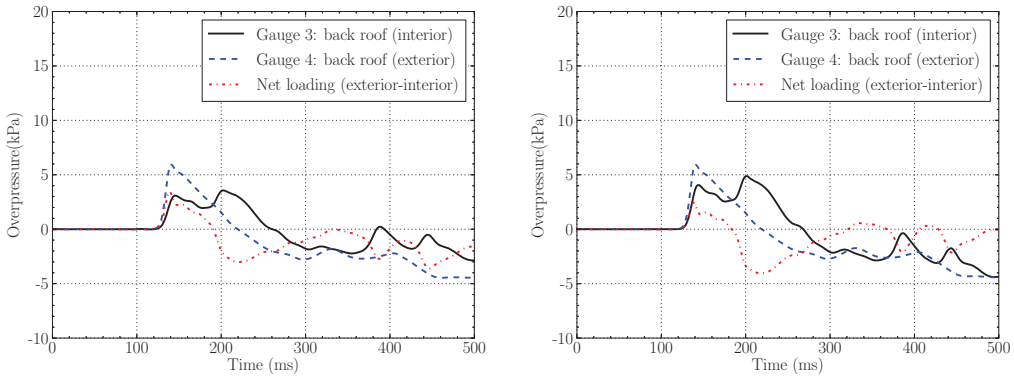
(a) Case 5 (b) Case 6

Figure 15: Overpressure loadings of front roof (Case 5 & 6)



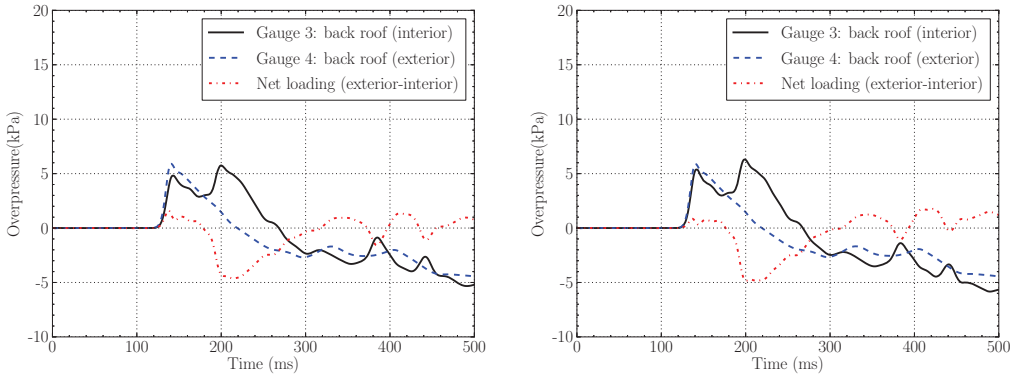
(a) Case 1 (b) Case 2

Figure 16: Overpressure loadings of back roof (Case 1 & 2)



(a) Case 3 (b) Case 4

Figure 17: Overpressure loadings of back roof (Case 3 & 4)



(a) Case 5 (b) Case 6

Figure 18: Overpressure loadings of back roof (Case 5 & 6)

Appendix B: Loading scenarios for parametric study of sub-assemblage model

The Appendix B presents the ranges of overpressures and impulses used in the parametric study of the sub-assemblage finite element model. The overpressures varied from 1 to 50 kPa and the impulses varied from 100 to 10000 kPa.ms. The modelling case numbers and corresponding positive durations are presented as follow:

Cases no.																					
Overpressures (kPa)	**50**	166	167	168	169	170	171	172	173	174	175	176	177	178	179	180	**50**
	40	151	152	153	154	155	156	157	158	159	160	161	162	163	164	165	**40**
	30	136	137	138	139	140	141	142	143	144	145	146	147	148	149	150	**30**
	20	121	122	123	124	125	126	127	128	129	130	131	132	133	134	135	**20**
	15	106	107	108	109	110	111	112	113	114	115	116	117	118	119	120	**15**
	10	91	92	93	94	95	96	97	98	99	100	101	102	103	104	105	**10**
	8	76	77	78	79	80	81	82	83	84	85	86	87	88	89	90	**8**
	6	61	62	63	64	65	66	67	68	69	70	71	72	73	74	75	**6**
	4	46	47	48	49	50	51	52	53	54	55	56	57	58	59	60	**4**
	3	31	32	33	34	35	36	37	38	39	40	41	42	43	44	45	**3**
	2	16	17	18	19	20	21	22	23	24	25	26	27	28	29	30	**2**
	1	1	2	3	4	5	6	7	8	9	10	11	12	13	14	15	**1**
		100	**150**	**200**	**300**	**400**	**600**	**800**	**1000**	**1500**	**2000**	**3000**	**4000**	**6000**	**8000**	**10000**	

Dutration (ms)																	
Overpressures (kPa)	**50**	4.0	6.0	8.0	12.0	16.0	24.0	32.0	40.0	60.0	80.0	120.0	160.0	240.0	320.0	400.0	**50**
	40	5.0	7.5	10.0	15.0	20.0	30.0	40.0	50.0	75.0	100.0	150.0	200.0	300.0	400.0	500.0	**40**
	30	6.7	10.0	13.3	20.0	26.7	40.0	53.3	66.7	100.0	133.3	200.0	266.7	400.0	533.3	666.7	**30**
	20	10.0	15.0	20.0	30.0	40.0	60.0	80.0	100.0	150.0	200.0	300.0	400.0	600.0	800.0	1000.0	**20**
	15	13.3	20.0	26.7	40.0	53.3	80.0	106.7	133.3	200.0	266.7	400.0	533.3	800.0	1066.7	1333.3	**15**
	10	20.0	30.0	40.0	60.0	80.0	120.0	160.0	200.0	300.0	400.0	600.0	800.0	1200.0	1600.0	2000.0	**10**
	8	25.0	37.5	50.0	75.0	100.0	150.0	200.0	250.0	375.0	500.0	750.0	1000.0	1500.0	2000.0	2500.0	**8**
	6	33.3	50.0	66.7	100.0	133.3	200.0	266.7	333.3	500.0	666.7	1000.0	1333.3	2000.0	2666.7	3333.3	**6**
	4	50.0	75.0	100.0	150.0	200.0	300.0	400.0	500.0	750.0	1000.0	1500.0	2000.0	3000.0	4000.0	5000.0	**4**
	3	66.7	100.0	133.3	200.0	266.7	400.0	533.3	666.7	1000.0	1333.3	2000.0	2666.7	4000.0	5333.3	6666.7	**3**
	2	100.0	150.0	200.0	300.0	400.0	600.0	800.0	1000.0	1500.0	2000.0	3000.0	4000.0	6000.0	8000.0	10000.0	**2**
	1	200.0	300.0	400.0	600.0	800.0	1200.0	1600.0	2000.0	3000.0	4000.0	6000.0	8000.0	12000.0	16000.0	20000.0	**1**
		100	**150**	**200**	**300**	**400**	**600**	**800**	**1000**	**1500**	**2000**	**3000**	**4000**	**6000**	**8000**	**10000**	

Specific impulse (kPa.ms)

Figure 19: Combination of overpressures and impulses with corresponding case number and positive duration

References

Dan Allason. Buncefield joint industry phase 2 experimental studies, detonation test 4. Technical report, GL Noble Denton, 2013. xiv, 87, 91, 93, 96

ANSYS. ANSYS v13.0 Workbench User's Manual, Centuray Dynamics,2010. 3, 11, 45, 51, 54, 66, 69, 70, 76, 250, 251

ASCE. *Design of Blast Resistant Buildings in Petrochemical Facilities*. Task Commitee on Blast Resistance Design, ASCE, Virginia, USA, 1997. 136, 161, 192, 268

G. Atkinson. Blast damage to storage tanks and steel clad buildings. *Process Safety and Environmental Protection*, 89:382–390, 2011. xiii, xvi, 16, 150, 151, 152, 251, 257

AutoReaGas. AutoReaGas User Documentation and Theory Manual, Century Dynamics,1994. 11

W.E. Baker, P.A. Cox, P.S. Westine, J.J. Kulesz, and R.A. Strehlow. *Explosion Hazards and Evaluation*. Elsevier, Amsterdam, 1983. 43, 250

A.V. Berg. The multi-energy method. *Journal of Hazardous Materials*, 12:1–10, 1985. xiii, 13

J.M. Biggs. *Introduction to Structural Dynamics*. McGraw-Hill, New York, 1964. 3, 36, 40, 241, 244, 248, 249

BMIIB. Explosion mechanics advisory group report. Technical report, London, 2007. 4

T. Borvik, A.G. Hanssen, M. Langseth, and L. Olovsson. Response of structures to planar blast loads - a finite element approach. *Computer and Structures*, 87: 507–520, 2009. 3, 50, 66, 131

S.D. Boyd. Acceleration of a plate subject to explosive blast loading - trial results. Technical report, DSTO Aeronautical and Martitime Research Laboratory, Australia, 2000. xiv, 76, 77, 82

Texas City BP. Investigation report: Refinery explosion and fire. Technical report, BP Texas City, Texas, 2005. 19

B. A. Burgan and D. Moutaftsis. Screening the vulnerability of buildings near hazardous sites. Technical report, Steel Construction Institute, 2009. 48

B.A. Burgan and D. Moutaftsis. Screening the vunerability of buildings near hazardous sites. Technical report, Steel Construction Institute, London, 2011. xvi, 153, 155, 156, 158

D.S. Burgess and M.G. Zabetakis. Bureau of mines investigation report 7752. Technical report, U.S. Bureau of Mines, 1973. 18

CA. Cabp standard fastener range, technical note tn-28 rev 3. Technical report, CA Building Group, 2008. xvi, 158, 159

P. Carlucci, C. Mougeotte, and Huidi J. Validation of ABAQUS explicit - CEL for classes of problems of interest to the U.S. Army . In *Proceedings of 2010 Simulia Customer Conference*, 2010. 51

Chemical Industries Association CIA. Guidance for the Location and Design of Occupied Building on Chemical Manufacturing Sites. CIA/CISHEC. 150

CONWEP. U.S. Army Corps of Engineers, CONWEP - conventional weapons effects, USA, 1991. 68

R.D. Cook, D.S. Malkus, M.E. Plesha, and R.J. Witt. *Concepts and Applications of Finite Element Analysis, 4th Edition.* John Wiley & Sons, U.S., 2002. 56

G.R. Cowper and P.S. Symonds. Strain-hardening and strain-rate effects in the impact loading of cantilever beam. Technical report, Providence, R.I. : Division of Applied Mathematics, Brown University, 1957. 47, 161

R.R. Craig. *Structural Dynamics An Introduction to Computer Methods*. John Wiley and Son, Inc, 1981. 41

A.Y. Elghazouli, C. Malaga-Chuquitaype, and Y. Liu. Ultimate behaviour of cladding assemblages in industrial buildings. In *Eurosteel 2014 International Conference, Naples, Italy, 2014*, 2014. xvi, 166, 167, 175, 225, 271

G.E. Fairlie. Efficient analysis of high explosive air blast in complex urban geometries using the AUTODYN-2d and 3d hydrocodes, analytical and experimental methods. In *15th Int Symposium on the Military Aspects of Blast and Shock*, 1997. 51

A. Soleiman Fallah and L.A.Louca. Pressure impulse diagrams for elastic-plastic-hardening and softening single-degree-of-freedom models subjected to blast loading. *International Journal of Impact Engineering*, 34(4):823–842, 2007. 50

L. Fan, J. Rondal, and S. Cescotto. Finite element modelling of single lap scew connection in steel sheeting under static shear. *Thin-wall structures*, 27:165–185, 1997. 176

U.S. Homeland Security 2003 FEMA, Federal Emergency Management Agency. FEMA426 Reference manual to mitigate potential terrorist attack against buildings. 26, 52

FLACSv9. Users Manual (2009) Users manual for FLACS version 9.0, GexCon AS, 20 January 2009. 11

Hadley. Ultrazed ultrabeam for purlins, cladding rails and floor joists in building shell construction. Technical report, Hadley Group, 2004. xvi, 157, 159, 184, 239

B.A. Izzuddin. A simplified model for axially restrained beam subject to extreme loading. *Steel Structures*, 5:421–429, 2005. 48

A.C. Jacinto, R.D. Ambrosini, and R.F. Danesi. Experimental and computational analysis of plates under air blast loading. *International Journal of Impact Engineering*, 25:927–947, 2001. 50, 81

LIM Jin-seong, KIM Tae-soo, and KIM Seung-hun. Ultimate strength of single shear bolted connections with cold-formed ferritic stainless steel. *Journal of Zhejiang University-SIENCE A (Applied Physics and Engineering)*, 14(2):120–136, 2013. 179

D.M. Johnson. The potential of vapour cloud explosions - lessons from the Buncefield accident. *Journal of Loss Prevention in the Process Industries*, 23:921–927, 2010. 18

G.R. Johnson and W.H Cook. A constitutive model and data for metals subject to large strains, high strain rates and high temperatures. In *Proceedings of the 7th International Symposium on Ballistics*, page 7, 1983. 47, 161

Norman Jones. *Structural Impact*. Cambridge University Press, U.K., 1997. 50

C.N. Kingery and G. Bulmash. Air blast parameters from TNT spherical air burst and hemispherical surface burst. Technical report, US Army Armament Research and Development Centre Ballistic Research Laboratory, 1984. 250

G.F. Kinney and K.I. Graham. *Explosive Shocks in Air*. Springer-Verlag, New York, 1985. xiii, 12, 22, 23, 24, 25, 28, 30, 31, 33, 34, 66

G.S. Langdon and G.K Schleyer. Inelastic deformation and failure of clamped aluminium plates under pulse pressure loading. *International Journal of Impact Engineering*, 28:1107–1127, 1999. 50

G.S Langdon and G.K. Schleyer. Inelastic deformation and failure of profiled stainless steel blast wall panels. part i: experimental investigations. *International Journal of Impact Engineering*, 31:341–369, 2006a. 49

G.S Langdon and G.K. Schleyer. Inelastic deformation and failure of profiled stainless steel blast wall panels. part ii: analytical modelling considerations. *International Journal of Impact Engineering*, 31:371–399, 2006b. 3, 49

G.S Langdon and G.K. Schleyer. Deformation and failure of profiled stainless steel blast wall panels. part iii: finite element simulations and overall summary. *International Journal of Impact Engineering*, 32:988–1012, 2006c. 3, 49

J.F. Lechaudel and Y. Mouilleau. Assessment of an accidental vapour cloud explosion. *Loss Prevention and Safety Promotion in the Process Industries*, 1, 1995. 19

Y.H Liang and L.A. Louca. Corrugated panels under dynamic loads. *International Journal of Impact Engineering*, 34:1185–1201, 2007. 49

L.A. Louca, M. Punjani, and J.E. Harding. Non-linear analysis of blast wall and stiffened panels subjected to hydrocarbon explosions. *Journal of Constructional Steel Research*, 37:93–113, 1996. 3, 49, 247, 273

L.A. Louca, J.W. Boh, and Y.S. Choo. Design and analysis of stainless steel profiled blast barriers. *Journal of Constructional Steel Research*, 60:1699–1723, 2004. 49

LS-DYNA. LS-DYNA 971 Manual,Livermore Software Technology Corporation. 3, 45, 50, 51

B. Luccioni, D. Ambrosini, and R. Danesi. Blast load assessment using hydrocodes. *Engineering Structures*, 28:1736–1744, 2006. 51

G.M. Makhviladze and S.E. Yakush. Large scale unconfined fires and explosions. In *Proceedings of the Combustion Institute Volume (29)*, pages 195–210, 2002. 19

M. Maremonti, G. Russo, E. Salzano, and V. Tufano. Post accident analysis of vapour cloud explosions in fuel storage areas. *Trans. IChemE*, 77, PartB, 1999. 19

W.P. Mercx, A.V. Berg, C.J. Hauhurst, N.J. Robertson, and K.C.Moran. Developments in vapour cloud explosion blast modeling. *Journal of Hazardous Materials*, 71(1-3):301–319, 2000. 14, 15

C. Mougeotte, P. Carlucci, S. Recchia, and H. Ji. Novel approach to conducting blast load analyses using Abaqus/explicit-cel. In *Proceedings of 2010 SIMULIA Customer Conference*, 2010. 52

C.E. Needham. *Blast waves (shock wave and high pressure phenomena)*. Springer, Amsterdam, 2010. 35

T. Ngo, P. Mendis, A. Gupata, and J. Ramsay. Blast loading and blast effects on structures - an overview. *EJSE Special Issue: Loading on structures*, pages 76–91, 2007. 225

O.C.Zienkiewicz and R.L. Taylor. *The Finite Element Method for Fluid Dynamics*. Butterworth-Heinemann, Burlington, 2000. 66

P.Leach. Design charts for elasto-plastic design of cladding panels subject to dynamic loading. In *Proc. Instn Civ. Engrs Strcts and Bldgs*, pages 56–61, 1993. 49

D.K. Pritchard. A review of methods for predicting blast damage from vapour cloud explosions. *Journal of Loss Prevention Process*, 2:187–191, 1989. 12, 14

A.M. Rememnikov. A Review of Methods for Predicting Bomb Blast Effects on Buildings, University of Wollongong Research Online. 51

E. Riks. An incremental approach to the solution of snapping and buckling problems. *International Journal of Solids and Structures*, 15:529–551, 1979. 61

C. Sadee, D.E. Samuels, and T.P. O'Brien. The characteristics of the explosion of cyclohexane at the Nypro (UK) Flixborough plant on 1 june 1974. *Journal of Occupational Accidents*, 3:203, 1977. 18

G.K. Schleyer and S.S. Hsu. A modelling scheme for predicting the response of elastic-plastic structures to pulse pressure loading. *International Journal of Impact Engineering*, 24:759–777, 2000. 3

G.K. Schleyer, S.S. Hsu, M.D. White, and R.S. Birch. Pulse pressure loadings of clamped mild steel plates. *International Journal of Impact Engineering*, 28: 223–247, 1999. 50

L. Schwer. Optional strain-rate forms for the Johnson Cook constitutive model and the role of the parameter $epsilon_0$. In *Proceedings of LS-DYNA Anwenderforum*, pages E–I–1–14, 2007. 47

SCI. Technical Note 5, Design Guide for Stainless Steel Blast Walls. Technical report, Steel Construction Institute, Ascot, 1999a. 49, 53

SCI. Technical note 10, an advanced sdof model for steel members subject to explosion loading: material rate sensitivity. Technical report, Steel Construction Institue, Ascot, 1999b. 53

SCI. Technical note 7, simplified methods for analysis of response to dynamic loading. Technical report, Steel Construction Institute, Ascot, 2002. 3, 48, 53

SCI. Buncefield explosion mechanism phase 1. Technical report, Health and Safety Excutive, London, 2009. xiii, xiv, xvi, 4, 5, 15, 17, 18, 85, 86, 87, 89, 90, 91, 148, 249, 273

P.D. Smith and J.G. Hetherington. *Blast and ballistic loading of structures*. Butterworth-Heinemann, Oxford, 1994. 1, 25

M. Spinelli and R. Vitali. Virtual threaded tire simulation as a desing predictive tool: Application to tire hydrodyplaning. In *Proceedings of SIMULIA Customer Conference*, 2009. xiv, 65

USACE. User's guide for the single-degree-of-freedom blast effects design spreadsheets (sbeds). Technical report, US. Army Corps of Engineers, 2008a. 40, 161, 236

USACE. Single degree of freedom structural response limits for antiterrorism design (pdc-tr06-08 rev 1). Technical report, U.S.Army Corps of Engineers, 2008b. 192

USDOA. Fundamentals of protective design of for conventional weapons, tm-5-855-1. Technical report, US Department of Army (USDOA), 1986. 51, 68

USDOD. Structures to resist the effects of accidental explosions. Technical report, US Department of Defence (USDOD), 2008. xiii, xiv, 25, 46, 47, 52, 76, 136, 161, 192

Frank M. White. *Fluid Mechanics*. The McGraw-Hill Companies, Inc., U.S., 2003. 21

B. Zarkrisson, B. Wikman, and H. Haggblad. Numerical simulations of blast loads and structural deformation from near-field explosion in air. *International Journal of Impact Engineering*, 38:597–612, 2011. 51